Department of Precision and Microsystems Engineering

Measuring the resonances of nanopillars through surface acoustic waves

Qiuxuan Wang

Report no : 2024.084
Coach : Dr. Tomas Manzaneque Garcia
Professor : Dr. Murali Ghatkesar
Specialisation : Micro- and Nano- Engineering
Type of report : Master's Thesis
Date : 20 September 2024

TU Delft Delft University of Technology

Measuring the resonances of nanopillars through surface acoustic waves

by

Qiuxuan Wang

to obtain the degree of Master of Science
at the Delft University of Technology,
to be defended publicly on September 30, 2024

Student number: 5694086
Project duration: September 1, 2023 – September 30, 2024
Thesis committee: Dr. M. K. Ghatkesar, TU Delft, supervisor
Dr. T. Manzaneque Garcia, TU Delft, supervisor

This thesis is confidential and cannot be made public until September 30, 2025.

An electronic version of this thesis is available at `http://repository.tudelft.nl/`.

TU Delft

Contents

1 Literature review **1**

2 Paper **43**

3 Appendix **61**

3.1 Device Design 61
3.1.1 Nanopillar coupling 61
3.1.2 SAW Delay Line Design 63
3.2 SAW Device Fabrication 75
3.2.1 AlN thin film 76
3.2.2 Lithography 78
3.2.3 Lift-off process of electrodes 85
3.2.4 Fabrication results 86
3.2.5 Fabrication variance 88
3.3 Two photon polymerization. 90
3.4 Focused Ion Beam Induced Deposition 102
3.5 Measurement 107
3.5.1 On wafer measurements 107
3.5.2 VNA measurements with PCB 120
3.5.3 TPP Pillars on devices 122
3.5.4 FIB Pillars on devices 127

1

Literature review

MSc Thesis Literature Survey

Measuring the resonances of nanopillars through surface acoustic waves

Qiuxuan Wang

Advisor: Tomas Manzaneque
Murali Ghatkesar

Date: February 5, 2024



Abstract

Resonant mass sensors are new emerging instruments for particle concentration measurement, which utilize the resonance frequencies of oscillatory structures. For this mass sensing technique, minimizing the size of resonators is a trend to achieve high sensitivity and resolution. MEMS and NEMS structures with great potential of achieving high mass resolutions ($< 1\ fg$) are adopted. Literature on different types of resonant mass sensors, with a specific focus on MEMS/NEMS based sensors, has been reviewed. Absence of integrated transduction methods for NEMS nanopillar resonators is identified as the gap in the state-of-the-art. Surface acoustic waves (SAWs) can be utilized for both actuating and measuring the vibrations of nanopillars. The goal of this thesis is to develop integrated transduction methods for nanopillar resonators using SAWs. A surface acoustic wave delay line device will be used to monitor the resonances of nanopillars. Placing nanopillars on the delay line, scattering parameters of the total system will be measured to investigate the interaction of surface acoustic waves and pillars' vibrations. Measuring the resonances of an array of nanopillars is anticipated. The research question: 'How to design and fabricate nanopillar resonator arrays, and characterize their resonances through surface acoustic waves' will be answered in this thesis.

Contents

1 Introduction **3**

2 Particle measurement **4**
2.1 Particulate Matter . . . 4
2.2 Overview of particle measurement instruments . . . 4
2.3 Resonant mass sensor . . . 5
2.4 Conclusion . . . 13

3 Important concepts for nanopillar resonators **14**
3.1 Nanopillar resonators . . . 14
3.2 Mass resolution . . . 15
3.3 Coupling between nanopillars . . . 16
3.4 Conclusion . . . 21

4 Technological basis **22**
4.1 Acoustic transduction . . . 22
4.2 IDT design . . . 25
4.3 Fabrication techniques . . . 31

5 Research approach **35**
5.1 Research question . . . 35
5.2 Planning . . . 36
5.3 Risk analysis . . . 37

1 Introduction

Airborne nanoparticles are gradually becoming a threat to human health. With the advances in nanotechnology and industrial development, new types of nanoparticles are released into the atmosphere. Portable devices that can measure the nanoparticle concentration in real time at any location are especially useful. Current air quality detection methods for particulate matter are mostly based on optical methods targeting PM_{10} and $PM_{2.5}$. For example, the optical particle counter (OPC) based on the light scattering has a minimum detectable size above 100 nm [30]. These particulate monitoring methods are not precise enough for ultrafine particle detection. Resonant mass sensors can be used to measure particle concentration from the resonance frequency shift induced by the collected particle mass. They are usually compact with a small size. These bring out the need for developing resonant mass sensors with high sensitivity and resolution for nanoparticle detection.

For resonant mass sensors, the sizes of resonators have to be miniaturized to achieve high sensitivities. In order to yield a mass resolution within the femtogram level, nanopillars with submicron dimensions can be used. An array of nanopillars will be explored as a solution in this project. To have a transduction method for the nanopillars' vibration that is feasible for miniaturized nanopillars and can be integrated on the same chip, a surface acoustic wave (SAW) delay line is used in this project. The SAW delay line device not only transduces the input electrical signals into SAWs actuating the nanopillars but also transduces the waves after interaction back into electrical signals for analysis. The research problem now is about designing a sensor that combines a SAW delay line and nanopillars to detect particle mass on the femtogram. For this master's thesis, the research question that needs to be answered is: How to measure the resonances of a nanopillar array through surface acoustic waves?

An overview of particle measurement techniques will be discussed in Chapter 2. With the focus on resonant mass sensors, the literature is explored to investigate state-of-the-art microelectromechanical system-based mass sensors. In Chapter 3, more detailed concepts of nanopillar resonators are discussed, including the analytical calculations of resonance frequencies, sensitivity, and mass resolution in mass sensing. Consideration of coupling between nanopillars is also brought up and discussed: strong coupling that can influence the resonance frequencies should be avoided in the later design. In the following Chapter 4, the technological basis of acoustic transduction, SAW device design, and fabrication are introduced. In the last chapter, Chapter 5, the research question of this project is summarized and the research approach is brought up with planning and risk analysis.

2 Particle measurement

2.1 Particulate Matter

Particulate matters are categorized into coarse particles (PM_{10}), fine particles ($PM_{2.5}$), and ultrafine particles ($PM_{0.1}$), with diameters smaller than 10 micrometers, 2.5 micrometers, and 100 nanometers respectively. As one of the most harmful air pollution types in the world, these suspended particles have a significant effect on causing lung diseases and other health problems. Through breathing, PM_{10} particles accumulate in the bronchi and lung regions, $PM_{2.5}$ particles can infiltrate the gas exchange regions with the lungs while $PM_{0.1}$ can potentially pass through the lungs and impact other organs [36]. $PM_{0.1}$ particles are believed to have greater harm and hazards that have not been well-studied. Thus, the ultrafine particles $PM_{0.1}$ are the main targets for the particle monitoring discussed in this work.

The carbonaceous matter is a major component of the ambient ultrafine particles. Black carbon, defined as the "carbonaceous component of PM that absorbs all wavelengths of solar radiation", is estimated to have a global emission of around 7600 gigagrams [25]. The properties of ambient air black carbon particles from three major sources are listed in Table 2.1. Engineered nanoparticles (ENPs) as another contribution of airborne ultrafine particles have gradually raised public attention. The increased application of ENPs rapidly increases their presence in nature. With the nano-sized feature, these artificially synthesized ENPs have special properties and are widely used in medicine, electronics, and other applications. For example, in cosmetic products titanium dioxide (TiO_2) nanoparticles and zinc oxide (ZnO) nanoparticles are used as UV filters for sun protection function [48]. Accordingly, engineered nanoparticles are widely applied in industrial and commercial products, and thus inevitably released into the environment. The most abundant ENPs in the environment: TiO_2, Ag, and ZnO nanoparticles are listed in Table 2.1.

Table 2.1: Speicific ultrafine particles

	Type	Particle size (nm)	Density (g/cm3)	Approximate mass (fg)
Engineered nanoparticles (ENPs) [13]	TiO_2	20-60	4.23	0.0177-0.478
	Ag	10-34	5.6	0.00293-0.115
	ZnO	2-30	10.49	0.0000439-0.148
Ambient black carbon particles [25]	Diesel Exhaust Emissions	60-100	1.5	0.170-0.785
	Gasoline Engine Exhaust	100-300	1.42-1.82	0.744-25.7
	Open Biomass Burning Emissions [32]	100-160	1.2-1.4	0.628-3.00

2.2 Overview of particle measurement instruments

For the monitoring of particulate matter, measurements are divided into two types. One is particle concentration measurement, which measures the amount of particles of a certain volume in number or mass. The other one is particle size distribution measurement, which requires both the measurement of size and concentration. In the size distribution type of measurement, techniques are usually based on the geometry size, inertia, mobility, and electrical mobility of the particle to classify or separate the particles [12]. In the particulate matter concentration measurements, the existing commercialized techniques are in three main fields: gravimetric methods, optical methods, and microbalance methods. The gravimetric methods determine the PM concentration by evaluating the mass collected by the filters. The principle of this kind of method is simple but performance is limited. Optical methods use either light scattering, light absorption, or light extinction as a combination of both. Particulate matters interact with the incident lights and make the influence dependent on the PM concentration. Microbalance

methods use the induced resonance frequency shift to read the mass of collected particles. The main instruments already used for PM detection are Tapered Element Oscillation Microbalance (TEOM) and Quartz Crystal Microbalance (QCM). Also by reading the frequency change, resonant mass sensors can be used for particle detection and are promising in PM monitoring. Besides QCM, Film Bulk Acoustic Resonator (FBAR), Surface Acoustic Wave (SAW), and some emerging MEMS/NEMS-based sensors have shown their strength in mass sensing. The classification and some common instruments of the above-mentioned methods are listed in Figure 2.1.

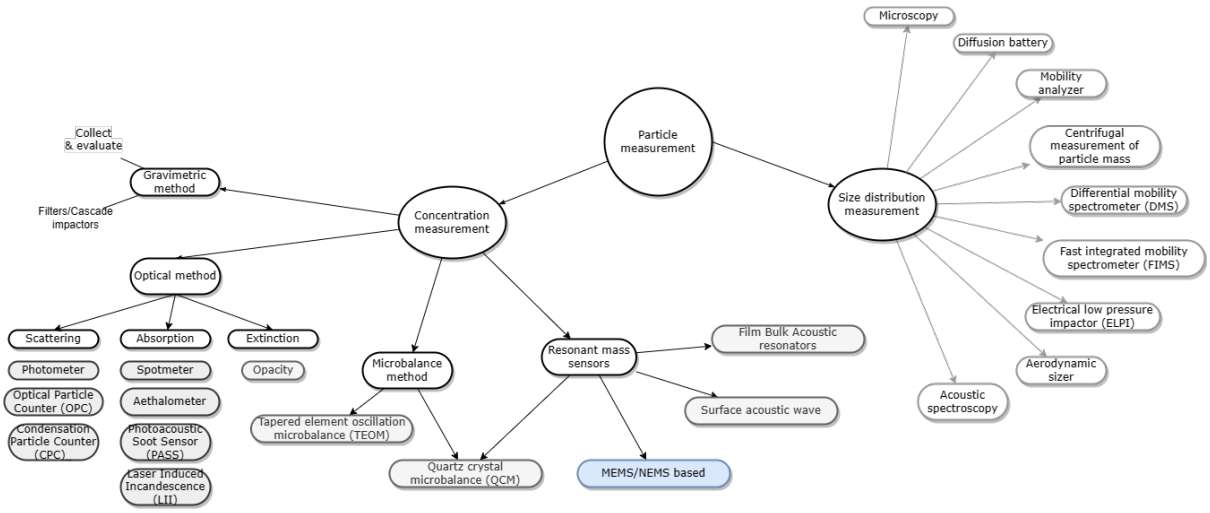


Figure 2.1: Particle measurement techniques

Gravimetric methods have limited detection range and long sampling time due to the particle collecting process with filters; optical methods involve laser beams making the system complicated and bulky. For resonant mass sensors, the resonance frequency is continuously monitored in real time. In addition, by miniaturizing the resonator, the sensors have the potential to achieve chip size and integration into cell phones. Overall, resonant mass sensors can achieve real-time sampling and are portable, further developments with these sensors are appealing.

2.3 Resonant mass sensor

2.3.1 Quartz crystal microbalance (QCM)

Quartz crystal microbalance sensor uses the piezoelectric effect of a quartz crystal plate which is sandwiched between the top and bottom electrodes. As shown in Figure 2.2, the Quartz plate will vibrate in thickness shear mode with an AC potential signal applied between the electrodes. The equation of resonance frequency shift Δf and added mass Δm was first given by Sauerbrey in 1959 [34]:

$$\frac{\Delta f}{f_0} = -\frac{2Nf_0\Delta m}{A_e\sqrt{\mu_q\rho_q}} \tag{2.1}$$

where f_0 is the unloaded resonance frequency, N = 1,3,... represents the odd harmonic overtone, A_e is the effective surface area, μ_q is the crystal shear modulus and ρ_q is the crystal density. The deposited mass Δm is assumed to be distributed evenly on the effective surface area.

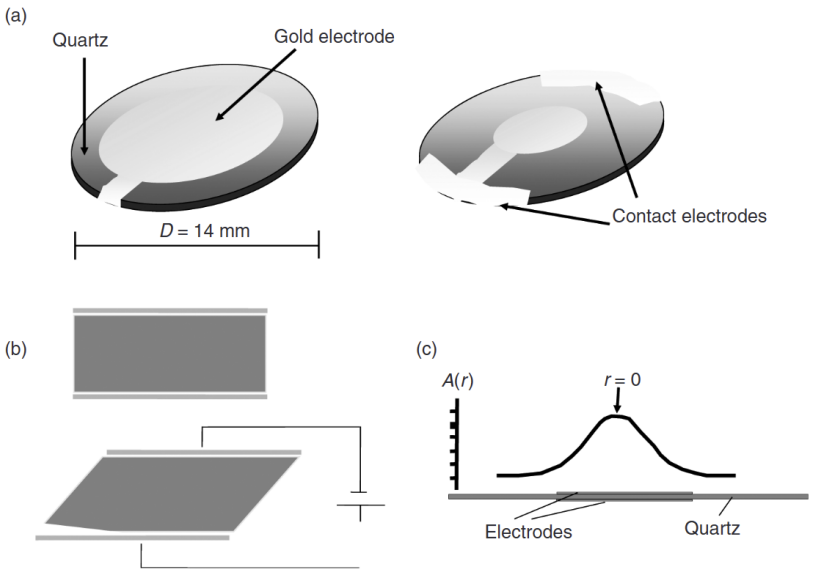


Figure 2.2: Quartz crystal microbalance design (a) Top and bottom view of a QCM. (b) Vibration mode with an applied AC voltage. (c) Vibration amplitude distribution along the diameter of the plate. [24]

In Yoshimine's study, a QCM with 27MHz fundamental frequency is observed with a sensitivity of $1.6Hz \cdot cm^2/ng$ in the air which accords well with Equation 2.1. With the Au-electrode area of their device of $3.3mm^2$, the sensitivity of frequency shift per added mass is calculated as $48Hz/ng$. The study result shows a frequency noise level of 0.05Hz from which a mass resolution of 1 pg can be calculated. [51]. The quality factor is influenced by the acoustic losses and electric losses and was determined to be around 20000 for a QCM device [43].

Quartz crystal microbalance is a well-developed technique for particle sensing. The principle requires added mass to be uniformly distributed on the quartz crystal surface and measures the added mass per unit area. QCM typically measures the mass on the nanogram level and the device size is usually on the millimeter scale which is large compared to MEMS resonators. It is commonly used to detect molecules for chemistry and biosensor applications.

2.3.2 Film bulk acoustic resonator (FBAR)

Film bulk acoustic resonator has a similar structure and uses bulk acoustic waves as well as QCM sensors, but the dimension is much smaller. Piezoelectric thin films are used between the electrodes which greatly reduce the active area into micrometer scale. The vibration exhibits thickness extensional mode or thickness shear mode depending on the crystal orientation of the piezoelectric film. To generate resonance, the sandwiched piezoelectric film needs to be isolated from the substrate to generate the standing wave, and two main types of structure designs using a Bragg reflector or an air cavity are used [52], as shown in Figure 2.3.

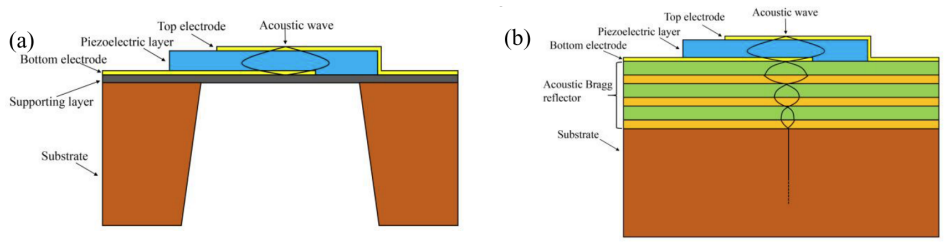


Figure 2.3: Two types of film bulk acoustic resonators: (a) air-cavity resonator and (b) solidly mounted resonator [49]

Sauerbrey's equation can still describe the frequency shift of FBAR with some modification [52]:

$$\Delta f = -\frac{2f_0^n}{A_e\sqrt{\mu\rho}}\Delta m \tag{2.2}$$

where n is a numerical parameter with a value between 1-2.

The footprint of an FBAR sensor is usually smaller than $0.05mm^2$ compared to around $150mm^2$ for a QCM device [7]. Due to the significantly smaller dimension, the working frequency and sensitivity of FBAR devices are far above QCM devices, which in a way compromises the inferior quality factor. In the work of Black et al, an FBAR sensor for particulate monitoring was designed and measured with a sensitivity of 1192 $Hz\ cm^2/ng$ at 1.6GHz resonance frequency, and the device resolution achieved 1pg [5]. Weber et al found the quality factor of an FBAR device to be 285 in air and gave an active area of $0.04mm^2$ [43]. With this active area value, the sensitivity of an FBAR device in the unit of Hz/pg can be estimated as 2980 Hz/pg.

Film bulk acoustic resonators have a significantly smaller size compared to QCM, which have similar structures but use piezoelectric thin films instead of quartz crystal. This reduction in size, especially in thickness direction which is reduced to the micrometer range, provides great advantages to FBAR: extremely high working frequency range and sensitivity. One shortcoming of FBAR is its comparatively low quality factor. Furthermore, for the use of particle concentration measurements, the reduction in active area compromises the sensor's sensitivity to concentration. However, FABR still shows its superiority among other resonant mass sensors due to its high performance, small size, and mature fabrication process.

2.3.3 Surface acoustic wave (SAW)

Instead of using the bulk acoustic wave, surface acoustic wave devices use the wave generated on the piezoelectric film by the deposited interdigital transducer (IDT). IDTs transduce the applied electric potential signal into the mechanical SAW signal at the piezoelectric substrate and vice versa. SAW devices have two forms, one is the SAW delay line and the other is the SAW resonator.

In a delay line device, two sets of IDTs are deposited with a distance separation, as shown in Figure 2.4. The sensing area is a region between the IDTs, where particles being sensed will come to rest and accumulate mass. Surface acoustic waves are generated by the input IDT on one side, propagating through the sensing area, and being converted back into an electric signal by the output IDT on the other side. Due to the existence of the added mass, a shift of center frequency can be observed. The center frequency of the unloaded device is determined by the distance between fingers in IDTs, which is discussed in Section 4.2.

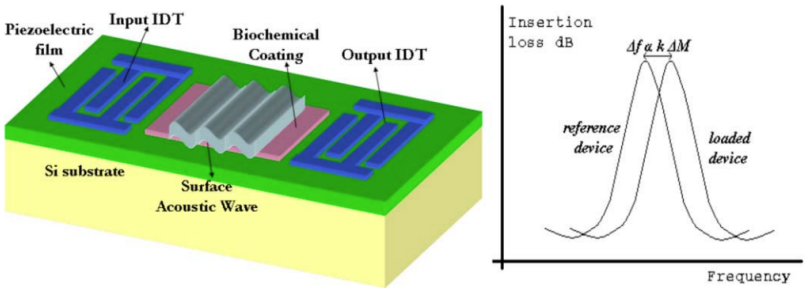


Figure 2.4: SAW delay line [39]

A SAW resonator has a pair of reflectors on two sides of the device in addition to IDTs. A two-port SAW resonator is shown in Figure 2.5. The two reflectors create a resonant acoustic cavity and form the surface acoustic wave generated by the IDT into standing waves and the center frequency is determined by the distance between reflector strips [3]. The mechanical energy is confined in the acoustic cavity, thus the SAW resonator has a higher quality factor than the SAW delay line. Similar to the SAW delay line sensor, the added particle mass will shift the device center frequency which is measured by an oscillator circuit in real-time.

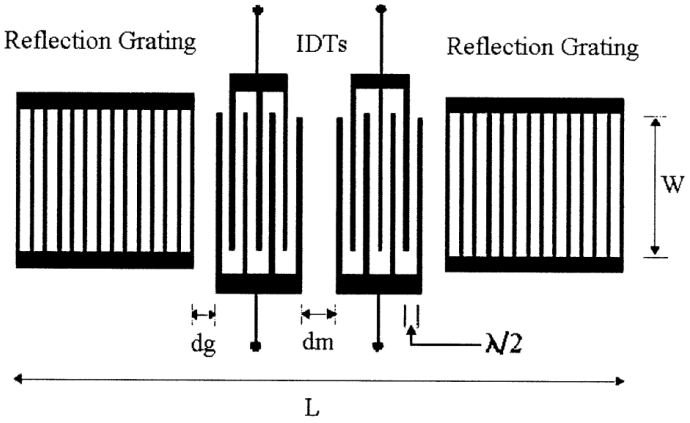


Figure 2.5: Two port SAW resonator [38]

Surface acoustic wave mass sensors are normally used to detect biological species. Tigli et al reported their COMS-SAW biosensor with a sensitivity of 0.1149 Hz/pg which adopted delay line configuration [39]. A two-port SAW resonator was used by Stubbs et al for a vapor phase biosensor and achieved a sensitivity of 4.3Hz/pg with a minimum detectable mass around a few picograms [38].

SAW devices utilize the perturbation in wave propagation caused by the surface modulation. The modulation can be deposited mass or other mechanical property changes. These kinds of devices are microelectromechanical systems and show better sensitivity than QCM. SAW devices have small sizes and are easy to fabricate, they are commonly used in sensing applications such as chemical sensors, biosensors, temperature sensors, etc.

2.3.4 MEMS/NEMS based

Micro-electromechanical systems (MEMS) and nano-electromechanical systems (NEMS) have been integrated into resonant mass sensors in recent studies.
Wasisto et al developed a mass sensor with a complete setup using MEMS cantilever resonator for the detection of airborne nanoparticles [42]. The cantilever shown in Figure 2.6 was etched from a silicon wafer with a dimension of 1250 μm in length, 30 μm in width, and 25 μm in thickness. The vibration of the cantilever was actuated by a piezoelectric actuator which is connected under the bottom end of

the cantilever. The piezoresistive method was used for the transduction of cantilever vibration by a full Wheatstone bridge. The measurement setup of the sensor is shown in Figure 2.7. The frequency of the resonator was measured as 43.92 kHz and the quality factor was fitted as 1206. With the resonance frequency value and the known resonator mass, the sensor sensitivity was calculated as 10 Hz/ng. For the application of nanoparticle detection, an electrostatic precipitator was used to attract the particles in order to enhance the collection efficiency.

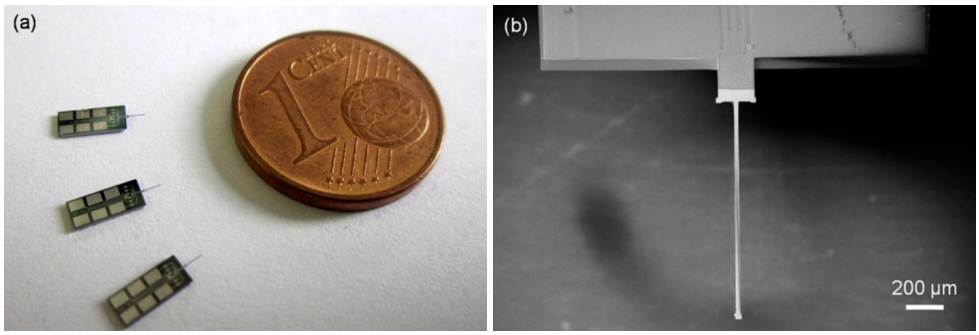


Figure 2.6: Fabricated MEMS cantilever particle mass sensor [42]

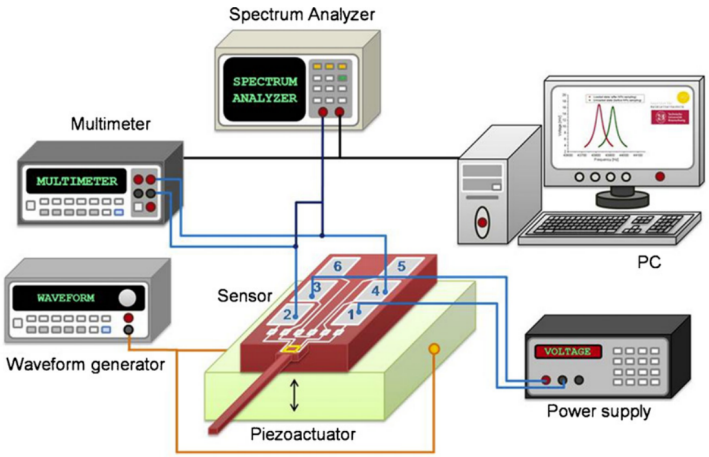


Figure 2.7: Frequency measurement setup for the MEMS cantilever sensor [42]

Joshi et al presented another MEMS cantilever mass sensor in a laminated structure [16]. A ZnO piezoelectric layer was sandwiched between two Pt electrode layers, all of which were deposited on a Si layer, with an additional mass-loading ZnO layer on top. The cross-section is shown in Figure 2.8. The cantilever has a length of 100 μm, a width of 60 μm, and a thickness of 8.1 μm. The cantilever was piezoelectric actuated by applying AC signals and the deflection was measured using a laser Doppler vibrometer, which is also shown in Figure 2.8. The resonance frequency was observed as 735.468 kHz and the mass sensitivity as 0.3138 Hz/pg. The quality factor of the unloaded cantilever calculated by $f/\Delta f$ was 782.

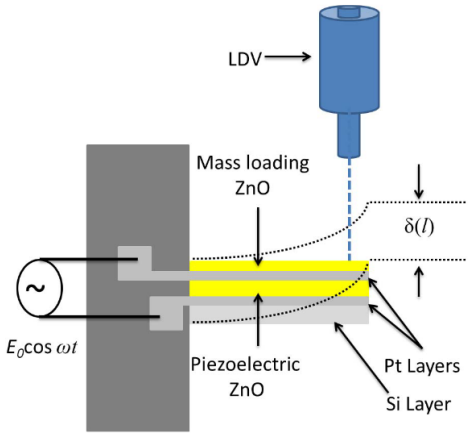


Figure 2.8: Cross-section view of the composite MEMS cantilever sensor [16]

A thin-film piezoelectric-on-silicon (TPoS) MEMS resonator was developed by Weng et al [45]. As shown in Figure 2.9, the resonator was composed of a suspended Si substrate and a piezoelectric PZT layer sandwiched by Au top electrodes and bottom Pt electrode. With an AC voltage signal applied to the top electrode on the input side, the resonator would undergo the designed length extension mode and the vibration would be read out from the output electrode. The size of the substrate was 680 $\mu m \times 200\ \mu m$. The piezoelectric layer and bottom electrode had dimensions of 250 $\mu m \times 200\ \mu m$, while the top electrodes measured 230 $\mu m \times 850\ \mu m$. The resonant frequency was calculated as 5.57 MHz from the COMSOL simulation and was measured as 5.12 MHz from open-loop and closed-loop measurements. A quality factor of 311 in ambient air was recorded. The sensitivity of the resonant sensor was measured to be 4.96 Hz/pg. The mass resolution, determined from the measured Allan deviation, was found to be 0.54 pg.

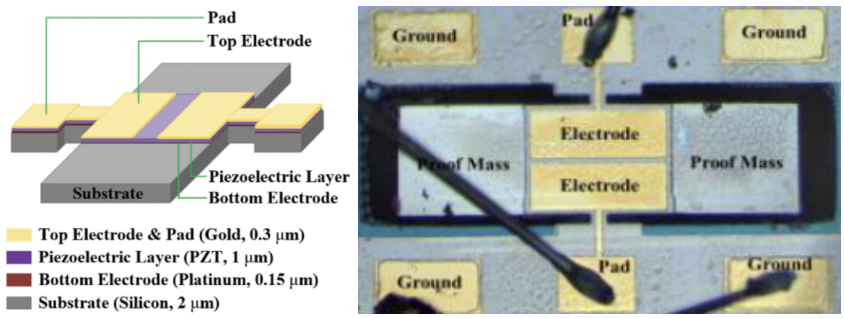


Figure 2.9: MEMS TPoS resonator [45]

Hajjam et al demonstrated a MEMS thermally actuated I-Shaped Bulk Acoustic Resonator for sub-micron air-borne particle measurement [14]. The resonator adopted a dog-bone shape, with current applied from one side to the other side, heat was generated mostly in the middle thin flexures, as the slender shape gives a higher resistance (Figure 2.10). The fluctuating current led to the temperature fluctuation and actuated the resonator's in-plane mode. The vibration was detected through the piezoresistive effect, which responded to the stress in the flexures from the vibration. The resonator was 2.7 μm thick and 29.9 μm wide, two flexures in the middle were 14 μm long and 1.9 μm wide. Additional dimensions indicated in Figure 2.10 are: b : 20 μm, c : 7 μm. The sensitivity of the device was calculated as 1727 Hz/pg and measured with 1593 Hz/pg. With a minimum detectable frequency shift of 10 Hz, the corresponding detectable mass is 7 fg. Nonetheless, the presence of temperature-induced frequency drift limited the mass resolution to 6 pg.

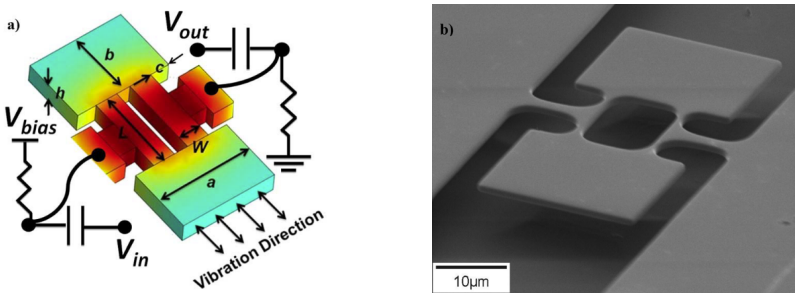


Figure 2.10: Thermally actuated I-Shaped Bulk Acoustic Resonator [14]

To further miniaturize the resonator dimension, Wasisto et al. developed nanopillars for nanoparticle measurements [41]. Nanopillars were fabricated by photo-lithography and etching processes from a silicon wafer. The resulting nanopillars have an average diameter of 650 nm and a height of 40 μm. As shown in Figure 2.11, the nanopillar was actuated by a piezo actuator attached beneath, and the resonant mode was observed in the scanning electron microscope (SEM) chamber. Experiments yielded a sensitivity of around 7.22 Hz/fg, which is approximately three times larger in magnitude than that of the previous MEMS resonators. The mass resolution was estimated to be 1.5 fg from the 10 Hz frequency resolution. Compared to the previous resonant sensors, the nanopillar significantly improved the mass resolution to the femtogram level.

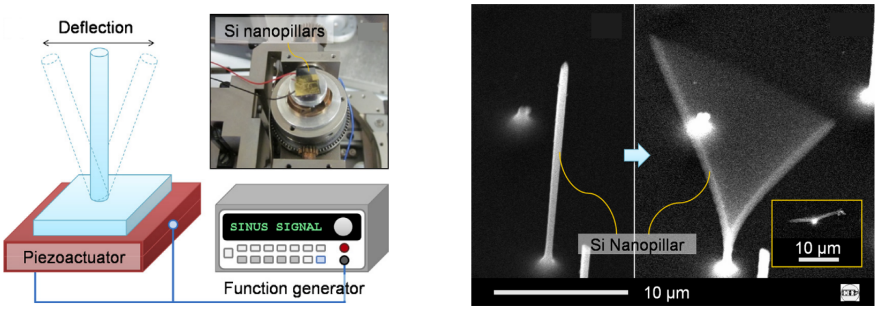


Figure 2.11: A resonant nanopillar sensor (a) Schematic of the measurement setup (b) SEM images of the stationary and resonant nanopillar [41]

Schmid et al presented a nanofiber resonator that achieved the detection of single 100 nm silver nanoparticles [35]. The nanofiber was etched from a silicon nitride layer and coated with a layer of Aluminum, resulting in dimensions of 50 μm in length, 1240 nm in width, and 150 nm in thickness. The actuation of the fiber was achieved magnetically by applying alternating current through the fiber while subjecting it to a static magnetic field. The read-out was realized by a laser Doppler vibrometer. The resonator showed an excellent sensitivity of 203 Hz/fg and a mass resolution of 740 ag.

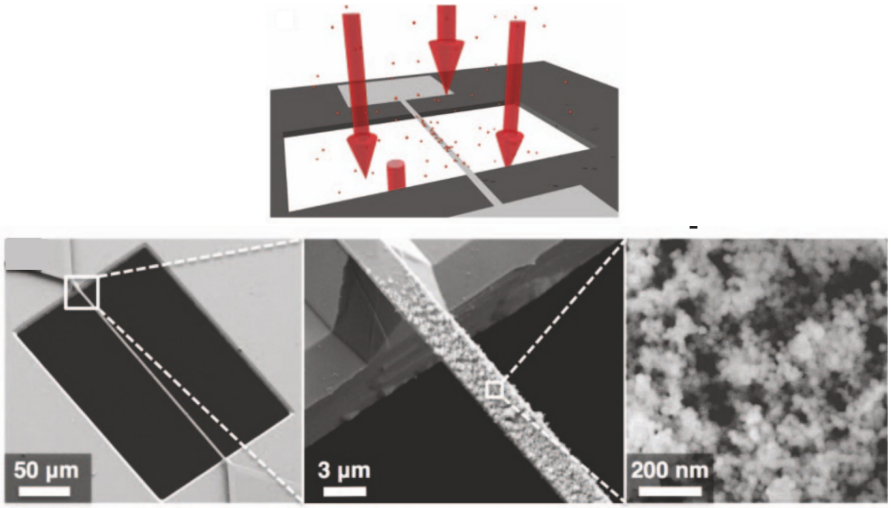


Figure 2.12: Resonant nanofiber [35]

Overall, a general trend can be observed in these MEMS and NEMS resonant sensors: as the dimensions decrease, the resonance frequency of the sensor increases. This higher frequency, in turn, results in higher sensitivity.

2.3.5 Summary

Representative sensors from different types of resonant mass sensors are listed and compared in the following table. The quartz crystal microbalance exhibits the lowest sensitivity but the highest quality factor. Surface acoustic wave sensors exhibit higher sensitivity than QCM but lower than the other options. Film bulk acoustic resonators have better sensitivity over MEMS resonators. However, one drawback of FBAR is the low quality factor. It can be seen that QCM, SAW, FBAR, and MEMS all exhibit mass resolutions on the order of picograms. Only NEMS resonators improved mass resolution to the femtogram level. NEMS resonators achieve supreme sensitivity and resolution due to their miniaturized dimensions.

Table 2.2: Comparison of different resonant mass sensor

	Sensitivity	Resolution	Quality factor
Quartz Crystal Microbalance (QCM)	0.048 Hz/pg [51]	1 pg [51]	20000 in air [43]
Surface Acoustic Wave (SAW)	0.1149 Hz/pg [39] 4.3 Hz/pg [38]	∼1 pg [38]	
Film Bulk Acoustic Resonator (FBAR)	2980 Hz/pg [5]	1 pg [5]	285 in air [43]
MEMS Resonator	4.96 Hz/pg [45] 1727 Hz/pg [14]	0.54 pg [45] 6 pg [14]	1206 in air [42]
NEMS Resonator	7220 Hz/pg [41] 203090 Hz/pg [35]	1.5 fg [41] 0.74 fg [35]	1200–1700 in vacuum [41]

QCM uses quartz crystal as the piezoelectric material, with dimensions usually a few millimeters. FBAR also utilizes bulk acoustic waves and has a similar structure as QCM, but it uses piezoelectric thin films instead of quartz crystal and the sizes are usually only a few hundred micrometers. Some MEMS devices also use bulk acoustic waves but with novel structures and actuation methods and further reduce the dimensions. For resonant sensors, the sensitivity is proportional to the resonance frequency. Smaller resonators have higher resonance frequencies. Thus, to achieve a mass resolution within 1 fg, resonators with dimensions in the nanometer scale are preferred.

2.4 Conclusion

Nanoparticles, with diameters less than one micrometer and masses usually below one femtogram, have severe negative impacts on human health. The emissions to the environment of these particles continue to be a pressing social problem. Thus, the detection of nanoparticles is of great importance. The research problem addressed in this thesis is the development of resonant mass sensors with mass resolutions within the femtogram level. This thesis project is focused on measuring the resonance frequencies for these resonant mass sensors.

Among all the existing ambient particle measurement techniques, the acoustic-based resonant mass sensors use the resonance frequency shifts induced by the added mass of the collected particles. The principle of this type of sensor gives it the quality of real-time measurement and small portable size. From the comparison in Chapter 2.3.5, it is discussed that MEMS and NMES based resonant sensors have superior sensitivity and mass resolution compared to other conventional resonant mass sensors like QCM, SAW, and FBAR. This is due to the smaller size of the NEMS/MEMS resonators and for these micro and nano systems further reducing the dimension can bring the sensitivity even higher. The takeaway message here is that NEMS-based resonators should be used to achieve the goal of high sensitivity and mass resolution of this project. Nanopillar as an easy-to-fabricate nanostructure is suggested for this project.

3 Important concepts for nanopillar resonators

3.1 Nanopillar resonators

Nanopillars, with their unique properties, have been used in various fields. In the application to photonic devices and solar cells, nanopillars show great potential in fluorescence enhancement[44] and light absorption[10]. Other than these, Martines et al reported a superhydrophobic surface texture with nanopillar arrays [27] and structures like nanopillars were found capable of increasing the adhesion of proteins and cells [17].

For the application of mass sensing, nanopillars are used as resonators. The first bending mode resonance is mostly used and the resonance frequency shift is associated with mass loading. The extremely small size of nanopillars enables them with large sensitivity as discussed in the last chapter. By putting an array of high surface-to-volume ratio nanopillars, good absorption and a large collection area for small substances can be achieved.

For a nanopillar, the bottom end is fixed to the substrate and the top end is free. The vibration of a nanopillar is similar to a cantilever beam and thus Euler-Bernoulli beam theory can be applied. In this project, the coordinate system is set so that the pillar height is in the z-direction and the horizontal component of pillar vibrational displacement is in the y-direction. The resonance frequency can be calculated from:

$$\frac{\partial^2 y}{\partial t^2} + \frac{EI}{\rho A}\frac{\partial^4 y}{\partial z^4} = 0 \tag{3.1}$$

and the boundary conditions:

$$\begin{aligned} &y = 0,\ \frac{dy}{dz} = 0 \quad at\ z = 0 \\ &\frac{d^2 y}{dz^2} = 0,\ \frac{d^3 y}{dz^3} = 0 \quad at\ z = h \end{aligned} \tag{3.2}$$

The resonance frequencies of the pillar take the form of

$$\omega_n = \frac{f_n}{2\pi} = \frac{\beta_n^2}{h^2}\sqrt{\frac{EI}{\rho A}} \tag{3.3}$$

where n represents the n^{th} flexure mode, and $\beta_1 = 1.875,\ \beta_2 = 4.694,\ \beta_3 = 7.854,\ \beta_4 = 10.996,\ ...$
Since the pillar cross-section is a circle with a diameter of d, the resonance frequencies are sorted as:

$$f_n = \frac{\beta_n^2 d}{8\pi h^2}\sqrt{\frac{E}{\rho}} \tag{3.4}$$

The sensitivity calculation of the nanopillar is general for resonant mass sensors. The added mass is assumed to be extremely small compared to the resonator's total mass, $\Delta m << m$.With the assumption that it can be treated as mass added uniformly to the whole resonator, the ratio of the effective mass change to the total effective mass is approximately equal to the added mass divided by the total mass.

$$\frac{\Delta m_{eff}}{m_{eff}} \approx \frac{\Delta m}{m} \tag{3.5}$$

For a simple harmonic resonator, the resonance frequency can be written as

$$f = \frac{1}{2\pi}\sqrt{\frac{k_{eff}}{m_{eff}}} \tag{3.6}$$

It can be obtained that

$$\frac{\Delta f}{\Delta m_{eff}} \approx \frac{\partial f}{\partial m_{eff}} = -\frac{f}{2m_{eff}} \tag{3.7}$$

The sensitivity is defined by $Sensitivity = \frac{\Delta f}{\Delta m}$ with extremely small frequency shift and mass change. Thus, with Equation 3.5 and Equation 3.7, sensitivity can be derived as

$$Sensitivity = \frac{\Delta f}{\Delta m} = \frac{\Delta f}{\Delta m_{eff}}\frac{\Delta m_{eff}}{\Delta m} = -\frac{f}{2m_eff}\frac{m_{eff}}{m} = -\frac{f}{2m} \tag{3.8}$$

3.2 Mass resolution

The mass resolution of a resonant sensor is determined by both the sensitivity of the sensor and the frequency resolution of the system.

$$\delta m = -\frac{2m}{f}\delta f = \frac{1}{Sensitivity}\delta f \tag{3.9}$$

3.2.1 Ultimate mass resolution

If the frequency resolution value is certain, sensors with higher sensitivity yield better mass resolution. Although frequency resolution is affected by many factors, the minimum detectable frequency shift of a system can be diminished by designing the extrinsic readout circuit. If ideally all noises in the external circuit are eliminated ultimately, thermomechanical noise will always exist limiting the sensor performance. Approaching this minimum frequency uncertainty by optimizing the readout system, the resolution is associated with the resonator and specifically related to the resonator design. The ultimate mass resolution of a resonant mass sensor is calculated from this frequency uncertainty contributed by the thermomechanical noise.

The thermomechanical force exerted on the resonator has a white noise frequency distribution. The one-sided spectral density is

$$S_{thm}(\omega) = 4M_{eff}\frac{\omega_0}{Q}k_BT \tag{3.10}$$

where M_{eff}, ω_0, and Q are the effective mass, resonance frequency, and quality factor of the resonator. k_B is Boltzmann's constant and T is the temperature. The power spectral density of frequency noise is approximated as [6]

$$S_\omega(\omega) \approx \frac{M_{eff}\omega_0^3 k_B T}{A_0^2 Q^3} \tag{3.11}$$

in a closed-loop measurement system. A_0 in the equation represents the amplitude of the resonator actuating signal. This relation is valid only for the large averaging time τ used in the Allan Deviation. Allan Deviation is commonly used to describe the frequency stability [6]

$$\sigma_y^2(\tau) = \int_{-\infty}^{\infty}\frac{S_\omega(\omega)}{\pi\omega_0^2}\frac{sin^4(\tau\omega/2)}{(\tau\omega/2)^2}d\omega \tag{3.12}$$

By substituting Equation (3.11) to the above equation, Allan Deviation of the frequency stability due to the thermomechanical noise can be calculated analytically as

$$\sigma_y^2(\tau) = \frac{M_{eff}\omega_0 k_B T}{A_0^2 Q^3}\frac{1}{\tau} \tag{3.13}$$

for large τ.

Both the sensitivity and Allan Deviation due to thermomechanical noise are considered to evaluate the mass sensor in order to achieve resolution within the femtogram. To achieve high mass resolution, low resonator mass, and high quality factor are desired.

3.3 Coupling between nanopillars

strain-coupled

Strain coupling exists between closely placed nanopillars. The dynamics of a coupled nanopillar pair was studied by Doster et al [8]. As shown in Figure 3.1 (a), two nanopillars of 310 nm radius and a distance of 1.3 μm were etched out of a substrate. The nanopillars were actuated by a piezo actuator and the corresponding vibrations were observed. When one of the nanopillars was driven to a large vibration amplitude, a small vibration of the other pillar was always observed, and this could be verified from the insets in Figure 3.1 (b). The involvement of the second nanopillar in the nanopillar resonant showed the existence of the coupling mode. This was a strong coupling between the nanopillar pair with the observation of an avoided level crossing. By tunning the eigenfrequency of one nanopillar to the frequency of the other pillar, the avoided crossing is shown in Figure 3.1 (b). In the process of obtaining this effect, a laser was focused on the tuned pillar and generated heat which decreased the resonant frequency, subsequently, the pillar without tuning also changed. Adding mass to a nanopillar has the same effect of reducing the resonance frequency, with more and more mass added to the pillar, the curves go to the right side of Figure 3.1 (b), and the resonance frequency of the second pillar turns at the point close to the current resonance frequency of the tuned pillar. This effect can be undesirable in particle mass sensing, as it is hard to interpret whether the frequency shifts due to the accumulated particle mass or coupling.

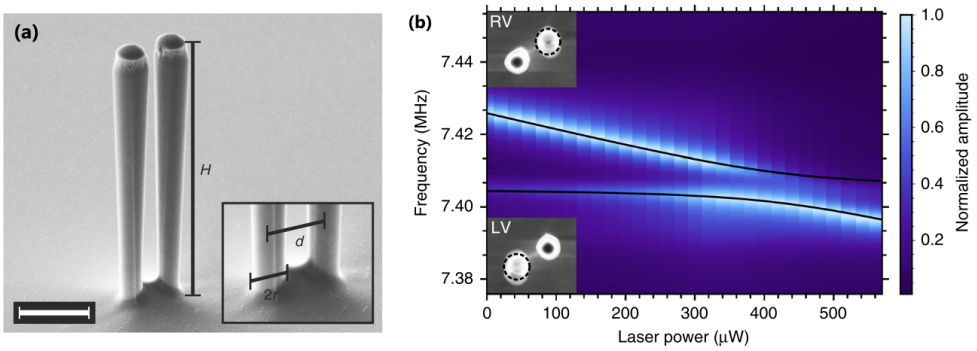


Figure 3.1: (a) A pair of nanopillars; (b) strong coupling with an avoided crossing by thermal tuning [8]

To avoid this strong strain coupling, separating either the eigenfrequencies of the nanopillars or the geometry distance between them is feasible. In the case of an identical pair of nanopillars, the geometry dependence of the coupling strength was studied [8]. As shown in Figure 3.2, increasing distance, reducing radius, and increasing height of pillars can all reduce the strength of strain coupling.

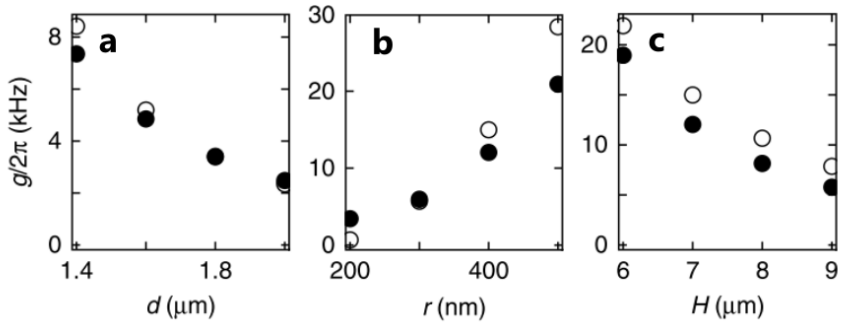


Figure 3.2: Coupling strength as a function of (a) distance between pillar pair d, (b) pillar radius r, and (c) pillar height H from simulation [8]

SAW-coupled

The coupling between nanopillars on a substrate through surface acoustic waves is different from the normal coupling in which the interaction of two resonators happens instantaneously. For the pillars placed on a piezoelectric substrate, the SAW generated on the substrate by the pillar takes time to propagate from one spot to another spot. Thus, the influence of one pillar on the other pillar has a time delay, which is the distance between two pillars divided by the wave velocity. A model for the coupling between a pillar pair through SAWs was presented and compared to the instantaneous spring-like coupling [20]. The equations of motion of two SAW-coupled resonators were given as:

$$\begin{aligned} \ddot{y}_1 + \frac{\omega_1}{Q_1}\dot{y}_1 + \omega_1^2 y_1 - \frac{F_{SAW}(\ddot{y}_2, d, \omega)}{m_1} = 0 \\ \ddot{y}_2 + \frac{\omega_2}{Q_2}\dot{y}_2 + \omega_2^2 y_2 - \frac{F_{SAW}(\ddot{y}_1, d, \omega)}{m_2} = 0 \end{aligned} \tag{3.14}$$

F_{SAW} is the force applied to the second resonator by the surface acoustic wave emitted from the first resonator, and given as $F_{SAW}(\ddot{y}, d, \omega) = A_{SAW}(d)(-gm\ddot{y})e^{-i\Delta\phi(d,\omega)}$. A_{SAW} represents the amplitude attenuation of the emitted SAW at the location of the second resonator, $\Delta\phi$ is the phase difference between the emitted SAW at the second resonator and the emitting resonator, and g is the coupling strength of the SAW to the resonator's vibration. With an initial condition that the emitting resonator was displaced and the second resonator at rest, the vibration amplitudes of two resonators in the SAW-coupled model were calculated and compared to the spring-coupled model by Kahler et al, as shown in Figure 3.3. Different from the spring-coupled case, two resonators exchanged energy until they reached the same amount of energy, as seen in Figure 3.3 b, the blue and yellow curves for two resonators coincided after around 1.5 μs. With the comparison, it could be seen that the energy dissipation is smaller in SAW coupling and thus higher quality factor due to the much slower amplitude decay.

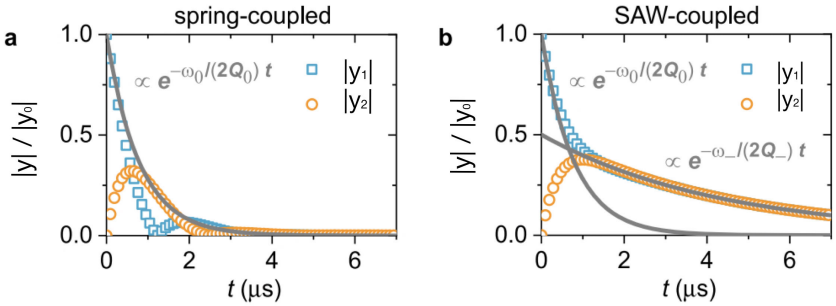


Figure 3.3: Amplitudes of two resonators in the time domain for (a)spring-coupled and (b)SAW-coupled model, modified from [20]. The grey line in (a) is the amplitude of a single resonator and the grey lines in (b) are that of a single resonator and two resonators in antisymmetrical vibrating mode.

Another study about SAW-coupled resonators was demonstrated by Raguin et al [31]. To investigate how the SAW actuated pillars coupled, the experiment setup as shown in Figure 3.4 (a) was used. Surface acoustic waves were emitted by an interdigital transducer, the vibration of pillars was captured by laser scanning heterodyne interferometry, and the effect of SAW impinging direction was investigated by positioning pillars as shown in Figure 3.4 (c),(d),(e).

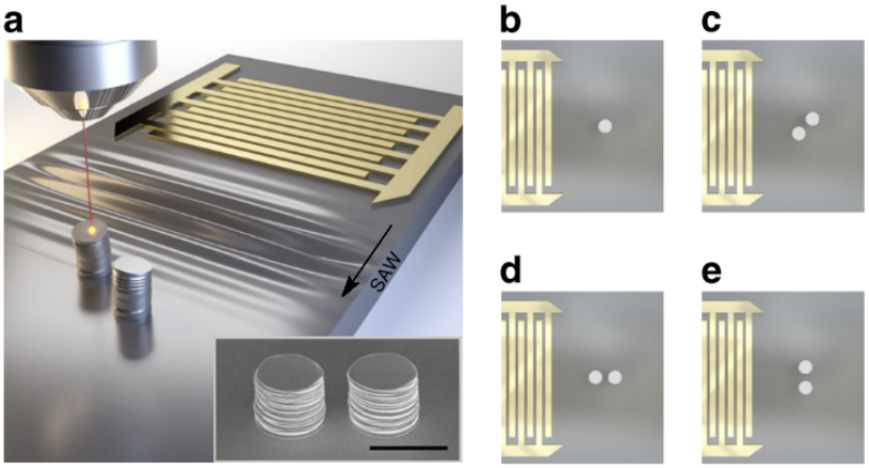


Figure 3.4: Experiment setup for SAW coupled pillar pair. (b) excitation of a single pillar, (c) diagonal excitation, (d) longitudinal excitation, and (e) transverse excitation. [31]

When the two pillars were closely placed with a gap distance of one-third of the pillar diameter, three modes were observed with the diagonal SAW direction. As shown in Figure 3.5 (a), the first mode existed around 70 MHz which is the resonance frequency of a single pillar and showed a symmetric shape on the frequency domain. Two more modes at higher frequencies were captured with asymmetric shapes indicating the coupling between pillars. Comparing Figure 3.5 (a) (b), when the SAW propagated along another pair of pillars in the longitude direction, two modes with large similarity to the mode(ii) and mode(iii) of diagonal excitation case were observed. The first mode in the diagonal case was reduced by positioning the pillars along the SAW direction. Raguin et al repeated the measurements of the longitudinal case with another pair of pillars and verified the existence of the two modes, as in Figure 3.5 (b) they were not obviously separated. With Figure 3.5 (a) (c), a similar conclusion was drawn that positioning the pillar pair transverse to the SAW direction reduced the mode(ii) in Figure 3.5 (a). The coupling between pillars with a small separation distance resembles the plasmonic coupling of nanoparticles [11] and is sensitive to the SAW propagation direction.

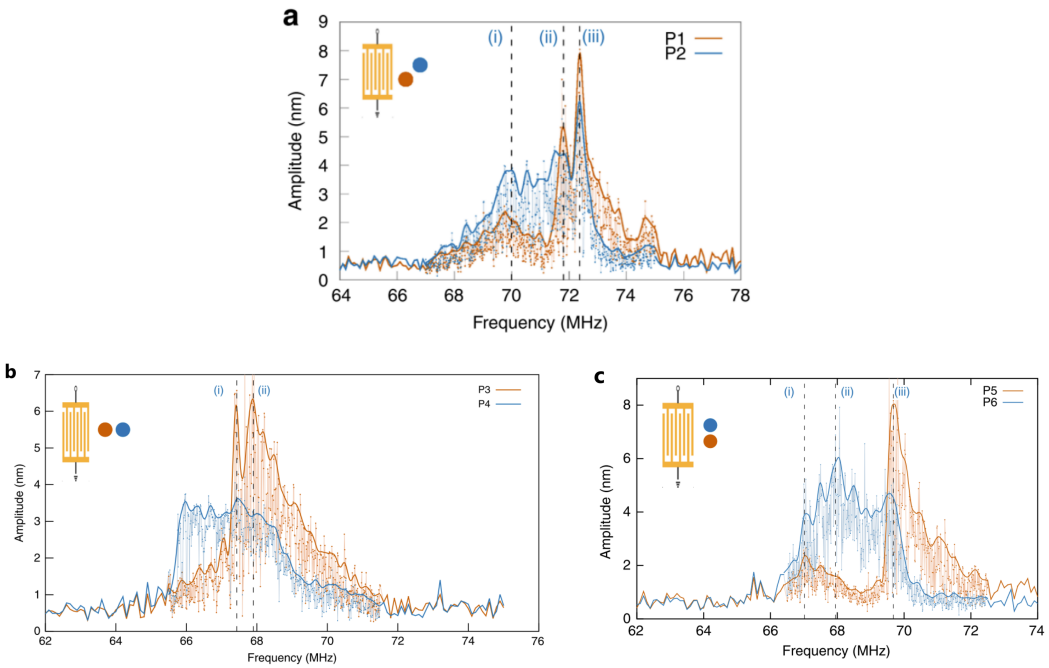


Figure 3.5: Frequency responses of closely-spaced pillar pairs. (a) diagonal excitation, (b) longitudinal excitation, and (c) transverse excitation. [31]

Placing the pillar resonators at a larger separation with a distance around the pillar diameter, two peaks of the two pillars were observed in both longitudinal and transverse excitations. SAW propagating direction had no influence on the mode selection of the pillar pair. The frequency response of the transverse excitation is shown in Figure 3.6. Dimension differences from the fabrication of the two pillars could be one of the factors that led to frequency shifts between two resonance peaks. At a frequency between the two resonances, the pillar pair underwent an orthogonal polarisation state indicating an avoided crossing of the two pillars' resonances, as the out-of-plane displacement field map at (ii) shows. This study produced a similar result to the strain-coupled study by Doster et al that the coupling with SAW between pillars also exhibited avoided crossings. To reduce the difficulties in resonance mode splitting, resonance peaks of nanopillars are desired to be well separated.

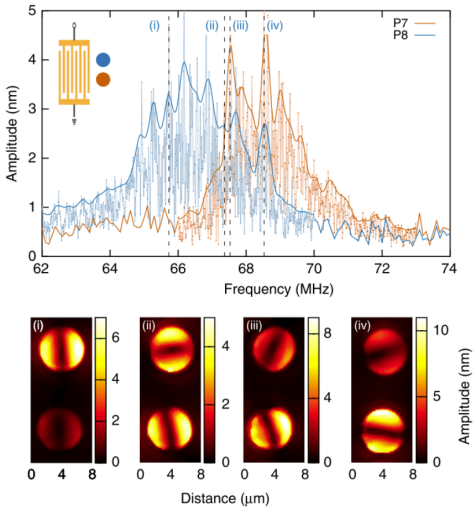


Figure 3.6: Frequency response and out-of-plane displacement field maps of a pillar pair with increased separation by transverse excitation. [31]

Kahler et al fitted their SAW coupling model to the experimental data of Raguin et al [20], shown

in Figure 3.7. The eigenfrequencies of single pillars were calculated from the fitting and are close to the two peak frequencies of the experiment result. This verified the assumption that the frequency shift was due to the pillars' dimension difference and proved that the eigenfrequencies of the coupling modes were almost identical to the resonance frequencies of the individual pillars.

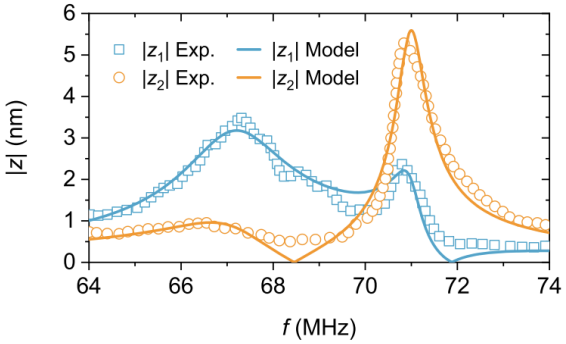


Figure 3.7: Frequency response of a pillar pair driven by SAW [20]

Benchabane et al proposed that the elastic energy of a sub-wavelength resonator excited by surface acoustic waves was confined at the vicinity of the resonator [4]. A pillar resonator on a piezoelectric substrate was excited by quasi-annular focused IDTs and compared to a reference sample without a pillar. The maximum displacement amplitudes at different distances x from the pillar center were measured. As seen in Figure 3.8 (a), when x = 0, the maximum amplitude at the center of the pillar was around 9 nm, significantly larger than the substrate amplitude in the reference sample. At $x = 2.5\mu m$ (Figure 3.8 (b)), which is less than $1\mu m$ from the pillar edge with $3.2\mu m$ pillar diameter, the maximum amplitude was reduced to 1 nm compared to 0.5 nm in the reference. With distance further away from the pillar center in Figure 3.8 (c) and (d), the amplitudes in the pillar sample and reference sample were around the same, which confirmed the negligible contribution to the elastic energy from the pillar. This also suggested that the coupling of pillars could be ignored with enough separation distance.

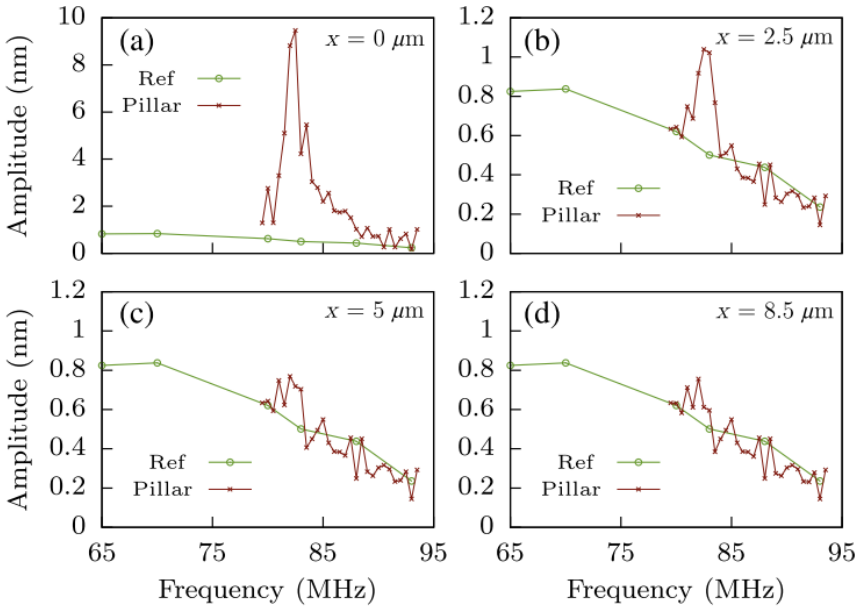


Figure 3.8: Maximum displacement amplitudes at different distances x from the pillar center [4] The red lines represent the sample with pillar and the green lines are the reference sample without pillar.

To sum up, surface acoustic wave coupling reduces the energy dispassion and improves the quality

factor, however, whether SAW predominates or not, coupling increases the difficulties in frequency response interpretation. The coupling strength can be stunned by adjusting the geometry dimensions in the resonator design. Also, it is shown in the research that eigenfrequencies of the resonators can be well resolved with careful design.

3.4 Conclusion

In theoretical modeling, both the resonance frequency and sensitivity of the nanopillar are related to the radius, height of the pillar, Young's modulus of the material, and density. The size of the pillar is easier to tune than the material properties, thus, only the geometry of the pillars will be varied for the desired performance of the resonators in this project. With the assumption that the nanopillar is treated as a cantilever beam with a cylindrical shape, the resonance frequency increases with the increase of the pillar radius and decrease of the pillar height, while changing height has a more significant effect. For the sensitivity, it is inversely proportional to the radius and cubic of the height, both decreases in radius and height will increase it. Therefore, in the design, the size of the pillar in both radius and height is considered to be reduced to achieve high sensitivity, while varying heights keeping the same radius will be used to distribute the frequencies of the pillars. For the mass resolution, if the frequency resolution is fixed, the higher the sensitivity, the better the mass resolution. But when the ultimate mass resolution is considered, the existence of the frequency resolution is due to the thermomechanical noise, and its value is related to the resonator's properties. Thus, after the design, the ultimate mass resolution should be calculated accordingly.

While distributing the resonance frequencies of the nanopillars, for the simplicity of interpreting the resonances of pillars, the geometry of each pillar and the geometrical spacing between pillars should be well designed to avoid strong coupling between nanopillars. Firstly, the situation of strong coupling with the generation of extra eigenmodes is not desired. Each pillar is expected to correspond to one resonance peak in the designed frequency domain. Secondly, the situation when coupling shifts the resonance frequencies of pillars such as in the avoided crossing effect should be avoided. Without influencing the resonance frequencies, SAW coupling between pillars can be beneficial as it reduces energy dissipation.

4 Technological basis

A general schematic of the proposed design in this project is shown in Figure 4.1. Two IDTs in circular arc shapes with a chirp design are deposited on the aluminum nitride piezoelectric thin film at a 90-degree angle. An array of nanopillars of different heights are placed with the center coincides with the geometric focal point of IDTs. The geometry of IDTs, the number of pillars, the arrangement of pillars, and their geometry will be designed in this project.

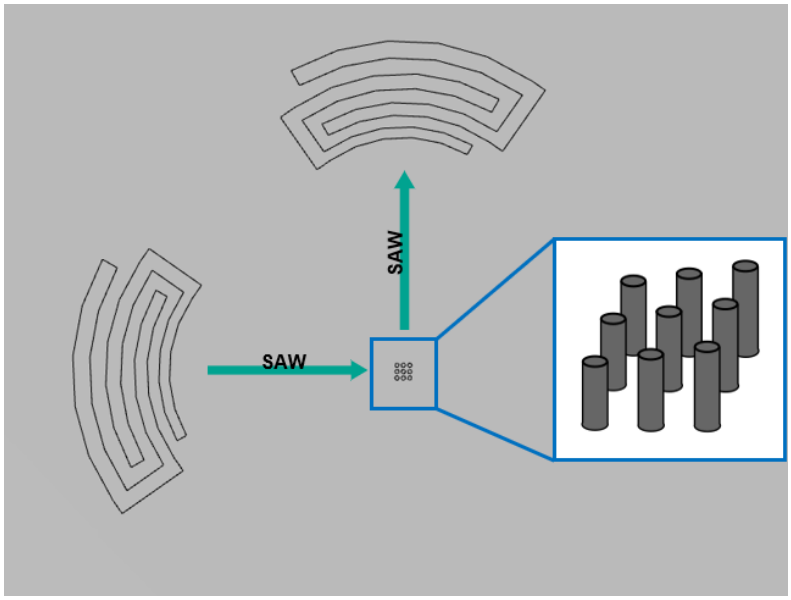


Figure 4.1: General schematic of the proposed design, number of IDT fingers, number of pillars shown here are just for illustration

4.1 Acoustic transduction

The transduction of nanopillars is relatively difficult to achieve compared to other MEMS resonators since their miniaturized size makes the piezoresistive readout infeasible. Optical technique is usually used to measure the vibration of nanopillars, however, it cannot be integrated into the chip. Acoustic waves can also be used to measure the nanopillars' vibration, with a SAW delay line device, waves are emitted from the IDT on one side propagating through the nanopillars, and received from the IDT on another side. Nanopillars are actuated by the SAW and the vibration will be characterized from the input and output signals. A SAW delay line and nanopillars can be integrated on the same chip resulting in a compact device.

4.1.1 Two-port network

The two-port network model can be used for the modeling of acoustic devices. A two-port network is a circuit with four terminals as shown in Figure 4.2. The current that goes in and out of each port should be in a steady state (DC or AC).

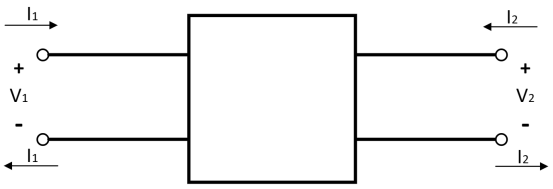


Figure 4.2: A two-port network

Several parameters are used to describe the network and take the form of a two-by-two matrix. Impedance parameters also known as Z-parameters relate the voltages at two ports to the currents. The admittance parameter (Y-parameters) matrix is the inverse of the Impedance matrix.

$$\begin{bmatrix} V_1 \\ V_2 \end{bmatrix} = \begin{bmatrix} z_{11} & z_{12} \\ z_{21} & z_{22} \end{bmatrix} \begin{bmatrix} I_1 \\ I_2 \end{bmatrix} \qquad \begin{bmatrix} I_1 \\ I_2 \end{bmatrix} = \begin{bmatrix} y_{11} & y_{12} \\ y_{21} & y_{22} \end{bmatrix} \begin{bmatrix} V_1 \\ V_2 \end{bmatrix}$$

Hybrid and inverse hybrid parameters relate the voltage and current at one port to those at the other port.

$$\begin{bmatrix} V_1 \\ I_2 \end{bmatrix} = \begin{bmatrix} h_{11} & h_{12} \\ h_{21} & h_{22} \end{bmatrix} \begin{bmatrix} I_1 \\ V_2 \end{bmatrix} \qquad \begin{bmatrix} I_1 \\ V_2 \end{bmatrix} = \begin{bmatrix} g_{11} & g_{12} \\ g_{21} & g_{22} \end{bmatrix} \begin{bmatrix} V_1 \\ I_2 \end{bmatrix}$$

With the incident signals mixed with reflected signals in radio frequency circuits, scattering parameters (S-parameters) and scattering transfer parameters (T-parameters) are commonly used. a_1, a_2 are the incident waves at port 1 and port 2, b_1, b_2 are the reflected waves at port 1 and port 2. The S-parameters and T-parameters are defined as:

$$\begin{bmatrix} b_1 \\ b_2 \end{bmatrix} = \begin{bmatrix} S_{11} & S_{12} \\ S_{21} & S_{22} \end{bmatrix} \begin{bmatrix} a_1 \\ a_2 \end{bmatrix} \qquad \begin{bmatrix} a_1 \\ b_1 \end{bmatrix} = \begin{bmatrix} T_{11} & T_{12} \\ T_{21} & T_{22} \end{bmatrix} \begin{bmatrix} b_2 \\ a_2 \end{bmatrix}$$

By this definition, S_{11} and S_{22} represent the reflections at port 1 and port 2, S_{12} and S_{21} represent the transmissions from port 2 to port 1 and from port 1 to port 2 respectively. The return losses are calculated as $-20log|S_{11}|$, $-20log|S_{22}|$ and the insertion losses are calculated as $-20log|S_{21}|$, $-20log|S_{12}|$. Conventionally, S-parameters are defined as ratios of the square root of the power. In the characterizations, they are usually connected to transmission lines of certain impedance and measured in terms of ratios of voltage with a network analyzer.

SAW delay line devices can be modeled as two-port networks, with current I_1 going in and out of the input IDT at port 1 and similarly for output IDT at port 2. For SAW delay lines, the networks are reciprocal and mostly symmetrical, giving $S_{12} = S_{21}$ and $S_{11} = S_{22}$. The typical reflection and transmission shown by S_{11} and S_{21} parameters take the shapes in Figure 4.3. When it is off the resonance frequency in the lower frequency range, the input signals are almost all reflected back giving S_{11} the value around 1 (0dB) and S_{21} around 0. As the frequency approaches the resonance frequency of the IDT, SAW is generated and radiated from the IDT, and S_{11} shows a negative peak. At the central frequency of the IDTs, S_{21} is observed with the highest value about 1 and S_{11} with the lowest value, which means signals are mostly transmitted to port 2. In the higher frequency range off-resonance, S_{11} value goes back to nearly 0dB with a small difference which is due to the excitation of bulk acoustic waves from the IDT. Due to the energy conservation, the sum of S_{11} square and S_{21} square should be less or equal to 1, each negative peak in S_{11} corresponds to a peak in S_{21}.

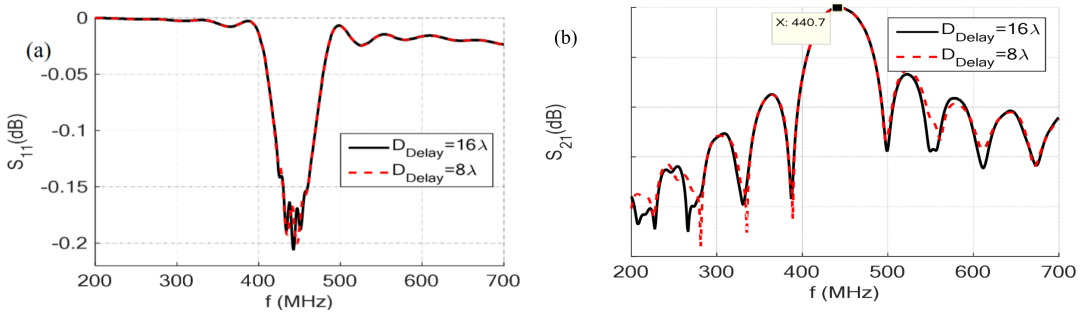


Figure 4.3: Scattering parameters (a) S_{11} and (b) S_{21} of an acoustic delay line in the paper by Belkhelfa and Serhane [2]

4.1.2 Impedance matching

The impedance matching is usually required for electrical devices designed to achieve maximum power transfer or minimum signal reflection. To yield the maximum power transfer, the impedances of the source and load should be complex conjugate with the same real part and opposite imaginary part ($R_S = R_L, X_S = -X_L$, where $Z_S = R_S + iX_S, Z_L = R_L + iX_L$). For the SAW delay line devices, the electrical power transmission should be maximized with the impedance in the input circuit and output circuit matching the device impedance. For the S-parameter measurements, a network analyzer is typically used with a 50Ω characteristic impedance in the measurement circuit. Since the impedance of an acoustic device is not 50Ω most of the time, matching networks are necessary before the input IDT and after the output IDT to improve the strength of the transmitted signal.

4.1.3 Circuit model for the proposed design

Similar to the SAW delay line discussed in Chapter 2.3.3 for direct mass sensing, the nanopillar array is placed at the center of the delay line here. The total system can be modeled as a two-port network. In the study of Kahler et al, the acoustic transduction of a nanopillar resonator by the SAW delay line was presented [19] and the resonant modes of a pillar pair were also detected [21]. The input IDT, output IDT, and the pillar on the delay line were treated as individual two-port networks. The total system was taken as a two-port network resulting from three cascaded two-port networks as illustrated in Figure 4.4. Both IDT 1 and IDT 2 include half of the delay line. Letting S_{IDT} and S_P represent the scattering parameter S_{21} of the IDT and pillar, the total transmission of the system can be represented by

$$S_{21}(f) = S_{IDT,1}(f)S_P(f)S_{IDT,2}(f) = S_{IDT}^2(f)S_P(f) \tag{4.1}$$

for isotropic piezoelectric substrates like AlN, since the two IDTs of a SAW delay line are always designed identically and the system is reciprocal and symmetrical.

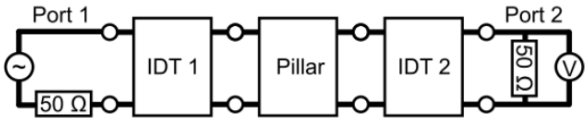


Figure 4.4: Circuit model for the SAW transduction system of pillar resonator [19]

In the research of Kahler et al, the scattering of the pillar was modeled from the scattering of light as

$$S_P(f) = S_{eff}\frac{f^2}{f_0^2 - f^2 + if\frac{f_0}{Q_0}} \tag{4.2}$$

where S_{eff} is an effective scattering parameter and is assumed to be constant in the small frequency range, f_0 is the eigenfrequency of the pillar resonator, and Q_0 is the quality factor of the pillar. In the case of multiple pillars, assume the differences in pillar location contributing to the phase differences and the coupling between pillars could all be ignored. The total scattering parameter of pillars was modeled as the sum of that of each pillar

$$S_P(f) = \sum_{n=1}^{N} S_{eff,n} \frac{f^2}{f_n^2 - f^2 + if\frac{f_n}{Q_n}} \tag{4.3}$$

with S_{eff}, f_n, and Q_n represent the effective scattering parameter, eigenfrequency, and quality factor of the n^{th} pillar, and N is the total number of pillars.

The frequency responses of the transduction of pillar vibration by SAW delay lines were measured from experiments by Kahler et al. The transmissions of single pillar and pillar pair characterized by S_{21} were shown in Figure 4.5. The peaks on the frequency responses indicated the captured resonances of the pillars and the model with Equation 4.1-4.3 fitted well with the experiment results. The acoustic transduction of nanopillar resonator by SAW delay lines was proved to be feasible for the single pillar case and the pillar pair case, showing great potential for the transduction of the nanopillar array.

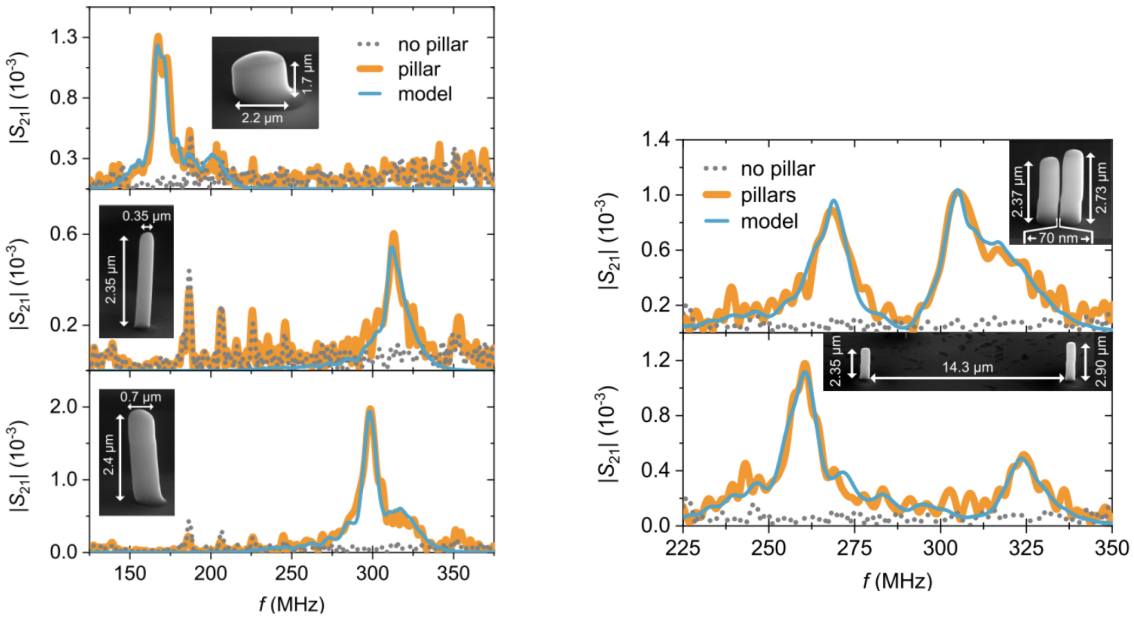


Figure 4.5: Frequency responses of devices with pillars and pillar pairs in different geometry [19][21]

4.2 IDT design

The interdigital transducer (IDT) is composed of periodically placed electrodes on a piezoelectric substrate. With electrical signals applied between two sets of electrodes of an IDT, periodic electric fields are produced and generate traveling surface acoustic waves on the piezoelectric substrate [46]. The input IDT transduces an electrical signal into a mechanical signal and acts as a filter. The properties of this filter such as the central frequency and bandwidth are defined by the IDT electrode pattern. Electrode fingers of IDT are placed with a period distance equal to the wavelength of the generated SAW which corresponds to the central frequency. In a conventional IDT design, each finger width is chosen as a quarter of the wavelength and the spacing between fingers takes the same value. Many configurations of the IDT pattern exist for different purposes, e.g. the split electrode, the single-phase unidirectional transducer electrode, the distributed acoustic reflecting transducer, ... [26]. In the SAW delay line device for this thesis project, the focused IDT and the chirp IDT design are considered with more acoustic energy concentrated to the nanopillars and larger bandwidth of the device.

4.2.1 Focused IDT

The fingers of focused interdigital transducers usually take a curved shape. Laude et al proposed the concept of inversely designing the IDT according to the wavefront of a point source to achieve focusing SAWs [22]. Ripples were usually observed around a point source, and the displacement field of SAWs was calculated by Green's function and the vertical displacement was shown in Figure 4.6 (a)(b). Designing an IDT as the shape of the wave surface with a distance of half wavelength between adjacent fingers, the resulting vertical displacement field map is shown in Figure 4.6 (c)(d). The subfigures on the left are the results of Y-cut lithium niobate substrate and the right figures are Z-cut lithium niobate. Due to the anisotropic phase velocity in different directions, the fingers of the IDT were designed accordingly to be homothetic to the wave surface. The resulting displacement field showed great similarity to that of a point source and a focus at the center of the IDT was observed.

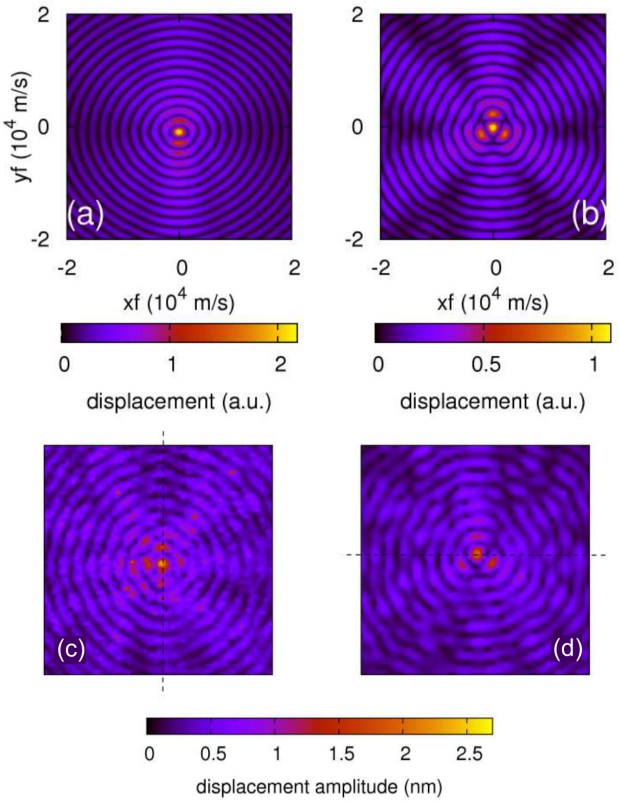


Figure 4.6: Vertical displacement fields: calculated from a point source on (a) Y-cut lithium niobate and (b) Z-cut lithium niobate; measured results from an annular IDT on (c) Y-cut lithium niobate and (d) Z-cut lithium niobate [22]

The focused IDTs are usually designed with circular arcs, but in general cases of anisotropic piezoelectric substrates, the group velocity direction differs from the phase velocity, degrading the focusing effect of circular IDTs. This beam steering effect shifts the focal area from the geometric center and elongates the focal region [29]. The slowness is defined as a function of the propagation direction and takes the value as the inverse of the phase velocity. The group velocity direction of the SAW at a certain propagation direction is the normal vector of the slowness curve at that propagation angle. To adjust the focal point of a FIDT to the geometric center, the electrode curve should be designed as the slowness curve, and the generated SAWs observed from the displacement field measurements are shown in Figure 4.7.

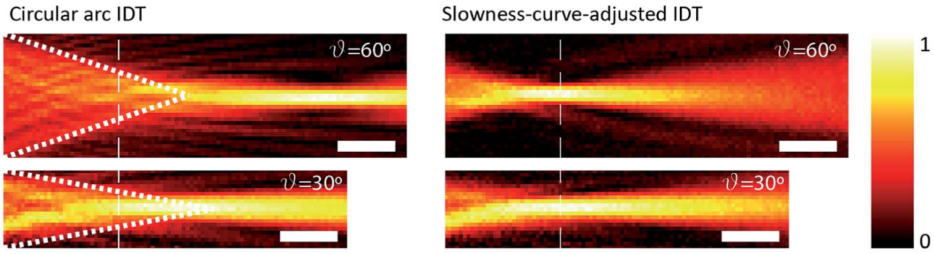


Figure 4.7: Displacement fields of circular arc IDT and slowness-curve-adjusted IDT from a laser Doppler vibrometer. The white vertical dashed lines represent the location of the geometric center on the x-axis. [29]

In the case of this thesis project, aluminum nitride thin film is used as the piezoelectric substrate with isotropic properties. Thus, the FIDTs will adopt the circular arc shape.

In the FIDT design, the number of finger pairs (N_p), the degree of arc (D_a), and the geometric focal length (f_L) define the electrode structure, as shown in Figure 4.8. The effect of these parameters on IDT performance has been investigated.

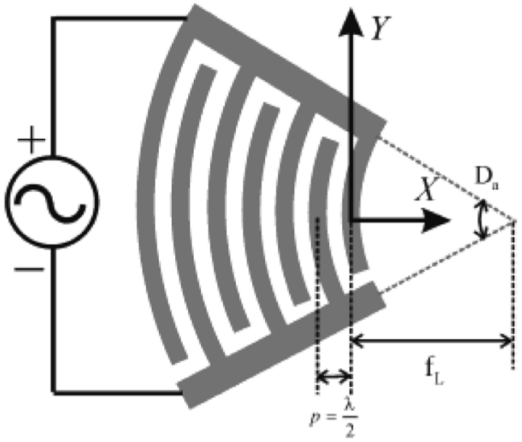


Figure 4.8: Focused IDT illustration [47]

In the research of [33], parameter design of circular arc IDTs was studied. It was found that a larger number of fingers provided a narrower bandwidth and less insertion loss. Increasing the focal length would increase the insertion loss but still yield higher acoustic energy at the focal point which was shown by the larger displacement amplitude. This is because, as the distance from the inner finger to the focal point increased, the aperture increased corresponsively. FIDTs with larger degrees of arc had larger displacement amplitudes as well as increasing the focal length and also yielded better focusing with smaller focus areas. It was also observed with a larger degree of arc, the insertion loss increased in their study, however, this was the effect of using circular arc IDTs on anisotropic substrates. What could also be a result of this anisotropy is that FIDTs designed for higher frequencies had better focusing effects and less insertion loss which deviated from conventional IDT properties.

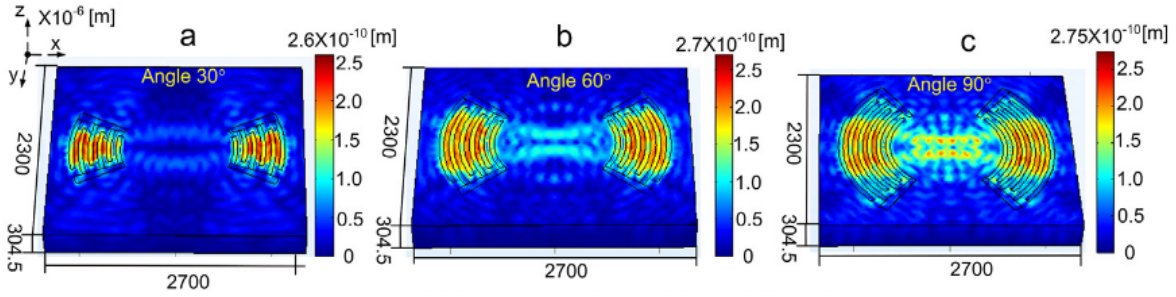


Figure 4.9: Surface deformation with different FIDT arc angles from simulations [53]

A study on the effects of IDT arc angles of the isotropic piezoelectric substrate also showed that larger arc angles yielded more significant focusing effects and higher acoustic energy [53]. As shown in Figure 4.9 (c), an evident focal region with high acoustic energy concentration in the middle of circular arc IDTs could be observed.

Wu et al investigated these parameters for both circular FIDTs and curve-adjusted FIDTs [47]. The results showed a similar tendency as the study of Sankaranarayanan and Bhethanabotla. The number of finger pairs did not have much influence on the focusing properties but increased the displacement amplitude when it was increased. Increasing the geometric focal length stabilized the focus and decreased the focal area. Increasing the degree of arc shrunk the focus area without influencing the amplitude of the focal point much.

For the IDT design of this thesis project, the anisotropy of the piezoelectric substrate can be ignored. Circular arc IDTs will be designed on the AlN thin film. The number of fingers should be sufficient to generate SAWs with enough energy to interact with pillars while considering its effect on bandwidth. A nanopillar array is desired to be placed at the center of the IDTs within the focal area. A large enough geometric focal length and degree of arc should be chosen to guarantee a distinct focusing effect, at the same time, the focal region should be large enough to include the pillar array. FIDTs and the nanopillar array will be designed iteratively. On the overall trend, increasing these parameters provides better performance, however, the total device footprint is also an important factor to consider.

4.2.2 Chirp IDT

The distance between the fingers in IDTs defines the frequency of the generated propagating SAWs. In the conventional IDT, finger spacings are kept constant. Although the bandwidth of an IDT is inversely proportional to the number of electrode fingers, it is limited to the vicinity of the central frequency. Chirp IDTs with varying finger widths and spaces are designed to achieve extremely wide bandwidths.

Fall et al studied several different configurations of chirp IDT design [9]. One of the simplest ways to space fingers was linear period modulation. In this configuration, a constant wavelength difference was set which means the wavelength of each period was linearly spaced, as shown in Figure 4.10. The time response and frequency response to a chirp input signal measured at a point in front of the IDT are shown in Figure 4.11. The chirp IDT was designed with a wide bandwidth from 20 MHz to 125 MHz. From the decreasing displacement magnitude with frequency, lower electromechanical coupling was found for higher frequency in this chirp IDT configuration.

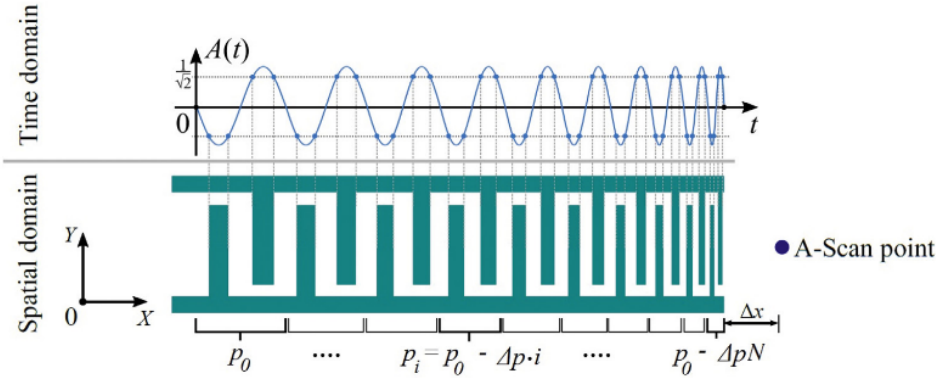


Figure 4.10: Linear-period chirp IDT configuration [9]

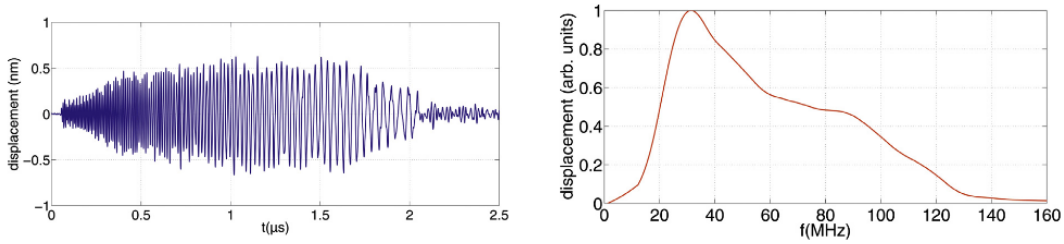


Figure 4.11: SAW generated by linear-period chirp IDT on time and frequency domain [9]

Another chirp IDT configuration is the linear-frequency modulation, Figure 4.12. From the settled IDT zone length L and SAW velocity c, the temporal signal duration D was calculated as $D = L/c = 1\mu s$. A chirp signal with the frequency linearly increased with time as $f = (f_c - B/2) + \frac{B}{D}t$ was set, where f_c is the center frequency of the designed frequency range and B is the bandwidth. The electrode fingers were designed based on this chirp signal, with each finger's center corresponding to the position of a signal peak and the width of each finger as the length interval where chirp signal magnitude was larger than $\frac{A}{\sqrt{2}}$. From the time response and frequency response shown in Figure 4.13, this configuration provided almost uniform excited SAW displacement amplitude over the designed frequency range.

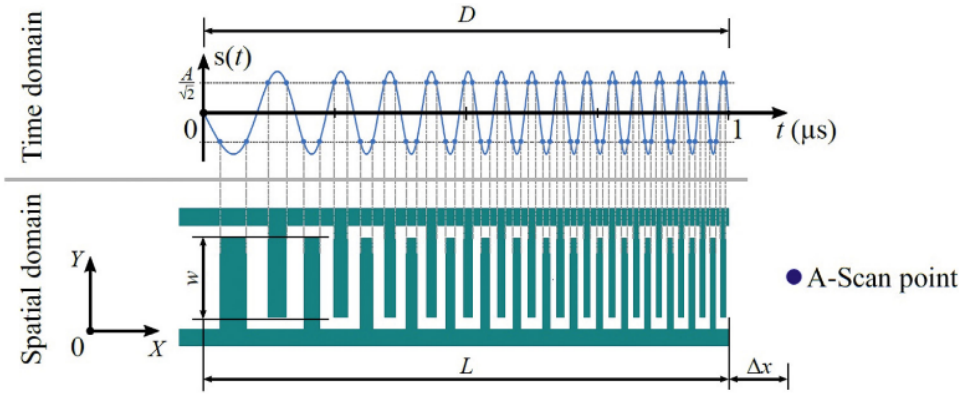


Figure 4.12: Linear-frequency chirp IDT configuration [9]

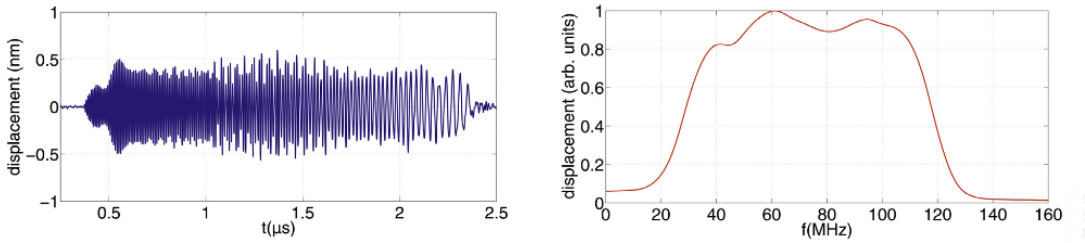


Figure 4.13: SAW generated by linear-frequency chirp IDT on time and frequency domain [9]

In addition to these two configurations, a chirp-scheme-optimized IDT was proposed by Fall et al. SAWs with higher frequency were believed to exhibit larger attenuation through propagation. Thus, in this configuration, electrode fingers contributing to higher frequency were repeated more times to enhance the SAW excitation, as shown in Figure 4.14. As desired, the measured SAW signals on the time domain and frequency domain shown in Figure 4.15 have higher amplitudes in the higher frequency range.

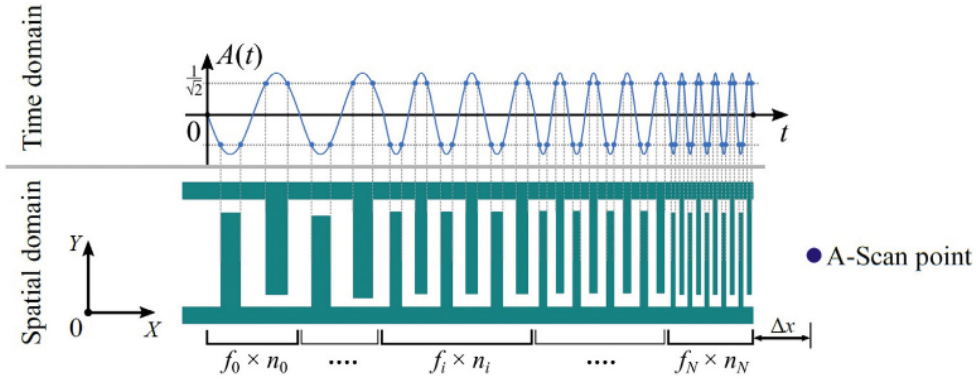


Figure 4.14: Chirp-scheme-optimized IDT configuration [9]

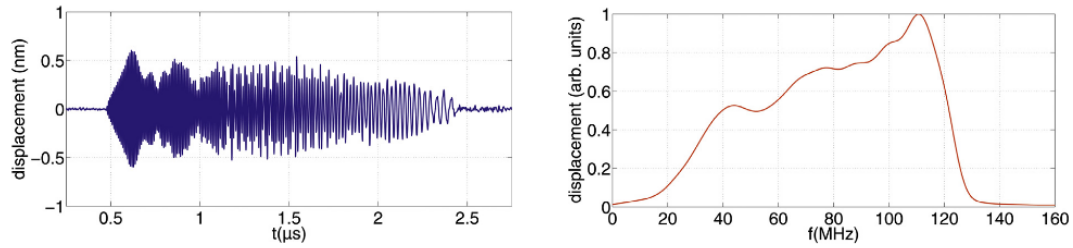


Figure 4.15: SAW generated by chirp-scheme-optimized IDT on time and frequency domain [9]

Combining the chirp design with the focused IDT design, it is desired in this project to produce a SAW device that can achieve focused SAW excitation and measurement with a wide bandwidth. The IDTs should take the form of circular arc fingers with varying finger spacing and width. For the circular arc FIDTs deposited on the isotropic piezoelectric substrate, whether the high-frequency components have higher or lower insertion loss will be investigated later with COMSOL simulation. To strengthen signals in a certain frequency range of the FIDTs, instead of using the chirp-scheme-optimized configuration, putting the corresponding components to the outer part of the FIDT (larger aperture) is an option. The detailed geometry of electrode patterns will be decided with the consideration of nanopillar array design.

4.3 Fabrication techniques

4.3.1 Fabrication of AlN SAW devices

AlN thin film

SAW devices commonly use the piezoelectric effect of bulk materials like quartz, lithium niobate (LiNbO3), or thin film materials like PZT, aluminum nitride (AlN), and zinc oxide (ZnO). Aluminum nitride is widely used for SAW devices due to its good piezoelectric properties, temperature and chemical stability, simplicity for fabrication, and CMOS compatibility. The most important property of high acoustic velocity beyond other materials makes it extremely suitable for high-frequency applications. Thus, AlN thin film is adopted for the SAW delay line device in this thesis project.

Aluminum nitride normally is in a wurtzite structure and the thin film is a polycrystalline of AlN. The wurtzite crystal structures of AlN are oriented in the c-axis direction with possibilities of two polarities [50] as shown in Figure 4.16. The AlN thin film is a random mixture of Al-polar and N-polar crystals having isotropic properties in the plane. The SAW delay line device will be fabricated from a silicon wafer with AlN deposited on a Si substrate. Rayleigh type of surface acoustic waves are generated on the device.

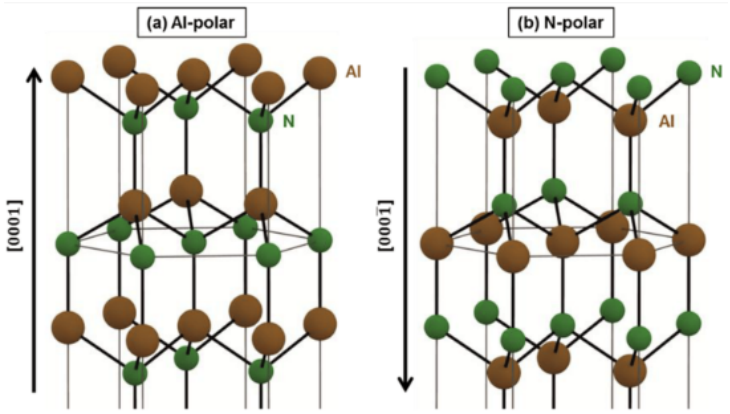


Figure 4.16: AlN crystal structure [50]

Reactive sputtering is used for the deposition of AlN thin film for acoustic wave devices, because of its advantages in low-temperature deposition, synthesis simplicity, CMOS compatibility, and the ability to create excellent crystalline structures with c-axis orientation. To have a good performance of the AlN thin film for the SAW devices, a 1 μm thick AlN layer is usually used since the deposition of further thickness will include Ar^+ and N_2 to the film. In reactive sputtering, Argon is used as the sputter gas and the energetic ions bombard the Al target, the Al atoms reach the substrate surface and react with the nitrogen gases subsequently forming AlN coating on the silicon wafer substrate. Pulsed DC mode is used as a substitution for RF power to reduce the insulating layer forming on the target by nitridation [40].

Fabrication process

The AlN SAW delay line device will be fabricated on a silicon wafer with aluminum chosen as the electrode material. From the existing studies and thesis projects at TU Delft, the processing flowchart is shown in Figure 4.17. First, a layer of 1 μm thick aluminum nitride layer is deposited on the [100] silicon wafer by reactive magnetron sputtering. After that, a few hundred nanometers thick aluminum electrode layer will be sputtered on top in the same chamber. A photoresist mask is used to pattern the electrode layer and subsequently, the Al layer is wet etched in 0.55% HF.

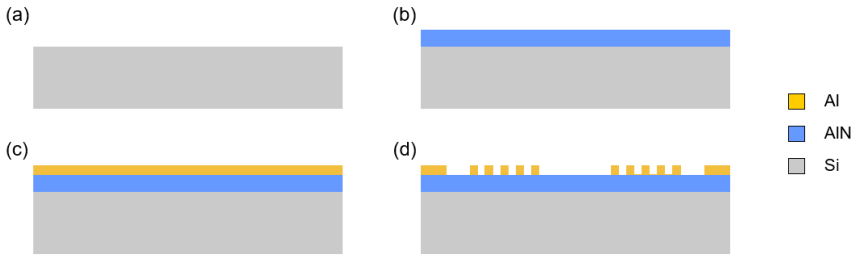


Figure 4.17: Processing flow chart of the AlN SAW delay line

4.3.2 Fabrication of nanopillars

Focused electron/ion beam induced deposition

Focused electron beam induced deposition (FEBID) and focused ion beam induced deposition (FIBID) have been used for direct write additive manufacturing of three-dimensional nanostructures. These techniques use the electron beam or ion beam to achieve the local deposition of organometallics at the focused point. The schematic of FEBID is shown in Figure 4.18 and FIBID has a similar structure. At first, the organometallic precursors are absorbed on the surface; and then in the focus area of the beam, the precursors decompose; subsequently, volatile organic ligands are removed and the rest products remain and condense on the surface.

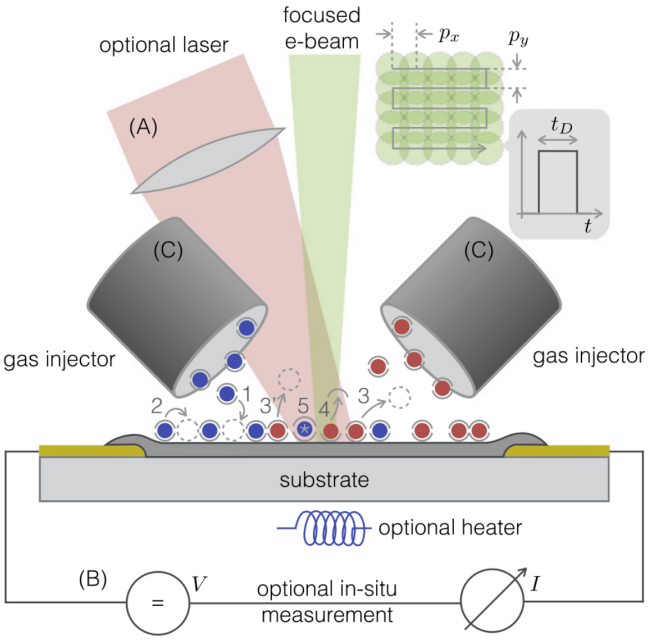


Figure 4.18: Schematic of FEBID [15]

The resulting structures from FEBID/FIBID usually contain a high portion of carbon and oxygen elements and enhancing the metal portion is one of the current research directions. Platinum precursors are commonly used for the deposition. For FIBID, the use of Ga^+ ion beams is well developed. Both FEBID and FIBID can achieve a resolution of a few nanometers, with FEBID having a higher resolution. However, FIBID has a higher deposition rate and the ability to deposit a higher portion of metal contents over FEBID.

Two-Photon Polymerization

Two-photon polymerization (TPP) is a commonly used technique for fabricating three-dimensional structures with submicron features. It is widely used for microfluidics, lab-on-a-chip, MEMS, etc, due to its high resolution around 100 nm and biocompatibility of polymer materials used. TPP is also suitable for the fast production of prototypes with good performance. The process uses femtosecond lasers to initiate the polymerization of monomers to form solid polymeric structures, as shown in Figure 4.19. The laser beam will be focused to a voxel size and the substrate to be printed will be moved by a piezo stage. The whole polymerization process is described by three phases [54], initiation, propagation, and termination, as shown in the inset of Figure 4.19. In the initiation process, the photoinitiators absorb two photons transiting to excited states and then decompose to radicals. Monomers together with the radicals form monomer radicals. Subsequently, during propagation, monomer radicals interact with more and more monomers and influence them. In the last termination process, monomer radicals combine with each other forming long chains of polymers.

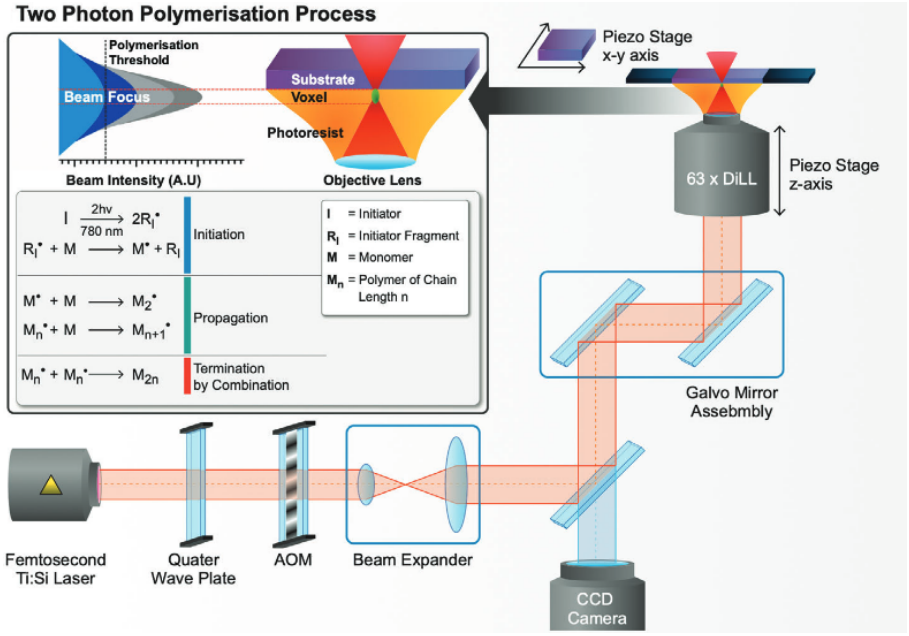


Figure 4.19: Schematic of TPP [28]

The materials for TPP printing are mostly acrylate-based, epoxide-based, and hybrid ceramic polymers such as IP photoresists from Nanoscribe, SU-8, and Ormocomp. Different ink leads to different material properties of the polymerized structure. Young's modulus of the TPP printed polymers is not very high, which is commonly below 5 GPa. The Young's modulus and density of different materials from measurements of Lemma et al's research are shown in Figure 4.20 (a) and (b). Figure 4.20 (a) not only shows the difference of materials but also indicates that the laser power of TPP influences Young's modulus. To ensure precision structures, different inks of TPP have specific ranges of laser powers and thus have specific ranges of Young's modulus values.

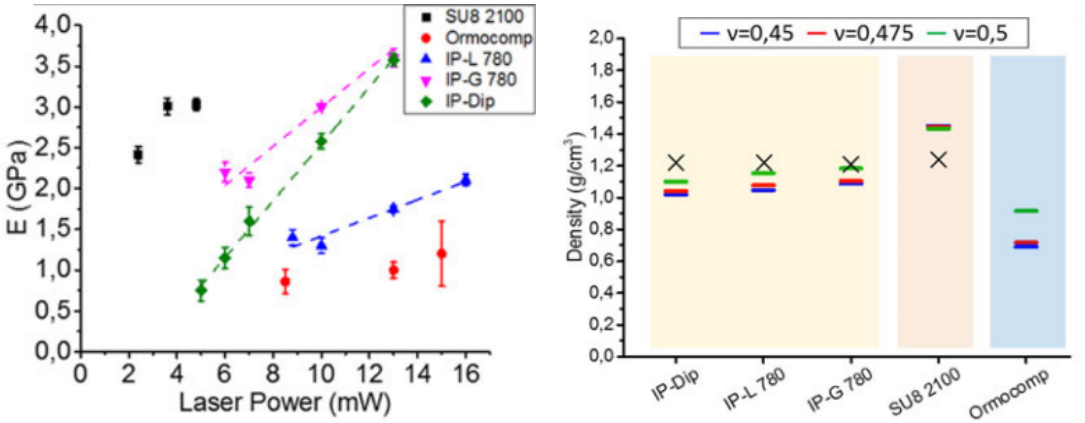


Figure 4.20: Experimentally obtained (a) Young's modulus and (b) density of different polymers by TPP [23]

The material selection not only influences properties like modulus and density but also influences the intrinsic damping of the printed structures. The intrinsic damping together with other external damping sources determines the quality factor of the resonator. Two-photon polymerization has the disadvantage of fabricating polymeric structures with low quality-factors. Stassi et al's research shows that polymeric NEMS cantilevers from standard printing without post-treatment have quality factors below 100 [37]. A suspended microchannel resonator fabricated with SU–8 photoresist was measured with a quality factor around 60 [1]. A microchannel cantilever with IP-S photoresist from Nanoscribe exhibited a quality factor of 174 [18].

5 Research approach

In previous chapters, the background application and state-of-the-art of the resonant mass sensors have been discussed. In order to develop mass sensors to monitor nanoparticles in future studies, this project will design resonators with sufficiently high resonance frequencies and develop an integrated transduction method to measure these frequencies. An array of nanopillar resonators combined on a surface acoustic wave delay line is proposed for the sensor.

From the existing studies, two gaps were found. Firstly, most of the existing resonant mass sensors do not have a mass resolution within 1 fg (refer to Table 2.2 and Table 2.1) to achieve single nanoparticle measurement. Thus, their sensitivities could be further improved. From the tendency shown in the literature, the resonators' sizes should be further reduced to enhance the sensitivities. Therefore, this project uses the nanopillar array and designs the pillars with miniaturized sizes. Secondly, integrated frequency transduction methods such as using SAWs have not been widely used for NEMS resonators. The piezoresistive readout is commonly used for resonant mass sensors, however, it is difficult to achieve for small structures like nanopillars. The optical method can be used to read the resonator's vibration, but it is not feasible to achieve a small size integrated on the same chip of resonators. Acoustic transduction is a good choice for nanopillars. Kahler et al have demonstrated the successful transduction of the resonance frequencies of a pillar pair [21]. However, measuring the resonances of more than two pillars together has not been done yet. SAW transduction of a nanopillar array will be performed in this project. In addition, using a nanopillar array, multiple resonators will be simultaneously detected for frequency shifts. Sampling particles will be distributed on different pillars giving more information about the particles' size distribution than using only one resonator.

The research goal of this project is:

To develop integrated transduction and measurement methods for nanopillar resonators using surface acoustic waves.

5.1 Research question

Based on the understanding of this project and the literature survey, the research question is proposed as:

How to design and fabricate nanopillar resonator arrays, and characterize their resonances through surface acoustic waves?

It is further divided into several sub-questions:

- What is the coupling strength between nanopillars?
- What is the design of the nanopillar array?
- What is the design of the SAW delay line device?
- What is the fabrication method to integrate the nanopillar array on the SAW device?
- What is the interpretation of resonances from the scattering parameters of the total system?
- What is the performance of the final device?

5.2 Planning

In order to answer the above questions, the project is divided into four phases. After the literature survey, the first task is to investigate the coupling between nanopillars, design the nanopillar array, and then design the SAW delay line accordingly. In the second phase, the SAW delay line device will be fabricated and measurements of the SAW devices will be conducted. For the third phase, the fabrication of the nanopillars on the SAW delay line should be achieved. In the last phase, the scattering parameters of the total system will be measured to find the resonances of each nanopillar and the characterization of the device will be performed. Milestones are set for these project phases:

- Milestone 1: Design and fabrication of the SAW delay line
- Milestone 2: Integration of the nanopillar array

The specific time arrangement of this project is shown in the Gantt chart in Figure 5.1.

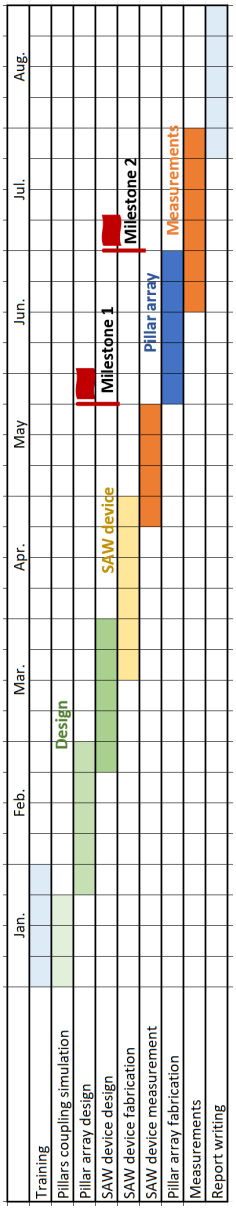


Figure 5.1: Gantt chart for the thesis project planning

5.3 Risk analysis

With the existing literature and reasonable theoretical speculation, by the end of this project, the resonances of nanopillars in the array will be successfully distinguished and read with an appropriately designed SAW delay line. However, problems and obstacles could be encountered in the progress. Some risks of this project are anticipated and possible mitigation plans are considered.

1. The bonding between nanopillars fabricated by two-photon polymerization and aluminum nitride surface is insufficient.

2. The quality factor of the nanopillar fabricated by two-photon polymerization is too poor.

For both two risks, the plan is to switch to using carbonaceous platinum nanopillars deposited by focused electron/ion beam induced deposition instead of polymer nanopillars. The FEBID/FIBID can achieve a fabrication resolution of a few nanometers and fabricate small structures with much higher quality factors.

3. Tolerance in the fabrication resulting in resonance frequency difference.

To mitigate this risk, the resonance frequency difference range will be estimated, and the nanopillars will be designed with enough resonance frequency spacing.

Bibliography

[1] C. Accoto, A. Qualtieri, F. Pisanello, C. Ricciardi, C. F. Pirri, M. D. Vittorio, and F. Rizzi. Two-photon polymerization lithography and laser doppler vibrometry of a su-8-based suspended microchannel resonator. *Journal of Microelectromechanical Systems*, 24(4):1038–1042, 2015.

[2] N. Belkhelfa and R. Serhane. Temporal study of one port and two ports saw delay lines for temperature sensing. In *2021 International Conference on Information Systems and Advanced Technologies (ICISAT)*, pages 1–5, 2021.

[3] D. Bell and R. Li. Surface-acoustic-wave resonators. *Proceedings of the IEEE*, 64(5):711–721, 1976.

[4] S. Benchabane, R. Salut, O. Gaiffe, V. Soumann, M. Addouche, V. Laude, and A. Khelif. Surface-wave coupling to single phononic subwavelength resonators. *Physical Review Applied*, 8, 9 2017.

[5] J. P. Black, A. Elium, R. M. White, M. G. Apte, L. A. Gundel, and R. Cambie. 6d-2 mems-enabled miniaturized particulate matter monitor employing 1.6 ghz aluminum nitride thin-film bulk acoustic wave resonator (fbar) and thermophoretic precipitator. In *2007 IEEE Ultrasonics Symposium Proceedings*, pages 476–479, 2007.

[6] A. Demir and M. S. Hanay. Fundamental sensitivity limitations of nanomechanical resonant sensors due to thermomechanical noise. *IEEE Sensors Journal*, 20:1947–1961, 2 2020.

[7] A. Dickherber, C. D. Corso, and W. D. Hunt. Optimization and characterization of a zno biosensor array. *Sensors and Actuators A: Physical*, 144(1):7–12, 2008.

[8] J. Doster, S. Hoenl, H. Lorenz, P. Paulitschke, and E. M. Weig. Collective dynamics of strain-coupled nanomechanical pillar resonators. *Nature Communications*, 10, 12 2019.

[9] D. Fall, M. Duquennoy, M. Ouaftouh, N. Smagin, B. Piwakowski, and F. Jenot. Optimization of interdigital transducers for the generation of surface acoustic waves over a large bandwidth (20–125mhz). *Sensors and Actuators A: Physical*, 273:303–310, 2018.

[10] Z. Fan, R. Kapadia, P. Leu, X. Zhang, Y.-L. Chueh, K. Takei, K. Yu, A. Jamshidi, A. Rathore, D. Ruebusch, M. Wu, and A. Javey. Ordered arrays of dual-diameter nanopillars for maximized optical absorption. *Nano letters*, 10:3823–7, 10 2010.

[11] A. Funston, C. Novo, T. Davis, and P. Mulvaney. Plasmon coupling of gold nanorods at short distances and in different geometries. *Nano letters*, 9:1651–8, 05 2009.

[12] B. Giechaskiel, M. Maricq, L. Ntziachristos, C. Dardiotis, X. Wang, H. Axmann, A. Bergmann, and W. Schindler. Review of motor vehicle particulate emissions sampling and measurement: From smoke and filter mass to particle number. *Journal of Aerosol Science*, 67:48–86, 2014.

[13] L. Goswami, K. H. Kim, A. Deep, P. Das, S. S. Bhattacharya, S. Kumar, and A. A. Adelodun. Engineered nano particles: Nature, behavior, and effect on the environment, 7 2017.

[14] A. Hajjam, J. C. Wilson, and S. Pourkamali. Individual air-borne particle mass measurement using high-frequency micromechanical resonators. *IEEE Sensors Journal*, 11:2883–2890, 2011.

[15] M. Huth, F. Porrati, and O. V. Dobrovolskiy. Focused electron beam induced deposition meets materials science, 1 2018.

[16] P. Joshi, S. Kumar, V. K. Jain, J. Akhtar, and J. Singh. Distributed mems mass-sensor based on piezoelectric resonant micro-cantilevers. *Journal of Microelectromechanical Systems*, 28(3):382–389, 2019.

[17] P. Kim, D.-H. Kim, B. Kim, S. Choi, S. Lee, A. Khademhosseini, R. Langer, and K. Suh. Fabrication of nanostructures of polyethylene glycol for applications to protein adsorption and cell adhesion. *Nanotechnology*, 16:2420–6, 10 2005.

[18] R. Kramer, E. Verlinden, L. Angeloni, A. Heuvel, L. Fratila-Apachitei, S. Maarel, and M. Ghatkesar. Multiscale 3d-printing of microfluidic afm cantilevers. *Lab on a Chip*, 20, 11 2019.

[19] H. Kähler, H. Arthaber, R. Winkler, R. G. West, I. Ignat, H. Plank, and S. Schmid. Transduction of single nanomechanical pillar resonators by scattering of surface acoustic waves. 10 2022.

[20] H. Kähler, D. Platz, and S. Schmid. Surface acoustic wave coupling between micromechanical resonators. *Communications Physics*, 5, 12 2022.

[21] H. Kähler, R. Winkler, H. Arthaber, H. Plank, and S. Schmid. Towards practical mass spectrometry with nanomechanical pillar resonators by surface acoustic wave transduction. 3 2023.

[22] V. Laude, D. G'erard, N. Khelfaoui, C. Jerez-Hanckes, S. Benchabane, and A. Khelif. Annular interdigital transducer focuses piezoelectric surface waves to a single point. 2007.

[23] E. D. Lemma, F. Rizzi, T. Dattoma, B. Spagnolo, L. Sileo, A. Qualtieri, M. De Vittorio, and F. Pisanello. Mechanical properties tunability of three-dimensional polymeric structures in two-photon lithography. *IEEE Transactions on Nanotechnology*, 16(1):23–31, 2017.

[24] Y. Liu, A. Jaiswal, M. A. Poggi, and W. D. Wilson. *Surface Plasmon Resonance and Quartz Crystal Microbalance Methods for Detection of Molecular Interactions*, chapter 16, pages 329–344. John Wiley Sons, Ltd, 2011.

[25] C. M. Long, M. A. Nascarella, and P. A. Valberg. Carbon black vs. black carbon and other airborne materials containing elemental carbon: Physical and chemical distinctions, 2013.

[26] D. Mandal and S. Banerjee. Surface acousticwave (saw) sensors: Physics, materials, and applications. *Sensors*, 22, 2 2022.

[27] E. Martines, K. Seunarine, H. Morgan, N. Gadegaard, C. D. W. Wilkinson, and M. O. Riehle. Superhydrophobicity and superhydrophilicity of regular nanopatterns. *Nano Letters*, 5(10):2097–2103, 2005. PMID: 16218745.

[28] S. Ohalloran, A. Pandit, A. Heise, and A. Kellett. Two-photon polymerization: Fundamentals, materials, and chemical modification strategies (adv. sci. 7/2023). *Advanced Science*, 10, 03 2023.

[29] R. O'Rorke, A. Winkler, D. Collins, and Y. Ai. Slowness curve surface acoustic wave transducers for optimized acoustic streaming. *RSC Advances*, 10:11582–11589, 03 2020.

[30] T. D. T. A. W. R. J. P. S. S. J. C. R. S. Gao, A. E. Perring and D. W. Fahey. A high-sensitivity low-cost optical particle counter design. *Aerosol Science and Technology*, 47(2):137–145, 2013.

[31] L. Raguin, O. Gaiffe, R. Salut, J. M. Cote, V. Soumann, V. Laude, A. Khelif, and S. Benchabane. Dipole states and coherent interaction in surface-acoustic-wave coupled phononic resonators. *Nature Communications*, 10, 12 2019.

[32] J. S. Reid, R. Koppmann, T. F. Eck, and D. P. Eleuterio. A review of biomass burning emissions part ii: intensive physical properties of biomass burning particles, 2005.

[33] S. Sankaranarayanan and V. Bhethanabotla. Design of efficient focused surface acoustic wave devices for potential microfluidic applications. *Journal of Applied Physics*, 103:064518–064518, 03 2008.

[34] G. Sauerbrey. Verwendung von Schwingquarzen zur Wägung dünner Schichten und zur Mikrowägung. *Zeitschrift fur Physik*, 155(2):206–222, Apr. 1959.

[35] S. Schmid, M. Kurek, J. Q. Adolphsen, and A. Boisen. Real-time single airborne nanoparticle detection with nanomechanical resonant filter-fiber. *Scientific Reports*, 3, 2013.

[36] D. E. Schraufnagel. The health effects of ultrafine particles, 3 2020.

[37] S. Stassi, I. Cooperstein, M. Tortello, C. Pirri, S. Magdassi, and C. Ricciardi. Reaching silicon-based nems performances with 3d printed nanomechanical resonators. *Nature Communications*, 12:6080, 10 2021.

[38] D. Stubbs, S.-H. Lee, and W. Hunt. Molecular recognition for electronic noses using surface acoustic wave immunoassay sensors. *IEEE Sensors Journal*, 2(4):294–300, 2002.

[39] O. Tigli, L. Bivona, P. Berg, and M. E. Zaghloul. Fabrication and characterization of a surface-acoustic-wave biosensor in cmos technology for cancer biomarker detection. *IEEE Transactions on Biomedical Circuits and Systems*, 4(1):62–73, 2010.

[40] A. T. Tran. *AlN piezoelectric films for sensing and actuation*. PhD thesis, Delft University of Technology, 2014.

[41] H. S. Wasisto, S. Merzsch, A. Stranz, A. Waag, E. Uhde, T. Salthammer, and E. Peiner. Silicon resonant nanopillar sensors for airborne titanium dioxide engineered nanoparticle mass detection. *Sensors and Actuators, B: Chemical*, 189:146–156, 2013.

[42] H. S. Wasisto, S. Merzsch, A. Waag, E. Uhde, T. Salthammer, and E. Peiner. Airborne engineered nanoparticle mass sensor based on a silicon resonant cantilever. *Sensors and Actuators, B: Chemical*, 180:77–89, 4 2013.

[43] J. Weber, W. M. Albers, J. Tuppurainen, M. Link, R. Gabl, W. Wersing, and M. Schreiter. Shear mode fbars as highly sensitive liquid biosensors. *Sensors and Actuators, A: Physical*, 128:84–88, 3 2006.

[44] S. M. Wells, I. A. Merkulov, I. I. Kravchenko, N. V. Lavrik, and M. J. Sepaniak. Silicon nanopillars for field-enhanced surface spectroscopy. *ACS Nano*, 6(4):2948–2959, 2012. PMID: 22385359.

[45] C. H. Weng, G. Pillai, and S. S. Li. A thin-film piezoelectric-on-silicon mems oscillator for mass sensing applications. *IEEE Sensors Journal*, 20:7001–7009, 7 2020.

[46] R. White and F. Voltmer. Direct piezoelectric coupling to surface elastic waves. Technical Report UCB/ERL M132, EECS Department, University of California, Berkeley, Oct 1965.

[47] T.-T. Wu, H.-T. Tang, Y.-Y. Chen, and P.-L. Liu. Analysis and design of focused interdigital transducers. *IEEE transactions on ultrasonics, ferroelectrics, and frequency control*, 52:1384–92, 09 2005.

[48] R. Yadwade, S. Gharpure, and B. Ankamwar. Nanotechnology in cosmetics pros and cons, 6 2021.

[49] Y. Yang, C. Dejous, and H. Hallil. Trends and applications of surface and bulk acoustic wave devices: A review, 1 2023.

[50] T. Yoshikawa, M. Reusch, V. Zuerbig, V. Cimalla, K. H. Lee, M. Kurzyp, J.-C. Arnault, C. Nebel, O. Ambacher, and V. Lebedev. Electrostatic self-assembly of diamond nanoparticles onto al- and n-polar sputtered aluminum nitride surfaces. *Nanomaterials*, 6:217, 11 2016.

[51] H. Yoshimine, T. Kojima, H. Furusawa, and Y. Okahata. Small mass-change detectable quartz crystal microbalance and its application to enzymatic one-base elongation on dna. *Analytical Chemistry*, 83:8741–8747, 11 2011.

[52] Y. Zhang, J. Luo, A. J. Flewitt, Z. Cai, and X. Zhao. Film bulk acoustic resonators (fbars) as biosensors: A review. *Biosensors and Bioelectronics*, 116:1–15, 2018.

[53] J. Zhou, X. Tao, J. Luo, Y. Li, H. Jin, S. Dong, J. Luo, H. Duan, and Y. Fu. Nebulization using zno/si surface acoustic wave devices with focused interdigitated transducers. *Surface and Coatings Technology*, 367:127–134, 2019.

[54] X. Zhou, Y. Hou, and J. Lin. A review on the processing accuracy of two-photon polymerization. *AIP Advances*, 5:030701, 03 2015.

2

Paper

To keep the paper concise, only the most important and related works are chosen to be discussed here. Other related works are put in the different sections of the appendix.

Measuring the resonances of nanopillars through surface acoustic waves

***Abstract*—Resonant mass sensors are emerging as innovative instruments for particle measurement, which utilize the resonance frequency shifts of oscillatory structures. Micro- and nano-pillars have been adopted as the resonators for the high sensitivity of this mass sensing technique. However, existing frequency measurement methods for micro- and nano-mechanical resonators are mostly based on piezoresistive readouts, which were challenged for the integration of such small structures as submicron pillars. In this paper, aluminum nitride surface acoustic wave (SAW) delay line devices were utilized to investigate the potential for measuring the resonance frequencies of several micro/nano-pillars simultaneously. SAW delay line devices for this resonance measuring application have been successfully designed, fabricated, and tested. Both two-photon polymerized (TPP) pillars and focused ion beam (FIB) deposited pillars have been incorporated into the delay line devices. COMSOL simulations in this work have demonstrated the feasibility of multi-resonance measurements. Small peaks, likely corresponding to pillar resonances, were detected and showed some correlation with the resonances. These results suggest that using SAW delay lines is a promising technique for multi-resonance detection of nanopillar arrays. This work paved the way for high-sensitivity mass sensor development with effective SAW devices and methods of incorporating pillars.**

I. INTRODUCTION

With the advances in nanotechnology and industrial development, new types of nanoparticles are released into the atmosphere. Such as TiO_2 and ZnO nanoparticles have been broadly used in the cosmetic industry due to their UV filtering properties [1]. Airborne nanoparticles are gradually becoming a threat to human health. Current air quality detection methods for particulate matter are mostly based on optical methods targeting PM10 and PM2.5. These particulate monitoring methods are not precise enough for ultrafine particle detection. Resonant mass sensors can be used with high sensitivity and resolution for nanoparticle detection.

Resonant mass sensors utilize the high sensitivity of their resonance state to the mass shifts and are widely used for small mass measurements. Especially the micro- and nano-mechanical resonators, which can achieve mass resolution beyond 1 attogram [2], have profound prospects for the detection of single biomolecules and nanoparticles. For the application to these extremely small particles, the resonators' size is reduced to smaller scales while the resonance frequency is moved to higher ranges. This trend brought up new challenges to the transduction of these micro or nanoscale resonators. Conventional transduction methods for micro-mechanical resonators include electrostatic, piezoresistive [3], thermal [4], electromagnetic, and many other techniques. However, for nanomechanical resonators with extremely small sizes such as nanopillars, these transduction methods are difficult to integrate. To monitor the vibrations of these nano-mechanical resonators, optical read-out such as using the laser Doppler vibrometer [5] and scanning electron microscopy (SEM) [6] are used in previous works. Still, an integratable transduction method for nano-mechanical resonators is desired for nano-electromechanical system (NEMS) mass sensor development.

Surface acoustic wave (SAW) delay lines are widely used for sensing applications. The surface acoustic waves are sensitive to surface change. After the interaction on the delay line, by analyzing the signals of emitted waves and received waves, pressure, mass, temperature, etc. can be measured. In the development of SAW biosensors, nanofibers [7] have been designed on the delay line to enhance the active area by increasing surface area. However, these ideas of adding nanostructures on the delay line only utilized the surface area increase and did not consider the wave scattering and the coupling of waves to the structures. Considering the nanopillar as an object to be detected, the SAW delay line can be used for the transduction of the nanopillar's resonance [8].

In this work, the idea of using surface acoustic waves for monitoring the nanopillar resonator was adopted. For the development of mass sensors based on this concept, it is essential to consider the transduction of multiple nanopillars with varying resonance frequencies or even an array of nanopillars. So, the goal of this work is to design working SAW devices based on aluminum nitride thin films and validate the idea of measuring the resonance frequencies of multiple pillars.

II. THEORY AND DESIGN

A. *Working principle*

1) Nanopillar coupling: Couplings of the mechanical resonances between nanopillars are expected to be observed with several of them printed closely on the SAW delay line. To investigate this coupling influence on frequency measurement, nanopillars are simulated on the piezoelectric substrate. The geometry of the substrate was constructed as a semi-sphere with 1 μm thick AlN film on top. A perfectly matched layer (PML) was defined to the outer semi-sphere to absorb waves imitating infinitely large substrate. Pillars assigned with the SU-8 photoresist material were built on the center of the substrate. The quality factor of the pillars was assigned a small value of 100 since the damping of such polymer pillars was expected to be large. Due to the symmetry, the simulation was done on half of the geometry. Figure.1 shows the geometry for the COMSOL simulation. The modeling was conducted in Solid Mechanics and Electrostatics physics with piezoelectric effect coupling. Strain coupling combined with SAW coupling between pillars can be investigated. Pillars were actuated into vibration by giving a horizontal force at the bottom of the second pillar. The vibration amplitudes at the top of both

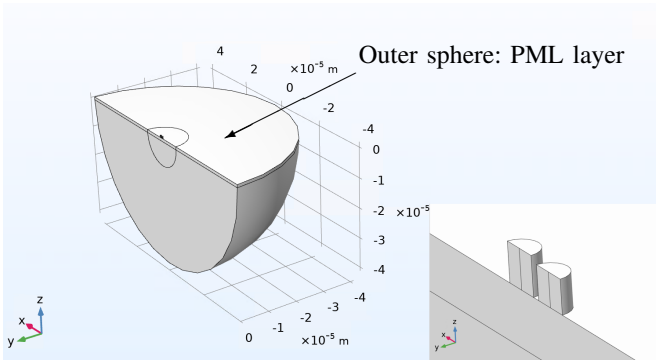


Fig. 1: COMSOL model for pillar coupling investigation

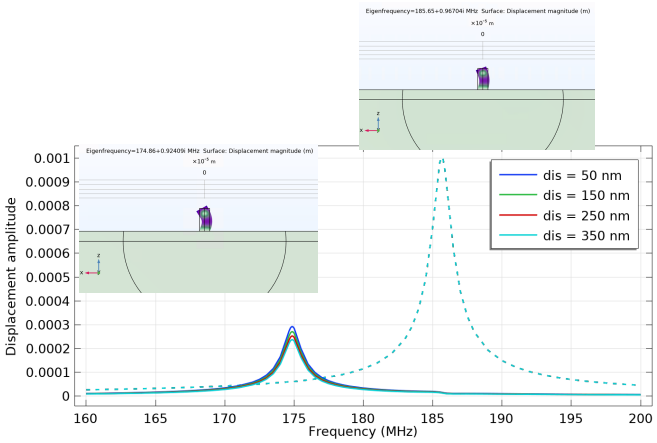


Fig. 2: Vibration amplitude of two coupled pillars from simulation. The solid curves represent the amplitudes of the first longer pillar and the dotted curves represent that of the second shorter pillar. Different colors represent the simulation result with different pillar distances. The displacement amplitude curves of the second pillar at different distances nearly overlap in the figure.

pillars were measured as a function of actuating frequency between 160-200 MHz where the second-order bending modes were expected, as shown in Figure.2. The solid lines represent the vibration of the first pillar and the dashed lines represent the second pillar. The peak on solid lines at around 175 MHz and the peak on dashed lines at 186 MHz represent the resonances of the two pillars. Besides the resonances, a slight rise of the first pillar's vibration amplitude at the second pillar's resonance frequency can be observed. This indicated the weak coupling between the two pillars. To verify the resonance frequencies of two pillars, the frequencies at two peaks were compared to those solved by the Eigenfrequency studies with only one single pillar on the substrate at each time. The eigenfrequencies and mode shapes of the two pillars are shown in the insets of Figure.2. A parametric sweep of the spacing between two pillars was performed to vary the coupling strength for studying the influence on the resonance frequencies. Figure.2 always shows two clear peaks at around 175 MHz and 186 MHz. There is no observable shift of resonance peaks when gradually placing two pillars closer to each other from 350 nm to 50 nm spacing. In this instance, the coupling between two pillars only affected the vibration amplitude without introducing new modes or shifting the resonance frequency significantly. Simulations with varied pillar geometries and order of bending modes have been done and showed similar results.

2) Transduction of nanopillars: Nanopillars were designed on the middle of the delay line. The emitted SAWs actuate the pillars into vibrations, but will also be partially scattered by the pillars [8]. The resonances of the pillars could be read out from the transmission of the total device. The performance of the SAW delay line device was simulated by a COMSOL model with Electrostatics, Solid Mechanics, and Electrical Circuit physics. Four nanopillars with slightly different geometry were built on the delay line, Figure.3. The quality factor Q of the pillars was again set as 100 and the damping ratio ζ was set as 1/2Q to introduce a reasonable amount of damping into the simulation. By comparing the device with pillars to the device without pillars, four dips can be clearly observed in the transmission, Figure.4 (a). These frequencies of the peaks, 127 MHz, 140 MHz, 153 MHz, 169 MHz, were verified to be the resonance frequencies of the four pillars by their vibration amplitude on the frequency domain, Figure.4 (b).

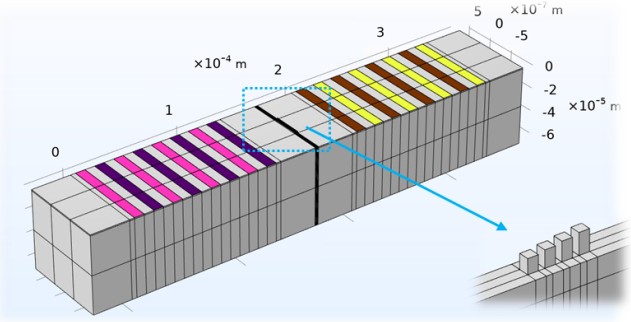
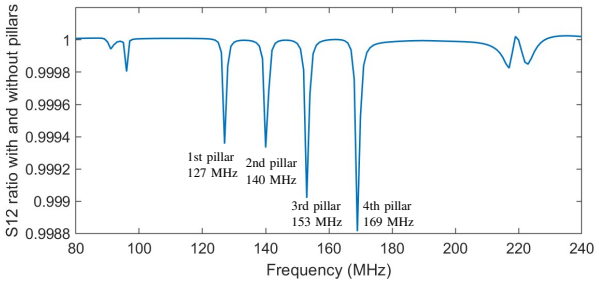


Fig. 3: COMSOL model of pillars on SAW device. The colored stripes represent the IDT electrodes: the pink IDTs were given electric signals at port 1, the dark blue IDTs were grounded at port 1, the yellow IDTs were given electric signals at port 2, and the dark brown IDTs were grounded at port 2.

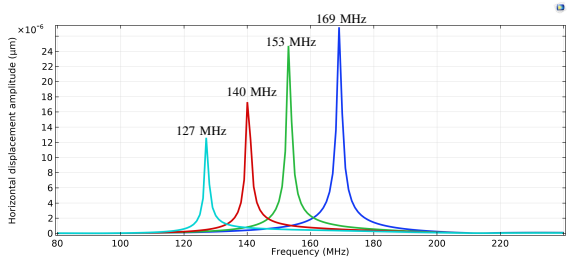
This simulation showed that when a pillar is at its resonance, the scattering of SAWs is comparatively large. This suggested the potential of identifying the resonances of multiple pillars using SAW delay line devices.

3) Focusing of acoustic energy: To have a better coupling between surface acoustic waves and nanopillars, the focused interdigital transducer (FIDT) was introduced. The curved shape of FIDT can greatly focus the surface acoustic waves around the geometry focus point [9], where the nanopillars would be printed. The simulation of an input FIDT with chirped frequency design was conducted to predict the resulting SAWs on the AlN thin film. From the vertical displacement field, distinct focusing effects can be observed within the designed frequency range. A typical displacement field at the central frequency of the bandwidth is shown in Figure.5.

The focusing area size can be estimated from the spatial distribution of the vertical displacement on the cross-section



(a) SAW device transmission ratio



(b) Pillars' amplitude: the four different colors represent the vibration amplitude of the four different pillars

Fig. 4: Simulation results of pillar resonances transduction.

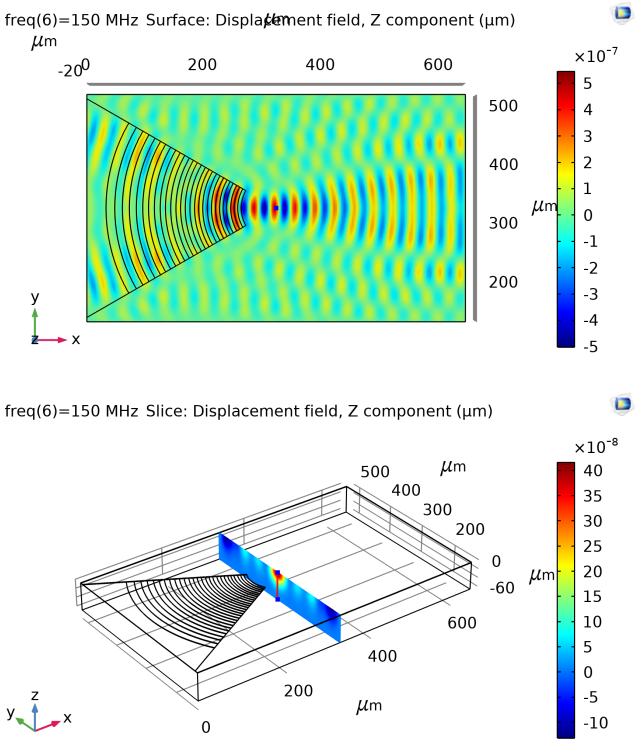


Fig. 5: Focused IDT simulation

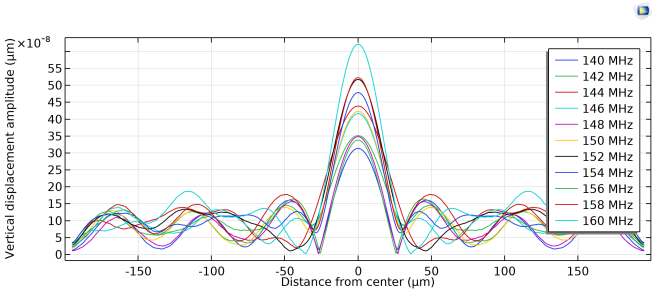


Fig. 6: 1D plot of the wave amplitude from FIDT simulation

that passes the geometrical focus point. 1D plots of different working frequencies are shown in Figure 6. The full width at half maximum (FWHM) of the SAW displacement spatial distribution was used to represent the focus area size, which is around 35um for the simulated design. The focus area of other FIDT designs used in this project is believed to have a similar size.

B. SAW delay line Design

Interdigital transducers with center frequencies of around 200 MHz to 400 MHz were designed for SAW delay line devices. The acoustic wave velocity in AlN film is around 5100 - 5760 m/s [10] [11]. IDTs were designed based on a conventional bi-directional configuration, with finger width and spacing equal to 1/4 of the designed wavelength. Based on the relation of IDT finger width to the center frequency, $d = \lambda/4 = v/4f$, IDTs were designed with width $3\mu m$, $3.5\mu m$, $4\mu m$, $4.5\mu m$, $5\mu m$, $5.5\mu m$, $6\mu m$, and $6.5\mu m$. The more fingers an IDT has, the higher the transmission it can achieve but also with a smaller bandwidth. COMSOL models of SAW delay line devices were built to assist the device design. The transmissions of 3 μm finger width straight devices from the simulation are shown in Figure.7. With the trade-off, 12, 18, and 24 finger pairs were chosen for IDTs to ensure good transmissions of the devices with adequate signal strength and sufficient bandwidth for measuring pillars.

The SAW delay line devices in this work were designed in two different configurations. One configuration used the conventional straight interdigital transducer fingers, hereafter referred to as straight devices. The other one used the IDT fingers in an arch shape to focus surface acoustic waves, hereafter referred to as focused devices. For the SAW delay lines of straight configuration, the aperture (finger overlap width) of IDTs was set over 1 mm for high enough transmission and the delay line length was set over 1.5 mm to mitigate the reflections. For the focused configuration, the curved IDTs (FIDT) were designed as circular arcs with an angle of 60 degrees for the isotropic AlN film. The geometric focal length was chosen so that the average finger overlap width was set over 1 mm corresponding to the straight design.

A straight device design and a focused device design of 3 μm finger width were shown in Figure.8 as examples. The straight device consists of two sets of IDTs facing each other. Pillars will be printed in the middle between two IDTs and the transmission between two ports will be measured to see how much waves will be scattered. The focused device consists of four sets of FIDTs for symmetry, with each FIDT rotated 90 degrees relative to the adjacent. Pillars will be printed in the center. Transmission will be measured pairwise either parallelly to receive transmitted waves after scattering

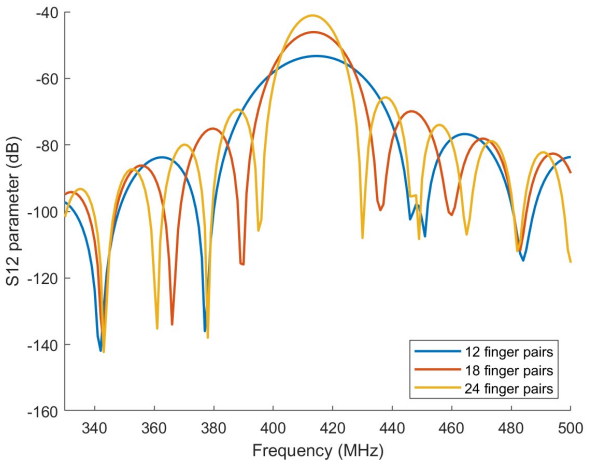
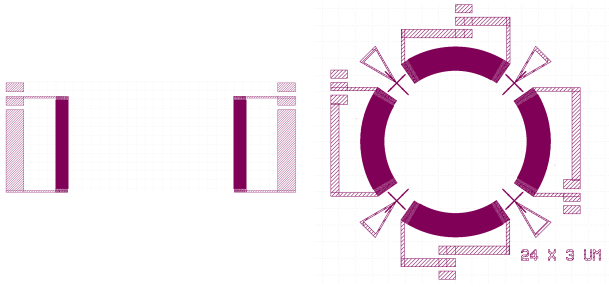


Fig. 7: Simulated transmission of SAW delay lines with 3 μm finger width and 1 mm aperature

or perpendicularly to only receive the scattered waves.



(a) Straight device (b) Focused device

Fig. 8: Straight and focused designs of SAW delay line with 3 μm finger width

III. FABRICATION

A. *SAW delay line fabrication*

The SAW device comprises a 1 μm-thick AlN thin film deposited on high-resistivity silicon, with 200 nm-thick Al interdigital transducers on top. In order to protect the AlN surface and have precise IDT patterns, a lift-off process was chosen instead of wet etching to pattern the electrodes. Figure.9 demonstrates the overall fabrication idea of the AlN SAW delay line devices. High resistivity Silicon wafers with (100) orientation and 500 $\mu m \pm 10$ μm thickness were used and firstly deposited with 1 μm AlN layer. Then, positive photoresist AR-P 5350 was patterned on top without damaging the AlN surface. After that, Aluminium was evaporated on the photoresist layer as the electrode layer. Finally, a lift-off process was taken to remove the photoresist mask and unwanted metal.

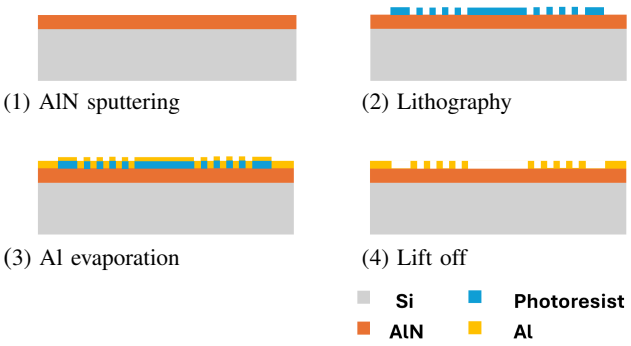


Fig. 9: Fabrication flow chart

1) AlN piezoelectric thin film: A pulsed DC magnetron sputtering technique was used to deposit AlN films in the EKL cleanroom. The deposition was conducted with the existing recipe in EKL using the Trikon Sigma 204. The pulsed DC power was set as 3 kW with a frequency of 250 kHz and a duration of 1616 ns. The substrate temperature was set as 400 $°C$ and the gas flow rates were set as Ar^+: 20 sccm; N_2 80 sccm.

Highly c-axis-oriented AlN polycrystals were expected to ensure good piezoelectric properties. X-ray diffraction (XRD) was used to characterize the deposited AlN films. Figure.10 indicates a strongly preferred (002) AlN orientation. The highest peak at around 69.15° comes from the (100) Si wafer. Other than the peak of AlN (002) at 36°, much less obvious peaks at 37.9°, 49.8°, and 66° can nearly be captured representing the (101), (102), and (103) orientation of AlN respectively. This XRD measurement result showed that the deposited AlN thin films were almost completely c-axis oriented which is the (002) direction, and were believed to have high piezoelectric coefficients.

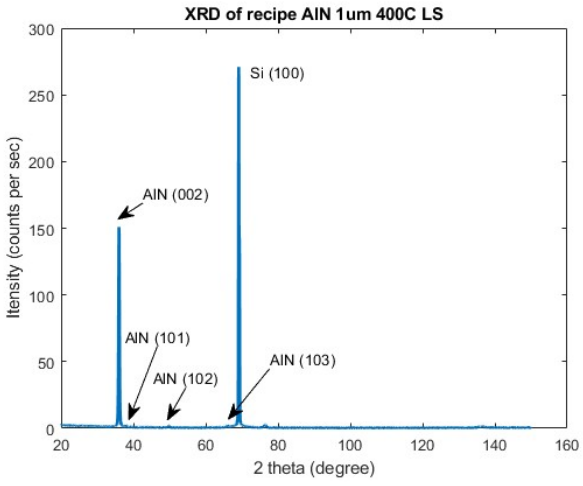


Fig. 10: X-Ray diffraction result of AlN thin film

Woollam Ellipsometer was used to measure the thickness of the deposited AlN thin films. This was measured optically based on the existing model of AlN on Si, measuring the interaction between light and the AlN film giving an average

thickness of around 850 nm. The film thickness was measured more accurately in the SEM cross-section image, Figure.11. The SEM image again showed highly c-axis oriented AlN crystals grown on the Si wafer confirming the XRD results, and the AlN film was measured with a thickness of 975.8 nm.

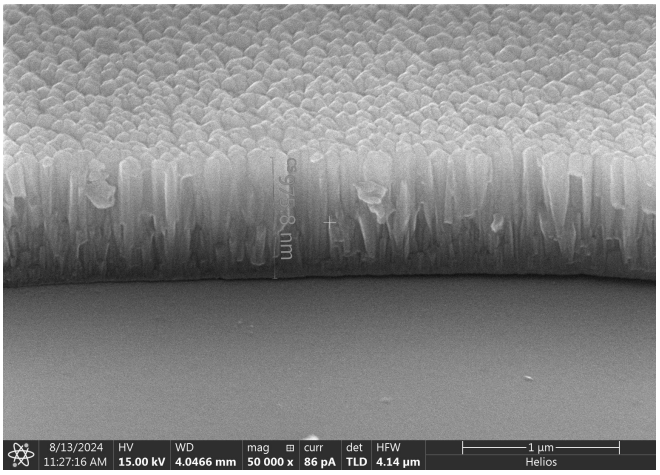


Fig. 11: SEM Cross-section image of AlN film on Si

An attempt resistivity measuring of the AlN thin film was made with the CDE ResMap 4-point probe. The result was outside of the sheet resistance measurement range: $2m\Omega/\square \ - \ 5M\Omega/\square$, which means the resistivity of the AlN film was much larger than $5M\Omega$ indicating the good dielectric property.

2) IDT Electrodes: Both gold and aluminum have high conductivity and are the most commonly used materials for SAW devices. However, Al was chosen over Au in this paper to avoid the considerable mass-loading effects of Au electrodes. The 100 nm thick Au electrode has an area mass density of 1.932 μg per mm^2, which is almost four times that of the 200 nm thick Al electrode (0.5404 $\mu g/mm^2$). The large mass of Au electrodes would influence wave propagation and enhance the reflection at the IDTs, which is less desired for SAW delay line devices. Devices with 10 nm Cr + 100 nm Au electrodes were also tested and compared with 200 nm Al electrode devices. Both the simulated and measured S12 parameters were compared and shown in Figure.12. It can be seen that the heavy mass of the IDTs can introduce dips in the device transmission caused by reflections. The mass also lowered the wave velocity on the AlN film, thus slightly reducing the device center frequency.

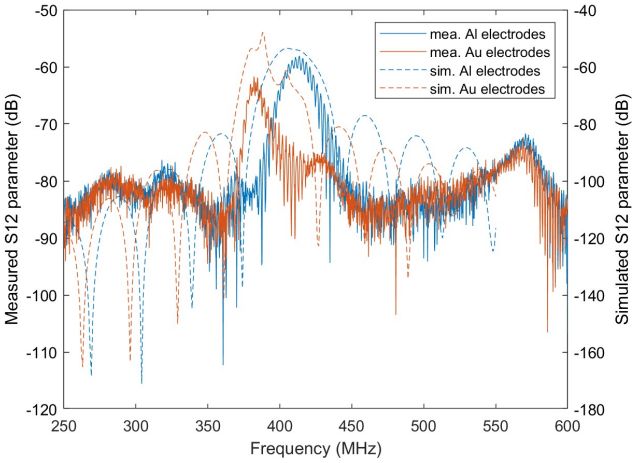


Fig. 12: Transmission curve comparison between Al and Au electrodes in both simulations and measurements.

3) Final SAW device: Figure.13 shows an example of a fabricated straight device with 5 μm finger width. Figure.14 shows an example of a fabricated focused device with 3 μm finger width. Figure.15 shows the details of fabricated interdigital transducers.

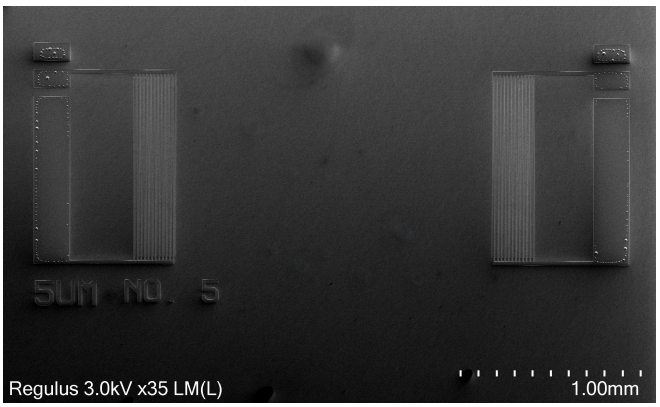


Fig. 13: SEM image of a straight SAW delay line device

B. *Two Photon Polymerization (TPP) Pillars*

Two-photon polymerization (TPP) was used to print polymer pillars with submicron dimensions at the center of the delay line devices. TPP polymers usually have a density around 1.2 g/cm^3 and Young's modulus around 0.5 to 4 GPa with different polymerization doses [12]. Nanoscribe Photonic Professional GT+ setup was used to print nanopillars in the Dip-in Laser Lithography (DiLL) mode with a 63x objective and IP-Dip2 resin. For those polymer pillars observed with the scanning electron microscope (SEM), the samples were coated with Au sputter coater with a current of 20 mA for 30 seconds to reduce the charging effect.

Dose tests on aluminum nitride surfaces were conducted at first. In these tests, pillars with heights and diameters of around 1 μm were printed and the slicing distance and hatching distance were set as 0.1 μm and 0.05 μm. Laser power and

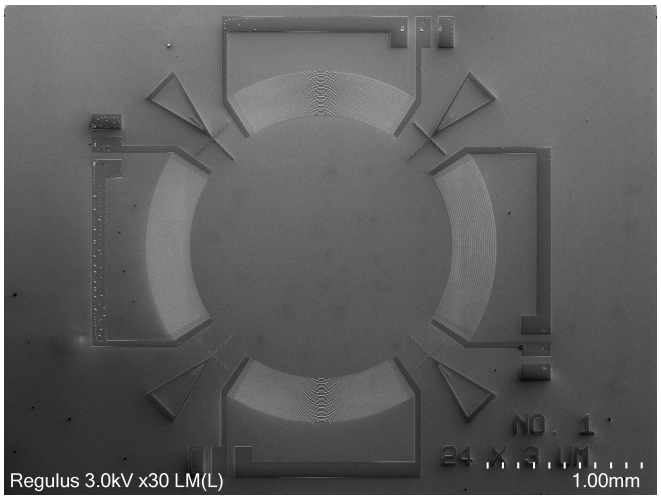


Fig. 14: SEM image of a focused SAW delay line device

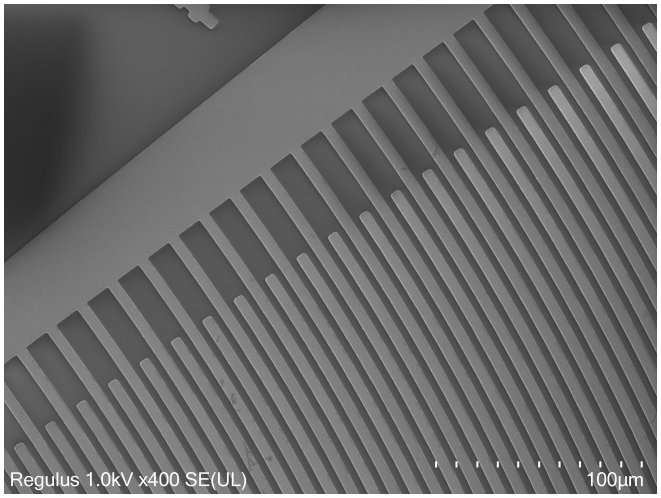


Fig. 15: SEM image of FIDT fingers

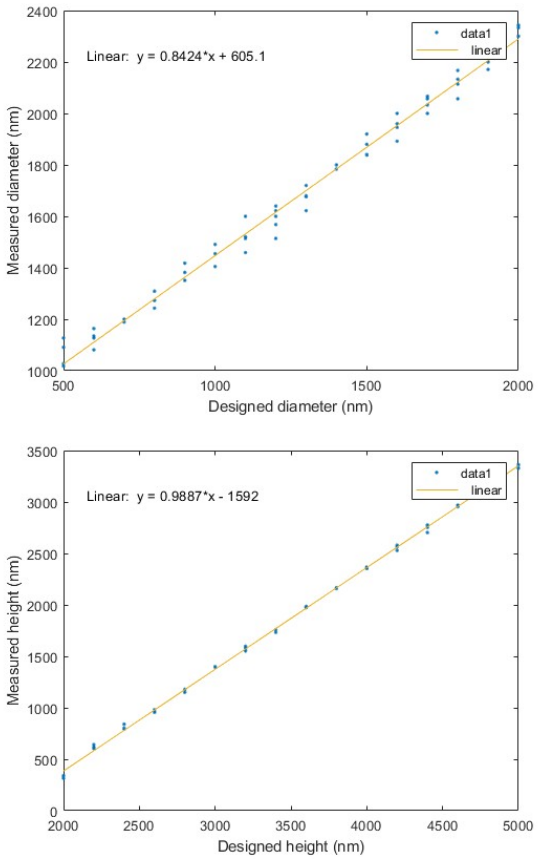


Fig. 16: Relation between the TPP printed and designed dimension

scan speed were chosen as 34% and 30 mm/s respectively from the dose tests.

Another set of calibration tests with pillar arrays of varying heights and diameters was conducted since the actual printed geometry usually deviates from the designed geometry. The real dimensions of the pillars were measured under SEM and fitted as a function of the designed dimensions, Figure.16.

Long pillars were printed and measured for their first-order bending frequencies with the laser Doppler vibrometer (LDV). The resonance frequencies of a pillar's bending modes are linear with $\frac{d}{h^2}$. For the first order bending mode $f_1 = \frac{1.875^2 d}{8\pi h^2}\sqrt{\frac{E}{\rho}}$, where d is the pillar's diameter and h is the pillar's height. For the second-order bending mode $f_2 = \frac{4.694^2 d}{8\pi h^2}\sqrt{\frac{E}{\rho}}$. Both pillar's resonance frequency and geometry can be measured, thus, the ratio of Young's modulus and density of the polymer material can be estimated. Figure.17 shows the SEM picture of a set of long pillars in a 90-degree side view.

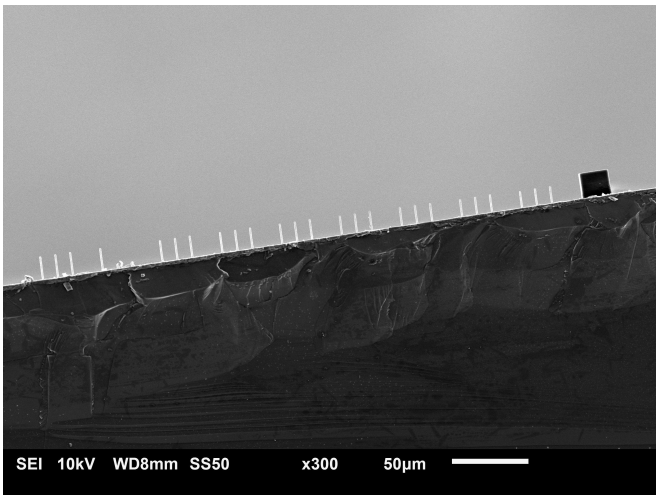


Fig. 17: SEM image of pillars for LDV

Right after the printing, these polymer pillars were measured with an LDV and a lock-in amplifier. A piece of die with pillars printed out of the plane was stuck to a piezoelectric actuator vertically with its side wall oriented upwards. With the bias, the pillars tended to bend up and down, and in this way, the vibrations were easily measured by vertical displacements. Displacements were measured with sweeping frequencies and data were given on the frequency domain. Figure.18 shows an example of the LDV measurements of three different pillars with the same design geometry. The amplitude of the signals in mV shows the relative amplitude of vertical displacements at the pillars' tip. The resonance peak at 2.66 MHz belongs to the substrate or holder since it is identical in measurements with different pillar geometry. The peak at 2.478 MHz represents the first-order bending mode of the pillars and it was reproducible in all three measurements. With a Lorentzian fit, the resonance frequency was estimated as 2.478 MHz, and the quality factor was estimated as 775, 1253, and 1373 for the three pillars respectively.

Sets of pillars with frequencies around 1-3 MHz and 6-9 MHz were printed, measured for frequencies with LDV as described above, and measured for dimensions with SEM. Pillars' quality factors were estimated from the Lorentzian fitting of the LDV results giving the value of around 1000 for all well-printed pillars. Their first-order bending frequencies were plotted as a function of $\frac{d}{h^2}$ and fitted with a fixed zero offset as shown in Figure.19. The slope of this linear function was determined by the polymer's material's properties and was fitted as 283.1 $MHz \cdot \mu m$. The first-order bending frequency of these polymer pillars has a relation with their geometry as $f_1[MHz] = 283.1[MHz \cdot \mu m]\frac{d}{h^2}[\mu m^{-1}]$. Hence the second-order bending frequency has the relation as $f_2[MHz] = 1776[MHz \cdot \mu m]\frac{d}{h^2}[\mu m^{-1}]$.

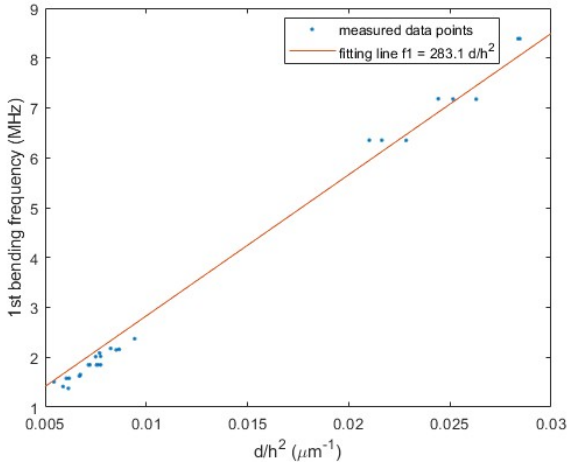


Fig. 19: Pillar's resonance frequency Fitting

Based on the material properties obtained from fitting the first-order bending frequency of long pillars, pillars with much lower aspect ratios were designed. The pillars were designed for both straight and focused SAW delay lines with the finger width of 3 μm, 3.5 μm, and 4 μm, so their estimated second-order bending frequencies lay within the devices' working

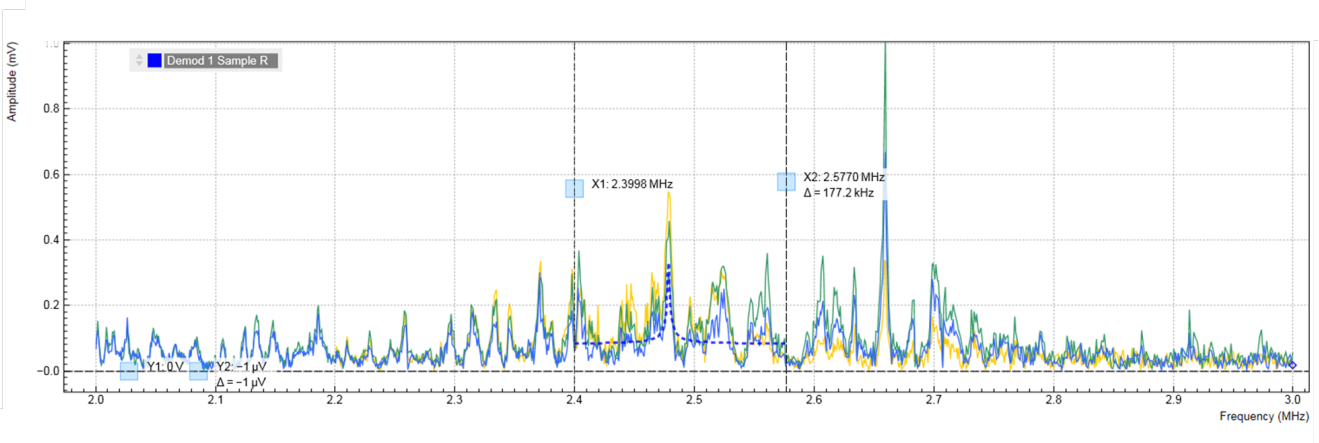


Fig. 18: Laser Doppler vibrometer measurement of a pillar's resonance. Blue, green, and yellow curves represent different measurements of three identical pillars.

frequency ranges. The designed real dimensions and estimated frequencies are shown in Table I.

TABLE I: TPP pillars with their corresponding resonant mode frequencies.

For device IDT widths	Diameter	Height	2nd bending
3 μm	1.279 μm	2.363 μm	407 MHz
3 μm	1.195 μm	2.264 μm	414 MHz
3 μm	1.111 μm	2.165 μm	421 MHz
3.5 μm	1.279 μm	2.561 μm	346 MHz
3.5 μm	1.026 μm	2.264 μm	356 MHz
3.5 μm	1.068 μm	2.264 μm	370 MHz
4 μm	1.026 μm	2.462 μm	301 MHz
4 μm	1.068 μm	2.462 μm	313 MHz
4 μm	1.026 μm	2.363 μm	326 MHz

To enhance the signal strength, pillars were repeated several times on the delay lines. For the straight devices, pillars were printed with 12 in a line as shown in Figure.20. For the focused devices, 7 of the same pillars were printed in a circle at the center of the delay line as shown in Figure.21. The other pillar design for the focused devices was putting three different pillars, with three columns of each type, making a total of 9 pillars, as shown in Figure.22.

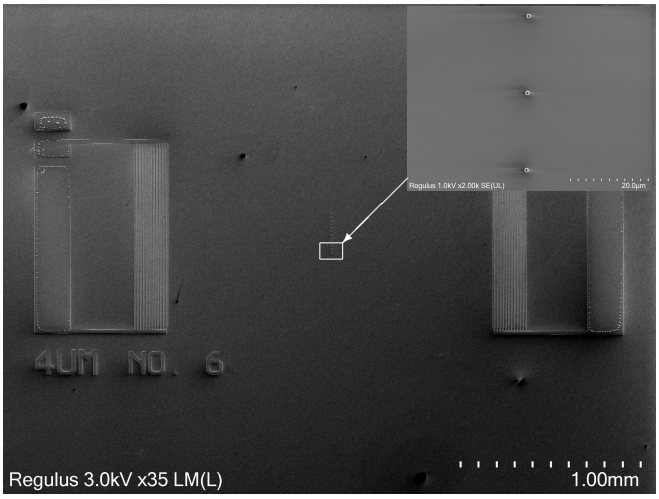


Fig. 20: SEM image of a straight device with pillars printed

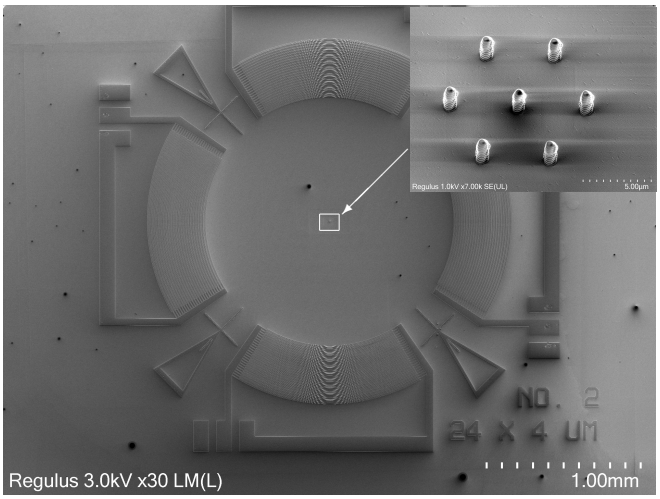


Fig. 21: SEM image of a focused device with seven identical pillars printed

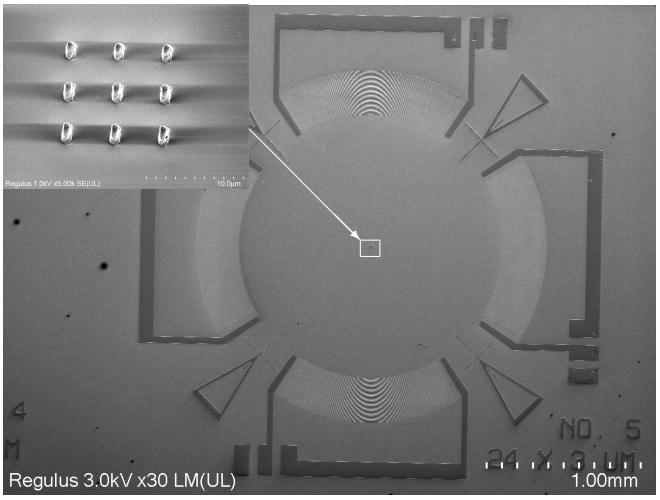


Fig. 22: SEM image of a focused device with nine pillars of three different geometries printed

C. *Focused Ion Beam Induced Deposition (FIBID) Pillars*

Focused ion beam induced deposition of platinum is a process combining chemical vapor deposition and sputtering. Trimethyl platinum precursor gas is fed over the pattern area by a GIS (gas injection system) needle. When the Ion beam scans point by point, the chemical bonds of the precursor gas break leaving the Pt deposited on the substrate but may also sputter the materials away. It is recommended by the system manual with the ion beam current of 2 - 6 $pA/\mu m^2$ and dwell time of 200 ns to achieve efficient deposition that the majority of the precursor gas can decompose but without leaving excess ions etching away the materials. The target diameter of the pillars was set as 0.5 μm and the cross-section area was calculated as 0.1963 μm^2. So, the ion beam current was expected to be chosen between 0.3926 - 1.1778 pA. An ion beam current of 1.1 pA was selected on the system. Due to the worn-out of the ion beam aperture, some of the apertures were wider than the defined sizes and this gave shifts between the

selected ion beam currents and the actual beam currents. The actual ion beam current was 1.80 pA instead of 1.1 pA. Pillars deposited with the above settings are shown in Figure.23.

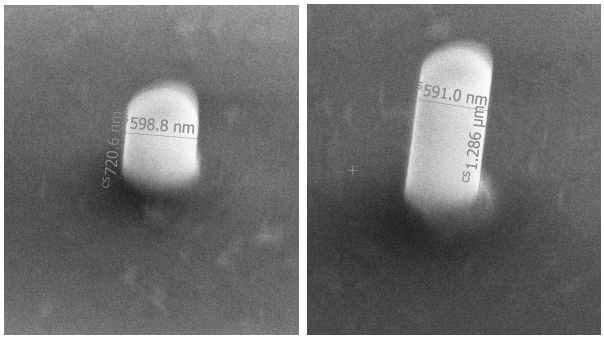


Fig. 23: SEM images of FIB Pt pillars

Young's modulus of 168 GPa and density of 13400 kg/m^3 was found from the literature [13] and was used to estimate the pillar's resonance frequencies. Pillars defined with a diameter of 500 nm and heights from 900 nm to 1150 nm were printed in several arrays for the focused devices with a center frequency of around 410 MHz. The actual deposited pillars were thicker with diameters around 650 nm. Figure.24 shows the SEM picture of a pillar array on the device. It can be seen that around each pillar, the AlN substrate was mildly etched resulting in a circular contour.

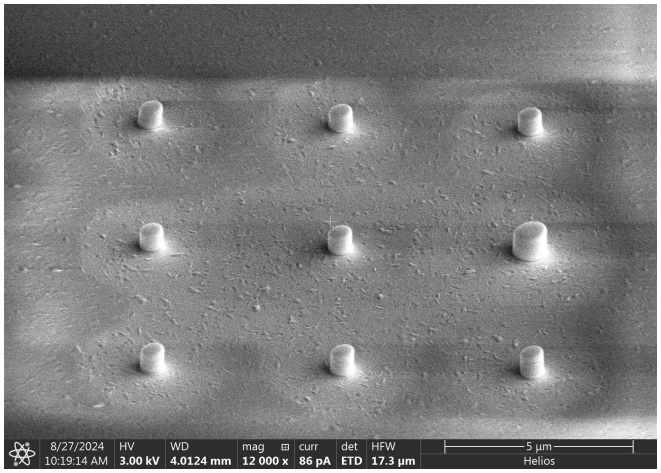


Fig. 24: SEM image of a FIB Pt pillar array

The resulting dimensions and the estimated first-order bending frequencies of the deposited Pt pillars in the arrays are shown in Table II.

TABLE II: FIB pillar designs with their corresponding resonant mode frequencies.

Pillar array 2			
	Diameter	**Height**	**1st bending**
	663.5 nm	0.8702 μm	433.5 MHz
	674.7 nm	0.8990 μm	413.1 MHz
	630.6 nm	0.8990 μm	386.1 MHz
	641.8 nm	0.9558 μm	347.6 MHz
	652.0 nm	0.8987 μm	399.4 MHz
	968.3 nm	1.241 μm	311.1 MHz
	652.0 nm	0.9843 μm	333.0 MHz
	663.5 nm	1.013 μm	319.9 MHz
	652.0 nm	1.056 μm	289.3 MHz

After several measurements which will be discussed in the following measurements section, further depositions on top of the pillars of array 2 were made to modify the pillars' resonances. As shown in Figure.25, a small volume of Pt was deposited on top of each selected pillar. These small Pt structures would add mass to the pillars and shift the resonances downward.

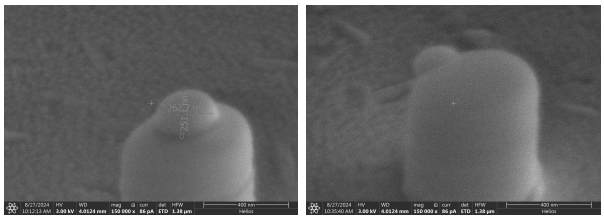


Fig. 25: Pillars with added mass

IV. SAW MEASUREMENTS

The first part of this section covers the measurement of SAW devices before placing the pillars, including transmission measurements for both straight and focused devices. For the focused devices, transmissions were measured in both parallel and perpendicular orientations. The second part discusses the measurements taken after depositing pillars onto the devices, focusing exclusively on the focused devices due to their ability to concentrate SAWs. Results from both TPP polymer pillars and FIB Pt pillars are presented.

The measuring of the SAW device transmission was conducted on the wafer with a probe station and the Keysight P9370A USB Vector Network Analyser. Short-Open-Load-Through (SOLT) calibrations were done before measurements to reduce the influence of setup imperfections and systematic errors.

A. *Transmission of SAW delay lines without pillars*

1) Straight devices: The transmissions of all straight devices were measured and all showed a high transmission band at the corresponding designed working frequency range, consistent with the simulation results. An example of the 3 μm finger width device with 12 finger pairs is shown in Figure.26, the results from measurement and simulation are compared in the same figure. Similar measurement results for 3.5 μm, 4 μm, 4.5 μm, ... devices are put in the supplementary.

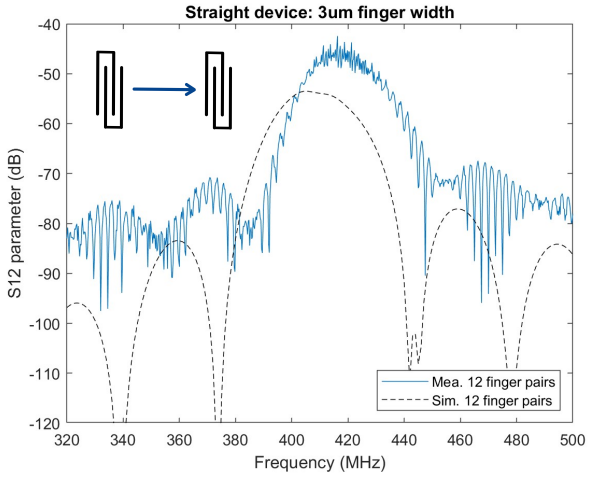


Fig. 26: Transmission of a straight device with 3um finger width

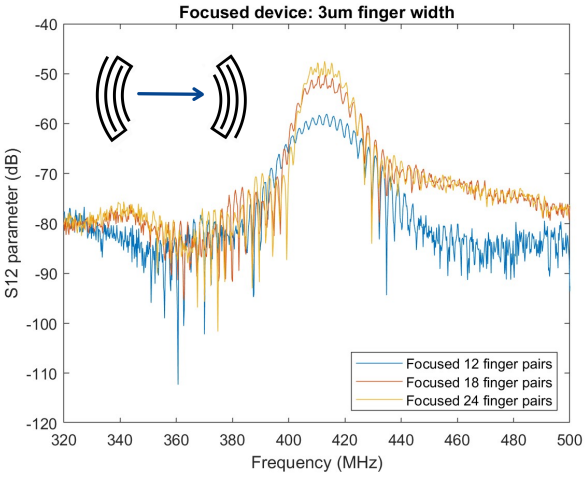


Fig. 27: Transmission of focused devices with 3um finger width and varying number of fingers

In Figure.26, the center frequency and bandwidth of the measured device closely match the simulation results. The small discrepancy in center frequency between the measurement and simulation is reasonable, as the actual wave velocity in the deposited AlN thin film may differ slightly from that used in the COMSOL model. The bandwidth of the devices also aligns well with the simulation. The slight difference in transmission magnitude may result from systematic errors in the measurement setup. During measurement, consistent background signals around -65 dB were observed almost across the entire measured frequency range, independent of the device design. These signals are likely caused electrically, not from the SAWs, and may have been added to the SAW transmission, resulting in the real transmission magnitude larger than the simulation.

2) Focused devices: The parallel transmission of the focused devices showed similar results as the straight devices with high transmission around the designed center frequency. Several devices with different numbers of fingers were compared, shown in Figure.27. The measured transmission shows a trend consistent with the theory that with the number of fingers increasing, the bandwidth becomes narrower and the transmission improves.

The perpendicular transmissions were also measured between two ports at 90 degrees, as shown in the inset of Figure.28 and 29. Ideally, there will be zero transmission from the surface acoustic waves, as the SAWs travel along the delay line focusing on the center point and then diverging to the FIDT on the other side. If there is nothing to interfere on the delay line, no SAW wave will propagate to the IDT at a 90-degree angle. In real measurements, due to the systematic error and parasitic effects from the wafer and pads of the device, the perpendicular transmission of the devices all showed background signals of a similar shape (Figure.28 and Figure.29) instead of only noise level at -100 dB. The measurements taken on different days varied in shape due to changes in the setup. Still, these background signals were consistent in different devices if under the same measurement conditions. The nearly overlapped curves of different designs in Figure.29 implied that the perpendicular transmission measurements of the bare SAW delay line devices did not capture the acoustic transmissions but only electrical noise.

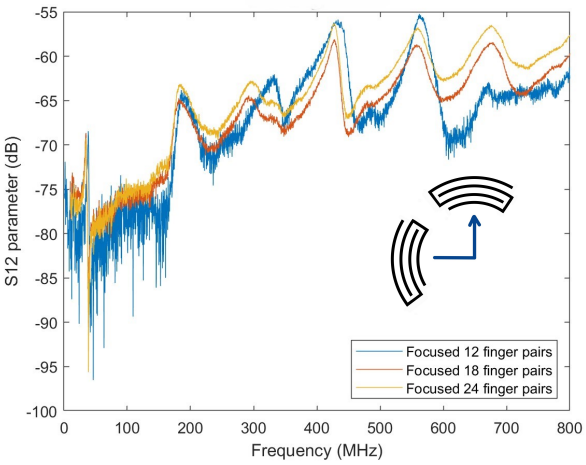


Fig. 28: Perpendicular transmission of focused SAW delay lines with the same center frequency (3um finger width) and varying number of fingers. Curves all showed an undesired background signal with high magnitude from the systematic error. The background signals varied as the data were measured on different days.

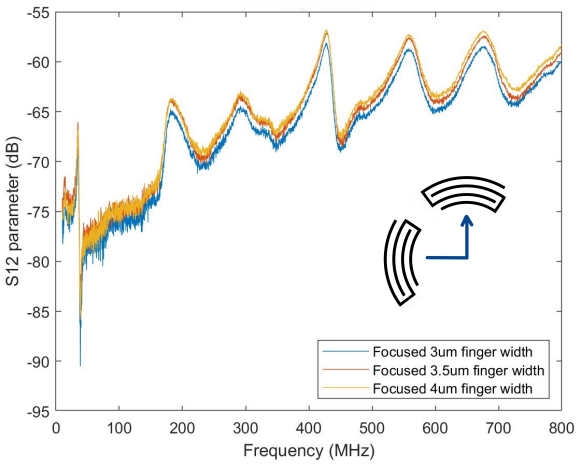


Fig. 29: Perpendicular transmission of focused SAW delay lines with 18 finger pairs and varying center frequencies. The measurements were done on the same day.

B. *Transmission of SAW delay lines with pillars*

The focused devices focus the acoustic waves in a small region, enhancing the interaction between the SAWs and pillars. Therefore, the focused devices were chosen to deposit pillars on and the results are discussed here. When pillars were deposited on the device, the parallel transmission measured how much SAW waves were transmitted along the delay line after some were scattered away by the pillars. This parallel transmission of a device with resonant pillars was expected to show dips at the pillars' resonance frequencies compared to the device without pillars (as shown in the ideal case from simulation in Section II). In reality, these dips can be very subtle and even hard to detect within the overall transmission, which led us to shift to perpendicular measurements. For the perpendicular transmission between two ports at a 90-degree angle, the output port was outside the SAW propagation path, thus, it would only receive the SAWs scattered by the pillars. Peaks at the resonance frequencies were expected on the perpendicular transmission curves.

1) TPP pillars: Indications of polymer pillar resonance were not observed in the parallel nor perpendicular measurement. The transmission ratio with and without pillars was also compared, but the scattering from the pillars was likely too weak compared to the noise level to provide any information. However, the pillar's scattering of surface acoustic waves was spotted in the perpendicular transmission as shown in Figure.30. In one of the focused devices with polymer pillars but without resonances, oscillations between 400 MHz to 420 MHz (as circled in the figure) were observed in addition to the background signal. With comparison to the parallel transmission of the same device, the observed vibrations occurred over the transmission band of the device. This implied that the emitted SAWs of almost all frequencies were scattered by the pillars and received by the 90-degree IDT, which verified the feasibility of receiving the scattered waves with the focused SAW delay line devices designed in this paper. It was promising to detect resonance peaks once sufficient resonances were there.

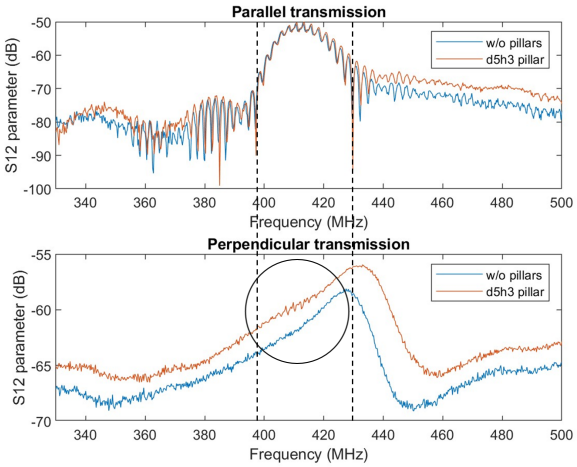


Fig. 30: Transmission of a SAW delay line with TPP pillars showing scattered SAWs

2) FIB pillars: Uncertainty and lack of reproducibility during the printing of two-photon polymerized polymer pillars led to the possibility that the estimated pillar resonances may not be accurate. Additionally, the quality factor of polymer structures was typically low, resulting in broad and weak resonance peaks. These were all likely to lead to the TPP pillar's resonances not being found. To mitigate these problems, measurements were switched to FIB-deposited platinum pillars, which were expected to provide more accurate frequency estimates and sharper resonance peaks.

The perpendicular transmission showed differences when FIB pillars were added. Figure.31 shows the perpendicular transmissions for three devices with the same design: one without pillars (blue curve), one with pillars but no expected resonances (red curve), and one with pillars that have expected resonances (yellow curve). The resonances of pillars on the device represented by the red curve were far from the device's working frequency range. The estimated resonances of pillars on the yellow curve device were aligned with the device's working frequencies, as shown in Table.II of the previous section and marked on the figure with grey dashed lines. Both the blue and red curves were smooth and flat compared to the yellow one, which shows some peaks around the resonance frequency of 413 MHz.

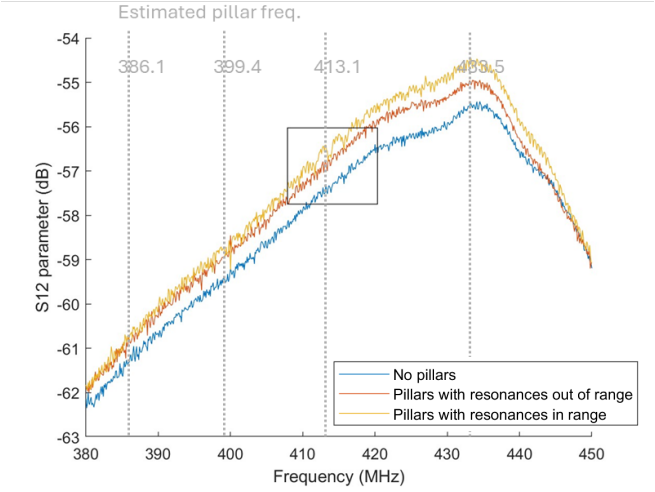


Fig. 31: Perpendicular transmission of SAW delay lines with and without FIB pillars

To have a better look at the peaks mentioned above, slow measurements with much higher resolution were taken to zoom into the range between 410 MHz and 420 MHz, as shown in Figure.32. It can be observed more clearly that the transmission of the device exhibited a wavy shape with small peaks around the estimated resonances when Pt pillars were deposited. Five small resonances around 413 MHz were suspected, these could be the different modes of the designed 413 MHz pillar due to the asymmetry. Two strategies were taken to investigate these suspected resonance peaks.

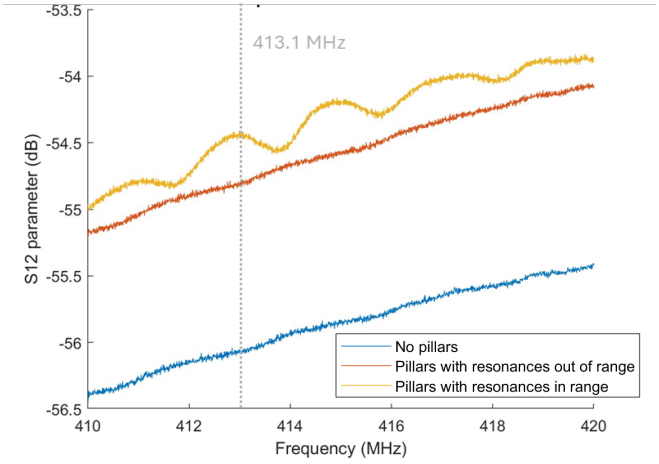


Fig. 32: Perpendicular transmission of SAW delay lines with FIB pillars, zoomed in with high resolution

Firstly, the device was left for three days and measured again, Figure.33. The new curve showed a similar shape but with peaks shifted around 1 MHz lower. This could be interpreted as the pillars absorbing moisture from the air and ultrafine particles falling on the pillars during the time interval. The mass sensitivity of a resonator is $S = \frac{\delta f}{\delta m} = -\frac{f}{2m}$. Assuming the peaks were from the resonance at 413 MHz and the -1 MHz shift in frequency was due to the mass loading, the added mass of a pillar, $\delta m = -2m\frac{\delta f}{f}$, was estimated as 1/207 of its original mass. Using the pillar density of 13400 kg/m^3 and dimension of 674.7 nm in diameter and 899.0 nm in height, the added mass δm was calculated as 20.81 fg which was a reasonable value for the absorption of water and extremely small particles.

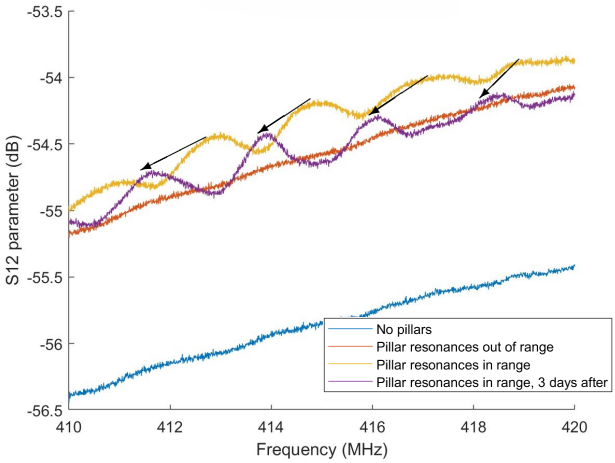


Fig. 33: Perpendicular transmission with FIB pillars after days

The other test was adding an extra small mass to each of the pillars. The added mass was achieved by depositing small volumes of Pt on top, as discussed in the fabrication section. The cables and calibration were modified before this measurement, so the device without pillars was measured again together with the modified pillars on the same day for comparison. As shown in Figure.34, the new curves showed a downward trend other than upward in previous measurements, and this was due to the change of background signals from the setup. The local peaks were concerned instead of overall trends in this measurement. The new transmission showed very different peaks after small Pt lumps were deposited. These lumps were assumed to add mass evenly over the whole pillar. The volume of the Pt lump was estimated from a diameter of 262 nm and a height of 250 nm, which were measured in an SEM image. Using the estimated resonance frequency of 413 MHz and the corresponding pillar dimension of 674.7 nm diameter and 899.0 nm height, a frequency shift was calculated from the added mass as $\delta f = -f\frac{\delta m}{2m} = -8.66\ MHz$. The 413 MHz resonance was speculated to have shifted about 8.66 MHz lower and lay outside of the measurement range in this new measurement. It can be guessed that the new peak at around 411 MHz in the measurement of modified pillars might have originated from a higher resonance that was previously beyond this measurement range.

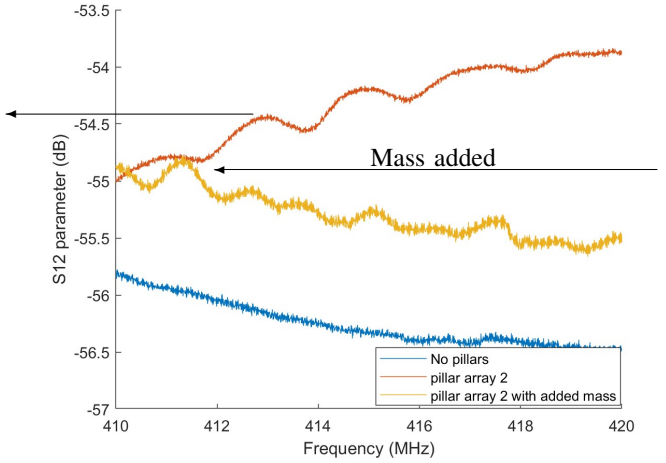


Fig. 34: Perpendicular transmission with modified FIB pillars.

V. Discussion

In this paper, capturing the micro/nano-pillar resonances using the SAW delay line has been implemented with both the COMSOL model and the real device. The simulations proved the feasibility of measuring the resonance frequencies of several pillars together and showed that the coupling between pillars does not interfere with the resonance frequencies in this application. These show the promising multi-resonance measurement for the development of ultrafine particle sensors. From both simulation and measurement results, the surface acoustic waves' interaction with the micro/nano-pillars can be weak. Thus, in the real case, how well the performance of resonance measurements depends on the quality of the S12 parameter measurement. Many factors could have limited the measurement of pillar resonances in this work. Several possible aspects are discussed below.

A. The resonance frequency of the pillar

Due to the limitation of the laser Doppler vibrometer frequency range, the resonance frequencies of the pillars designed in this work cannot be measured directly. All the pillars in this work were designed based on resonance frequency estimation. Since the material properties of TPP polymers are greatly dependent on the energy dose during the polymerization process, and the properties of FIB Pt structures are also influenced by the impurity introduced by the carbonaceous matters and gallium ions, it is crucial to know the actual Young's modulus and density of pillar's material.

The information of $\sqrt{\frac{E}{\rho}}$ for the TPP polymer was obtained by fitting the resonance frequencies of long pillars. However, there still exist many factors that could cause errors to the obtained $\sqrt{\frac{E}{\rho}}$.

- Different doses for long and short pillars:
  Even though the laser power, the scan speed, and the slicing and hatching distance of the pillar were all kept the same in order to fix the dose, the real dose could still be quite different for different geometries. This means that the ratio of Young's modulus and density we measured from the long pillars may not be that for the short pillars.
- Environmental factor: The change of temperature and humidity in the environment could modify the properties of the pillar.
- Reproducibility:
  It is observed during printing that for different prints the system may find different interface locations to start the printing. As shown in Figure.35, pillars represented quite different interface locations as the starting position was set the same for all prints and a base of the same thickness was designed for all pillars. It also happened that, the same printing file and setting printed out different pillars, as shown in Figure.36.

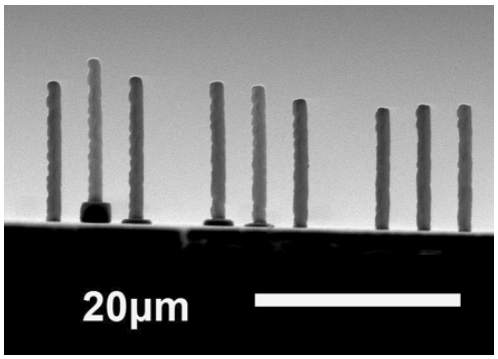


Fig. 35: Difference of interface location

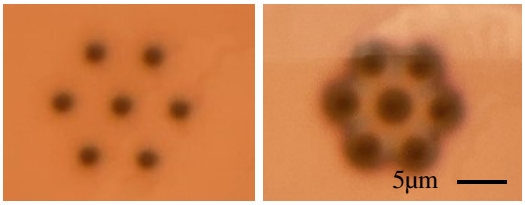


Fig. 36: Reproducibility of pillars

For the pillars by focused ion beam induced deposition, the same strategy to predict material properties was not used since the deposited pillar's height was limited by the system constraints. The FIB-deposited Pt properties were found in the literature. The material properties used by other researchers were different in different papers. There is possibly a large shift between the estimated resonance frequency and the real resonance frequency of the designed pillar.

All these factors discussed above could result in the pillars' resonances falling outside the working frequency range of the SAW device.

B. Quality factor

Both the two-photon polymerization and focused ion beam-induced deposition cannot provide accurate geometry in such a small submicron scale. Some vibrometer measurements with the TPP pillar's resonance have indicated that the pillar might have a relatively small quality factor. As in the example shown in Figure.37, the resonance peak was widespread to a large

frequency range with low amplitude, and the quality factor was fitted to be only 21.

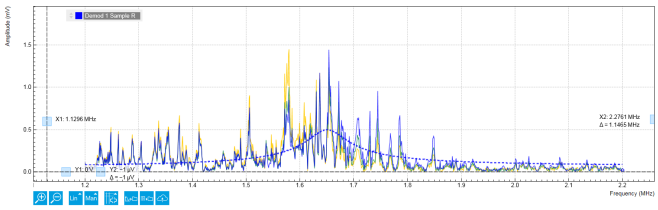


Fig. 37: LDV results of TPP pillars with low Q factor. Yellow, green, and blue data were from measurements of three different pillars with the same design geometry. The dashed line was from the resonance peak fitting

Another simulation of pillars on the SAW delay line was conducted with different pillar quality factors assigned, Figure.38. It can be seen that when the quality factor of pillars dropped to the orders of magnitude of 10, the resonance peaks were not able to be detected anymore.

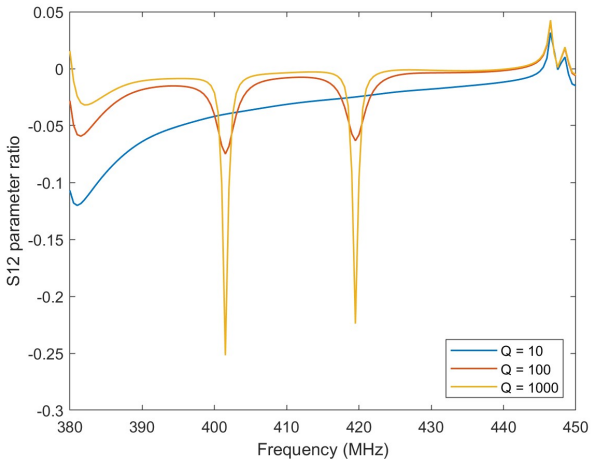


Fig. 38: Simulation of pillars on SAW device with sweeping Q

C. Electrical transmission

As mentioned in the measurement section of perpendicular transmission, there was always an undesired background signal with a consistent shape. This signal was not due to the acoustic waves but pure electrical transmission and it could be as high as -60 dB during the measurements. Unfortunately, the calibration kit and the probe station were not good enough to cancel this strange transmission. The signal after calibration with both probes unloaded is shown in Figure.39, which can be seen that this undesired transmission was already as large as -75 dB even without loading. These signals from the setup problem were too high and possibly buried the signal information about the pillars.

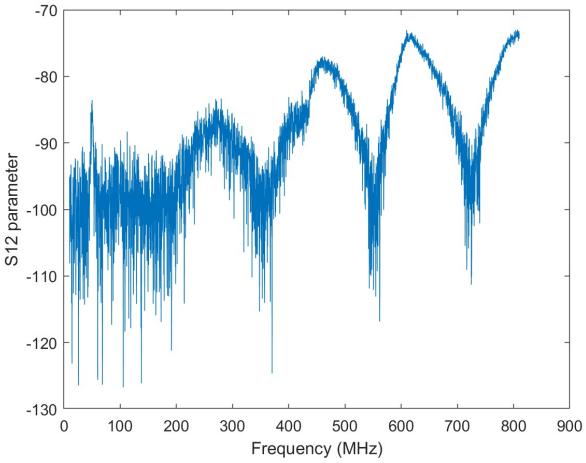


Fig. 39: Background signals

D. Actuation strength of the pillar

Signals of SAWs scattered by the pillars have been observed but without significant peaks at the resonances. It is suspected that the pillars were not actuated into vibration or the vibration magnitude was too low to scatter more waves. The maximum signal power that the portable vector network analyzer can supply is 0 dBm which is 1 mW. This power was given to a COMSOL model and the displacement amplitudes of vibrating pillars were solved, Figure.40. The simulated horizontal displacements of the pillars were smaller than 0.34 nm, which is extremely small compared to the SAW wavelength and the pillar dimension. The quality factor in the model was set to 500, if in the real case the quality factor was much poorer, the vibration amplitude would be even smaller. Such small vibrations are only able to be detected in simulations without noise but not in real cases. This could explain why no peaks or only tiny peaks were observed in the measurements.

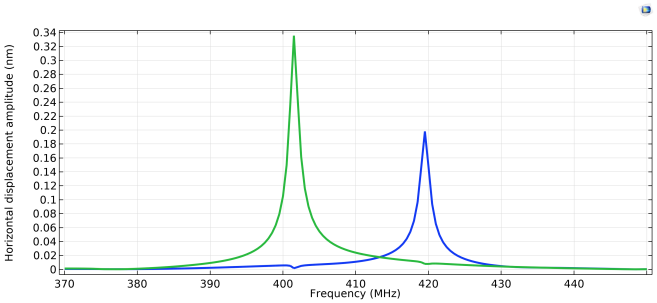


Fig. 40: Simulated pillars' amplitudes with 1 mW power at IDTs

VI. Conclusion

This study aimed to build the foundation for developing resonant mass sensors using surface acoustic wave transduction with the application for nanoparticle sensing. Initially, COMSOL models demonstrated the feasibility of detecting the resonances of pillars from the SAW device transmission.

Subsequently, SAW delay line devices with sufficient bandwidth and high center frequencies of up to 410 MHz, were designed, fabricated, and tested. The transmissions of these devices were measured and showed a good match to the simulated results. Printing polymer nanopillars with the two-photon polymerization and depositing platinum pillars with the focused ion beam on the aluminum nitride piezoelectric thin films were realized. Surface acoustic waves scattered by the polymer pillars have been successfully received with the focused configuration at 90 degrees. With the limited experimental conditions, small peaks were noticed with the device on which a Pt pillar array containing a resonance estimated at 413 MHz was deposited. The highest observed peak, located around 414 MHz, was very close to the estimated resonance of the pillar. It is suspected that these peaks represent the resonances of the pillars. Furthermore, the observed peaks would shift frequencies over time and with the addition of mass on the pillars, implying their relevance to the pillars' resonances.

Overall, this work demonstrates the potential of detecting resonances of multiple micro/nanopillars together using SAWs, laying the groundwork for the future development of resonant mass sensors for ultrafine particle detection.

REFERENCES

[1] Rachana Yadwade, Saee Gharpure, and Balaprasad Ankamwar. Nanotechnology in cosmetics pros and cons. *Nano Express*, 2(2), Jun 2021 2021/06//. Copyright - © 2021. This work is published under http://creativecommons.org/licenses/by/4.0/ (the "License"). Notwithstanding the ProQuest Terms and Conditions, you may use this content in accordance with the terms of the License; Last updated - 2023-11-30.

[2] Mo Li, Hong Tang, and Michael Roukes. Ultra-sensitive nems-based cantilevers for sensing, scanned probe and very high-frequency applications. *Nature nanotechnology*, 2:114–20, 02 2007.

[3] Hutomo Suryo Wasisto, Stephan Merzsch, Andreas Waag, Erik Uhde, Tunga Salthammer, and Erwin Peiner. Airborne engineered nanoparticle mass sensor based on a silicon resonant cantilever. *Sensors and Actuators B: Chemical*, 180:77–89, 2013. Transducers 2011.

[4] Arash Hajjam, James C. Wilson, and Siavash Pourkamali. Individual airborne particle mass measurement using high-frequency micromechanical resonators. *IEEE Sensors Journal*, 11:2883–2890, 2011.

[5] Silvan Schmid, Maksymilian Kurek, Jens Q. Adolphsen, and Anja Boisen. Real-time single airborne nanoparticle detection with nanomechanical resonant filter-fiber. *Scientific Reports*, 3, 2013.

[6] Hutomo Suryo Wasisto, Stephan Merzsch, Andrej Stranz, Andreas Waag, Erik Uhde, Tunga Salthammer, and Erwin Peiner. Silicon resonant nanopillar sensors for airborne titanium dioxide engineered nanoparticle mass detection. *Sensors and Actuators, B: Chemical*, 189:146–156, 2013.

[7] Tsung-Tsong Wu, Yung-Yu Chen, and Tai-Hsu Chou. A high sensitivity nanomaterial based saw humidity sensor. *Journal of Physics D: Applied Physics*, 41(8):085101, mar 2008.

[8] Hendrik Kähler, Holger Arthaber, Robert Winkler, Robert G. West, Ioan Ignat, Harald Plank, and Silvan Schmid. Transduction of single nanomechanical pillar resonators by scattering of surface acoustic waves. 10 2022.

[9] Vincent Laude, Davy Gérard, Naima Khelfaoui, Carlos F. Jerez-Hanckes, Sarah Benchabane, and Abdelkrim Khelif. Subwavelength focusing of surface acoustic waves generated by an annular interdigital transducer. *Applied Physics Letters*, 92(9), March 2008.

[10] Lin Shu, Bin Peng, Chuan Li, Dongdong Gong, Zhengbing Yang, Xingzhao Liu, and Wanli Zhang. The characterization of surface acoustic wave devices based on aln-metal structures. *Sensors*, 16(4), 2016.

[11] G. Bu, D. Ciplys, M. Shur, L.J. Schowalter, S. Schujman, and R. Gaska. Surface acoustic wave velocity in single-crystal aln substrates. *IEEE Transactions on Ultrasonics, Ferroelectrics, and Frequency Control*, 53(1):251–254, 2006.

[12] Enrico Domenico Lemma, Francesco Rizzi, Tommaso Dattoma, Barbara Spagnolo, Leonardo Sileo, Antonio Qualtieri, Massimo De Vittorio, and Ferruccio Pisanello. Mechanical properties tunability of three-dimensional polymeric structures in two-photon lithography. *IEEE Transactions on Nanotechnology*, 16(1):23–31, 2017.

[13] Stefan Enderling, John Hedley, Liudi Jiang, Rebecca Cheung, Christian Zorman, Mehran Mehregany, and Anthony Walton. Characterization of frequency tuning using focused ion beam platinum deposition. *Journal of Micromechanics and Microengineering*, 17:213, 12 2006.

Recommendations and Future Work

Based on the results and discussions presented in the previous paper section, several immediate and long-term steps are recommended.

One of the most critical actions is to obtain good S-parameter measurement data. To eliminate unwanted background signals from the instruments and minimize parasitic effects, it is recommended to switch to a different probe station. Previous measurements revealed grounding issues and other problems with the current setup that calibration could not resolve. It is worth repeating all measurements once we have access to a better probe station and GSG probes. In the long term, it is also recommended to measure device transmission with a PCB board instead of on-wafer. To address the issues encountered during PCB measurements (as discussed in the appendix), a more dedicated PCB design should be made considering the impedance matching and mitigating potential parasitic effects from wire bonding.

Another important task is to confirm the nanopillars' resonance frequencies. Ideally, this could be done using a more advanced laser Doppler vibrometer with a higher frequency range to measure the resonance directly. With the existing instruments, the thing we can do to get more insight into the properties of the FIB-deposited Pt is to deposit Pt structures, such as cantilevers, and measure their mass, stiffness, and resonances. These measurements would allow a more accurate estimation of the nanopillar's resonance. Furthermore, depositing more Pt pillars with varying dimensions and observing more peaks would help verify the suspected resonance frequencies by tracking how they change with size.

The other thing we can try is increasing the power applied to the device during VNA measurements. This could provide stronger actuation of the pillar's vibration and provide more obvious resonance peaks. This can be attempted with a new VNA with higher power, or by connecting an amplifier to the current VNA.

For future work, there are several things we can try to further build the device towards sensing applications. Modifying pillars' mass by both depositing a small volume and etching away a small volume can be done to characterize the nanopillar resonator's mass sensitivity. Additionally, further design, fabrication, and testing of SAW delay line devices with the chirped design are recommended to achieve a much wider bandwidth which would allow more pillar resonances to be measured simultaneously on the same device.

3

Appendix

3.1. Device Design

3.1.1. Nanopillar coupling

As discussed in the literature survey, couplings between nanopillars are expected to be observed with several of them printed on the SAW delay line. To study the coupling strength and its influence on frequency measurement, COMSOL simulations of nanopillars on thin film AlN piezoelectric substrate are simulated separately.

The geometry of the substrate was constructed as a semi-sphere with $1\ \mu m$ thick AlN film on top. A perfectly matched layer (PML) was defined to the outer semi-sphere to absorb waves imitating infinitely large substrate. Pillars assigned with the SU-8 photoresist material were built on the center of the substrate. Due to the symmetry, the simulation was done on half of the geometry. Figure.3.1 shows the geometry for the COMSOL simulation. The modeling was conducted in Solid Mechanics and Electrostatics physics with piezoelectric effect coupling.

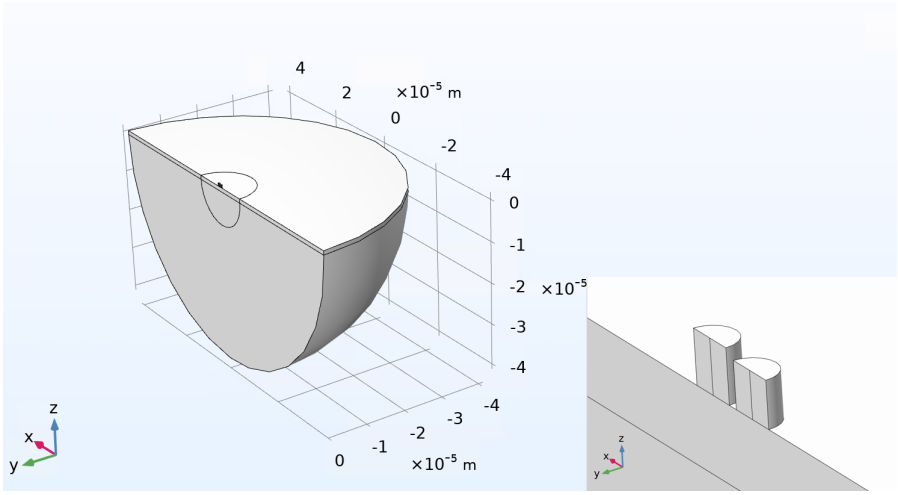


Figure 3.1: COMSOL model for pillar coupling investigation

Two nanopillars with slightly different geometry were placed next to each other on the substrate. They were actuated into vibration by giving a load at the bottom of one pillar. The vibration amplitude at the top of both pillars was measured as a function of actuating frequency, as shown in Figure.3.2. The solid lines represent the vibration of the first pillar and the dashed lines represent the second pillar. Besides the peaks at around 175 MHz and 186 MHz representing the resonances of the two pillars respectively, a slight rise of the first pillar's vibration amplitude at around 186 MHz can be observed. This indicated the weak coupling between the two pillars. A parametric sweep of the spacing between two pillars was performed to vary the coupling strength and investigate the influence of coupling on the

resonances. Figure.3.2 always shows two clear peaks and no observable shift of resonance peaks with two pillars gradually placed closer to each other from a spacing of 350 nm to only 50 nm. In this instance, the coupling between two pillars only affected the vibration amplitude, not introducing new modes nor shifting the resonance frequency. To verify the resonance frequency of the pillar's bending mode read from the peak, it was compared to the one solved by the Eigenfrequency study of a single pillar on the substrate. Figure.3.3 shows the resonance frequencies and mode shapes of the second bending mode of the two pillars measured in Figure.3.2. The eigenfrequency of the pillar with a diameter of 1050 nm and height of 2200 nm was solved as 185.65 MHz and that of the pillar with the same diameter and height of 2300 nm was solved as 174.86 MHz, which corresponded exactly to the peaks in Figure.3.2.

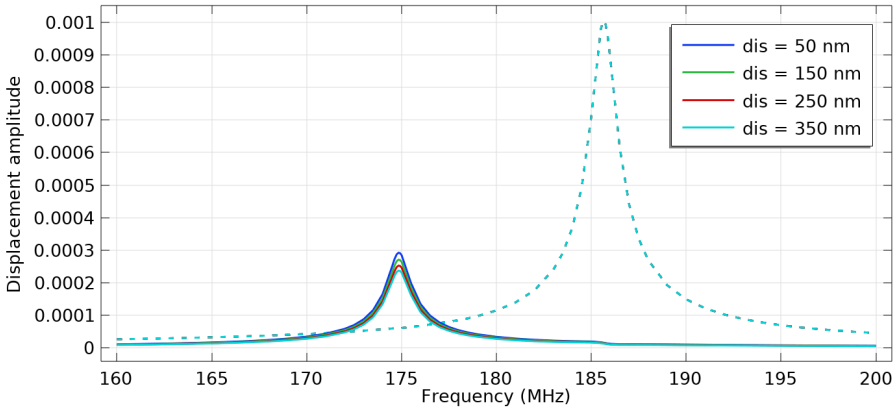


Figure 3.2: Vibration amplitude of two coupled pillars from simulation

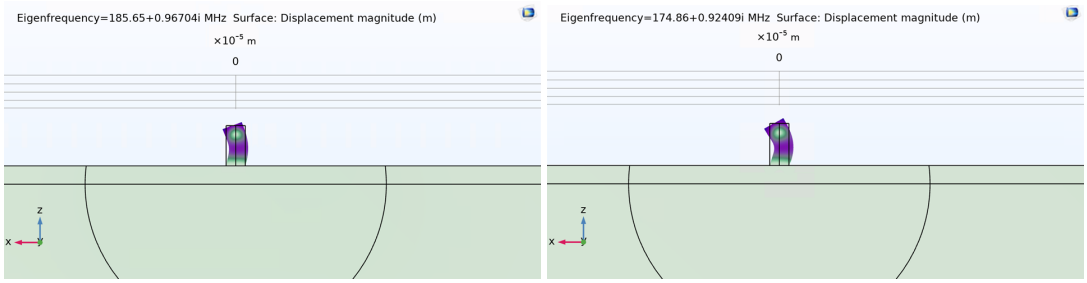


Figure 3.3: Mode shapes of two pillars

Couplings of the first bending modes were investigated as well and showed similar outcomes, Figure.3.4. In addition to previous simulations of polymer pillars, platinum-based pillars were also simulated, Figure.3.5. Compared to the polymer pillar case, the coupling introduced peaks of Pt pillars were more prominent which indicated a stronger coupling effect.

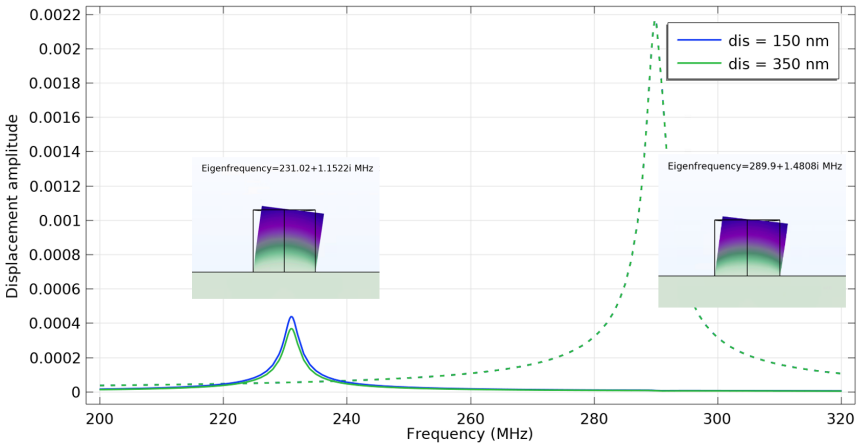


Figure 3.4: Vibration amplitude of two coupled pillars in the first bending mode

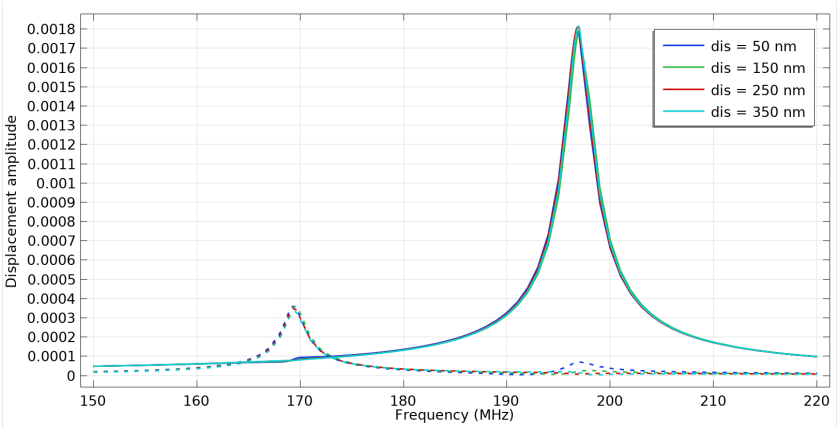


Figure 3.5: Vibration amplitude of two platinum-based pillars

From the above simulations, the resonance peaks of the pillars were all well separated. Pillars resonated exactly at the frequency solved by the Eigenfrequency study. Changing the distance between pillars within a certain range did not shift the resonance peaks. It can be concluded that the coupling between polymer nanopillars is weak. Thus it can be reasonably inferred that coupling has negligible influence on the pillars' vibration with the certain material and geometry chosen in this project.

3.1.2. SAW Delay Line Design

Non-chirp design

Surface acoustic wave delay lines with different frequency bands were designed to correspond to the resonance frequencies of different nanopillars. In the delay line device design, two interdigital transducers (IDT) were placed facing each other at a distance of two times the wavelength. A typical IDT structure was used, in which the finger width and spacing were equal to a quarter of the designed wavelength. The finger width of an IDT determines the central frequency. Both wide aperture (overlap length of the finger pairs) and large number of finger pairs provide high transmission. Increasing the number of finger pairs at the same time decreases the bandwidth. All these design parameters determine the performance of the SAW device, and they were selected based on the COMSOL simulation.

The COMSOL model with Electrostatics, Solid Mechanics, and Electrical Circuit physics was built to simulate the transmission of the SAW delay line. Instead of building the whole Si wafer, perfectly matched layers (PMLs) (light blue) were assigned to two sides and the bottom of the geometry to absorb waves imitating an infinite domain, Figure.3.6. Dark brown and dark blue stripes were connected to the ground, pink stripes and yellow strips were connected to the input signal and output signal respectively,

representing the IDT fingers. With the Frequency Domain study, scattering parameters S11 and S21 of the delay line device were calculated.

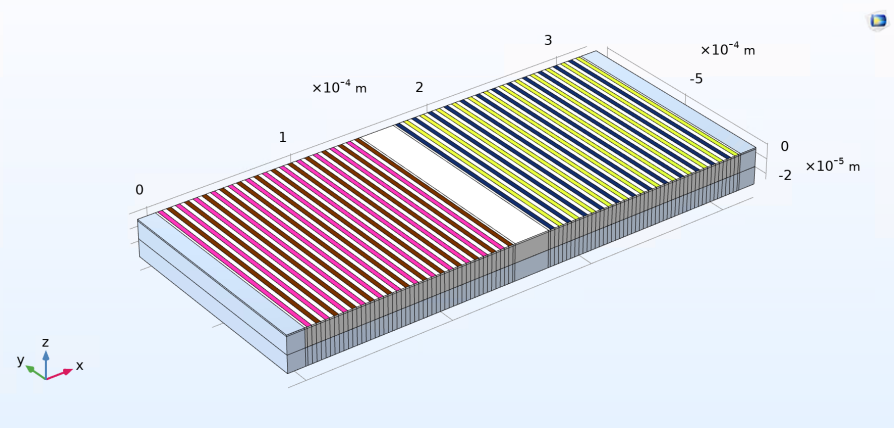


Figure 3.6: COMSOL model for SAW delay line

Figure.3.7 shows the design selections with different working frequency ranges and their transmission from simulation. The aperture was set as 1 mm for all designs to ensure enough transmission for the measurement later. Other design parameters of the selected design are shown in Table.3.1

Wavelength (μm)	Finger width (μm)	Number of finger pairs	IDT length (μm)	Central frequency (MHz)
26	6.5	18	468	192
24	6	18	432	208
22	5.5	12	264	228
20	5	12	240	250
18	4.5	12	216	278
16	4	12	192	312
14	3.5	12	168	356
12	3	12	144	414
12	3	6	72	420

Table 3.1: Parameters of non-chirp straight IDT designs

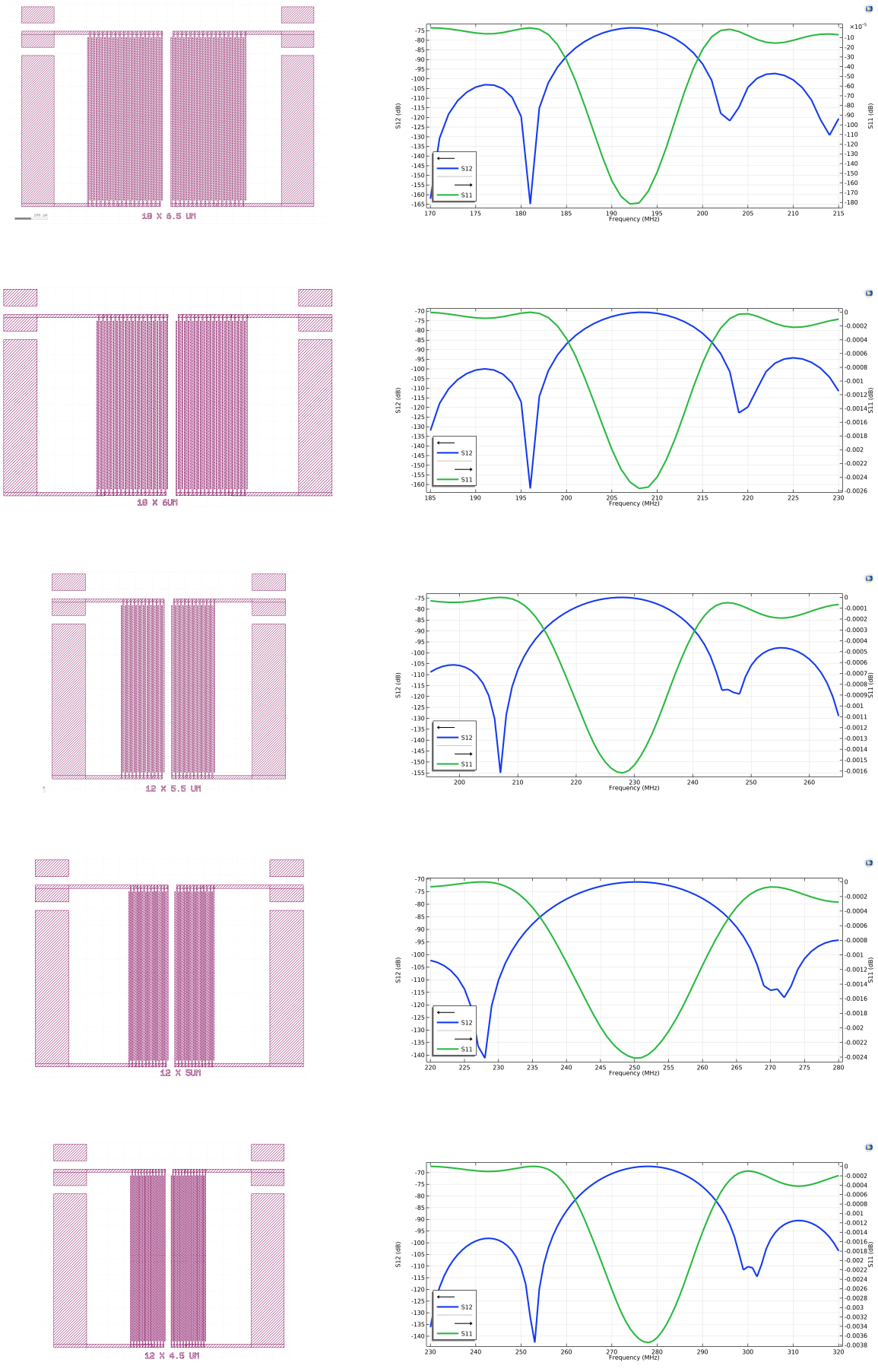


Figure 3.7: Non-chirp straight IDT designs

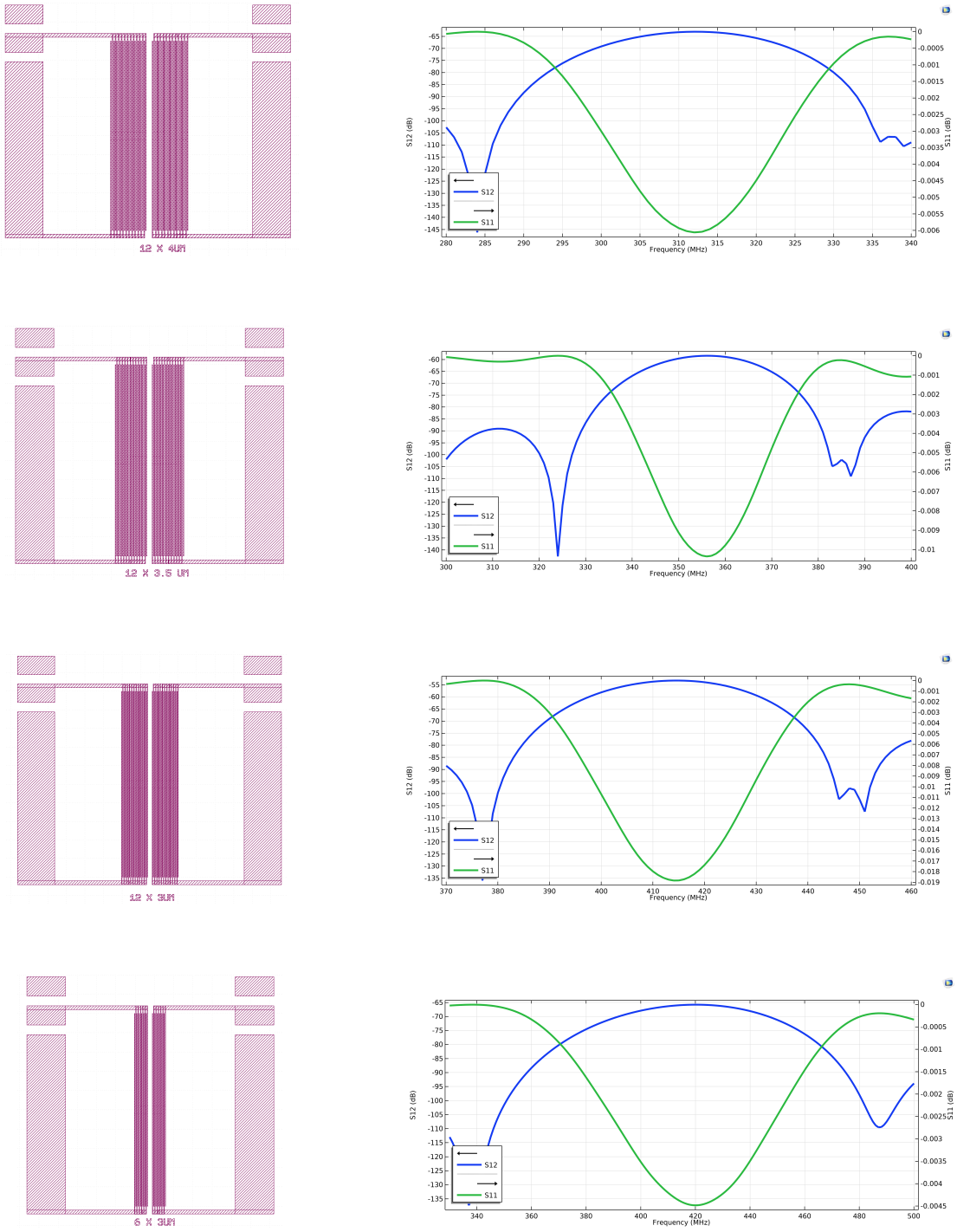


Figure 3.7: Non-chirp straight IDT designs (following the figure in the previous page)

These SAW delay line designs each cover a small range of frequencies with measurable transmission. Their simulated working frequency ranges are shown in Figure.3.8. In this project, non-chirp SAW delay lines were designed to cover resonance frequencies from 180 MHz to 450 MHz.

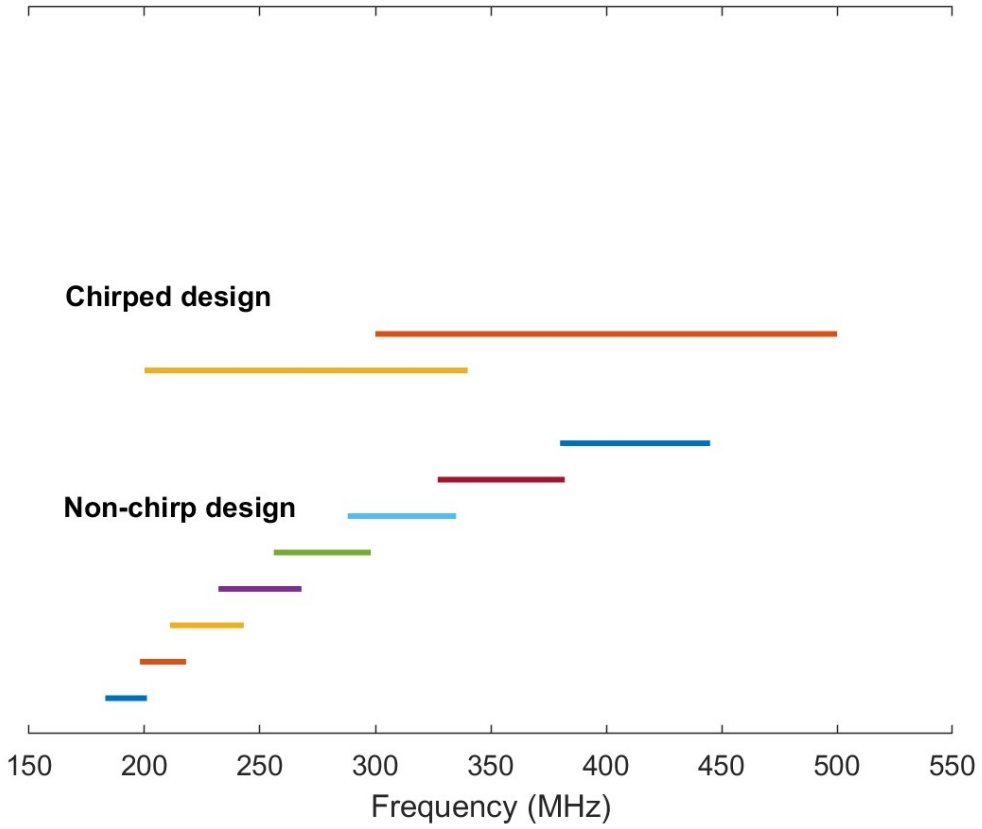


Figure 3.8: Working frequency ranges of IDT designs

Chirped design

In order to have a wider bandwidth to observe two or more pillars' resonance with one device, chirped IDTs were designed. Two frequency ranges of 200 - 340 MHz and 300 - 500 MHz were aimed at, Figure.3.8. With the desired frequency range, the width of the finest finger corresponded to the highest frequency and the width of the widest finger corresponded to the lowest frequency. The variation of fingers in between can be designed based on a linear-period modulation or a linear-frequency modulation. The comparisons of these two modulations on two designed frequency ranges are shown in Figure.3.9. The two different configurations both showed nearly uniform transmission on designed frequency ranges with similar amplitude. The linear-period modulation had better performance at the lower frequency while the linear-frequency one had better performance at the higher frequency. The linear-frequency modulation was chosen for this project because of its slightly higher transmission.

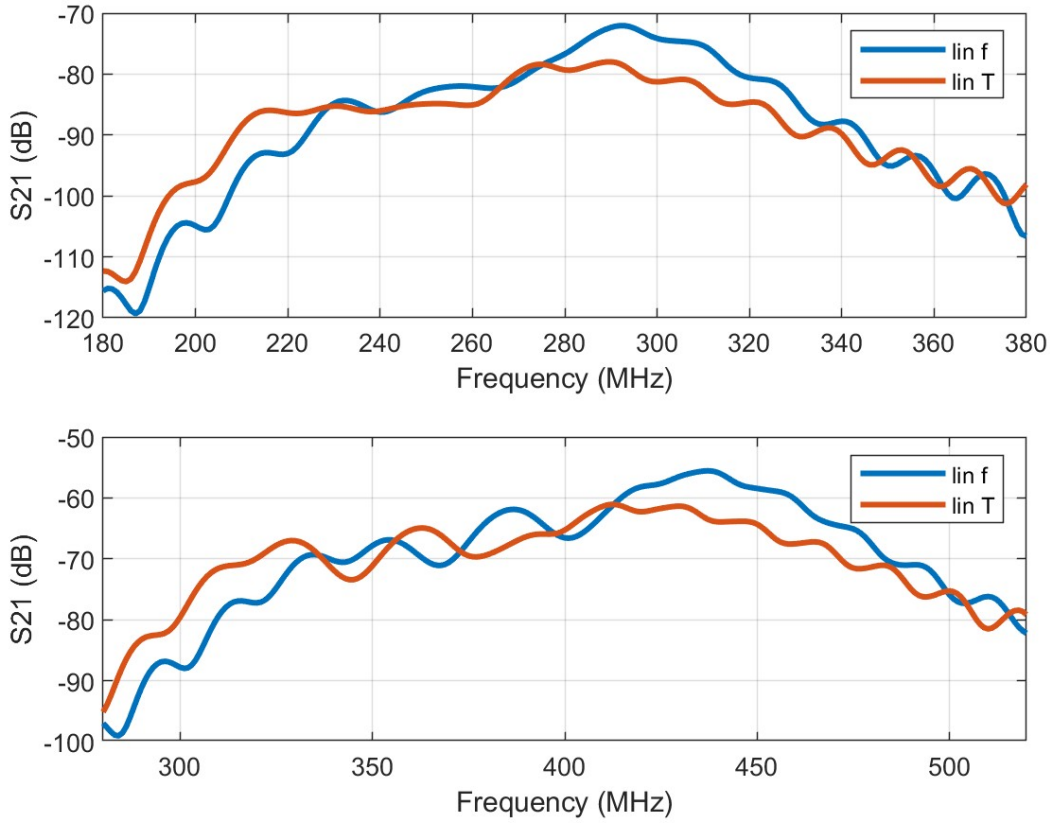


Figure 3.9: Comparison between linear-frequency and linear-period designs

Several chirped IDTs designed on 200-340MHz and 300-500MHz are shown in Figure.3.10, with IDT length varying from 0.3 mm to 1mm.

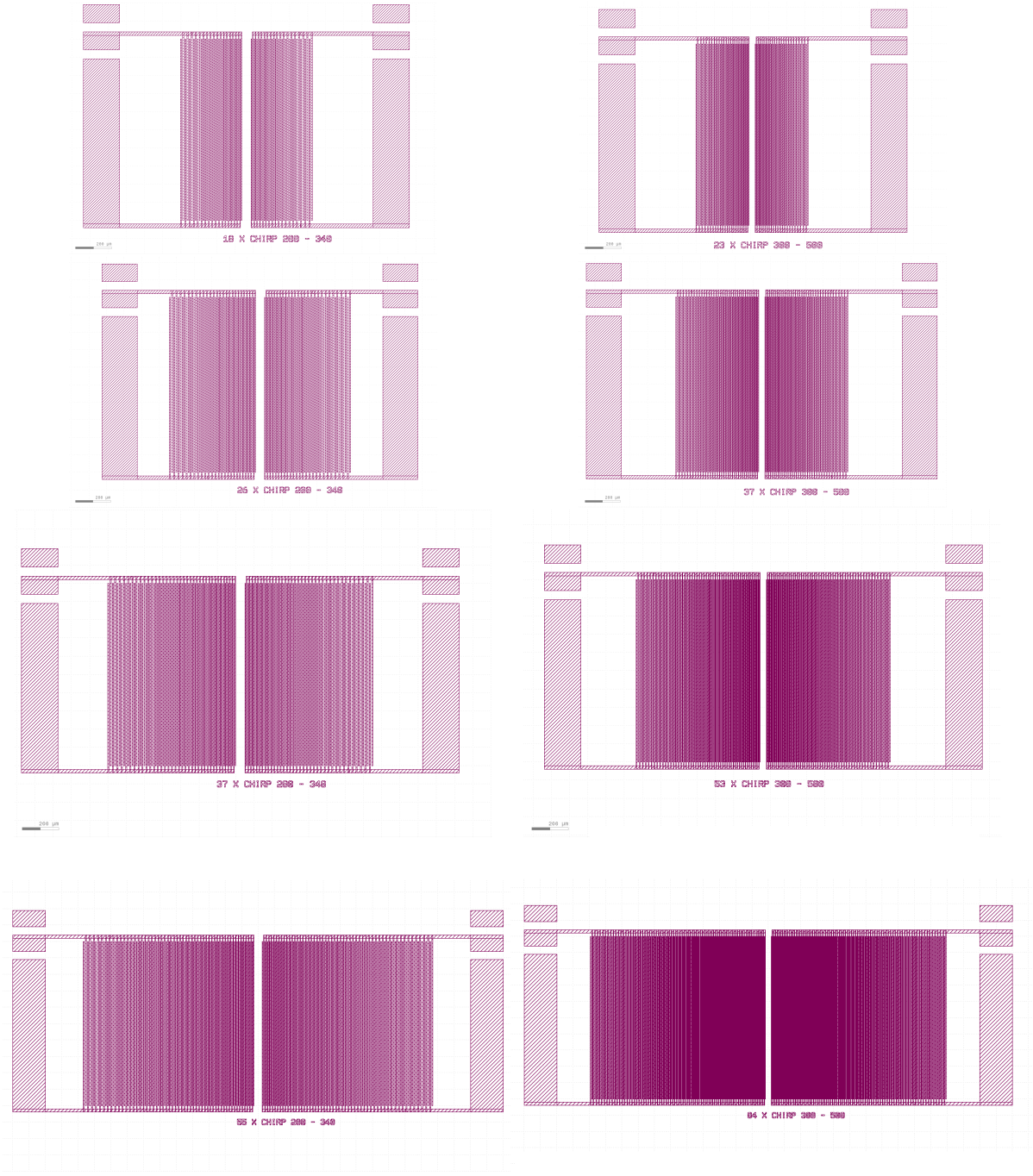
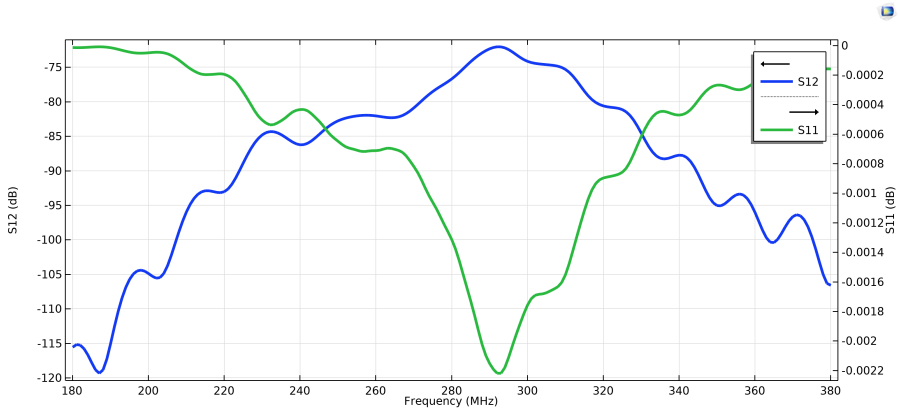
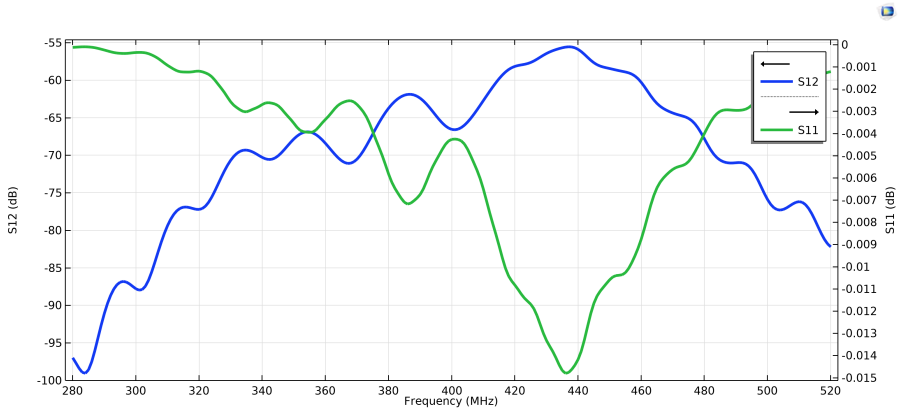


Figure 3.10: Chirped IDT designs

The S-parameter curves in Figure.3.11 are from the simulation results of the designs with the least finger numbers (the first two in Figure.3.10). The rest of the chirped IDT designs were expected to provide similar curve shapes but higher transmission due to their increased finger numbers.



(a) 200-340MHz design



(b) 300-500MHz design

Figure 3.11: S-parameters of the chirped IDT designs from simulation

Focused IDT design

In order to have better interaction with nanopillars, focused IDT (FIDT) with fingers in the shape of an arc was used. The degree of arc for all the designs used in this project was set as 60 degrees, which can provide adequate focus area and wave amplitude. The focused IDT shape can greatly focus surface acoustic waves around the geometry focus point, where the nanopillars would be printed later. Simulations of a single focused IDT with chirped frequency were conducted. The resulting SAW at the central frequency of the bandwidth can be observed from the vertical displacement field, which shows a distinct focusing effect, Figure.3.12.

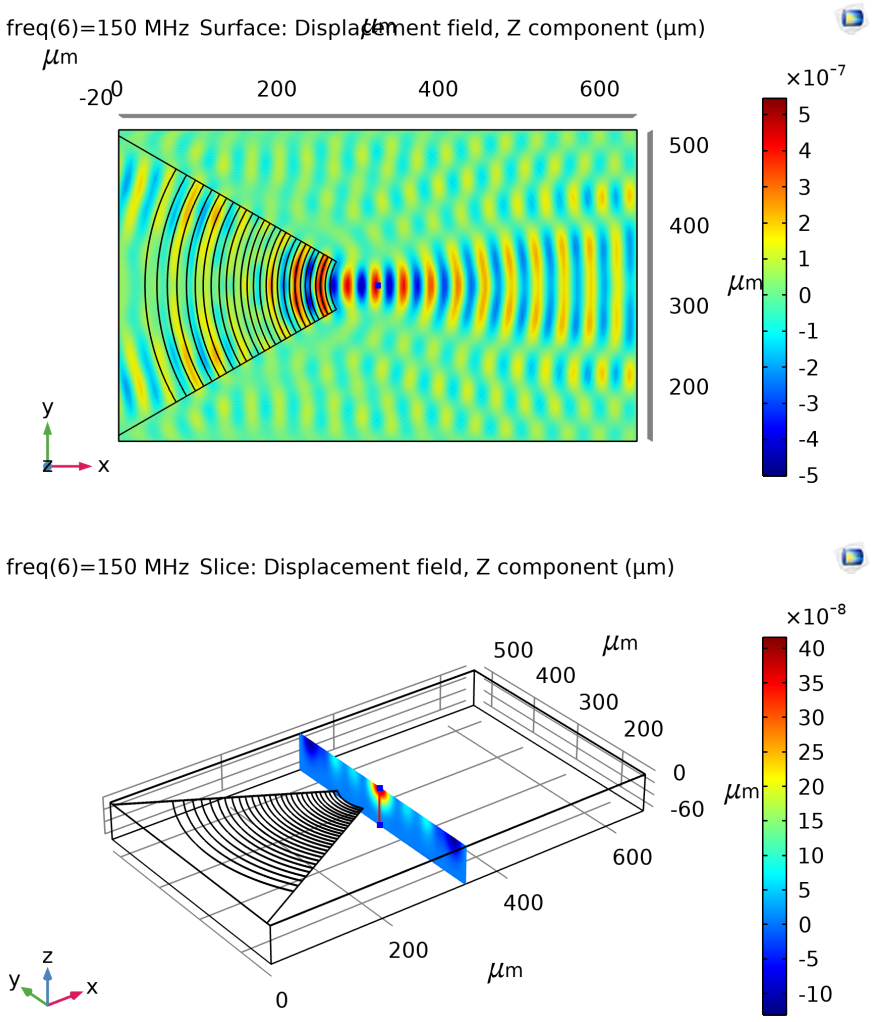


Figure 3.12: Focused IDT simulation

The focusing area size can be estimated from the spatial distribution of the vertical displacement on the cross-section that passes the geometrical focus point. 1D plots of different working frequencies are shown in Figure.3.13. The full width at half maximum (FWHM) of the SAW displacement spatial distribution was used to represent the focus area size, which is around $35\mu m$ for the design in Figure.3.12. The focus area of the FIDT designs used in this project is believed to have a similar size.

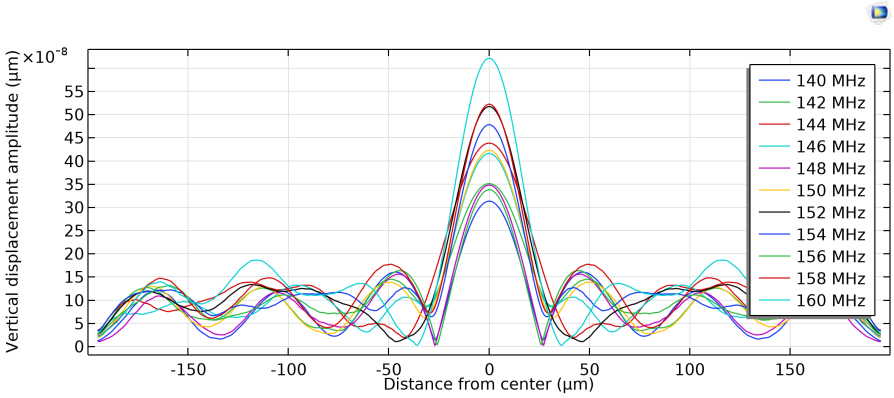


Figure 3.13: Spatial distribution of vertical displacements of a FIDT

The same finger spacings as the straight IDT designs were adopted for FIDT designs. To achieve similar transmissions as straight IDTs, the geometric focal lengths of FIDTs were chosen so that the distance from the middle finger to the focus point was 1 mm. With $60°$ degree of arc, this gave similar overlapping finger lengths as the straight IDT design.
For the SAW delay line device based on FIDTs, different from those with straight IDTs, four FIDTs were placed with $90°$ between adjacent FIDTs in each device. This layout can collect the SAW signals passing through the nanopillars and the SAW signals scattered by the pillars.

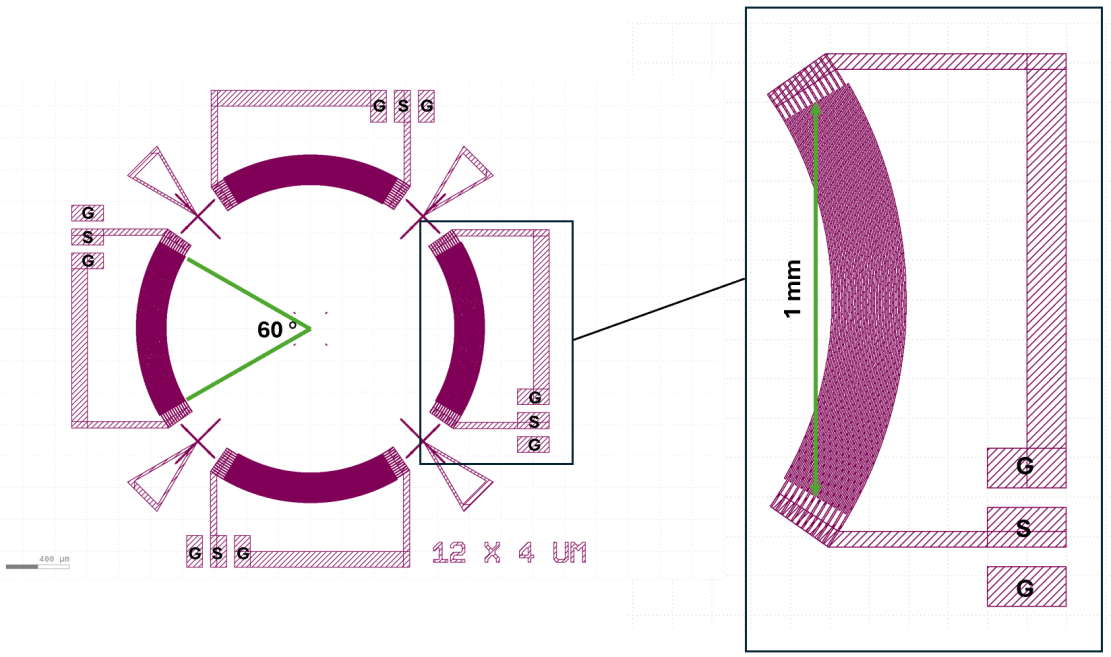


Figure 3.14: Detailed FIDT delay line design

One example of the SAW delay line based on FIDT is shown in Figure.3.14. GSG pads are connected to FIDTs, and external and internal alignment marks are added to the design for locating in the later pillars' printing. Other FIDT designs in this project are shown in the Figure.3.15 below.

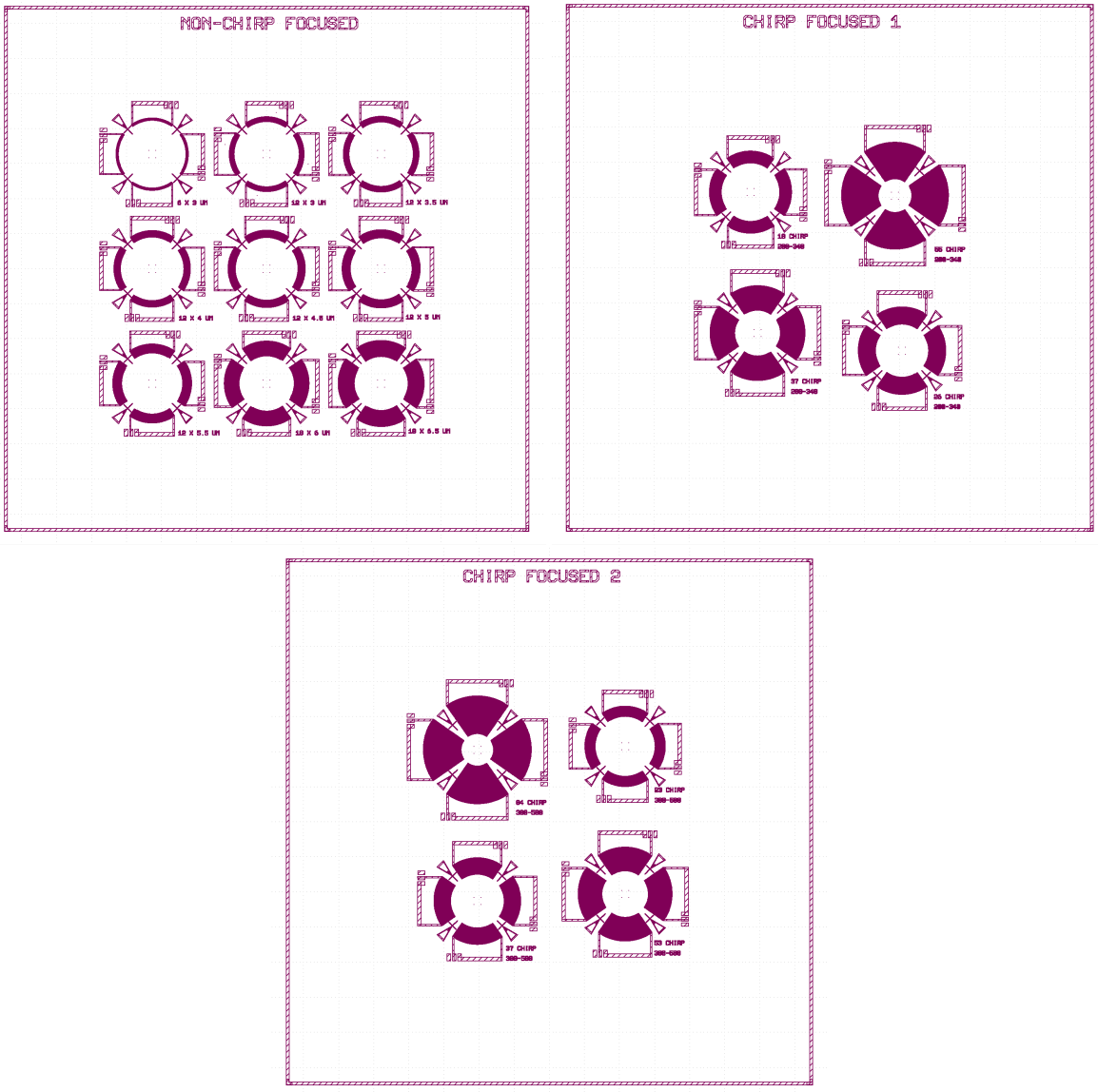


Figure 3.15: Focused IDT designs

Improvement of design

After the S-parameter measurements of the first design wafer, a new pattern was designed to improve the SAW device performance. The delay line distance between two IDTs was increased for straight SAW devices, as shown in Figure.3.16.

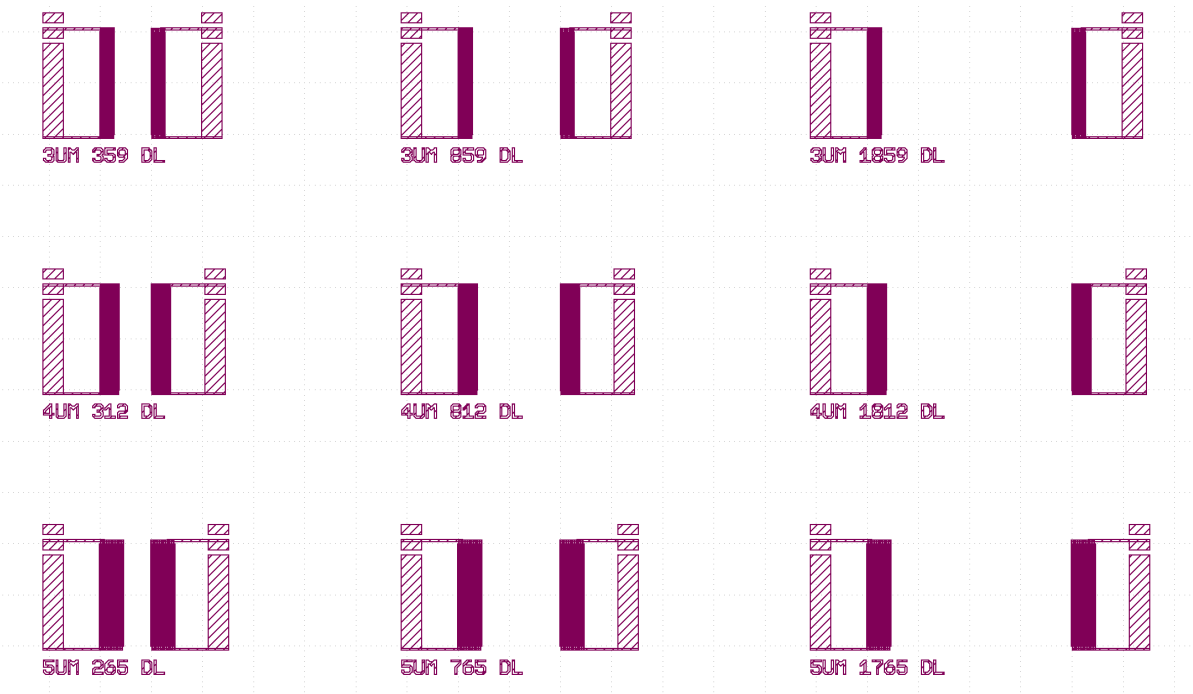


Figure 3.16: Sraight devices in design 2

The number of fingers of the Focused designs was increased from 12 pairs to 18 and 24 pairs, Figure.3.17 shows the design of 3um, 3.5um, and 4um devices as an example.

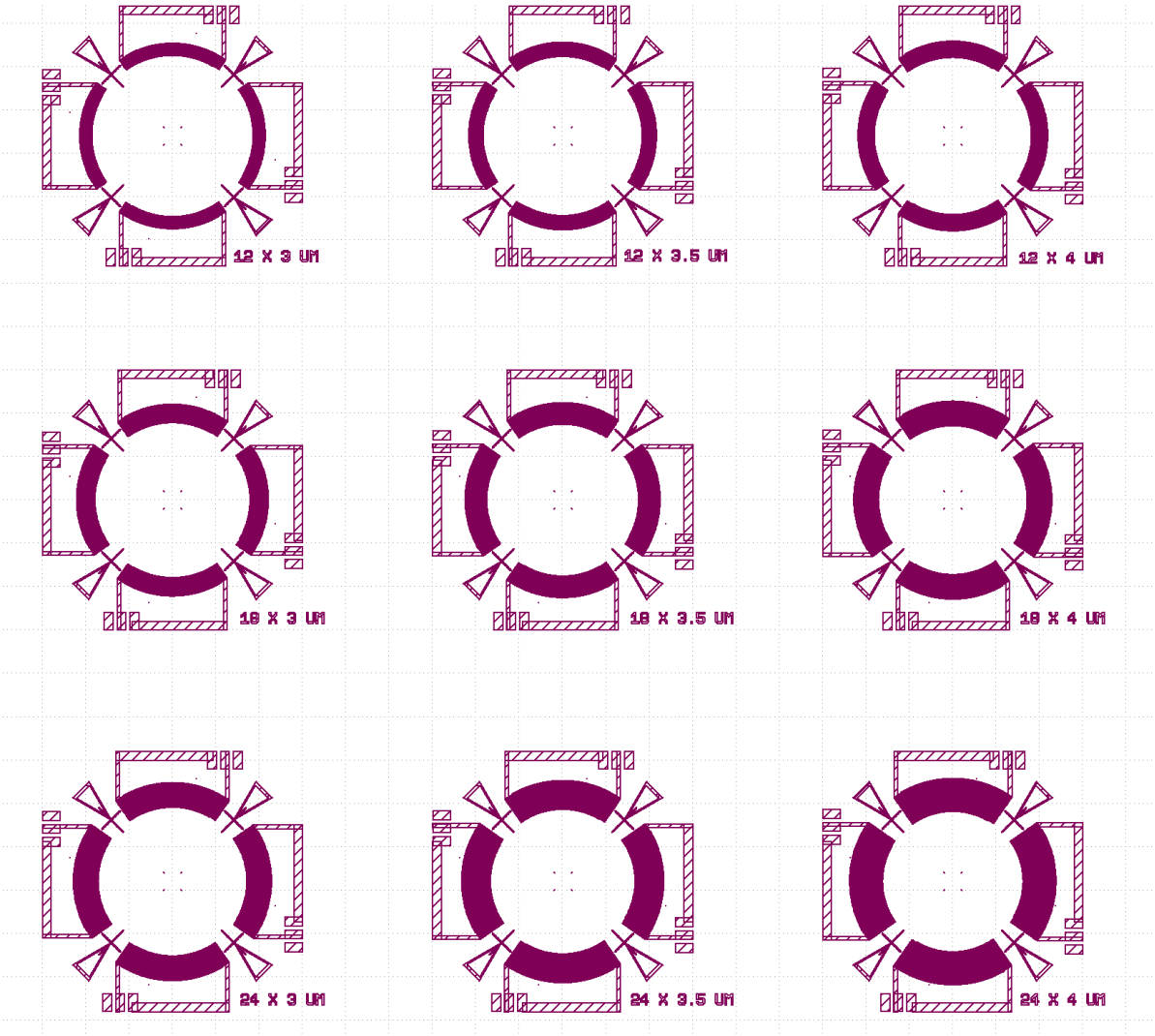


Figure 3.17: Focused devices in design 2

Based on design 2, the delay line length of the straight devices was chosen to be around 1800 um, which is consistent with the 1 mm aperture focused devices. The number of finger pairs for focused designs was chosen as 24 pairs for the final devices.

In design 3, focused devices with aperture (geometrical focal length) increased to 1.5 mm and 2 mm were added. The inner alignment markers on the delay lines were all removed in the final designs to reduce the factor that would lead to reflections as much as possible. Only outer markers were left for pillar locating in the final devices.

The results of these changes and improvements are discussed in the measurement section.

3.2. SAW Device Fabrication

The SAW device comprises a $1\ \mu m$-thick AlN thin film deposited on high-resistivity silicon, with $200\ nm$-thick Al electrodes on top. In order to protect the AlN surface and to get precise patterns, a lift-off process was chosen instead of wet etching to pattern the electrodes. Figure.3.18 demonstrates the overall fabrication idea of the AlN SAW devices. The complete processing flow chart is attached to the end.

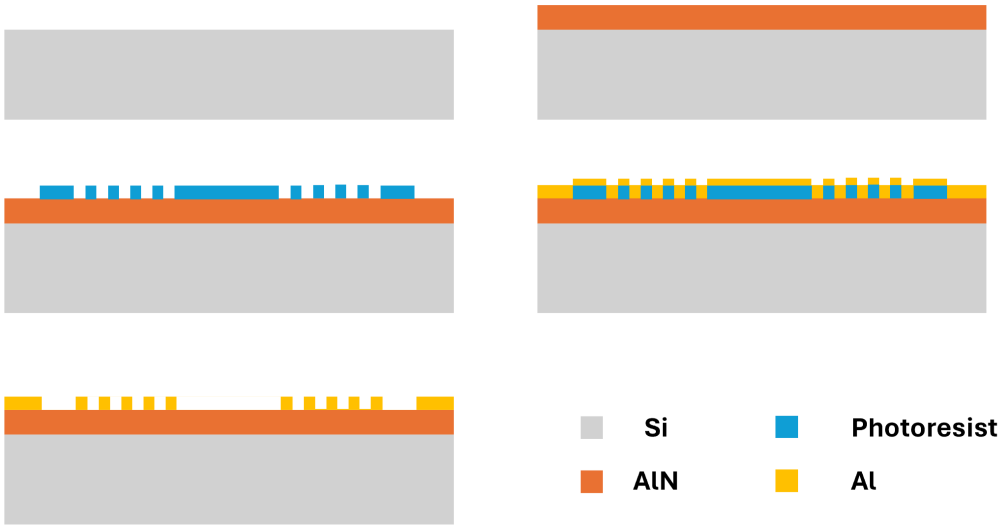


Figure 3.18: Fabrication flow chart

3.2.1. AlN thin film

AlN films with polycrystals lying in the c-axis direction are desired for the SAW devices. The surface acoustic waves usually penetrate into the substrate for a certain depth. Thus, thicker AlN film theoretically provides better transmission. However, the quality of the AlN film declines with deposition over $1\mu m$. $1\mu m$ was set as the target thickness of the AlN thin film deposited for the devices in this project.

Reactive sputtering is commonly used for AlN deposition. Since dielectric, AlN, will be formed during the sputtering, a pulsed DC magnetron sputtering technique was used in the EKL cleanroom. The deposition was conducted with the existing recipe in EKL using the Trikon Sigma 204. The pulsed DC power was set as 3 kW with a frequency of 250 kHz and a duration of 1616 ns. The substrate temperature was set as $400\ ^{\circ}C$ and the gas flow rates were set as Ar^{+}: 20 sccm; N_2 80 sccm.

Woollam Ellipsometer was used to measure the thickness of the deposited AlN thin films. 13 points were chosen over the wafer to give the result of average thickness and standard deviation. Wafers from different batches were measured and the result is shown in Figure.3.19, the average thickness of the deposited AlN films was around 850 nm.

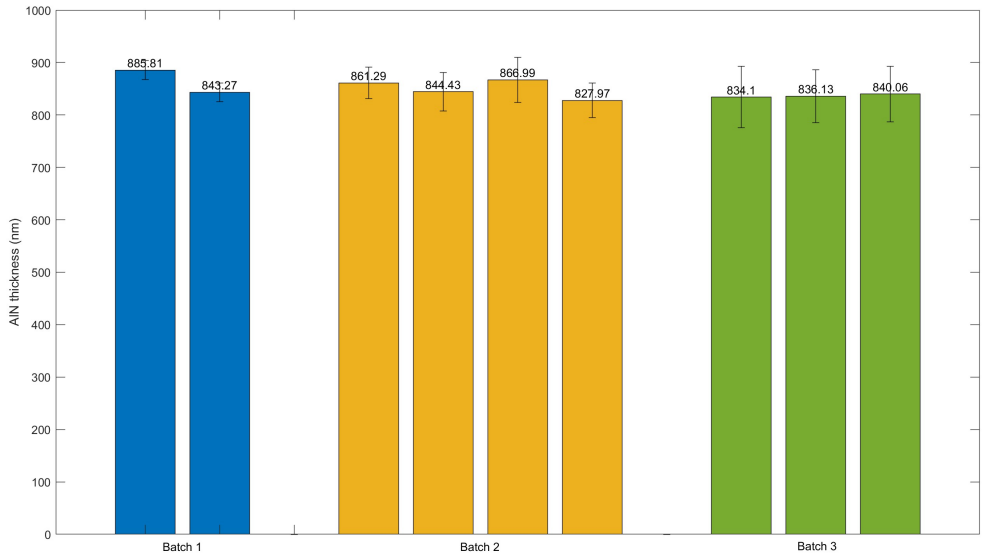


Figure 3.19: AlN film thickness

X-ray diffraction (XRD) was taken for one wafer with properly sputtered AlN thin film at the X-ray Facilities Group of TUDelft with the help of Drs. R.M. Huizenga. The result is shown in Figure.3.20, which indicates a strong preferred (002) AlN orientation. The highest peak at around $69.15°$ comes from the (100) Si wafer. Other than the peak of AlN (002) at $36°$, much less obvious peaks at $37.9°$, $49.8°$, and $66°$ can nearly be captured representing the (101), (102), and (103) orientation of AlN respectively.

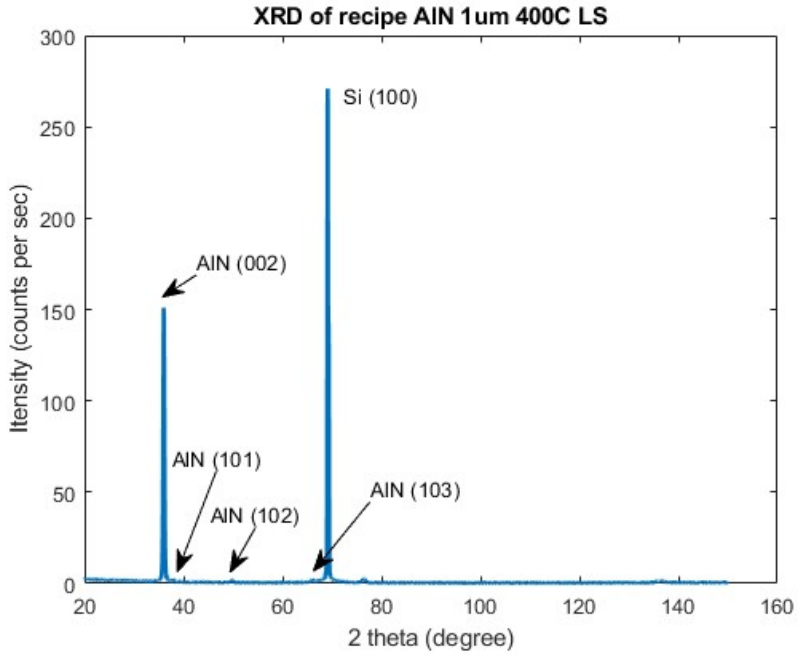


Figure 3.20: AlN XRD 2 theta plot

A Gaussian fit of the AlN peak (002) was conducted to estimate the full width at half maximum (FWHM), Figure.3.21, giving a width of around $0.29°$. From the Scherrer Equation

$$B(2\theta) = \frac{K\lambda}{Lcos\theta} \tag{3.1}$$

K is the shape factor, typically chosen as 0.9; λ is the X-ray wavelength, which equals to 1.54056 Å since Cu Kα radiation is used; $B(2\theta)$ is the FWHM in radius. Thus, the crystallite size L of the AlN can be roughly estimated as 29 nm.

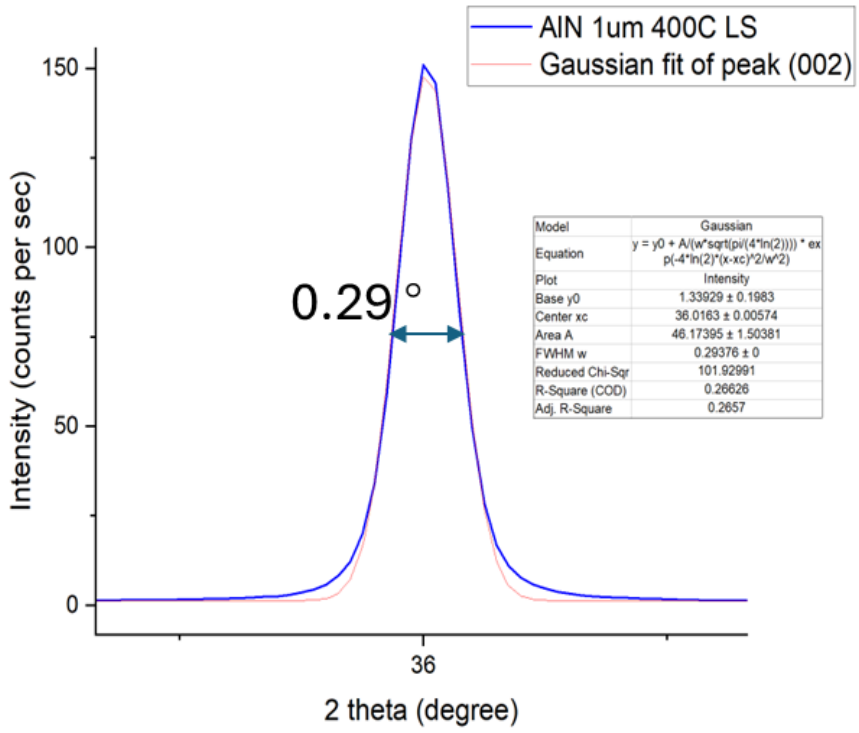


Figure 3.21: Gaussian fit of AlN (002) peak

The attempt resistivity measuring of the AlN thin film was done with the CDE ResMap 4 point probe. The measurement was outside of the sheet resistance measurement range: $2m\Omega/\square - 5M\Omega/\square$, which means the resistivity of the AlN film was much larger than $5M\Omega$ indicating the good dielectric property of AlN.

3.2.2. Lithography

At first, the ASML PAS 5500/80 wafer stepper in the EKL cleanroom was considered to pattern the negative photoresist nLOF 2020 for the lift-off process. A brightfield mask was designed as Figure.3.22. The four images will be selected separately and exposed to different dies over the whole wafer.

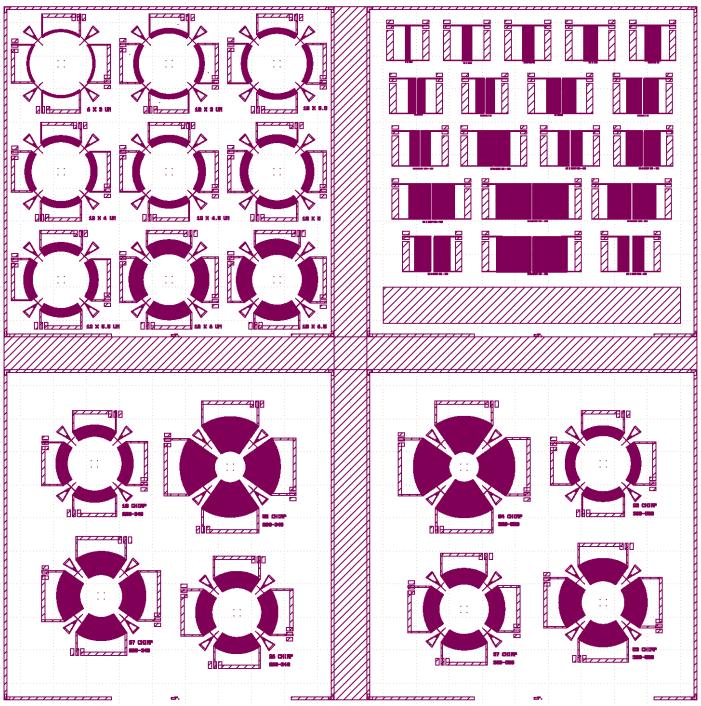


Figure 3.22: First mask design

For time and cost efficiency, a laser writer in Kavli Nanolab was used for maskless photolithography instead of a traditional mask. Positive photoresist AR-P 5350 was used and the write pattern is shown as Figure.3.23, which was designed on the wafer scale.

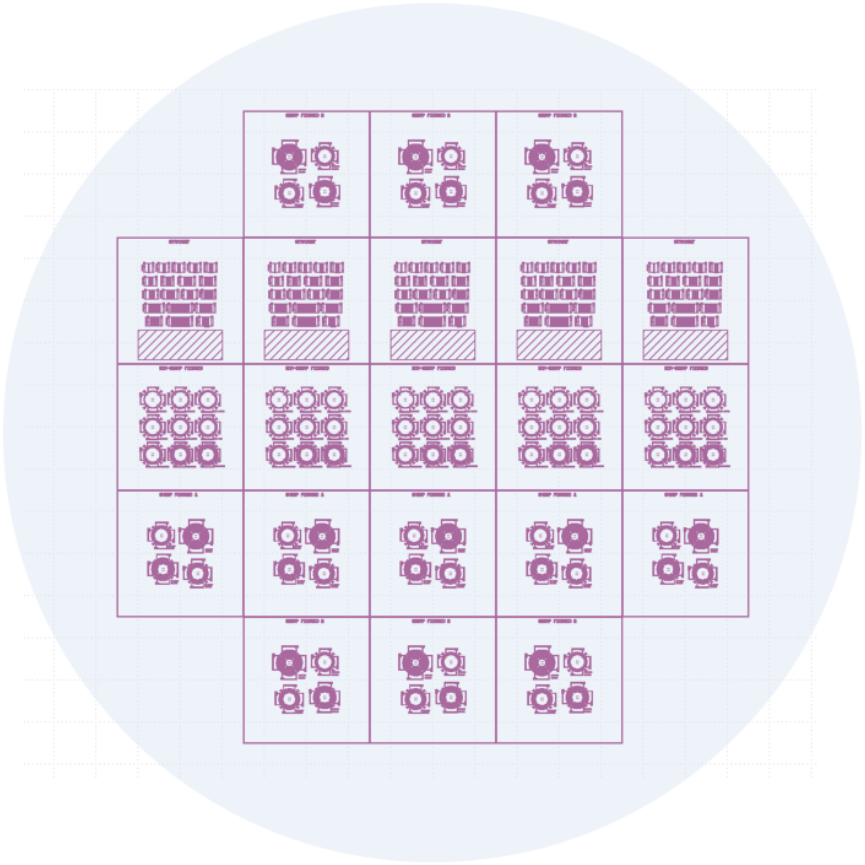


Figure 3.23: First wafer pattern design

In the first few times, the lithography part at Kavli Nanolab was done with the help of the PhD student Xiaoxi Zhao. The wafers were first cleaned with acetone and then applied with a hexamethyldisilazane (HMDS) treatment to increase the adhesion of photoresist. After that, the AR-P 5350 resist was spin-coated on the wafer at 4000 rpm for 60 s to have a thickness of about 1.0 um. 105 °C, 4 min hot plate was used for tempering. Then, the laser writer was used for the exposure at the suitable energy dose and defocus. Subsequently, AR 300-35, 1:2 was used for development for 60 s.

Etching of AlN by TMAH:
At first, the negative photoresist nLOF 2020 was chosen. Problems occurred using this photoresist. The developer used for the resist in Kavli Lab was MF 322, which is a tetramethylammonium hydroxide (TMAH) based developer. TMAH can be used as an option for AlN etching and provides a very high etch rate with 25 wt% at 82 $^{\circ}C$([2]). During the first fabrication, the AlN layer was damaged in the development step with MF 322. SEM pictures have been taken with the damaged device, Figure.3.24. Around the electrode area (where the resist was dissolved by the developer), wide borders can be observed. The borders have similar grain patterns to the Al electrode from the top view and they resemble trenches when viewed from a tilted angle. From the SEM pictures, it can be inferred that the edge is a result of the etching of AlN beneath the undercut of the resist, which is later deposited with a slight amount of Al during electrode evaporation.

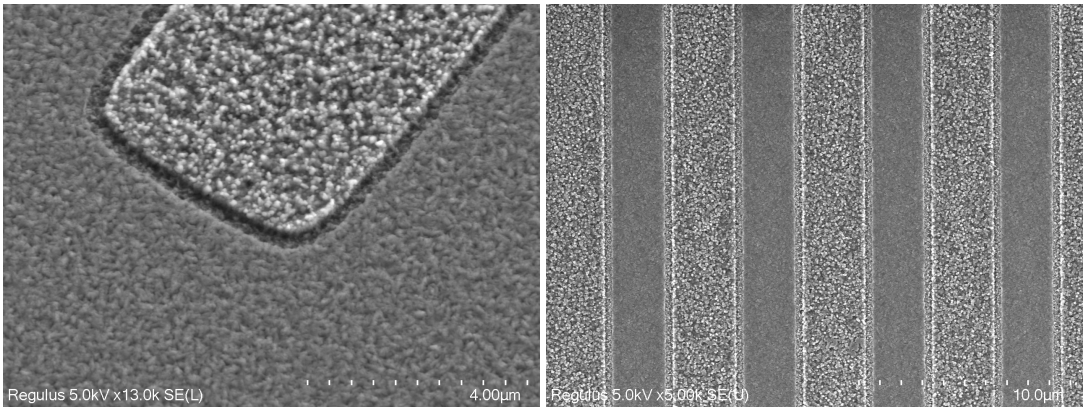
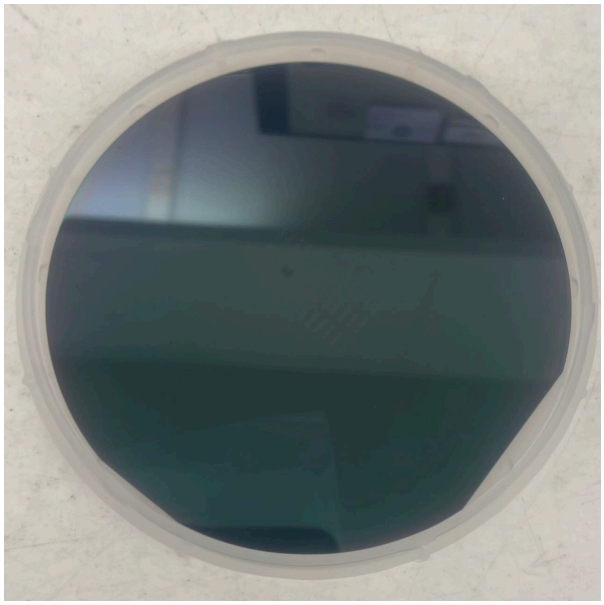
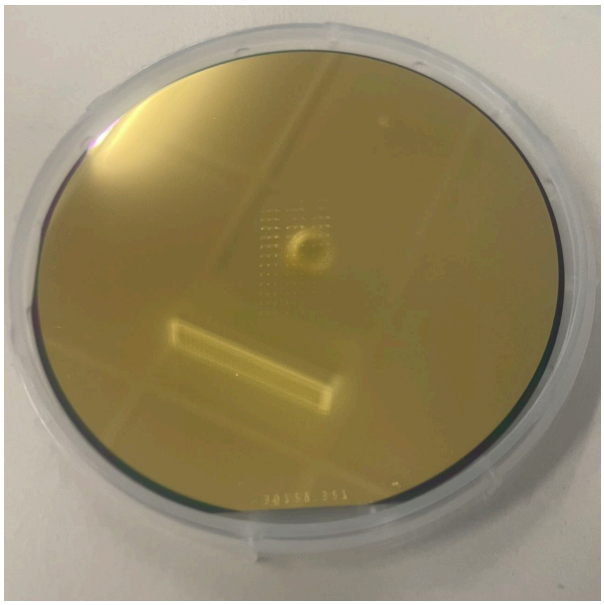


Figure 3.24: SEM image of electrodes on AlN with TMAH etched

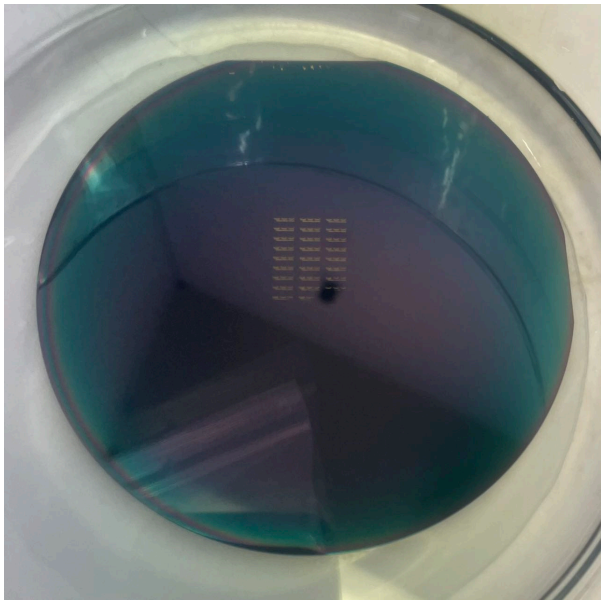
Dose test for laser writer:
The exposure of the photoresist was on the AlN surface. A dose test was conducted with dose energy varying from 35 - 100 mJ/cm^2 (step 5 mJ/cm^2) and defocus choosing as 0, 2, or 4 with the laser writer. After finishing the whole process flow with the dose test wafer, Figure.3.25, the litho-test structures were inspected under the microscope.



(a) Dose test wafer after lithography



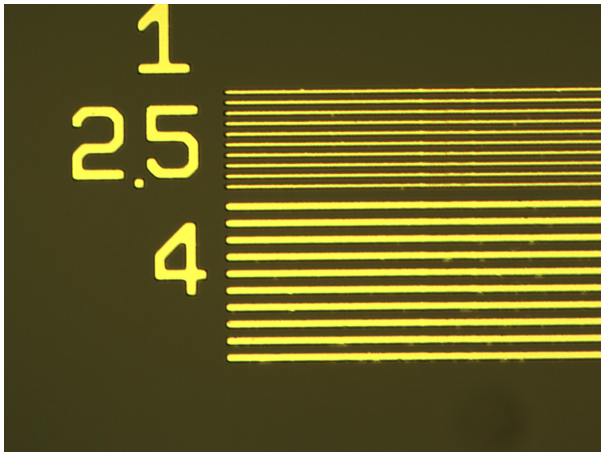
(b) Dose test wafer after electrode evaporation



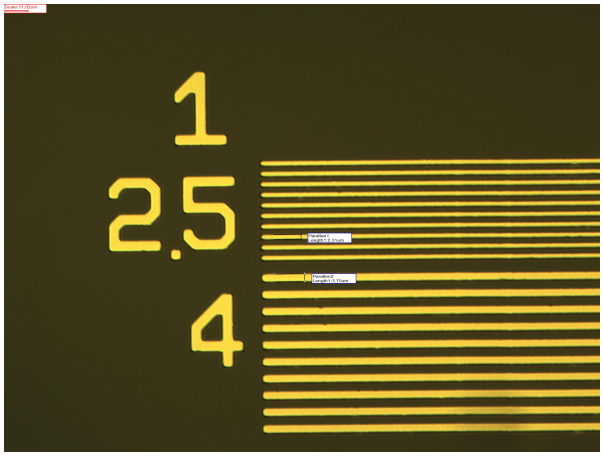
(c) Dose test wafer after lift-off

Figure 3.25: Pictures of the dose test wafer during the process

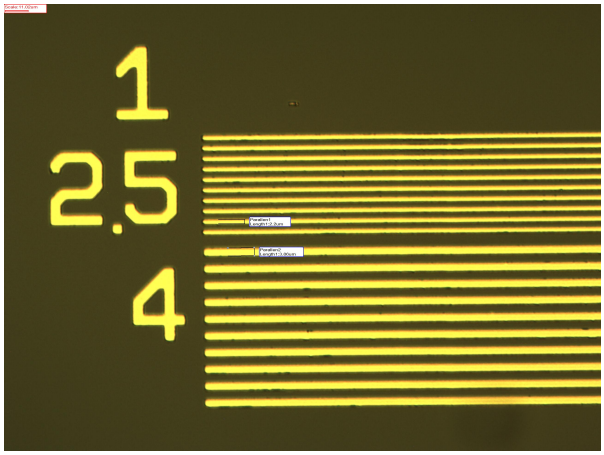
Under the microscope, structures exposed to doses below 85 mJ/cm^2 were clearly observed to be underexposed, while those exposed to doses exceeding 95 mJ/cm^2 were clearly observed to be overexposed. For the dose energy 85, 90, and 95 mJ/cm^2, the results are shown in Figure.3.26. By comparing the strip width, it was observed that dose: 90 defoc: 2 and dose: 95 defoc: 0 gave the best precision. With dose: 90 defoc: 2, the designed 2.5 um fingers were measured around 2.53 um, and the designed 4 um fingers were measured around 4.11 um. With dose: 95 defoc: 0, the designed 2.5 um fingers were measured around 2.54 um, and the designed 4 um fingers were measured around 4.08 um. The energy dose of 90 mJ/cm^2 and 2 defocus was chosen for the fabrication of the final devices.



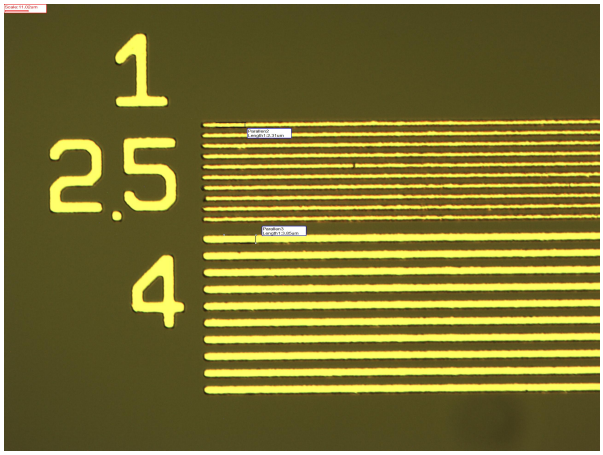
(a) Dose: 85; Defoc: 0



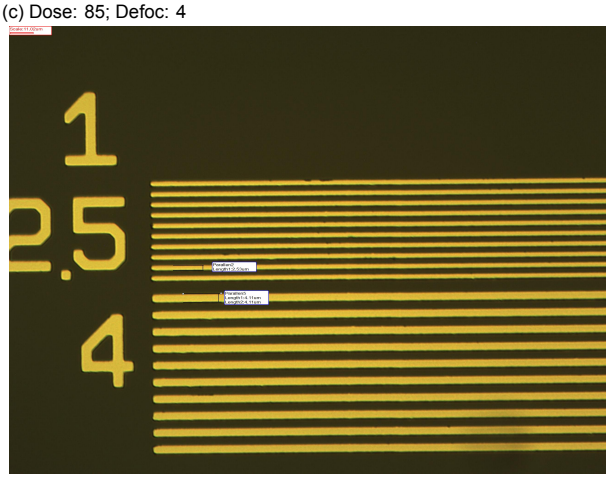
(b) Dose: 85; Defoc: 2



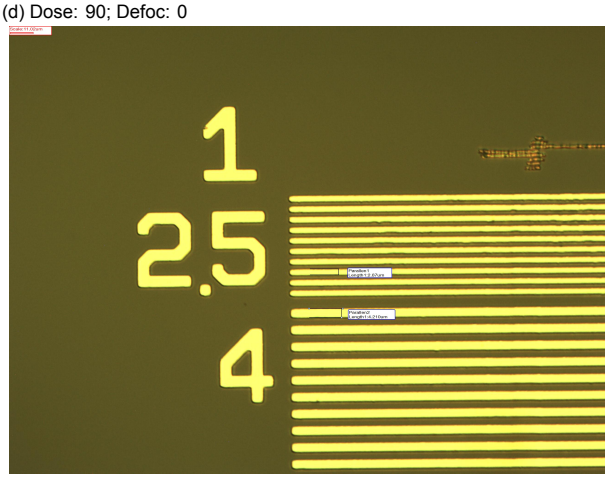
(c) Dose: 85; Defoc: 4



(d) Dose: 90; Defoc: 0

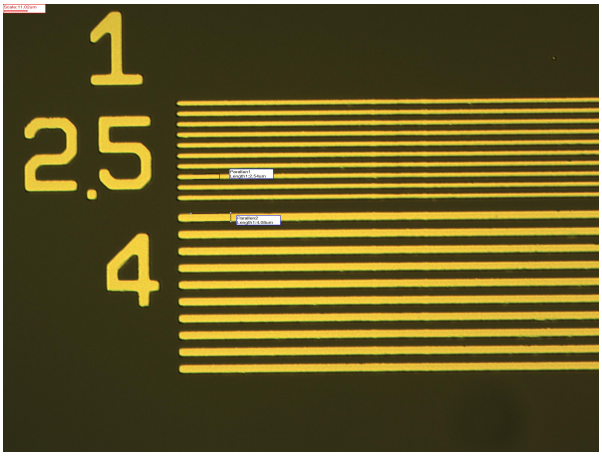


(e) Dose: 90; Defoc: 2

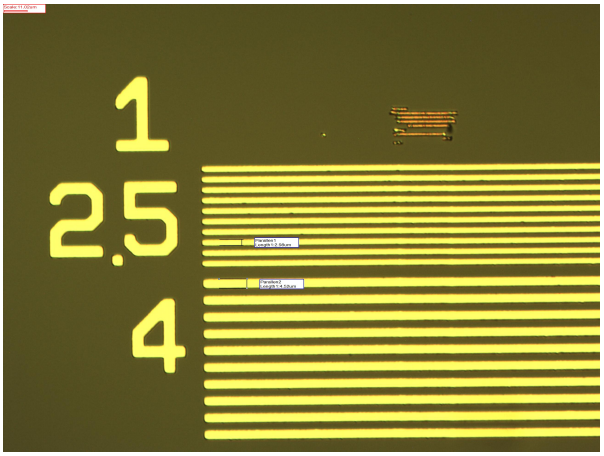


(f) Dose: 90; Defoc: 4

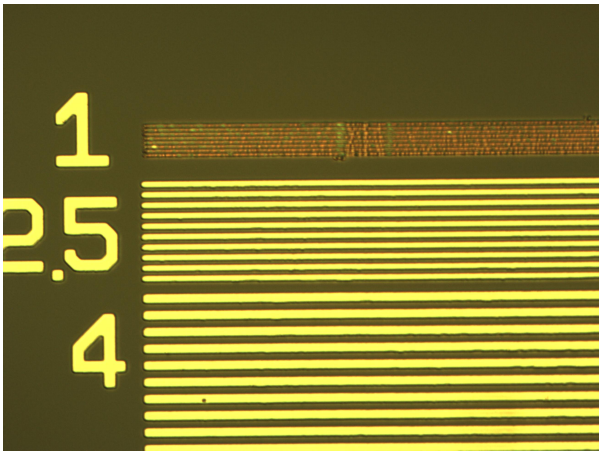
Figure 3.26: Does test results



(g) Dose: 95; Defoc: 0



(h) Dose: 95; Defoc: 2



(i) Dose: 95; Defoc: 4

Figure 3.26: Does test results

3.2.3. Lift-off process of electrodes

After patterning the photoresist, a descum process is necessary to remove the unwanted residues for high precision of the electrode patterning. This was done by giving O_2 plasma flash for 1 min in Tepla Plasma 300. The power was set as 600 watts and the O_2 was set as 250 ml/min.

Electrode material To choose electrode material for acoustic wave devices, low resistivity and high acoustic impedance are the general considerations. Both Au and Al have low resistivity and thus high conductivity and are the most commonly used materials for SAW devices. However, the Au electrode can have considerable mass-loading effects due to its high density (19.32 g/cm^3), which will influence wave propagation and enhance the reflection at the IDTs and is less desired for SAW delay line devices. Al electrode (2.695 g/cm^3) with light weight is used more frequently. In this project, electrode deposition of 100 nm Au on top of 10 nm Cr and 200 nm Al have all been tested. The 10 nm Cr thin layer is used to enhance the adhesion of the Au electrode to the AlN surface.
The simulation results of S-parameters with 100 nm Au and 200 nm Al IDTs are shown in Figure.3.27. The simulation of Al electrode device shows a more ideal transmission curve while Au electrode device has some reductions in the transmission as the rough curve around 250 MHz indicates.

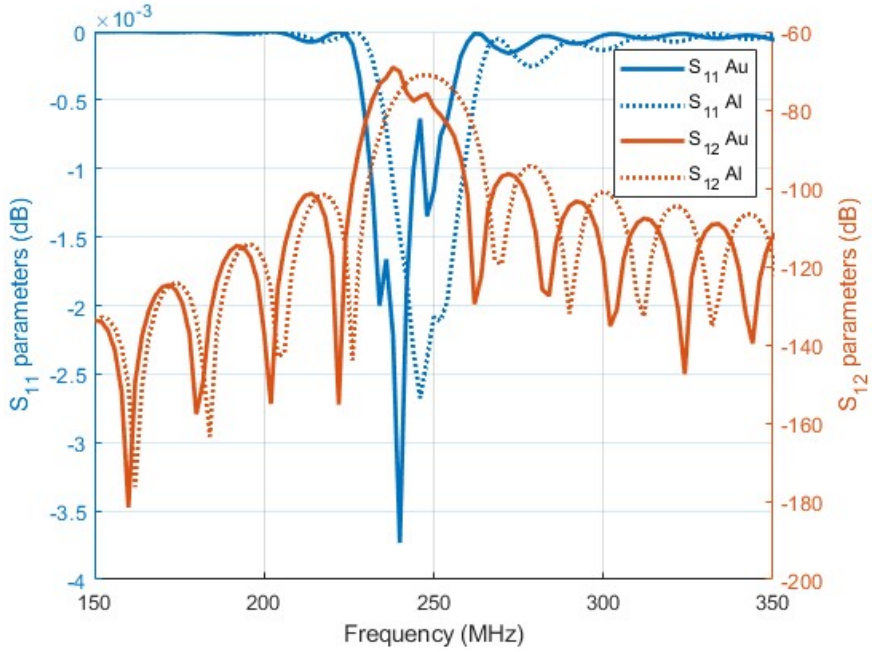


Figure 3.27: Simulated S12 curve of Au and Al electrodes

Lift-off chemicals Lift off with TechniStrip NI555 at 80 degrees Celsius with ultrasonic bath; with acetone at room temperature; with AR 600-71 commercial remover at 50 degrees Celsius were all tested and provided good lift-off results. The wafers were always left in the chemicals overnight to ensure complete and clean lift-off. They were picked up in the next day and cleaned in acetone, isopropanol, and DI water in sequence.

3.2.4. Fabrication results

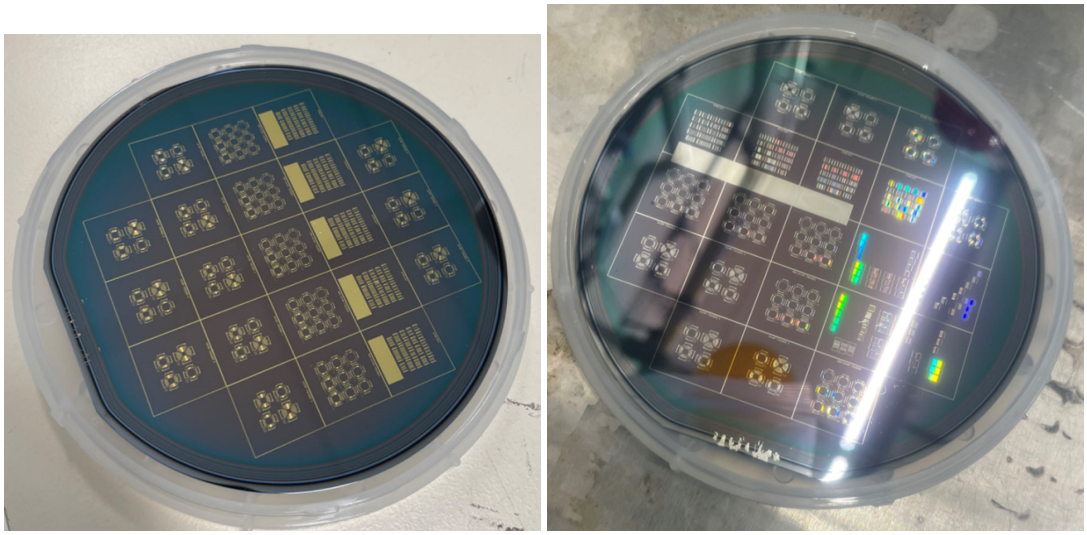


Figure 3.28: Photos of wafer design 1 and 2

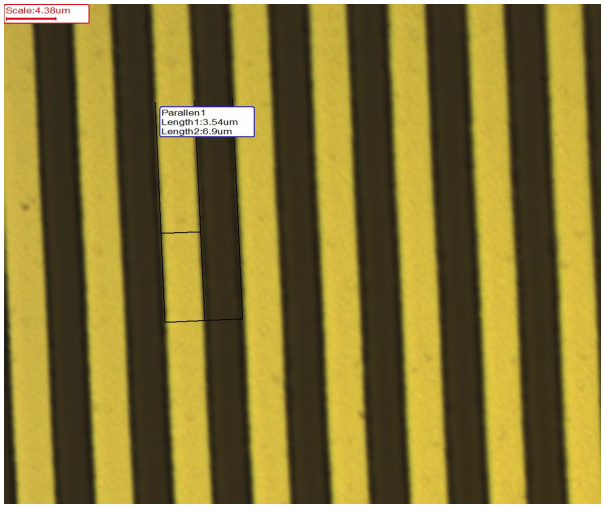


Figure 3.29: Microscope photo of electrodes of wafer design 2

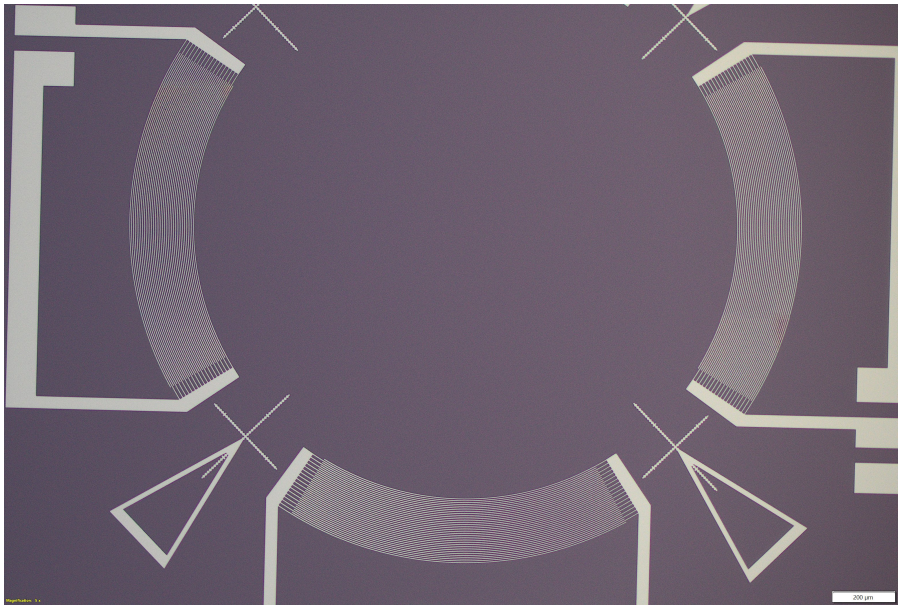


Figure 3.30: Microscope photo of a focused device of wafer design 6

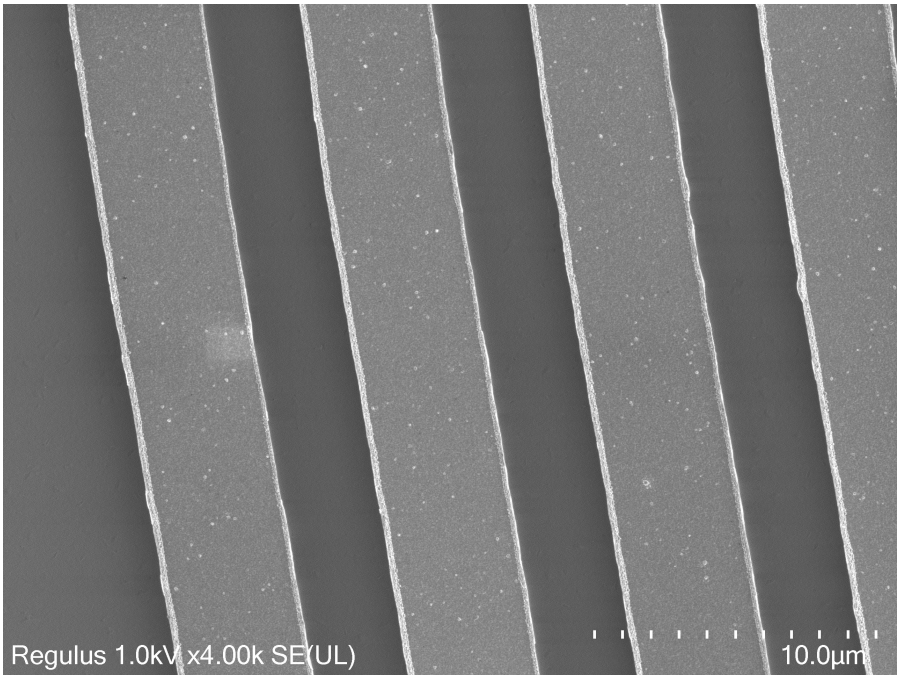


Figure 3.31: SEM photo of electrodes of wafer design 6

3.2.5. Fabrication variance

Even though the fabrication conditions were kept as consistent as possible with the greatest effort for each fabrication, the performance of laser writer and metal evaporation systme varied slightly each time. There was a short time between each manufacturing. So, the output power of laser writer could have drifted, the sensitivity of photoresist could have degraded, the amount of evaporation metals in crucible changed,... All these small factors led to the variance of fabrication results. One of the results was the inconsistence of electrode finger width and gap.

In some fabrications, the precision of electrode width was extremely high giving less than 50 nm difference from the design pattern. However, there were non-negligible differences between finger and gap widths in some cases, as shown in Figure.3.32. Both the finger width and finger spacing were designed as 5 μm, but the finger was measured to be 6.07 μm and the gap was measured to be 4.01 μm. A guess is that some metals were deposited beneath the undercut of photoresist during evaporation, since the electrode edge showed variance in height. Another cause was the instability of the laser writer, as the fingers were observed nonuniform in the resist pattern before evaporation.

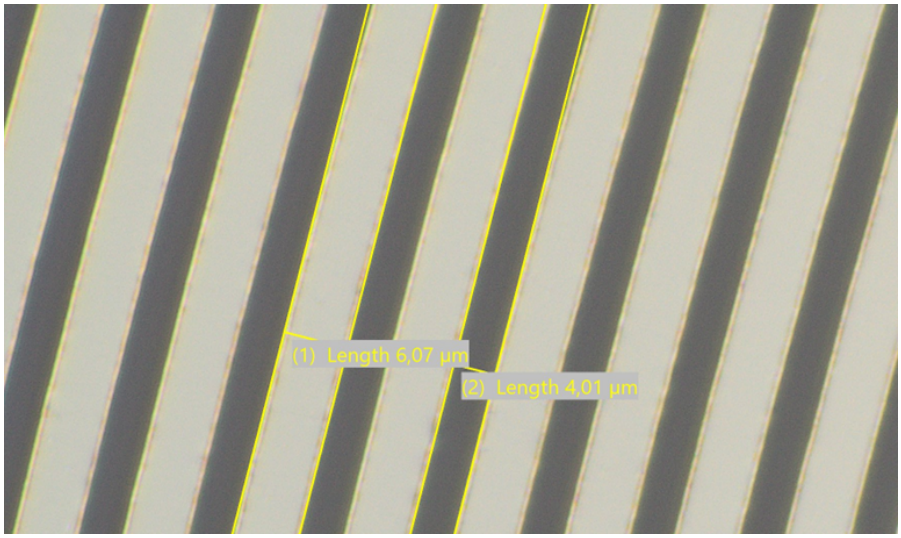


Figure 3.32: IDT finger microscope picture showing variance in width

COMSOL simulations were conducted to see the influence of this nonuniformity in electrode widths. The model was built with 200 nm thick Al electrodes of 6 μm wide spaced in 4 μm, Figure.3.33. The S12 parameter of this model was compared to S12 of a model with 5 μm finger width and 5 μm finger gap. As shown in Figure.3.34, this device variance due to fabrication has almost no influence on the SAW transmission. So the fabricated devices were all good to go for further measurements and deposition of pillars.

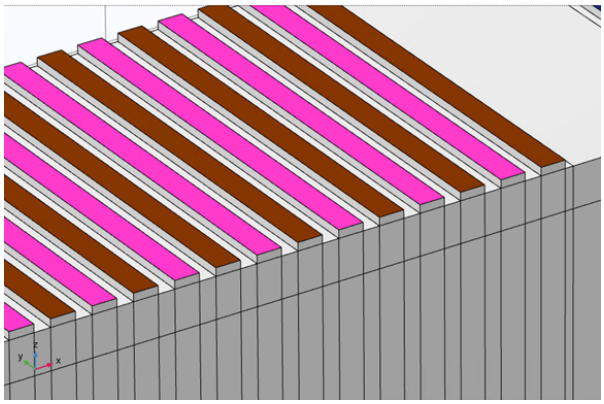


Figure 3.33: COMSOL model with unequal finger and gap widths

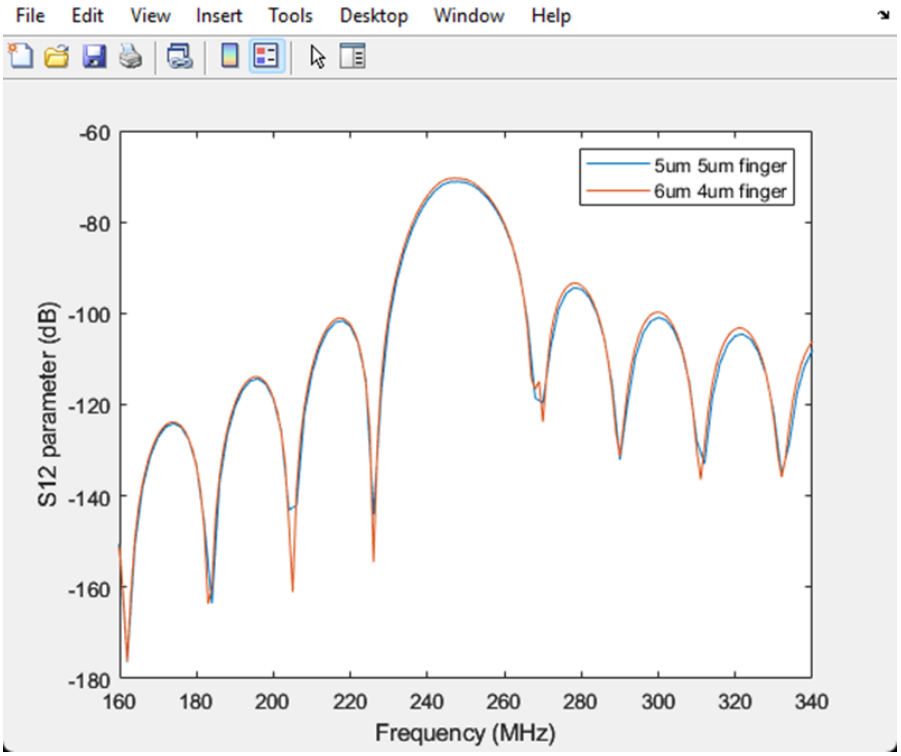


Figure 3.34: Simulated S12 with unequal finger and gap widths

3.3. Two photon polymerization

Nanoscribe Photonic Professional GT+ set up in the Department of Precision and Microsystems Engineering was used to print nanopillars on the SAW delay lines. The printing adopted the Dip-in Laser Lithography (DiLL) mode with a 63x objective and resin IP-Dip2.

To observe the polymer pillars with the scanning electron microscope (SEM), the samples were coated with Au sputter coater with a current of 20 mA for 30 seconds to reduce the charging effect.

Dose test

At first, a dose test with laser power varies from 20% - 56% and laser scan speed varies from 10 mm/s - 50 mm/s was conducted to print pillars with different doses. Pillars were observed under SEM to find the optimal dose. An overall SEM picture of pillar array is shown in Figure.3.35. With underexposure, the pillars were not printed, and with overexposure, the resin tended to bubble during printing. Doses with laser power 25% - 35% and scan speed 20 mm/s - 30 mm/s were chosen from the first dose test and a second dose test was conducted with smaller steps, Figure.3.36. In the end, laser power 34% and scan speed 30 mm/s were chosen for printing nano/micro-pillars with diameters around 0.5 um - 2 um.

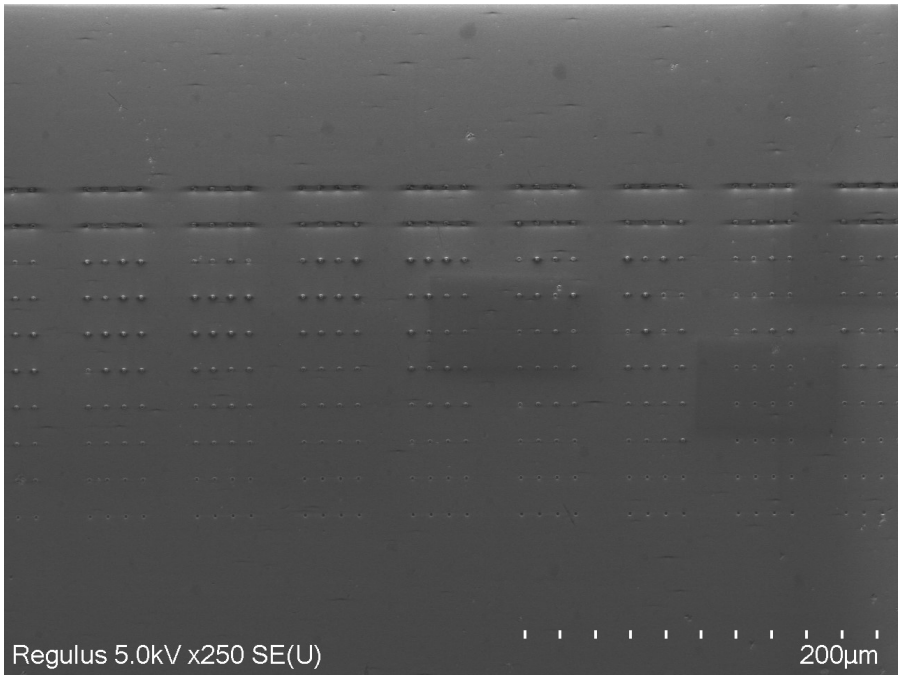


Figure 3.35: First dose test for printing nanopillars

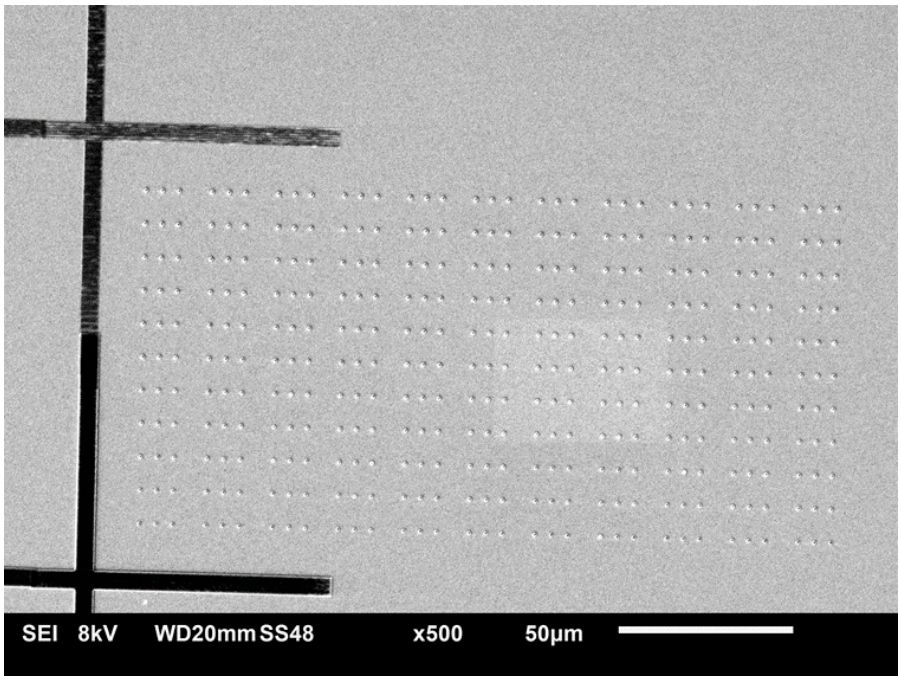


Figure 3.36: Second dose test for printing nanopillars

Printing dimension

The actual dimensions of the printed pillar would deviate from the design dimensions of the printing file. A set of pillars with a fixed design diameter of 1.5 um and varying design height from 2um to 5um and a set of pillars with a fixed design height of 4 um and varying design diameter from 0.5 um to 2 um were printed and measured under SEM.

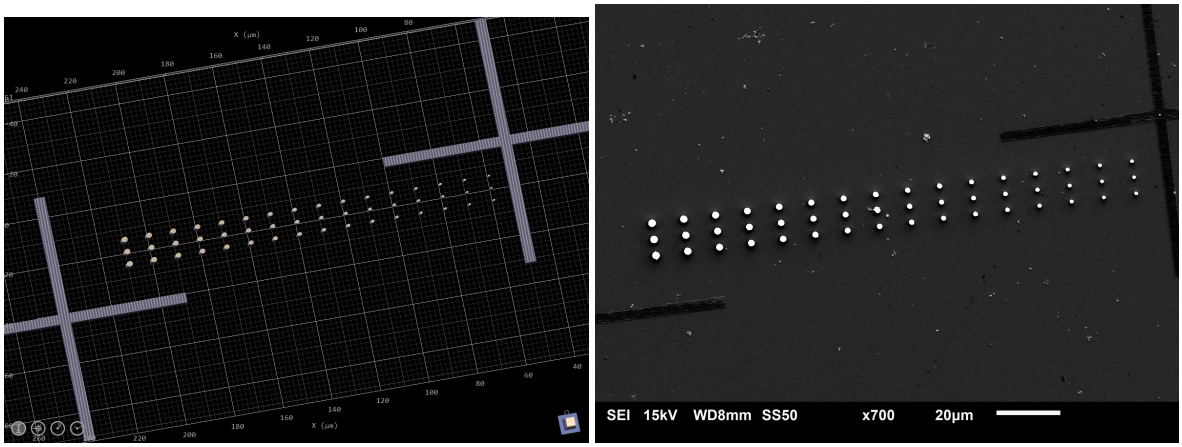


Figure 3.37: Diameter sweep of TPP pillars. Left: design file; right: SEM picture

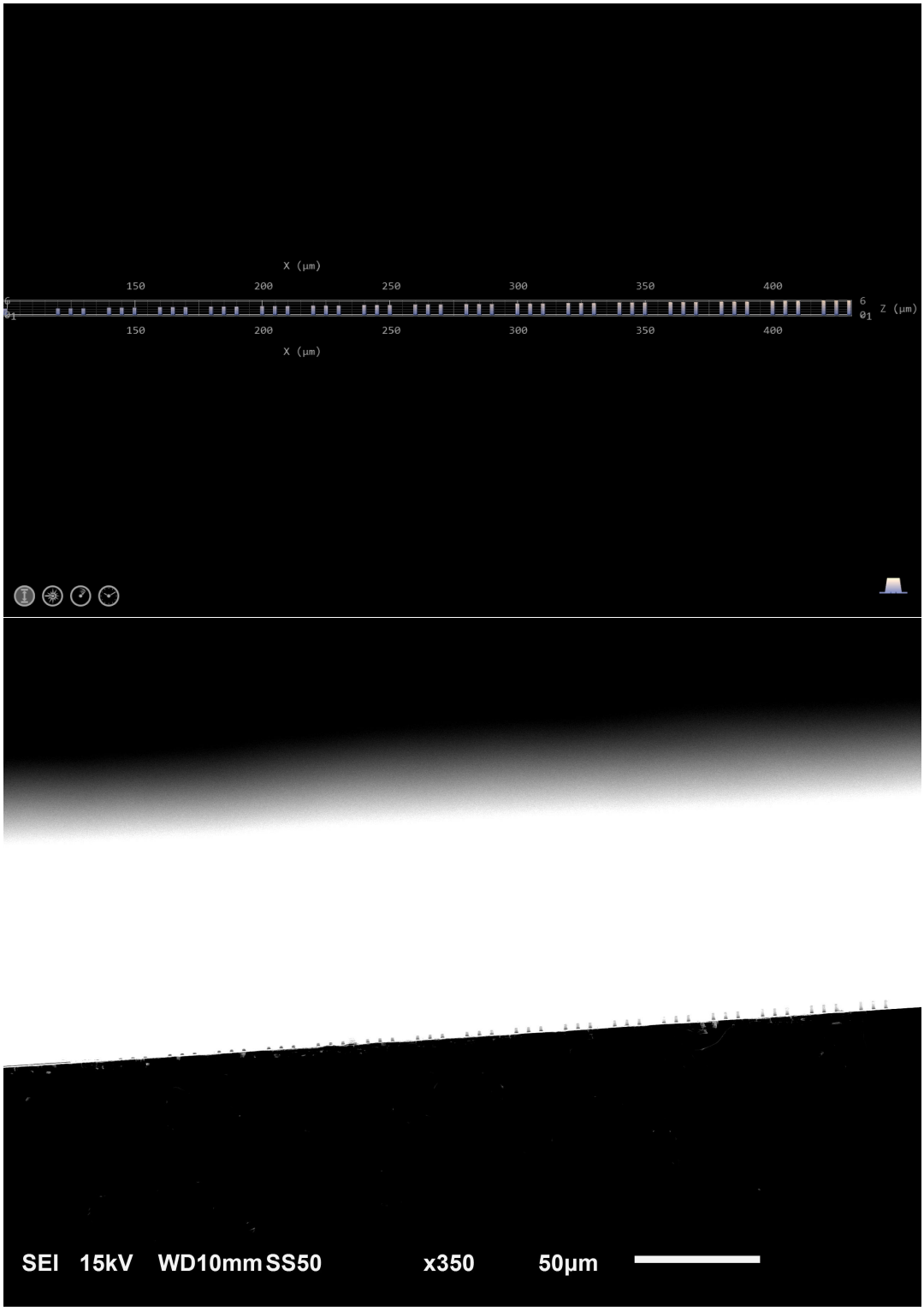


Figure 3.38: Height sweep of TPP pillars. Top: design file; bottom: SEM picture

The diameters of pillars were measured with a top view (Figure.3.37) and the heights were measured in a 90-degree tilted view (Figure.3.38). The relation between designed dimensions and measured dimensions was found, Figure.3.39.

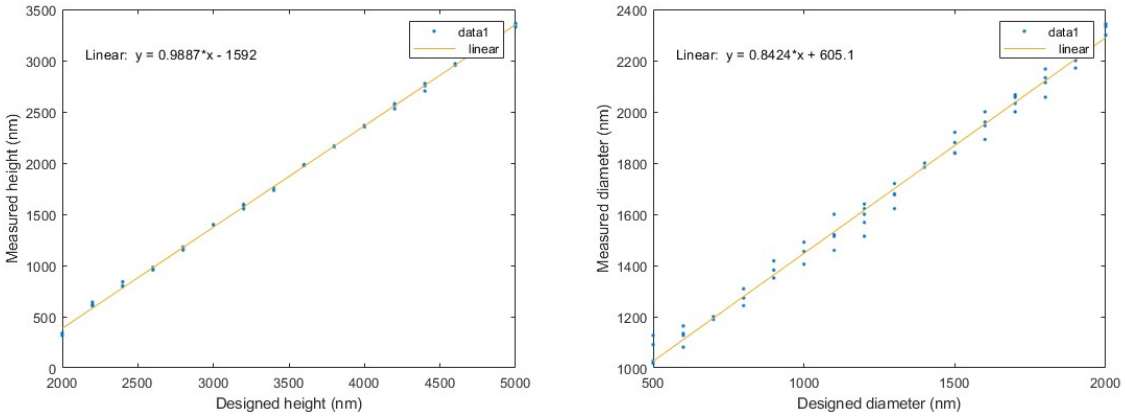


Figure 3.39: Fitting of the relation between designed dimensions and real printed dimensions

Laser Doppler Vibrometer measurements of pillars

In order to have a precise estimation of a pillar's resonance frequency, long pillars were printed and measured with a Laser Doppler Vibrometer (LDV) to calculate the ratio of the pillar's Young's modulus and density.

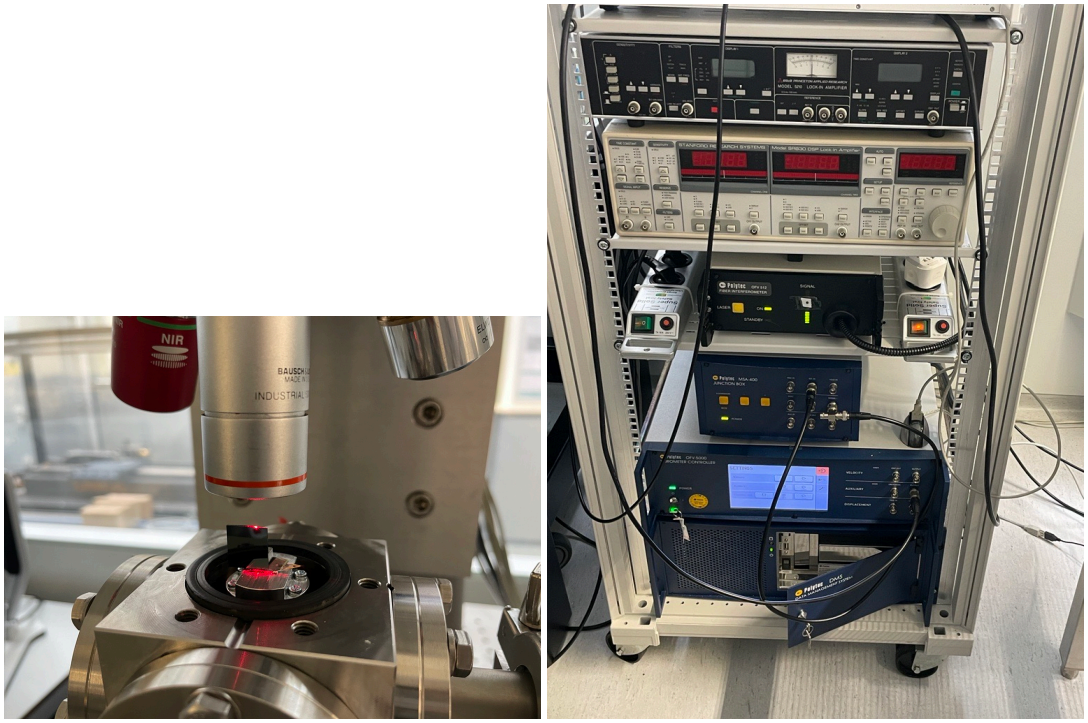


Figure 3.40: Laser Doppler vibrometer setup

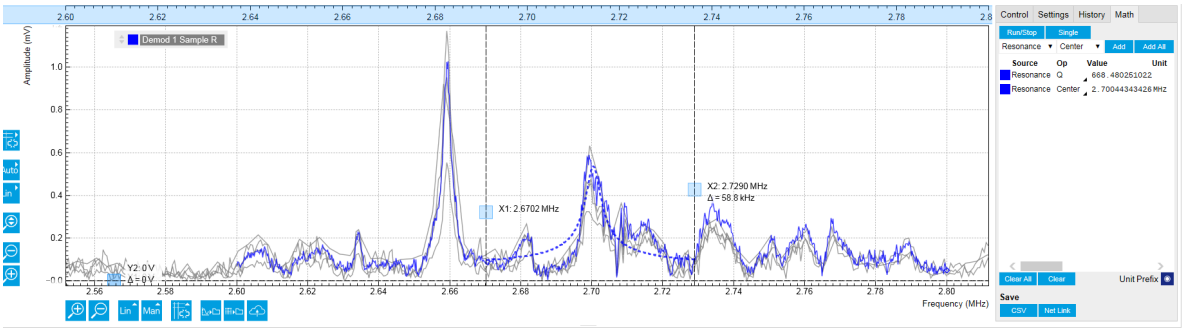


Figure 3.41: LDV results of pillars with heights around 11.3 um

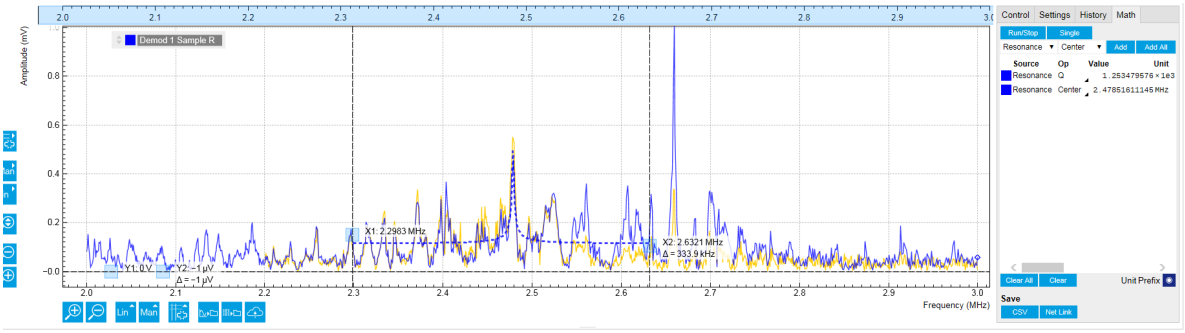


Figure 3.42: LDV results of pillars with heights around 11.6 um

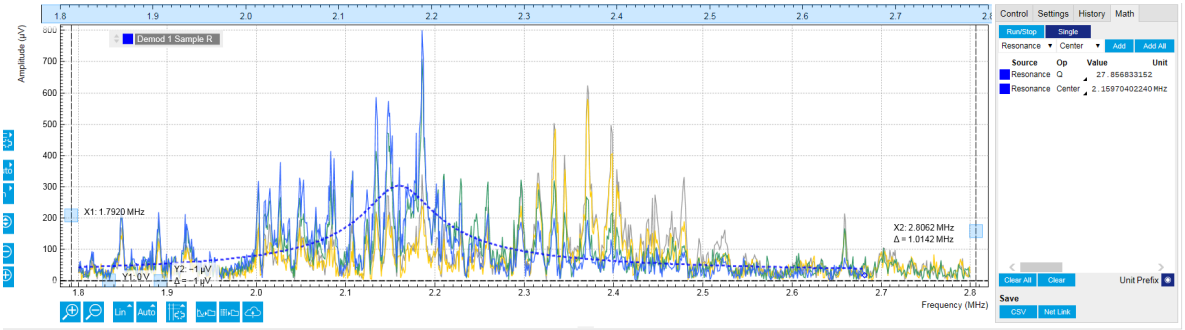


Figure 3.43: LDV results of pillars with heights around 12.4 um

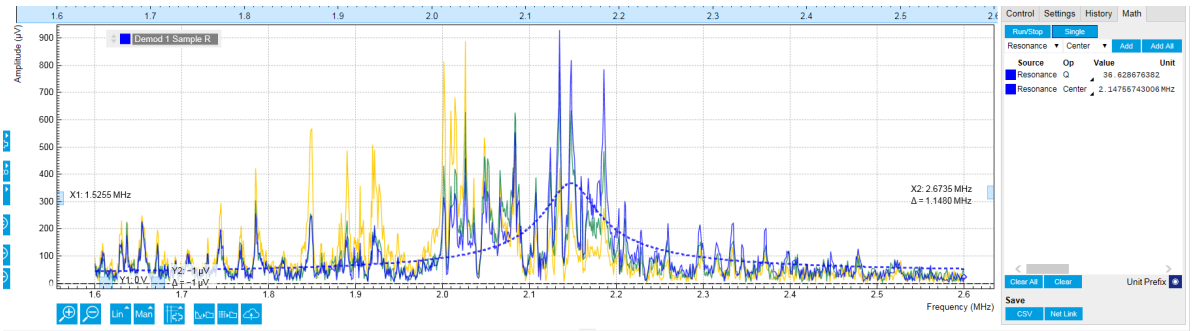


Figure 3.44: LDV results of pillars with heights around 12.8 um

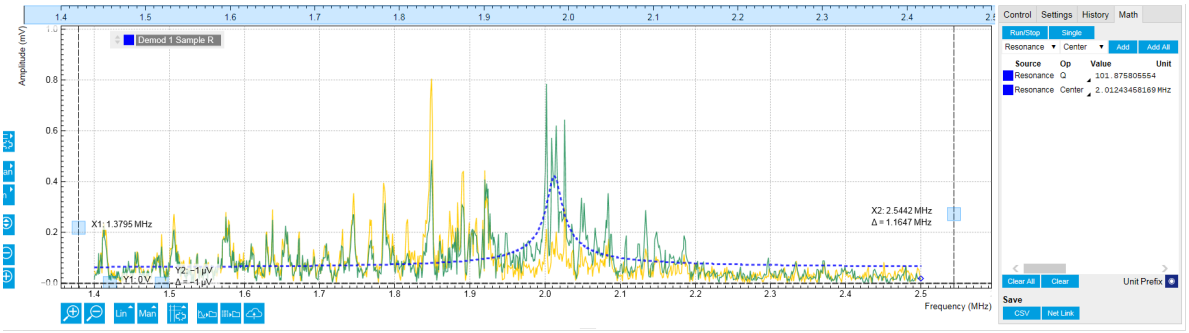


Figure 3.45: LDV results of pillars with heights around 13.3 um

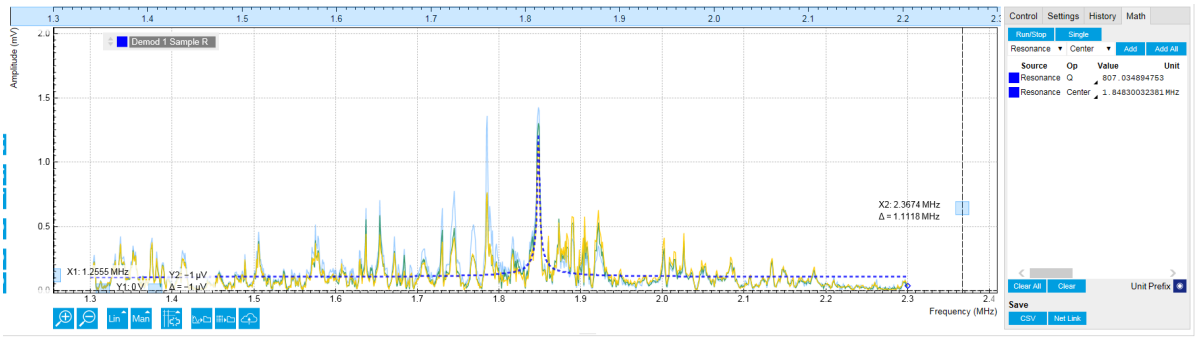


Figure 3.46: LDV results of pillars with heights around 13.7 um

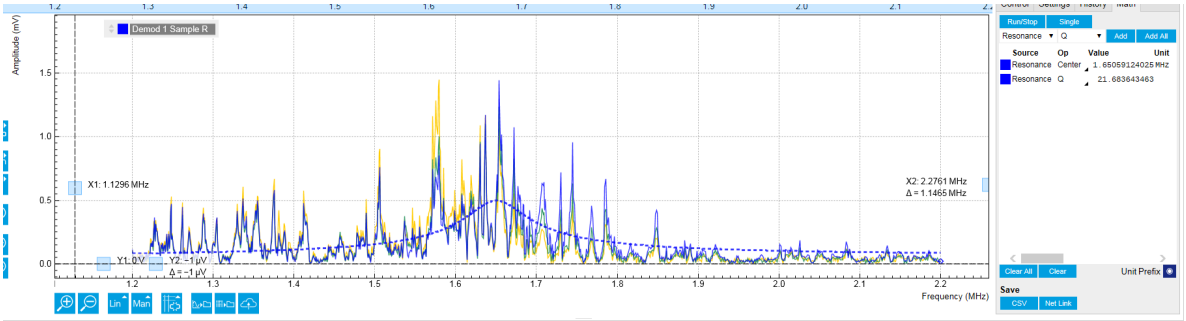


Figure 3.47: LDV results of pillars with heights around 14.3 um

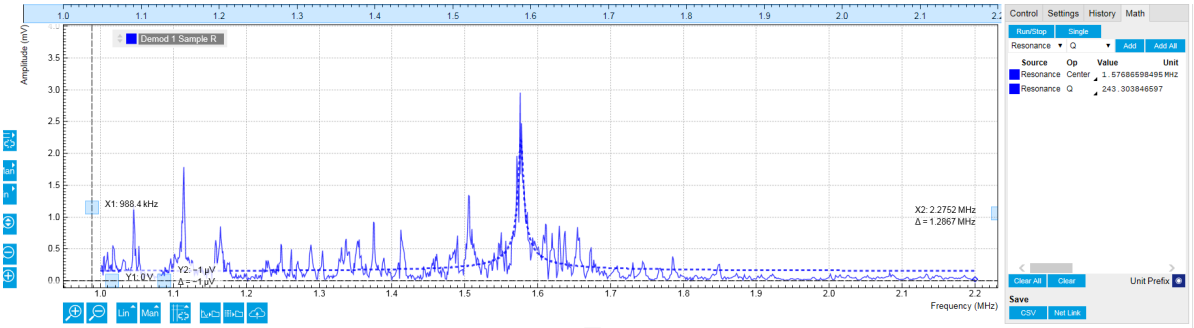


Figure 3.48: LDV results of pillars with heights around 14.8 um

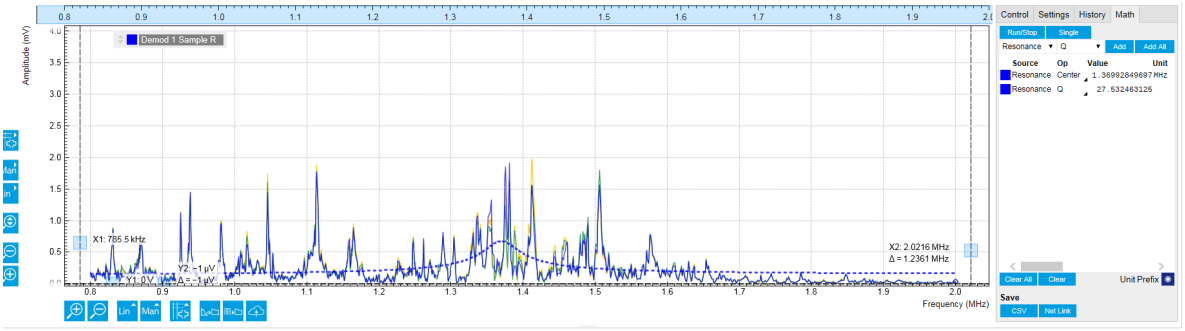


Figure 3.49: LDV results of pillars with heights around 15.3 um

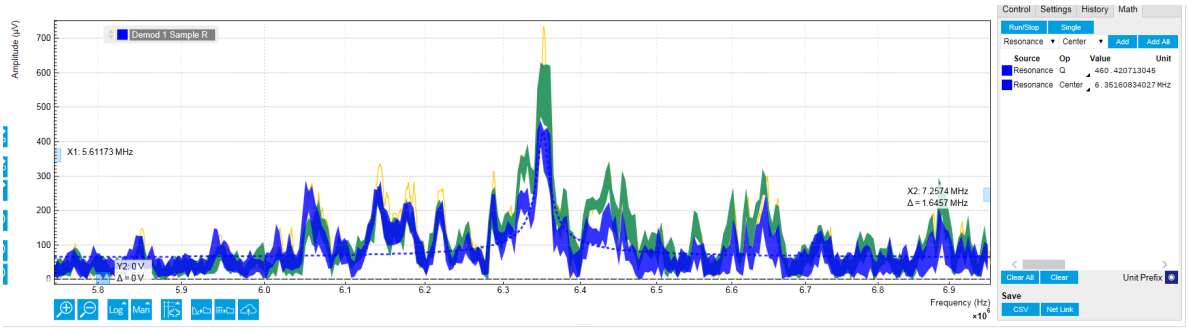


Figure 3.50: LDV results of pillars with heights around 7.4 um

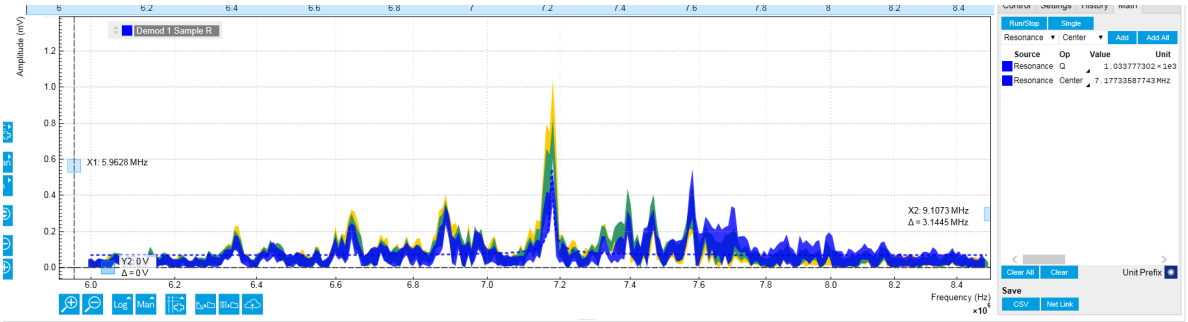


Figure 3.51: LDV results of pillars with heights around 6.9 um

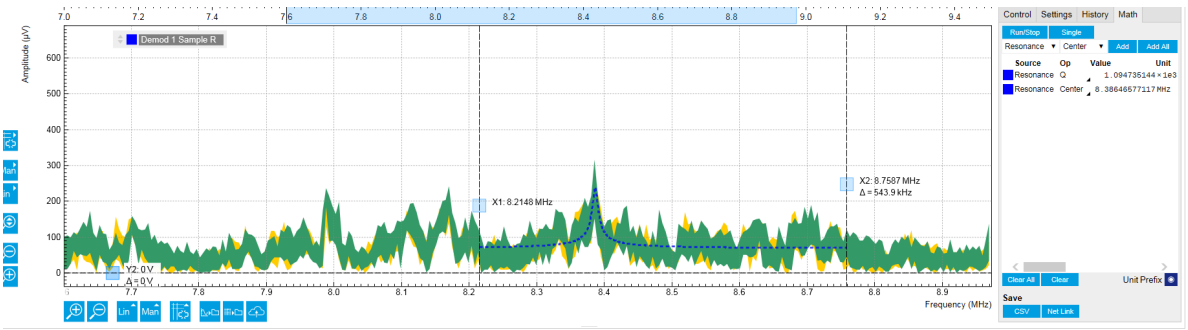


Figure 3.52: LDV results of pillars with heights around 6.4 um

Fitting of the pillars' resonance frequencies as a function of pillars' diameters and heights, the result is shown in Figure.3.53. The slope of the data points from the set of shorter pillars was consistent with

that from the set of longer pillars. This indicated that using this fitted function can predict the pillar's resonance frequency well.

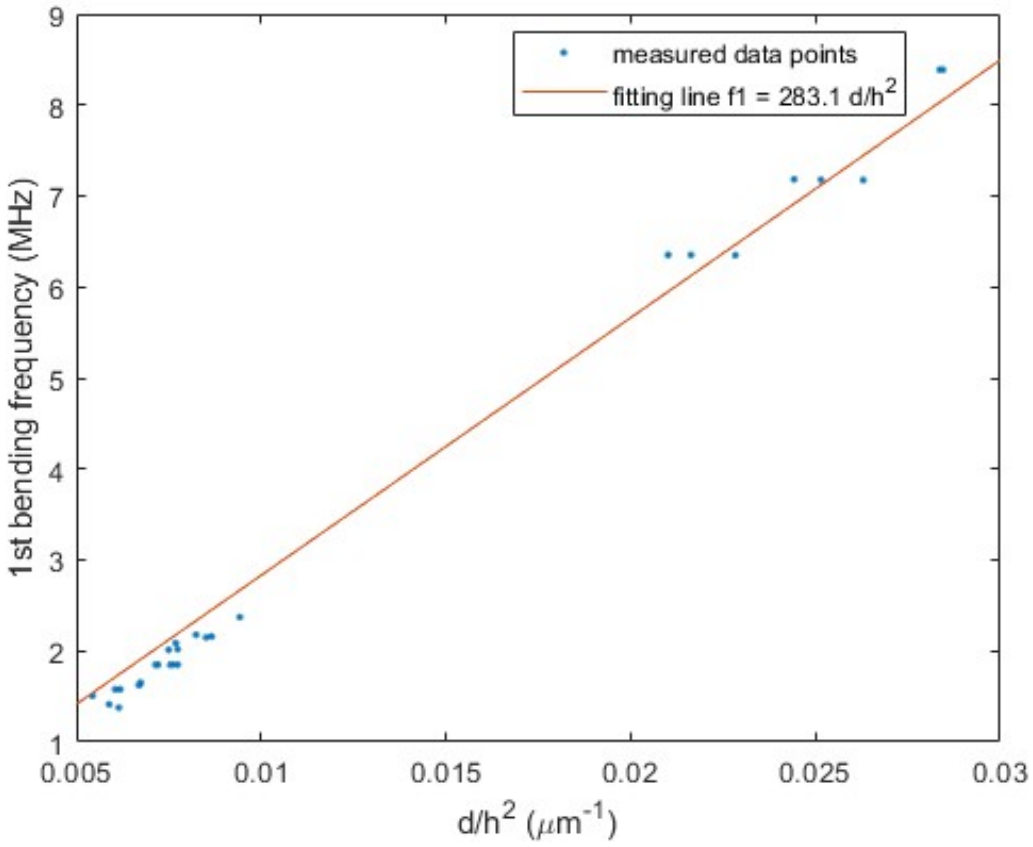


Figure 3.53: Fitting of the pillar resonance frequency as a function of pillar geometry

Pillar design on SAW device

Based on the fitting of resonance frequency done before, the second-order bending frequency of a pillar was estimated as $f_2[MHz] = 1776[MHz \cdot \mu m]\frac{d}{h^2}[\mu m^{-1}]$. So the designs of the pillars are shown in the table below in order to fit into the SAW delay line devices.

Table 3.2: TPP pillar designs

Device	Target diameter	Dia. for TPP file	Target height	Ht. for TPP file	2nd freq.
3 μm	1.195 μm	0.7 μm	2.363 μm	4 μm	380 MHz
3 μm	1.237 μm	0.75 μm	2.363 μm	4 μm	393 MHz
3 μm	1.279 μm	0.8 μm	2.363 μm	4 μm	407 MHz
3 μm	1.195 μm	0.7 μm	2.264 μm	3.9 μm	414 MHz
3 μm	1.111 μm	0.6 μm	2.165 μm	3.8 μm	421 MHz
3 μm	1.153 μm	0.65 μm	2.165 μm	3.8 μm	437 MHz
3 μm	1.195 μm	0.7 μm	2.165 μm	3.8 μm	453 MHz
3.5 μm	1.195 μm	0.7 μm	2.561 μm	4.2 μm	324 MHz
3.5 μm	1.237 μm	0.75 μm	2.561 μm	4.2 μm	335 MHz
3.5 μm	1.279 μm	0.8 μm	2.561 μm	4.2 μm	346 MHz
3.5 μm	1.026 μm	0.5 μm	2.264 μm	3.9 μm	356 MHz
3.5 μm	1.068 μm	0.55 μm	2.264 μm	3.9 μm	370 MHz
3.5 μm	1.111 μm	0.6 μm	2.264 μm	3.9 μm	385 MHz
3.5 μm	1.153 μm	0.65 μm	2.264 μm	3.9 μm	399 MHz
4 μm	0.942 μm	0.4 μm	2.462 μm	4.1 μm	276 MHz
4 μm	0.984 μm	0.45 μm	2.462 μm	4.1 μm	288 MHz
4 μm	1.026 μm	0.5 μm	2.462 μm	4.1 μm	301 MHz
4 μm	1.068 μm	0.55 μm	2.462 μm	4.1 μm	313 MHz
4 μm	1.026 μm	0.5 μm	2.363 μm	4 μm	326 MHz
4 μm	1.068 μm	0.55 μm	2.363 μm	4 μm	340 MHz
4 μm	1.111 μm	0.6 μm	2.363 μm	4 μm	353 MHz

For the straight devices, 12 repeated pillars of the same geometry were printed in a vertical line in the middle of the delay line of each device. For each SAW delay line design, one device was printed with various pillars, where each type of pillar was repeated four times, resulting in a total of 28 pillars. The center-to-center distance between each pillar was set as 5 μm. Figure.3.54 and 3.55 illustrate the design of these pillar arrays for straight devices.

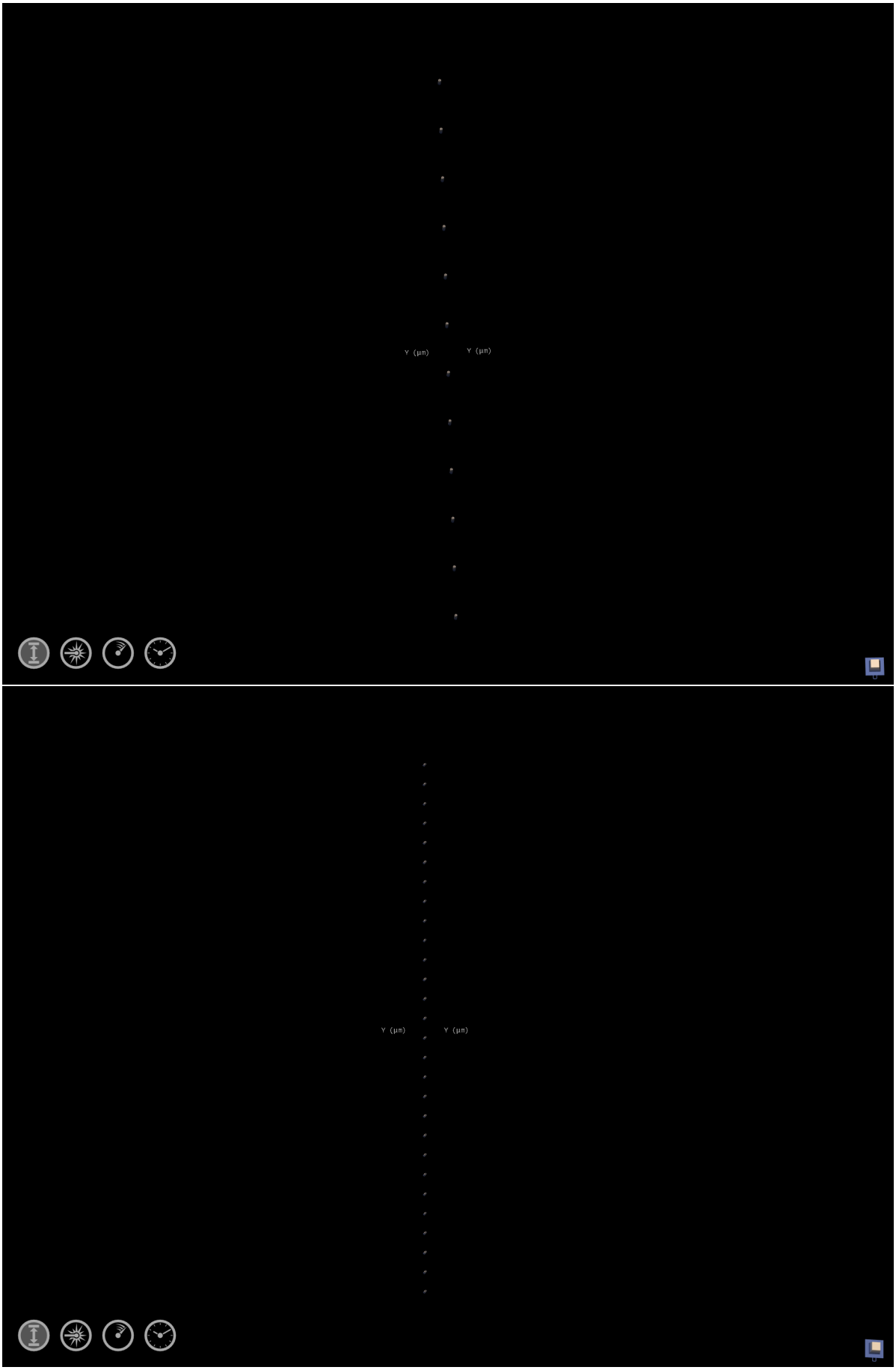


Figure 3.54: Nanoscribe file of pillar array design for straight devices. Top: 12 repeated pillars; Bottom: 28 pillars of 7 different geometry

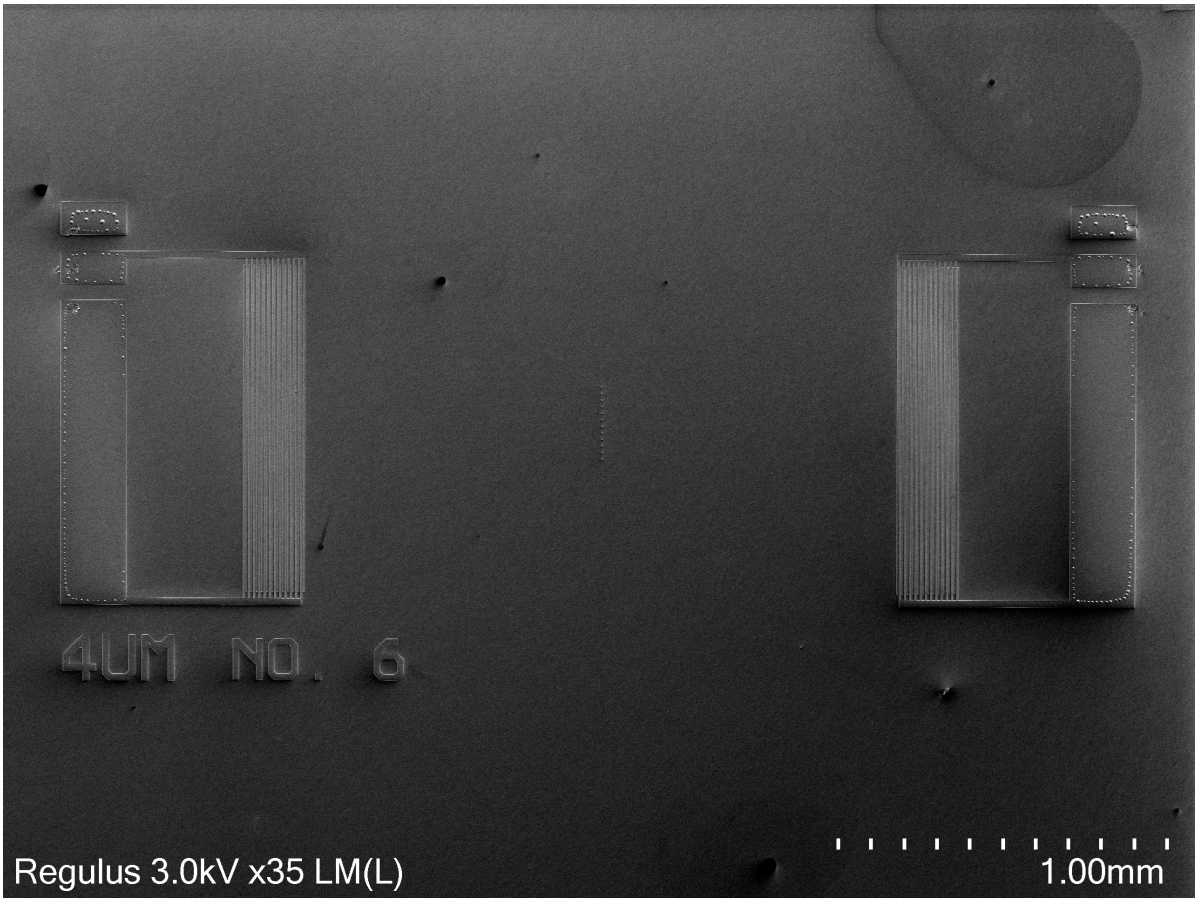


Figure 3.55: SEM image of a straight device with pillars printed

For the focused devices, 7 repeated pillars of the same geometry were printed inside a circle in the center of each device. There was also one device for each design printed with pillars of 3 different geometries, with 3 repeated for each, resulting in a 3 by 3 array. The center-to-center distance between each pillar was again set as 5 μm. Figure.3.56 and 3.57 shows the design of these pillar arrays. Figure.3.58 shows an example of a focused device printed with pillars.

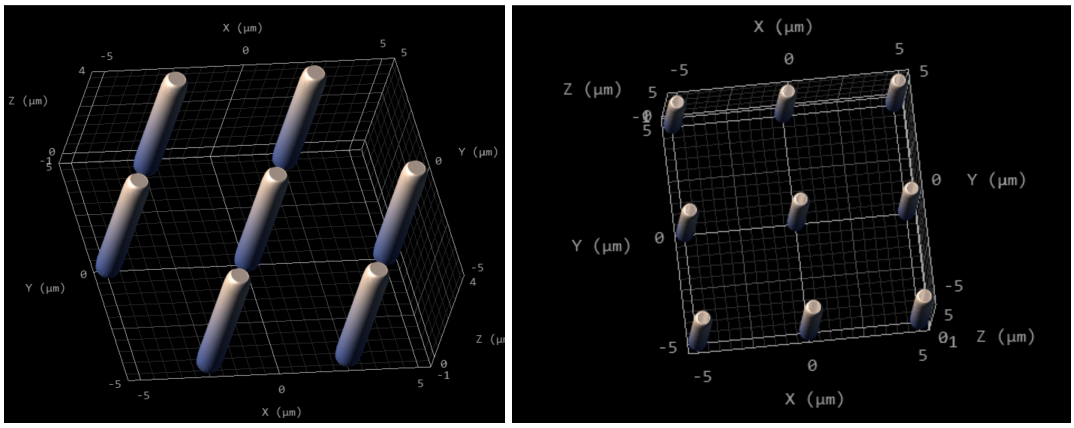


Figure 3.56: Nanoscribe file of pillar array design for focused devices. Left: 7 repeated pillars; Right: 9 pillars of 3 different geometry

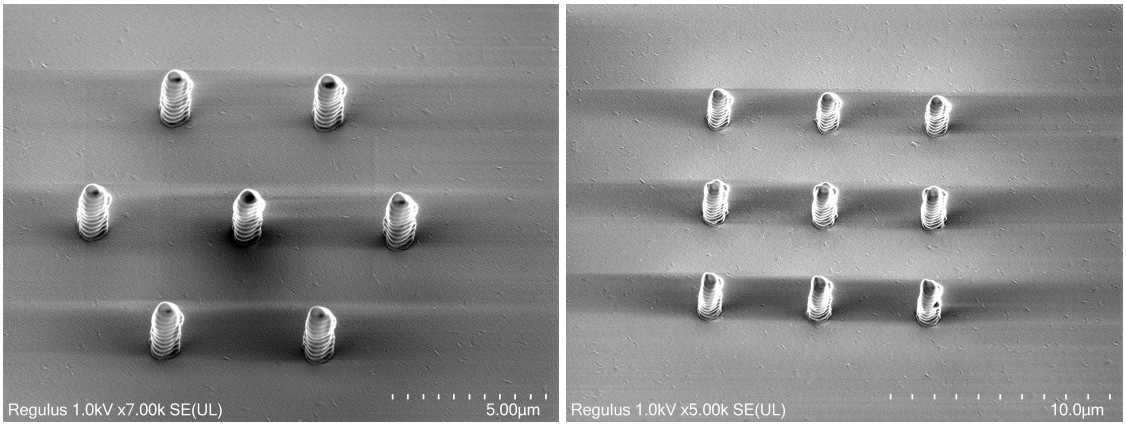


Figure 3.57: SEM images of printed pillar arrays for focused devices

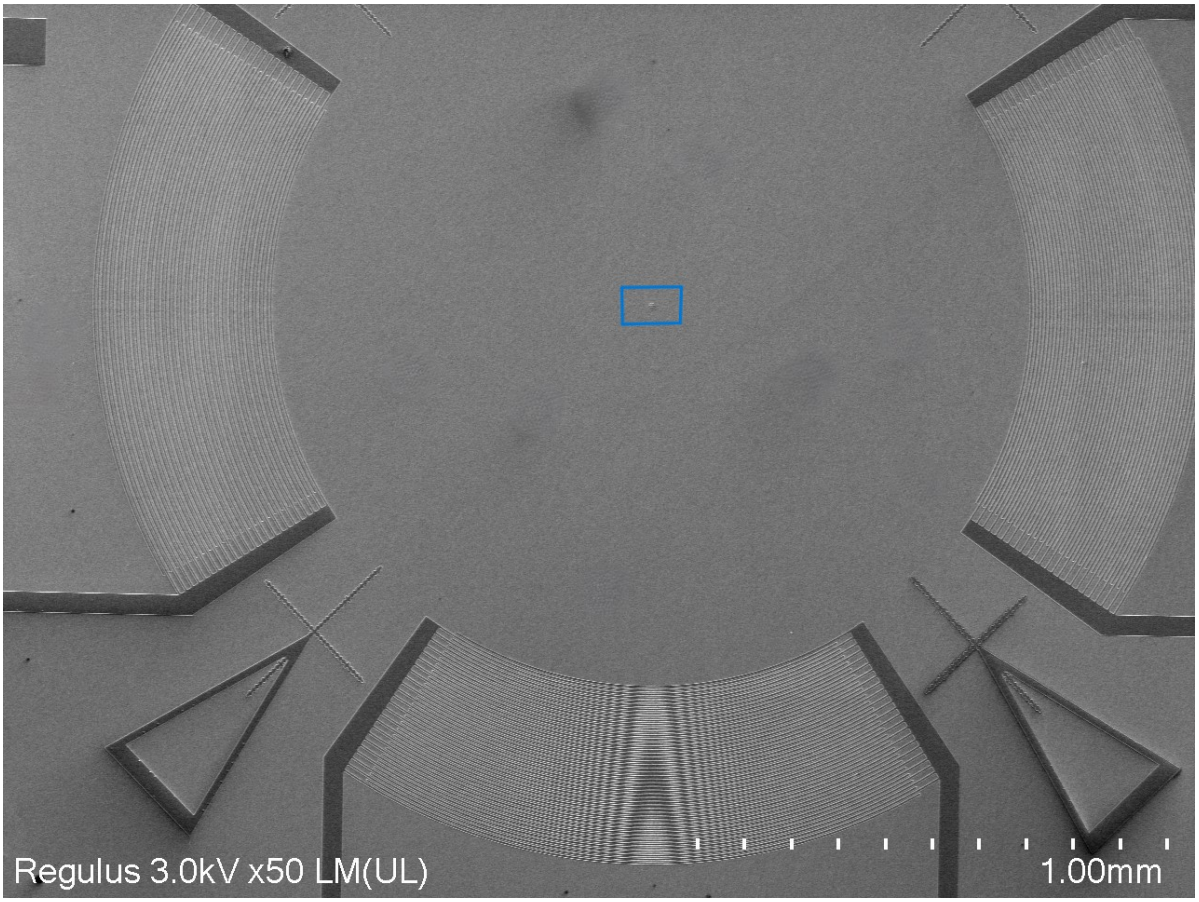


Figure 3.58: SEM image of a focused device with pillars printed in the center

The morphology of two-photon polymerized pillars is also shown in Figure.3.57

3.4. Focused Ion Beam Induced Deposition

The deposition of platinum using the focused ion beam is a process combining chemical vapor deposition and sputtering. Trimethyl platinum precursor gas is fed over the pattern area by a GIS (gas injection system) needle. When the Ion beam scans point by point, the chemical bonds of the precursor gas break leaving the Pt deposited on the substrate but may also sputter the materials away.

It is recommended by the system manual with the ion beam current of 2 - 6 $pA/\mu m^2$ and dwell time

of 200 ns, which will result in a deposition speed of about 1 μm / 60 s in thickness.It was aimed at achieving this most efficient setting, that the majority of the precursor gas can decompose but without leaving excess ions etching away the materials. The target diameter of the pillars was set as 0.5 μm and the cross-section area was calculated as 0.1963 μm^2. So, the ion beam current was expected to be chosen between 0.3926 - 1.1778 pA. At first, the current setting of 7.7 pA and 1.1 pA were tested to deposit a pillar with 0.5 μm diameter and 4 μm height. The results are shown in Figure.3.59. Due to the worn-out of the ion beam aperture, some of the apertures were wider than the defined sizes and this gave shifts between the selected ion beam currents and the actual beam currents. The actual ion beam current of the two selected settings was 1.80 pA instead of 1.1 pA and 16.77 pA instead of 7.7 pA.

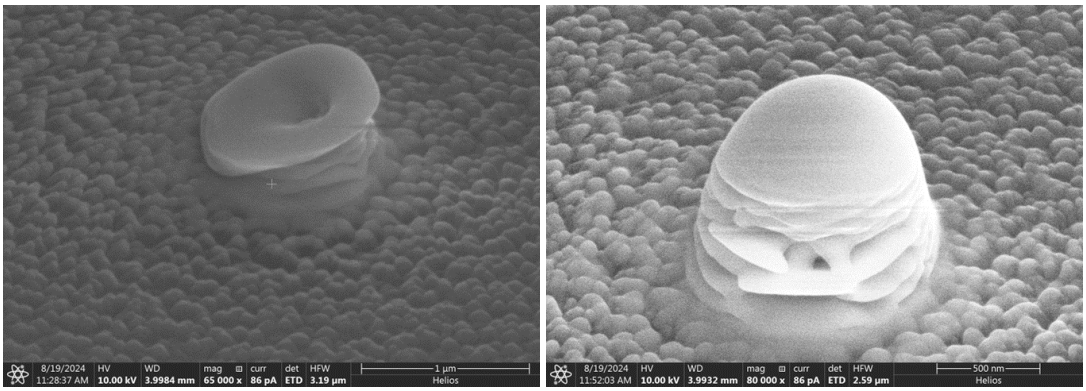


Figure 3.59: SEM image of FIB Pt pillars deposited with 1.1 pA and 7.7 pA current

It can be seen that the 7.7 pA selection gave too much current resulting in etching after some deposition. The 1.1 pA could deposit materials, but it was not efficient as it took around 20 min to deposit the structure in the figure and the dimensions were far away from what was assigned. From the literature, Young's modulus and density of FIB deposited platinum for analytical modeling were used as 168 GPa and 13400 kg/m^3 with a similar setting [1]. Pillars with a first-order bending frequency of around 410 MHz were targeted. After a few trials, a pillar array with diameters of around 650 nm and heights varying from 870 nm to 1056 nm was printed on one of the 3 μm devices as shown in Figure.3.60.

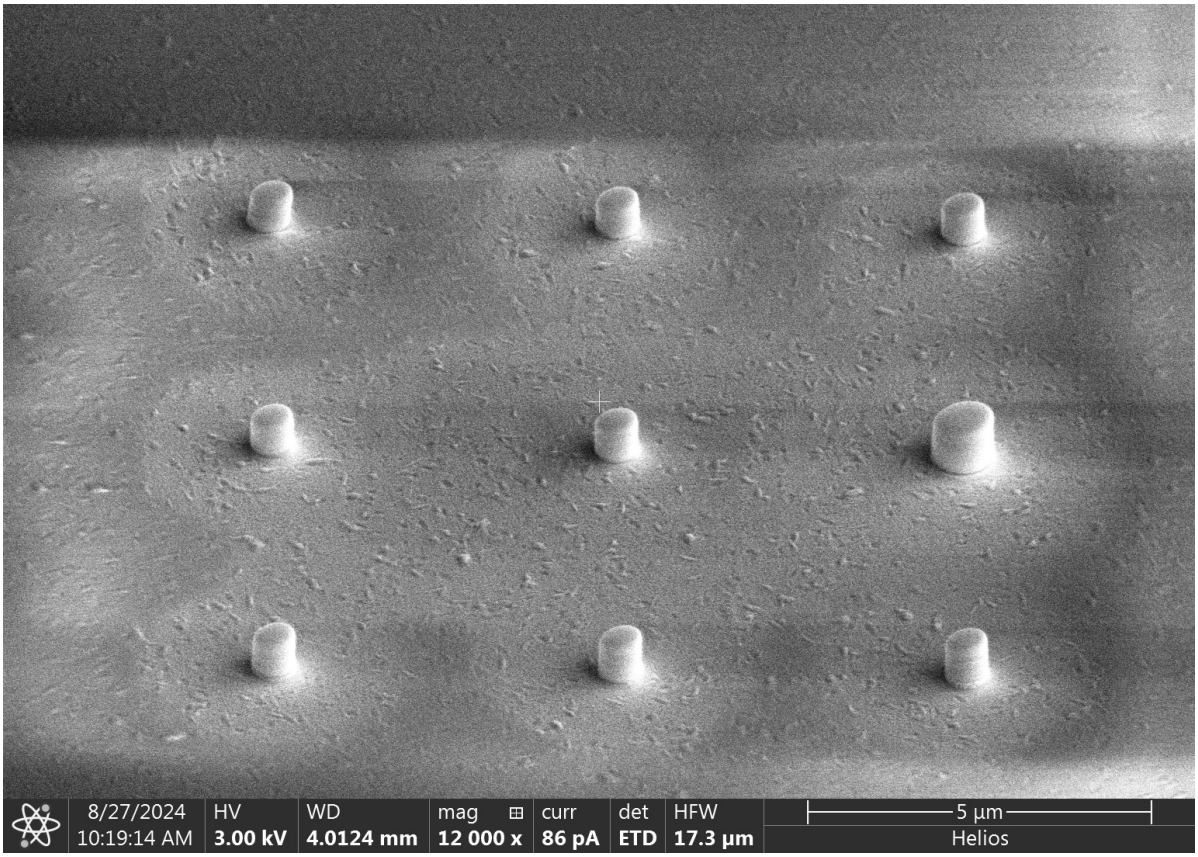


Figure 3.60: SEM image of FIB pillar array 2

A second array with diameters of around 650 nm and slightly larger heights than the first array is shown in Figure.3.61.

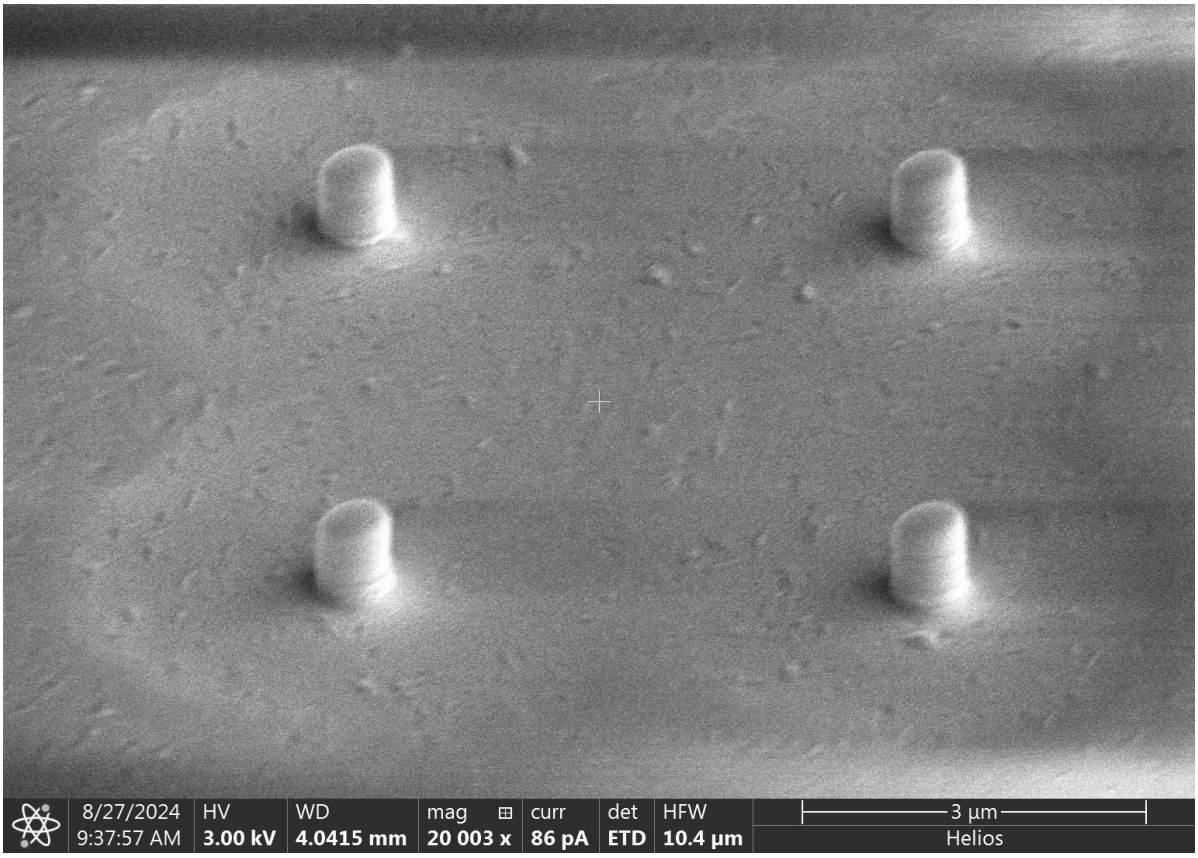


Figure 3.61: SEM image of FIB pillar array 1

After changing the Pt crucible a third pillar array was printed. Three pillars with designed diameters of 500 nm and heights of 1050 nm, 1100 nm, and 1150 nm were printed in a column. Each pillar was printed three times in a row. The result is shown in Figure.3.61. The heights of the three 1050 nm pillars were measured as 1054nm, 1034 nm, and 1054 nm. The heights of the three 1100 nm pillars were measured as 1082nm, 1130 nm, and 1109 nm. The heights of the three 1150 nm pillars were measured as 1150 nm, 1171 nm, and 1144 nm. The printed heights of pillars were all around the designed heights, however, the diameter varied from 599 nm to 658 nm compared to the designed value of 500 nm.

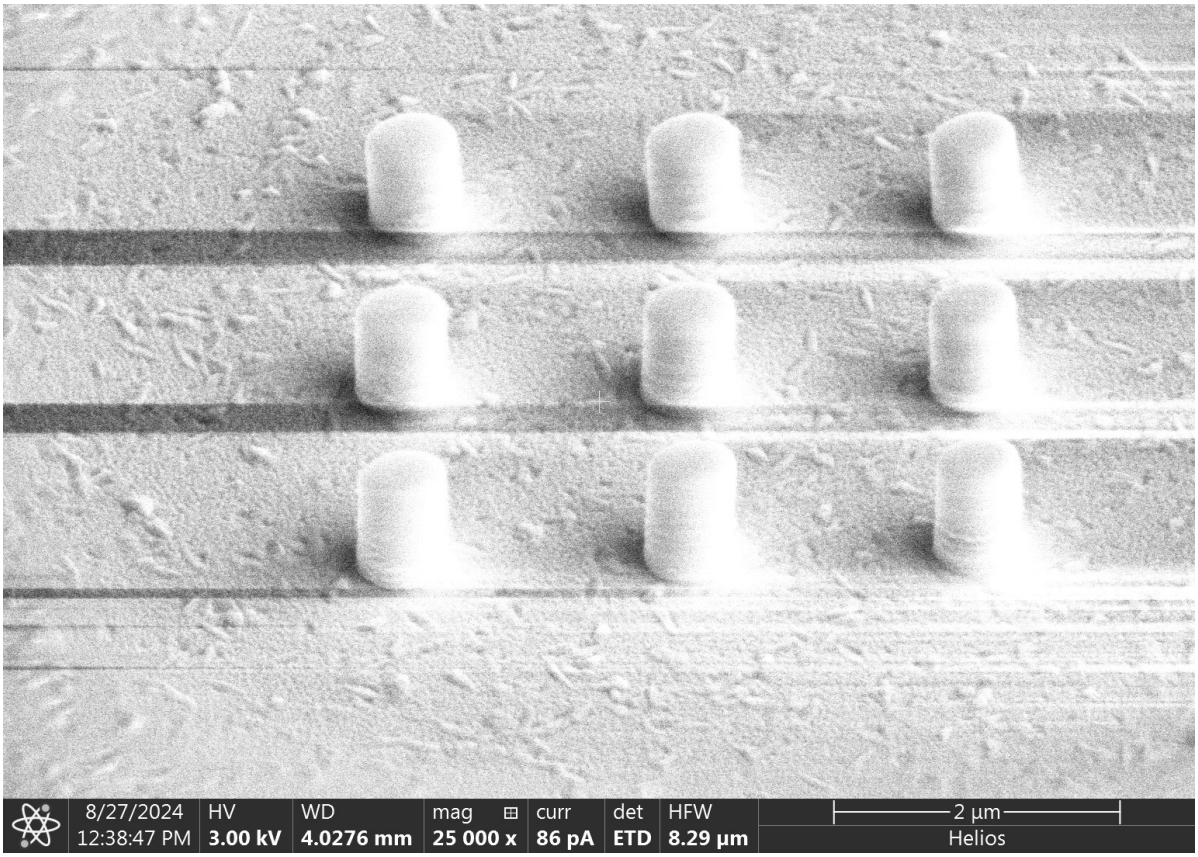


Figure 3.62: SEM image of FIB pillar array 3

The measured dimensions and the resulting resonance frequencies from estimation are shown in the table below:

Table 3.3: FIB pillars

Pillar array 2			**Pillar array 3**		
Diameter	**Height**	**1st bending**	**Diameter**	**Height**	**1st bending**
663.5 nm	0.8702 μm	433.5 MHz	642.1 nm	1.054 μm	286.0 MHz
674.7 nm	0.8990 μm	413.1 MHz	658.3 nm	1.034 μm	304.6 MHz
630.6 nm	0.8990 μm	386.1 MHz	599.0 nm	1.054 μm	266.8 MHz
641.8 nm	0.9558 μm	347.6 MHz	658.4 nm	1.082 μm	278.3 MHz
652.0 nm	0.8987 μm	399.4 MHz	653.8 nm	1.130 μm	253.3 MHz
968.3 nm	1.241 μm	311.1 MHz	621.1 nm	1.109 μm	249.9 MHz
652.0 nm	0.9843 μm	333.0 MHz	637.3 nm	1.150 μm	238.4 MHz
663.5 nm	1.013 μm	319.9 MHz	632.8 nm	1.171 μm	228.3 MHz
652.0 nm	1.056 μm	289.3 MHz	605.3 nm	1.144 μm	228.8 MHz

Small volumes of Pt were deposited onto the pillars in array 2 to change the pillar's resonance, Figure.3.63. Due to the low precision of locating, some nubbles were deposited on the side wall of pillars.

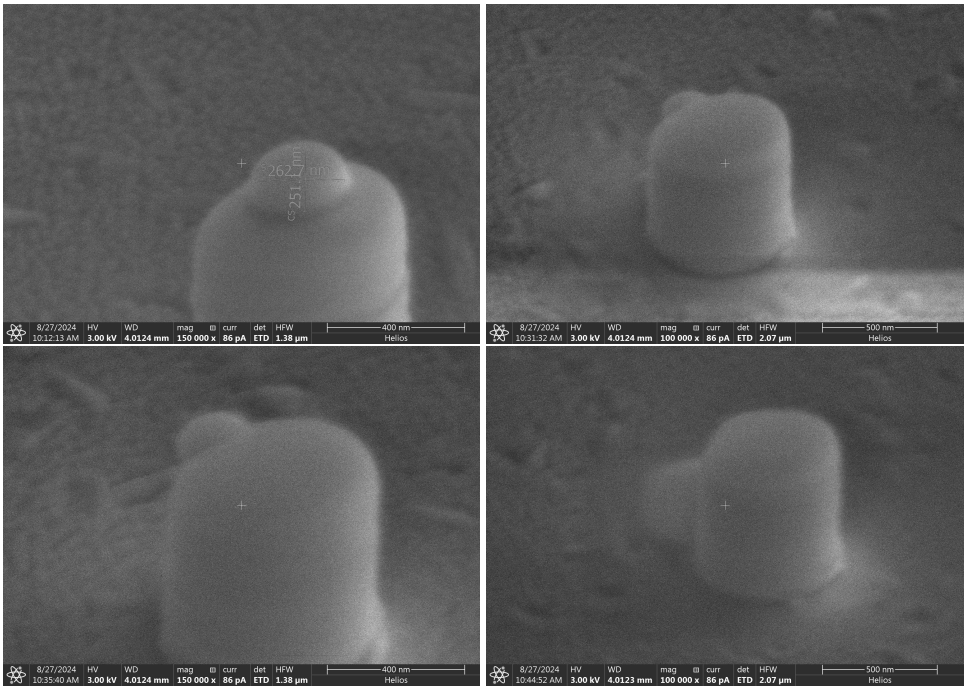


Figure 3.63: SEM image of FIB pillars with deposited mass

3.5. Measurement

3.5.1. On wafer measurements

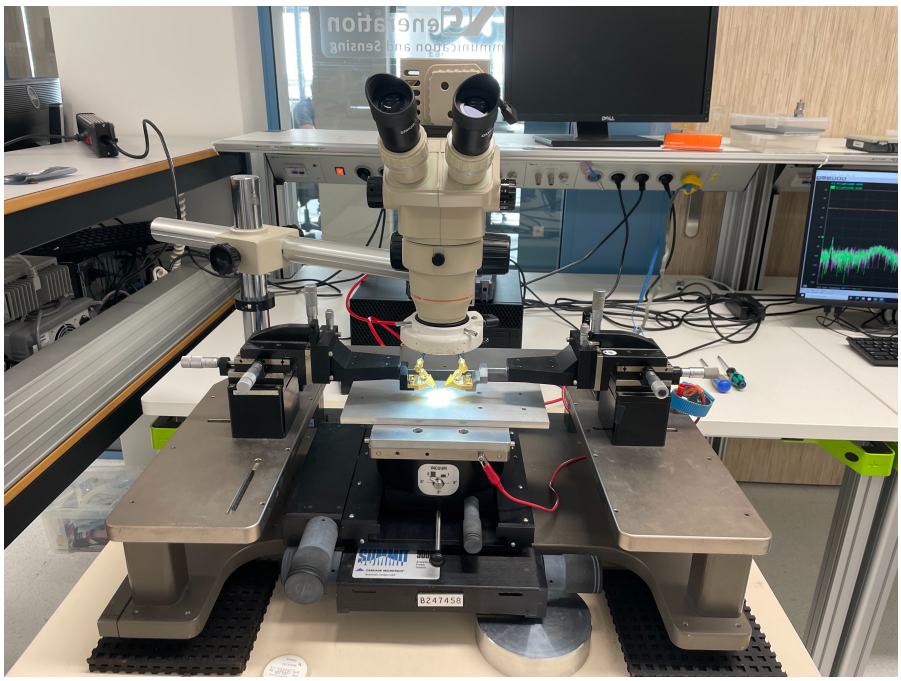


Figure 3.64: Probe station setup for VNA measurements

The measurements of the SAW devices were done with RF GSG probes, a probe station, and a Keysight P9370A USB Vector Network Analyser, Figure.3.64. Before the measurement, Short-Open-Load-Through (SOLT) calibrations were done to reduce the influence of setup imperfections and systematic errors every time. The Impedance Standard Substrate P/N 101-190 and CSR-3 Calibration

Substrate were used respectively for the calibration of parallel and perpendicular S-parameters measurement. After calibration, the S-parameters with probes in the unloaded state are shown in Figure.3.65. The S11 and S22 representing signal reflection at two ports were all 0 dB indicating total reflection when both probes were unloaded. The S12 and S21 representing signal transmission between two ports were at very low values around -80 dB contributed by the noise indicating negligible transmission.

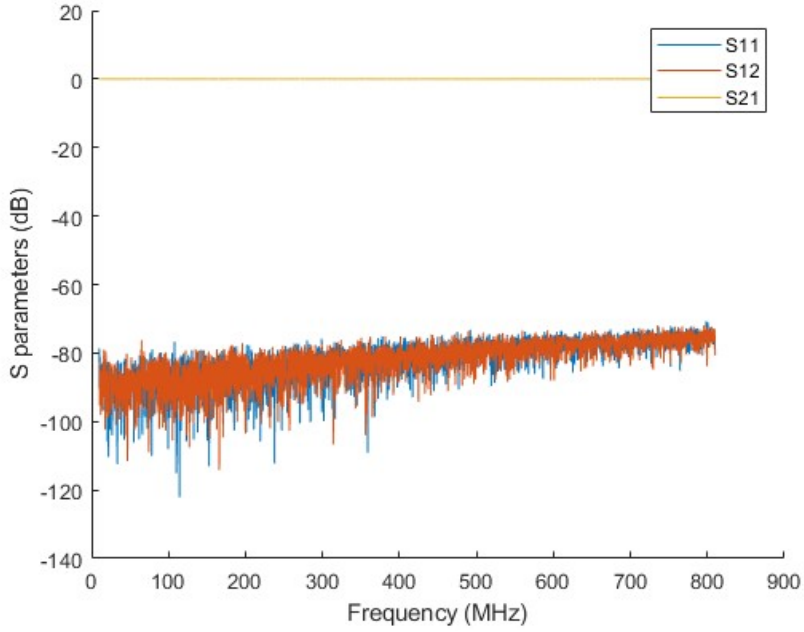
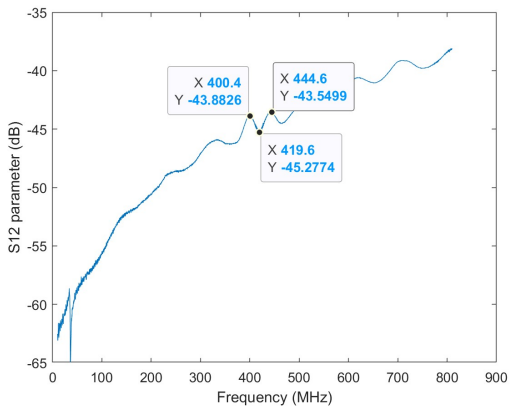


Figure 3.65: VNA noise after calibration

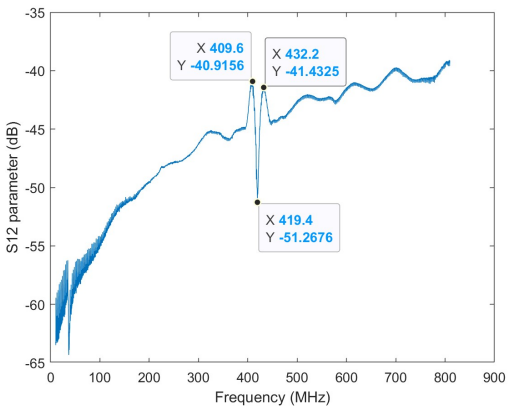
For the measurement of SAW delay line devices without pillars, the signal power was set as -5dBm and the IF bandwidth was set as 1 kHz. The power and IF bandwidth were sufficient since further increasing the power and reducing the IF bandwidth did not influence the results much. For the measurement with pillars, the power was increased to 0 dBm, the largest value the vector network analyzer could provide, and the IF bandwidth was reduced to 200 Hz. This was to ensure enough actuation of pillars and low noise value for recognizing the pillar's signal.

Single frequency straight IDT

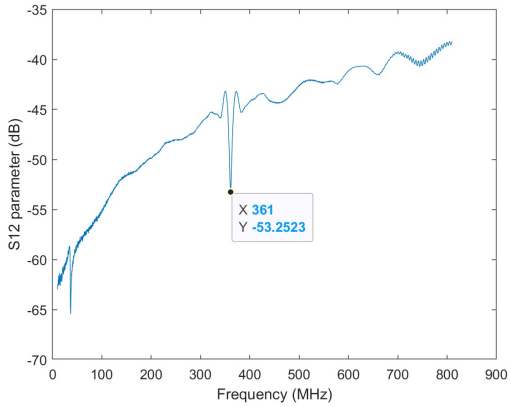
The S-parameters measurement results of the single frequency straight devices on wafer design 1 are shown in Figure.3.66. The measured center frequencies of the devices were consistent with the simulations, however, a negative peak of the device transmission was always measured.



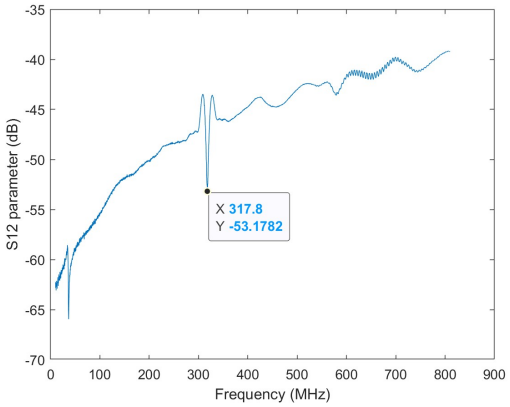
(a) 6 pairs 3um fingers



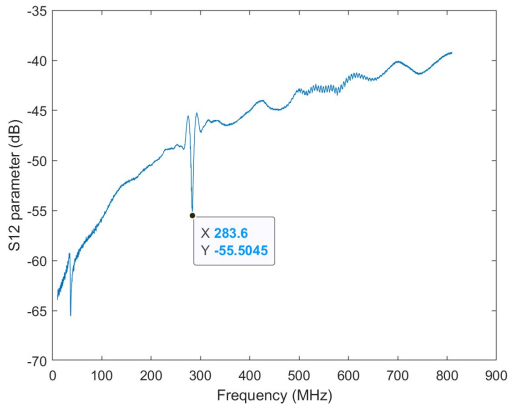
(b) 12 pairs 3um fingers



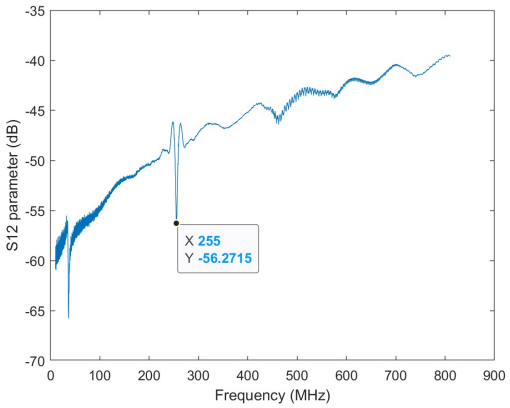
(c) 12 pairs 3.5um fingers



(d) 12 pairs 4um fingers

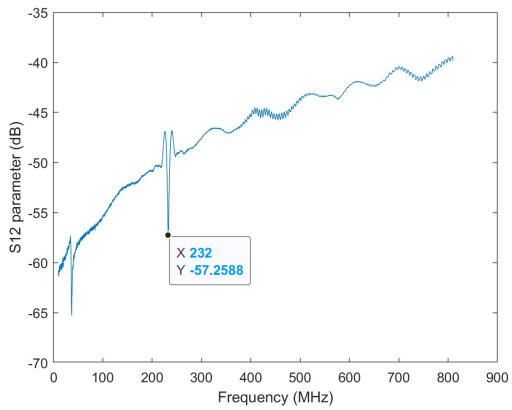


(e) 12 pairs 4.5um fingers

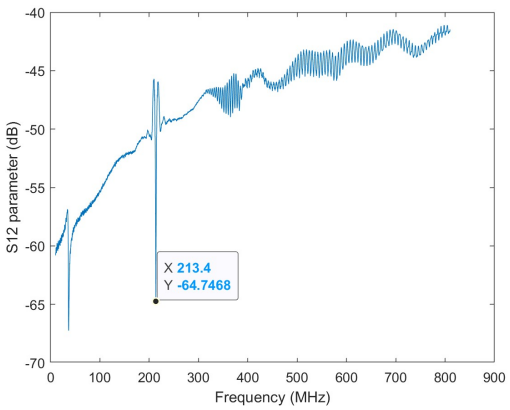


(f) 12 pairs 5um fingers

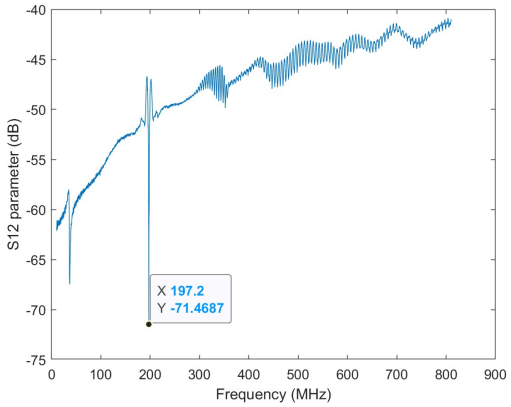
Figure 3.66: S-parameters of single frequency straight IDTs



(g) 12 pairs 5.5um fingers



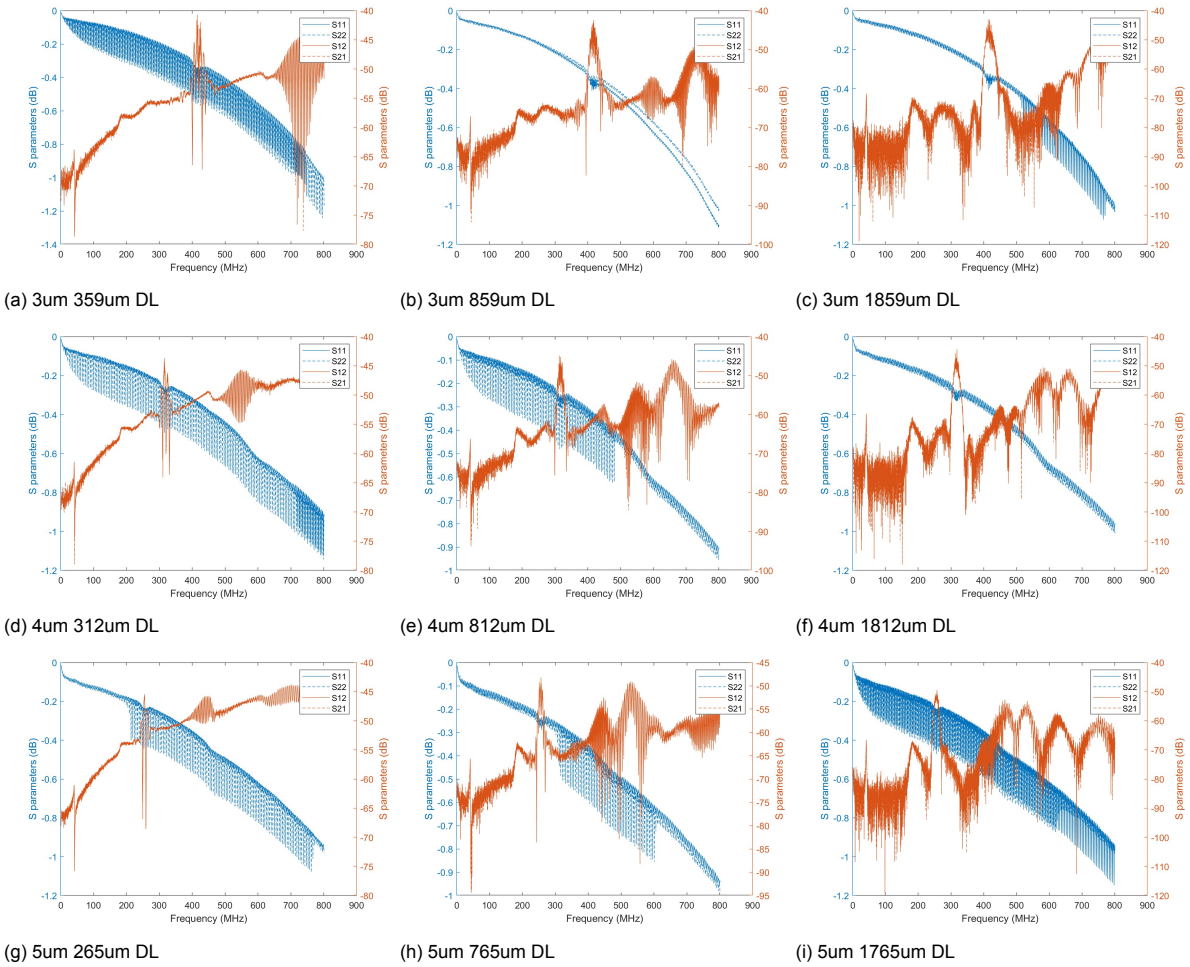
(h) 18 pairs 6um fingers



(i) 18 pairs 6.5um fingers

Figure 3.66: S-parameters of single frequency straight IDTs

The distance between two IDTs in the first straight designs is very short with only two times the emitted SAW length. The fingers of IDTs also acted as reflectors and the devices gave a more SAW resonator-like performance. The deep negative peak was not observed in the S12 measurement of focused devices. Due to the much longer delay line distance, the reflections caused by the IDT electrodes were reduced. The focused shape of IDTs may also help to reduce the reflections. The measurement results of single-frequency straight devices with increased delay line length are shown in Figure.3.67



(a) 3um 359um DL (b) 3um 859um DL (c) 3um 1859um DL

(d) 4um 312um DL (e) 4um 812um DL (f) 4um 1812um DL

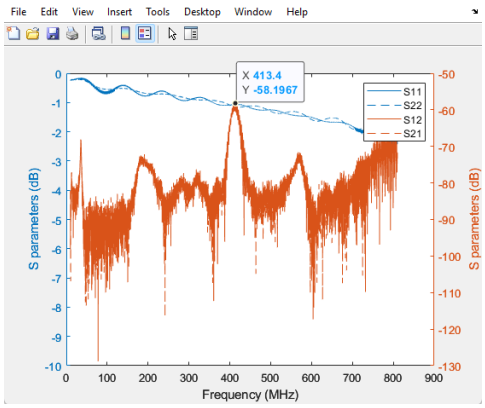
(g) 5um 265um DL (h) 5um 765um DL (i) 5um 1765um DL

Figure 3.67: S-parameters of single frequency straight IDTs with long delay line

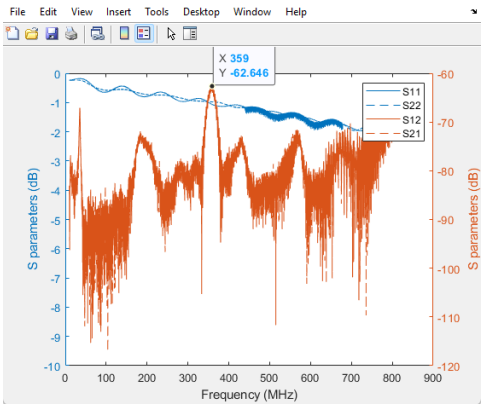
Devices with the same IDT design and gradually increased delay line length were compared. It can be obviously seen that, as the delay line became longer, the reflections became weaker, i.e., the S12 within the designed frequency range became smoother.

Single frequency focused IDT

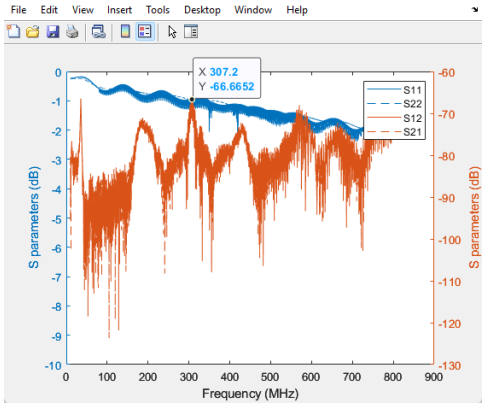
The VNA measurements of FIDT devices with 1mm aperture and 12 finger pairs are shown as below:



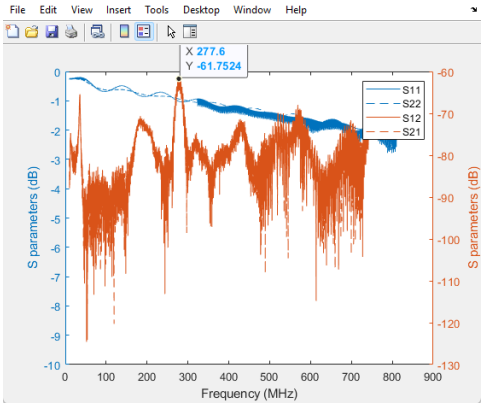
(a) 12 pairs 3um fingers



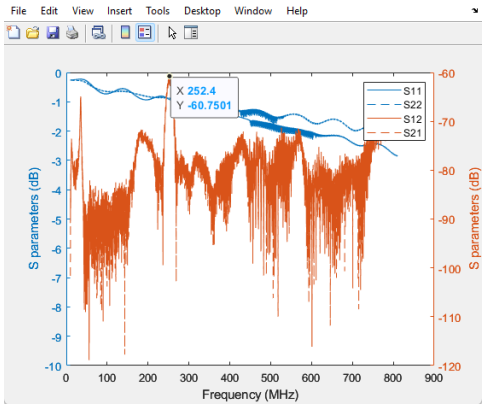
(b) 12 pairs 3.5um fingers



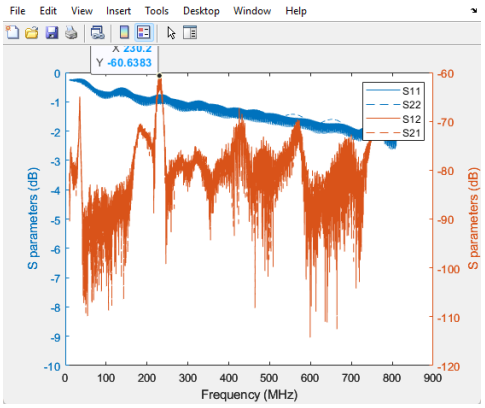
(c) 12 pairs 4um fingers



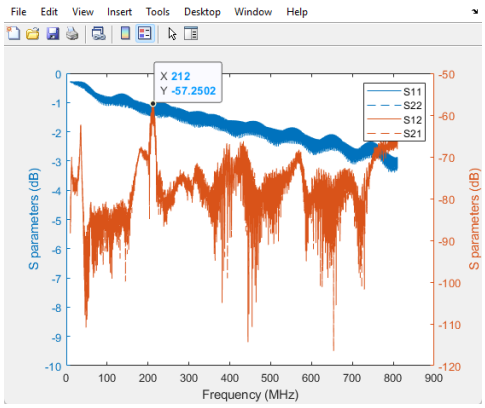
(d) 12 pairs 4.5um fingers



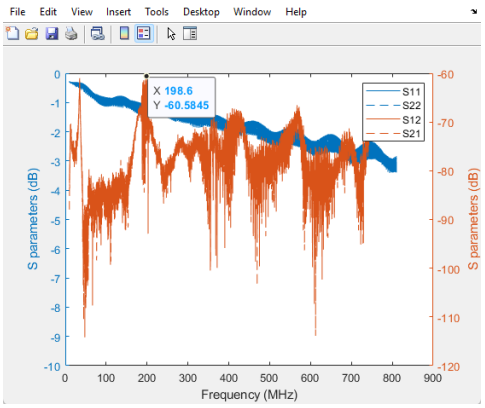
(e) 12 pairs 5um fingers



(f) 12 pairs 5.5um fingers



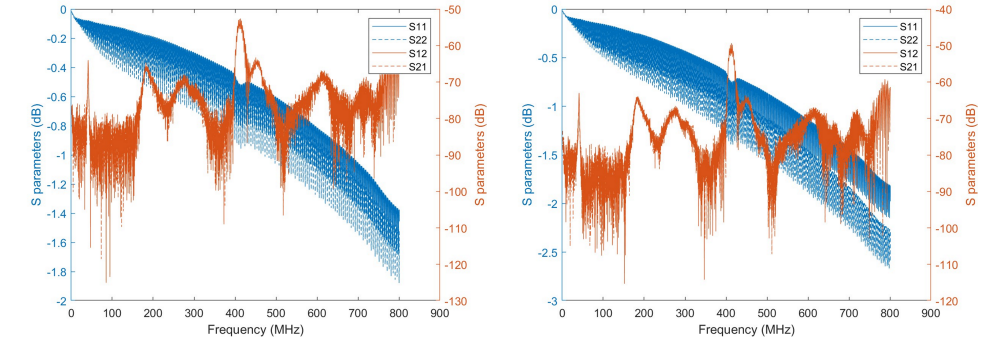
(g) 12 pairs 6um fingers



(h) 12 pairs 6.5um fingers

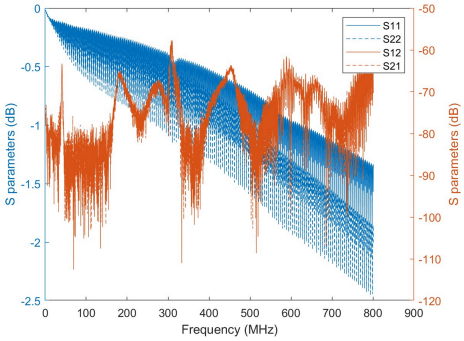
Figure 3.68: S-parameters of single frequency FIDT

The S-parameters measurements of single frequency focused design devices were similar to the simulated results. The devices had a higher transmission on the designed working frequency range, and as the designed center frequency became smaller, the bandwidth became narrower. With increasing the number of fingers, the transmission around the center frequency increased a little and the bandwidth shrunk slightly. The measurements of devices designed with 18 and 24 finger pairs are shown as below:

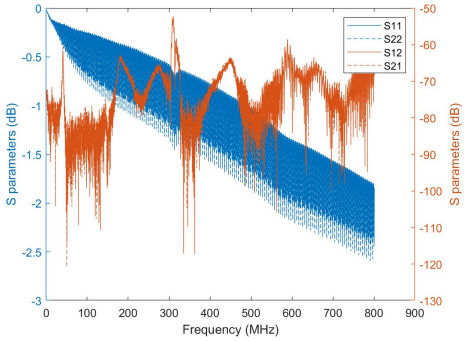


(a) 18 pairs 3um fingers

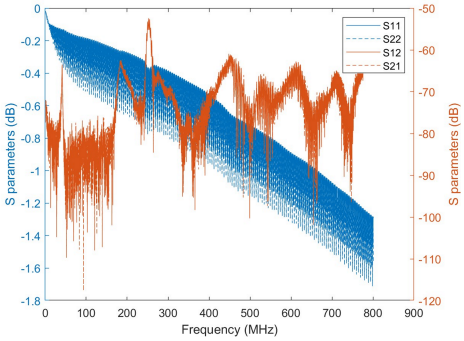
(b) 24 pairs 3um fingers



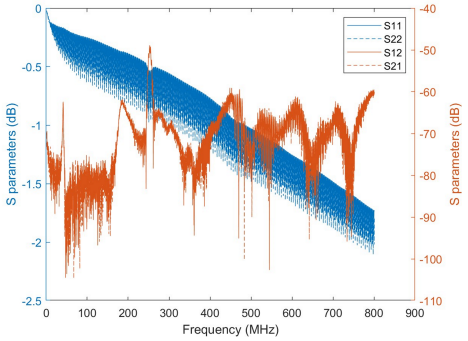
(c) 18 pairs 4um fingers



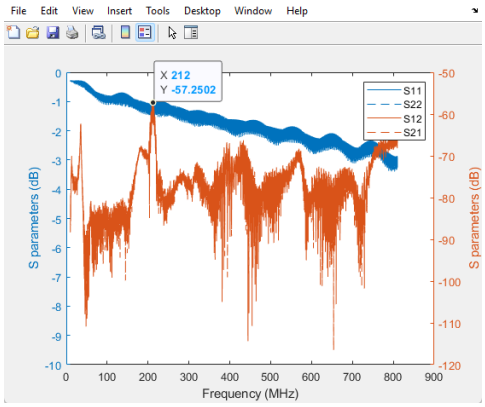
(d) 24 pairs 4um fingers



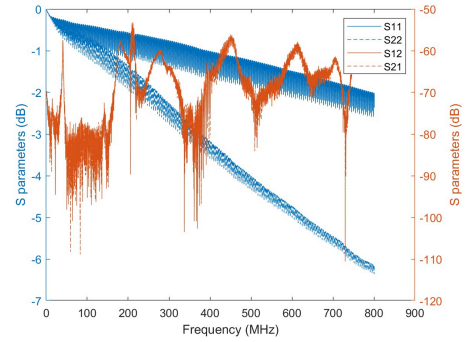
(e) 18 pairs 5um fingers



(f) 24 pairs 5um fingers



(g) 18 pairs 6um fingers

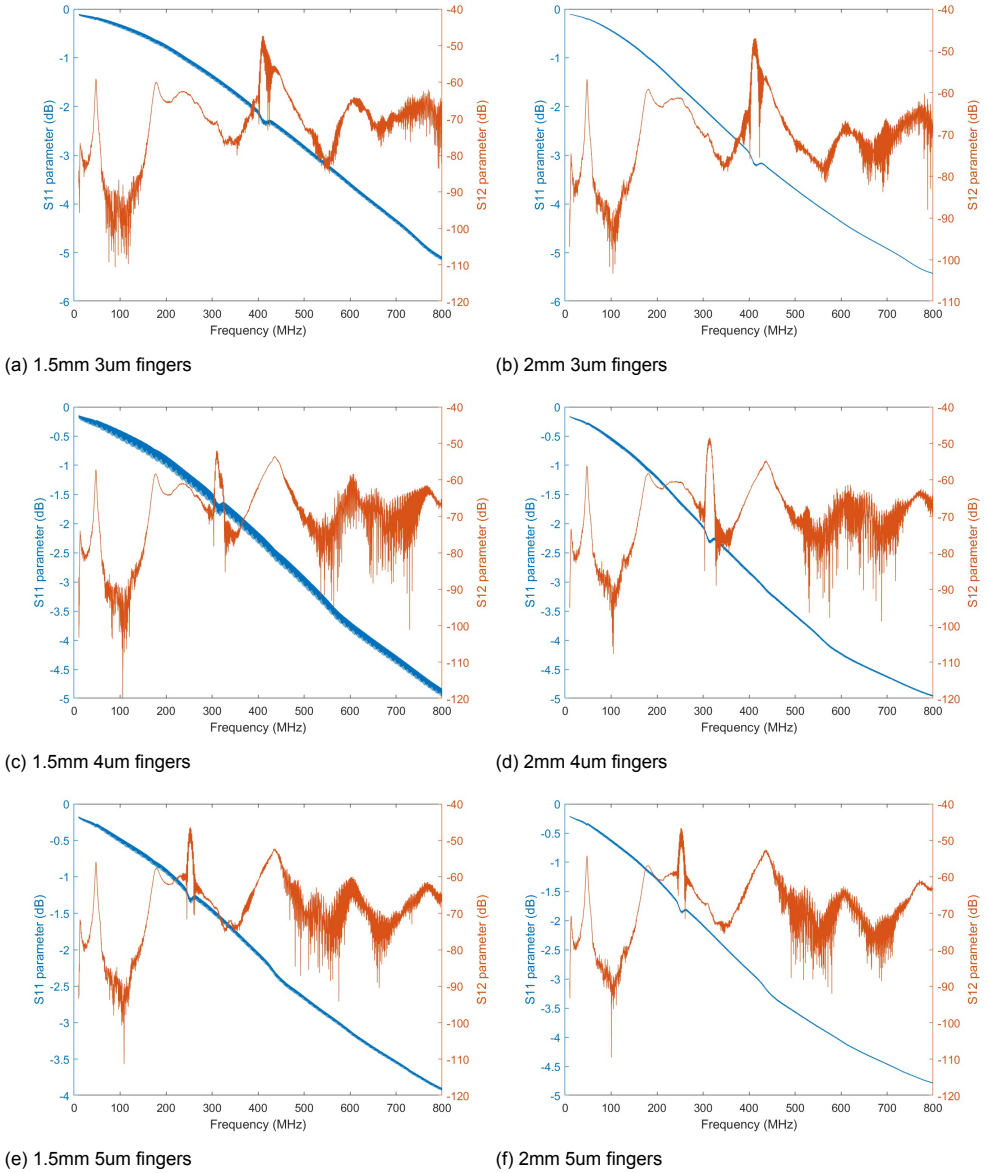


(h) 24 pairs 6um fingers

Figure 3.69: S-parameters of single frequency FIDT with increased finger pairs

Increasing the delay line distance will increase the loss of signals, however, it can mitigate the reflections and becomes a positive design direction. Especially for focused configuration, the overlapping

distance of fingers increases at the same time, which will increase the transmission. The measurements of devices designed with a gemotrical length of around 1.5 mm and 2 mm are shown as below:



(a) 1.5mm 3um fingers

(b) 2mm 3um fingers

(c) 1.5mm 4um fingers

(d) 2mm 4um fingers

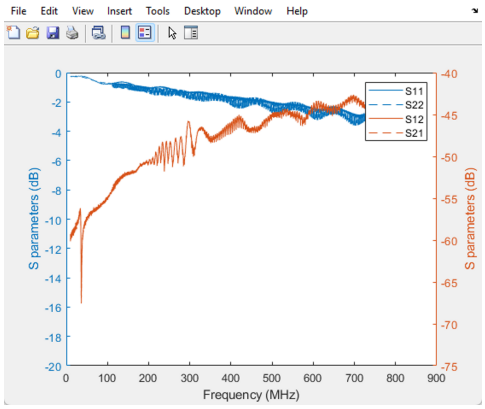
(e) 1.5mm 5um fingers

(f) 2mm 5um fingers

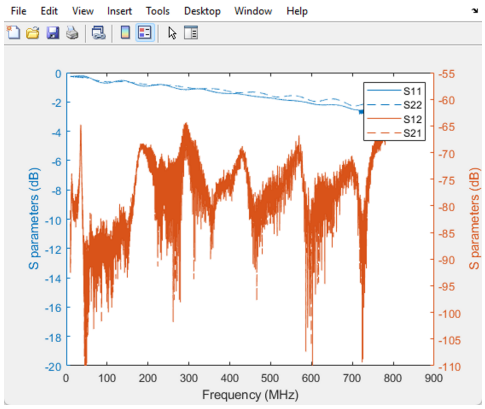
Figure 3.70: S-parameters of single frequency FIDT with increased delay line length

Chirped IDT

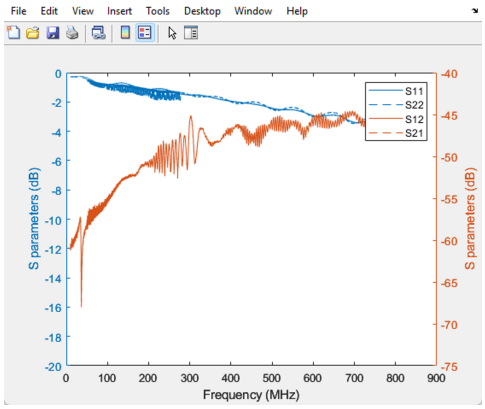
For both straight and focused devices, IDTs with chirped frequency were designed, fabricated, and measured. A lot of reflections were observed for both the straight devices and the chirped devices. Further reducing the number of finger pairs to 3 or increasing the delay line distance have been tested. However, the reflections were not mitigated.



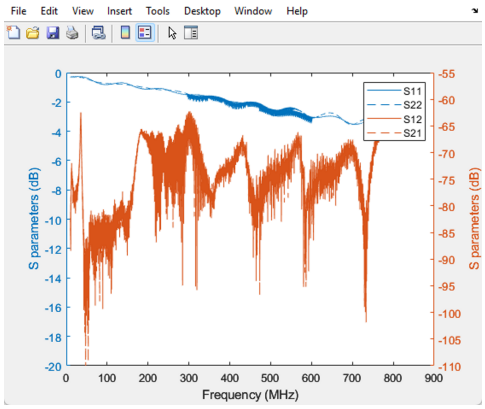
(a) 18 pairs straight



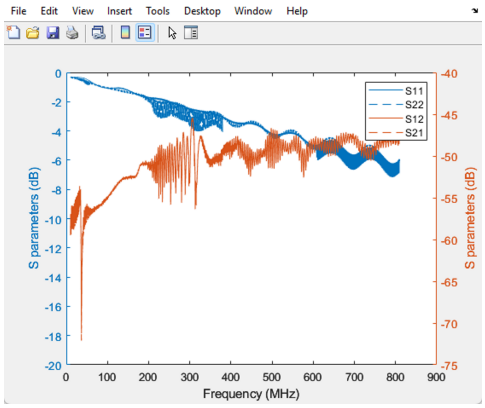
(b) 18 pairs focused



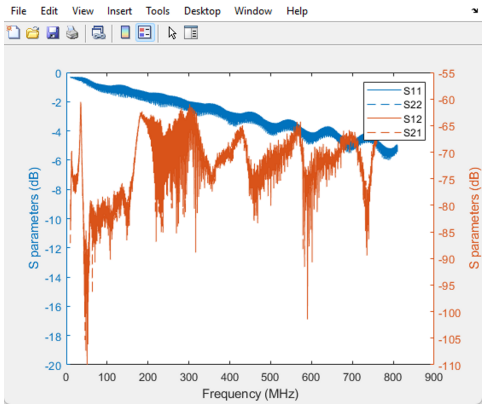
(c) 26 pairs straight



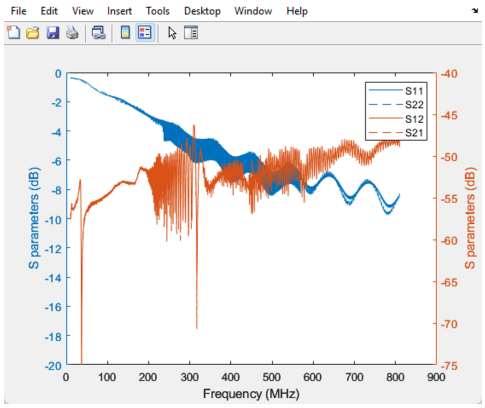
(d) 26 pairs focused



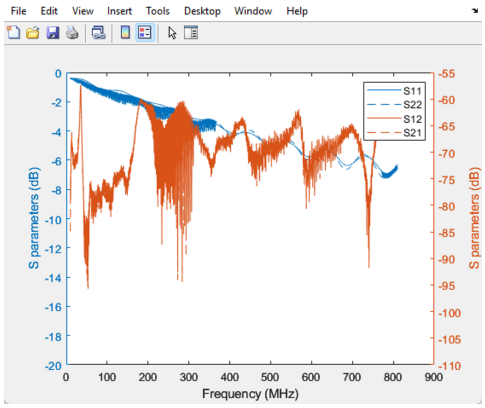
(e) 37 pairs straight



(f) 37 pairs focused

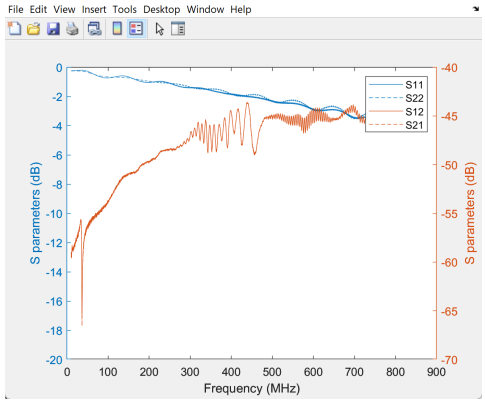


(g) 55 pairs straight

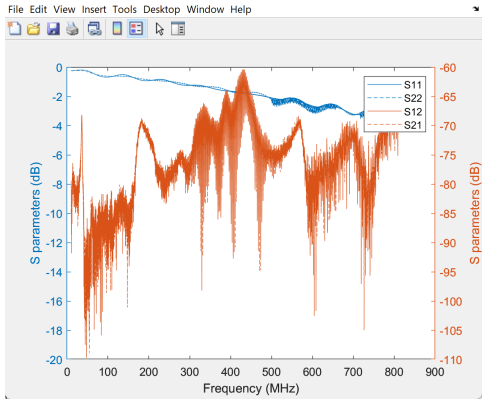


(h) 55 pairs focused

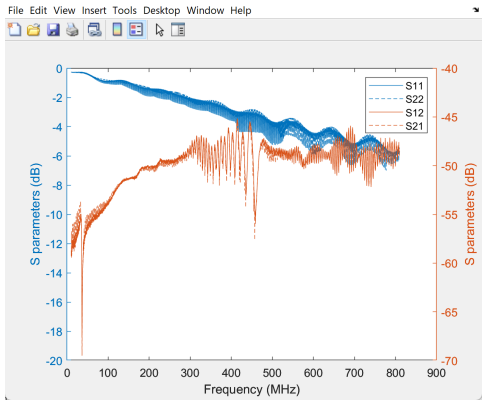
Figure 3.71: S-parameters of chirped design on 200-340 MHz



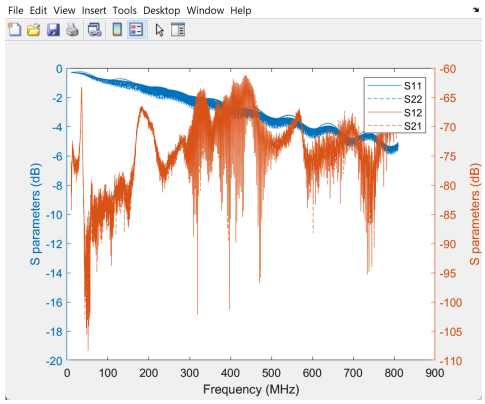
(a) 23 pairs straight



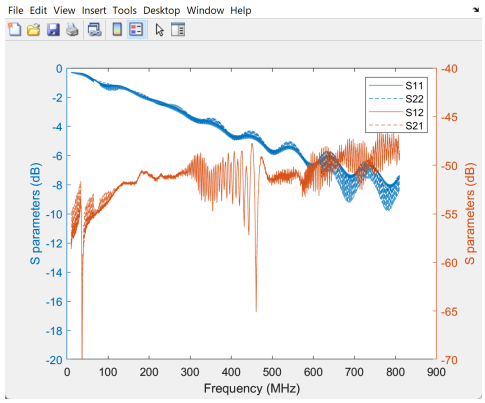
(b) 23 pairs focused



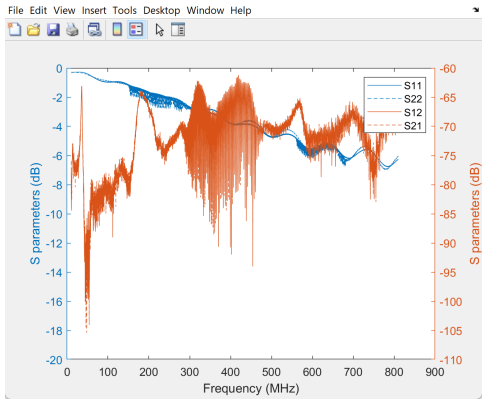
(c) 37 pairs straight



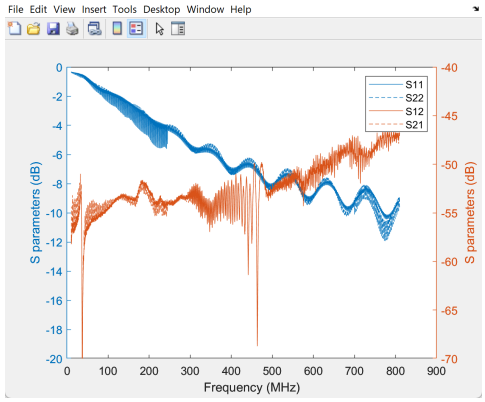
(d) 37 pairs focused



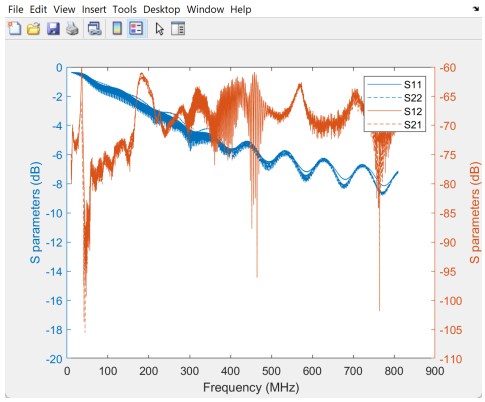
(e) 53 pairs straight



(f) 53 pairs focused



(g) 84 pairs straight



(h) 84 pairs focused

Figure 3.72: S-parameters of chirped design on 300-500 MHz

Reflections in 4 μm finger width device

It was observed in the measurements of devices of 4 μm finger width that a noticeable dip always exists at around 314 MHz for focused devices (Figure.3.73). This was not observed with devices designed on other frequency ranges or straight devices. The center frequency of devices with 16 μm wavelength was around 318 MHz. The wave velocity could be estimated as $16\mu m \cdot 318MHz = 5088m/s$. So, the wavelength of the waves that were greatly reflected was around $5088m/s/314MHz = 16.2\mu m$. It was first guessed that the inner marker was the main contribution since it had a width along the wave propagation direction of around a quarter of this wavelength. However, the dip was also observed after the markers were removed. As this was not a problem for straight designs, focused IDTs gave comparatively large reflections at 314 MHz somehow. 4 μm focused devices with increased delay line length were measured and compared as shown in Figure.3.74. It can be noted that increasing the delay line length can effectively decrease the reflections.

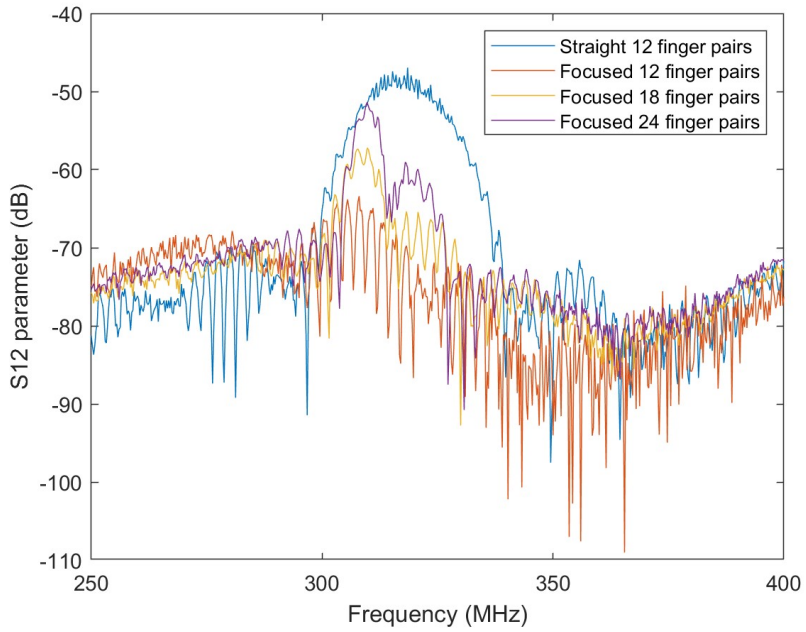


Figure 3.73: S12 of 4um focused devices with different number of finger pairs

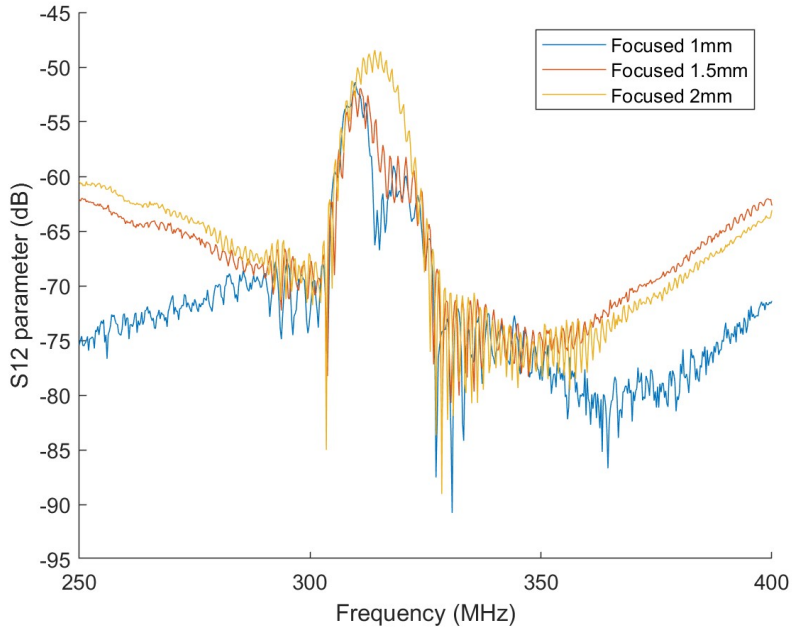


Figure 3.74: S12 of 4um focused devices with different delay line length

Transmission of the final devices

From the VNA measurements of the fabricated SAW devices, several straight and focused devices with 3 μm, 4 μm, and 5 μm finger width with good performances were chosen for further measurements with pillars deposited.

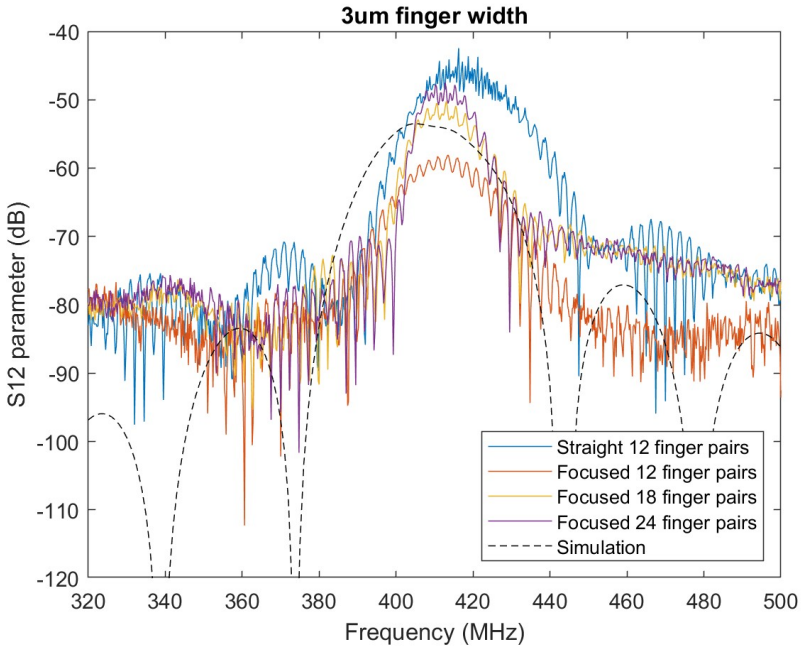


Figure 3.75: Transmission of 3 μm devices

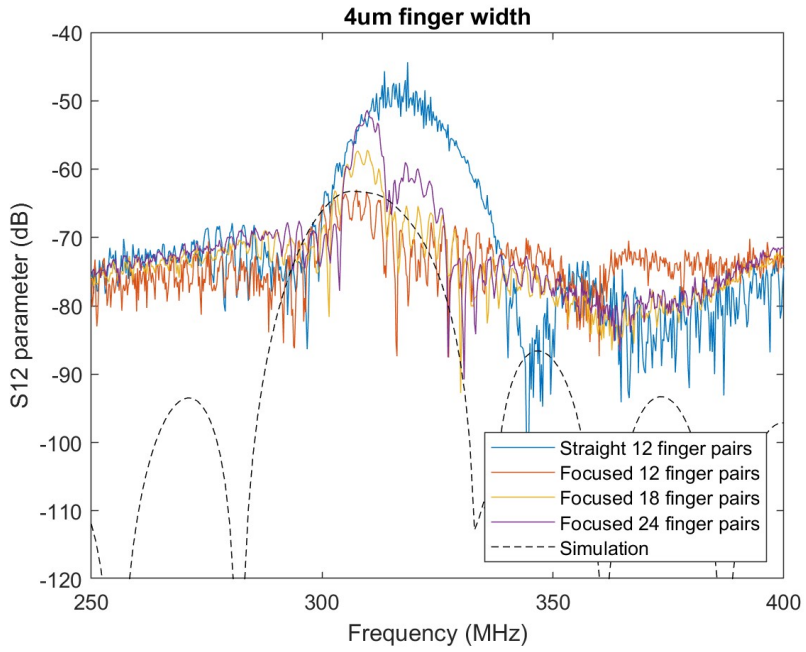


Figure 3.76: Transmission of 4 μm devices

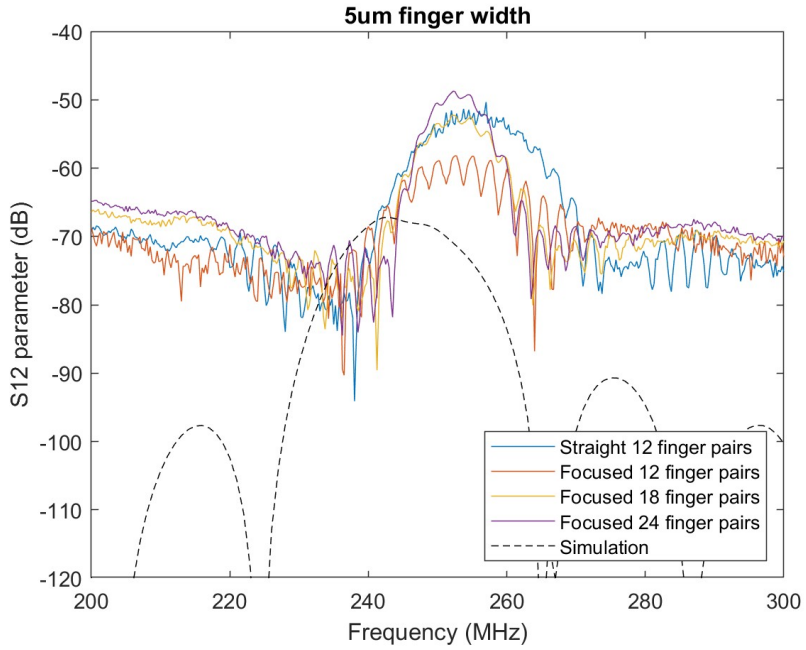


Figure 3.77: Transmission of 5 μm devices

3.5.2. VNA measurements with PCB

A PCB has been designed for the measurements of several devices on a die. Ten devices on the outside edges of the die would be connected to the SMA connectors by the traces on the PCB. The whole die would be connected to the ground by the large metal pad at the center of the PCB. Each device would have three ports connected to three SMA connectors enabling both the parallel and perpendicular transmission measurements. The devices were printed with pillars in the center before the wire bonding. The PCB board was designed with the help of MSc student Maodong Yang and technician Zu Yao Chang from the EI group. The chip was wire-bonded to the PCB by Zu Yao.

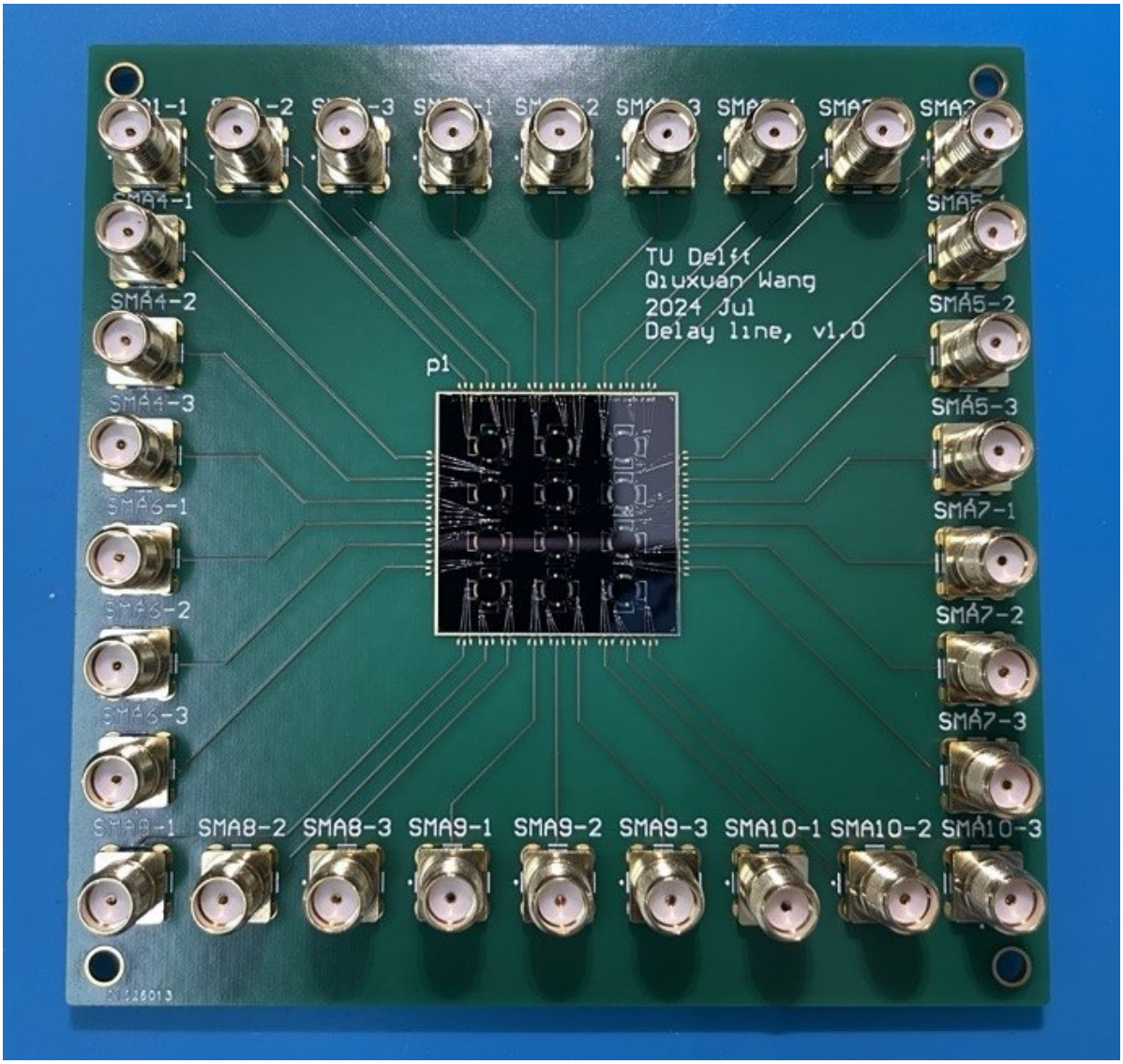


Figure 3.78: Picture of the PCB board with wire-bonded chip and soldered SMA connectors

There were four repeated devices with 3um finger width, two repeated devices with 3.5um finger width and four repeated devices with 4um finger width to be measured. For each device design, there was one device left empty without pillars for comparison. Other devices were printed with pillars estimated with 407MHz, 414MHz, 420MHz, 346MHz, 356MHz, 370MHz, 301MHz, 313MHz, 326MHz, which should lie in the device bandwidth. Here are some examples of the VNA measurement results, Figure.3.79.

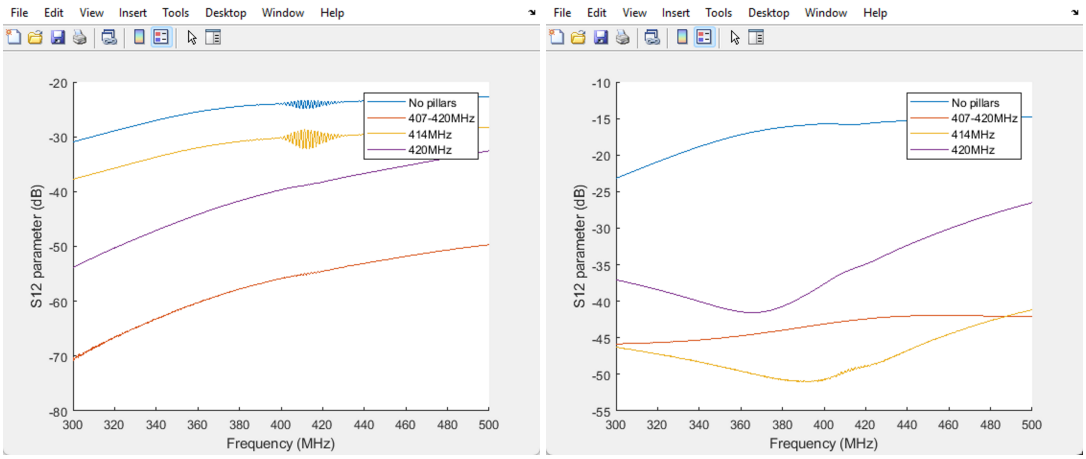


Figure 3.79: Transmission measurement results on PCB

3.5.3. TPP Pillars on devices

Surface acoustic waves scatterd in 90 degrees

Lots of different pillar and pillar array variations were printed on SAW devices with the Nanoscribe printer. During the measurements of these devices with pillars, it was observed that these pillars can successfully scatter surface acoustic waves. Figure.3.80 shows the example of a device printed with pillars of around 5 μm in diameter and 3 μm in height. It can be observed that at the designed transmission band, there were obvious vibrations in transmission different than other bands which was not observed in devices without pillars. This showed that SAWs were scattered in all different directions and the waves that propagated in 90 degrees after the scattering were received by the IDT in 90 degrees. These micro-scale pillars had mild effects in scattering the waves propagating along the delay line, so the signal strength of the scattered waves was small. It was expected that, when the pillars were at resonances, they could have much stronger scattering of waves at that resonance frequency.

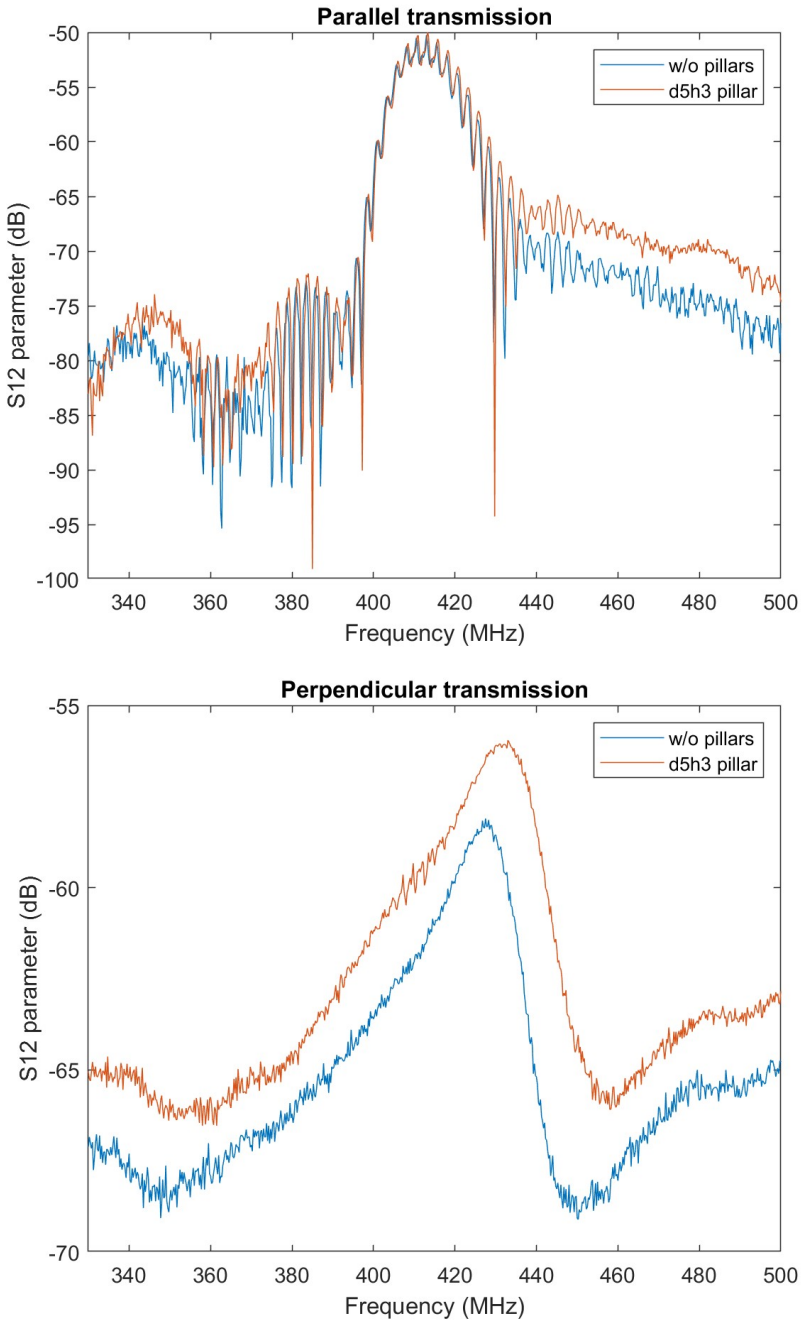


Figure 3.80: Transmission of a device with TPP pillars showing wave scattering

At pillar's estimated resonance frequency

Pillars with more accurately estimated resonance frequencies were printed on devices and measured with the resulting device S-parameters.

Straight devices of 3 μm finger width were printed with pillars of estimated frequencies of 380 MHz, 393 MHz, 407 MHz, 414 MHz, 420 MHz, 437 MHz, and 453 MHz. The transmission between two ports of the device is shown below:

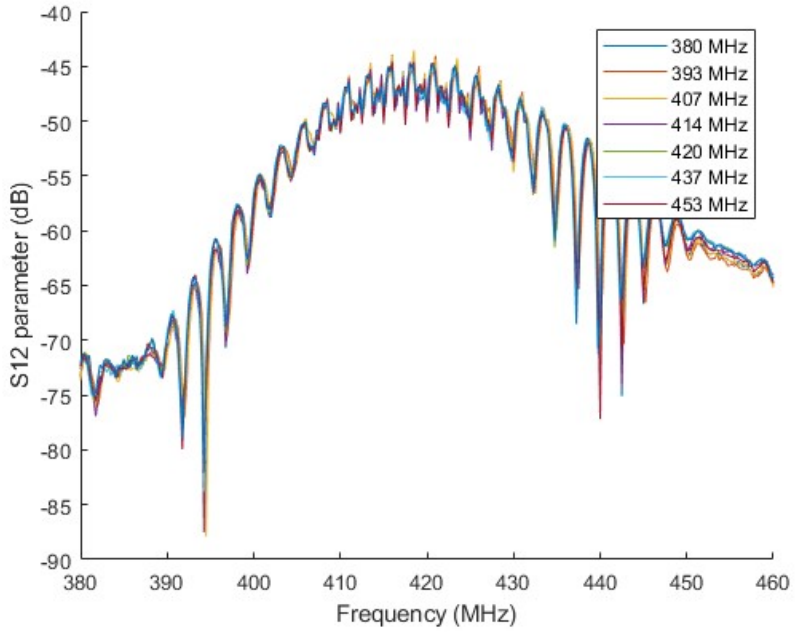


Figure 3.81: Transmission of 3um straight devices with different pillars

Straight devices of 4 μm finger width were printed with pillars of estimated frequencies 276 MHz, 288 MHz, 301 MHz, 313 MHz, 326 MHz, 340 MHz, and 353 MHz. The transmission between two ports of the device is shown below:

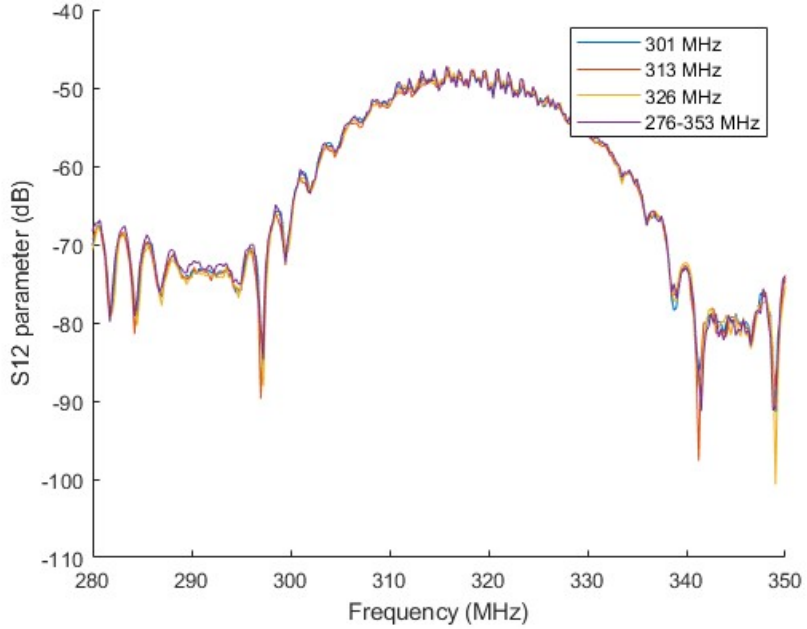


Figure 3.82: Transmission of 4um straight devices with different pillars

Focused devices of 3 μm finger width were printed with pillars of estimated frequencies 407 MHz, 414 MHz, and 420 MHz. The S-parameters between two ports in 180 degrees (parallel transmission) and 90 degrees (perpendicular transmission) were measured. The S12 for parallel and perpendicular transmissions, the S11 and phase of S12 for perpendicular transmission are shown below:

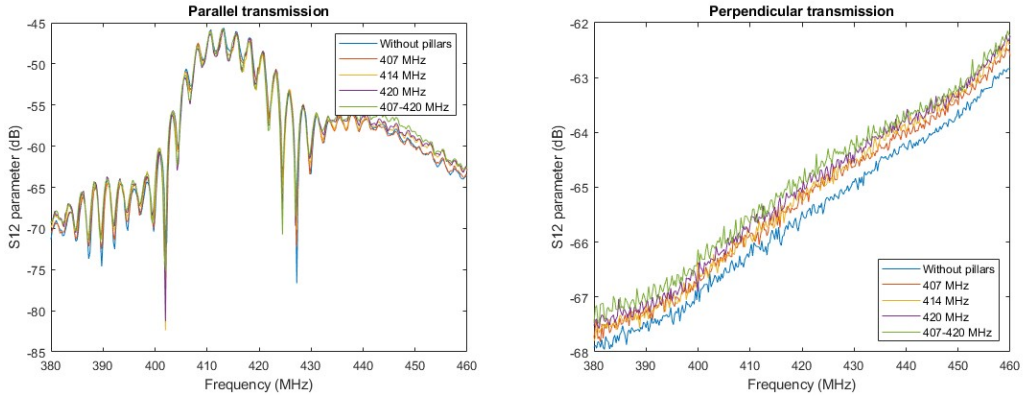


Figure 3.83: Transmissions of 3um focused devices with different pillars

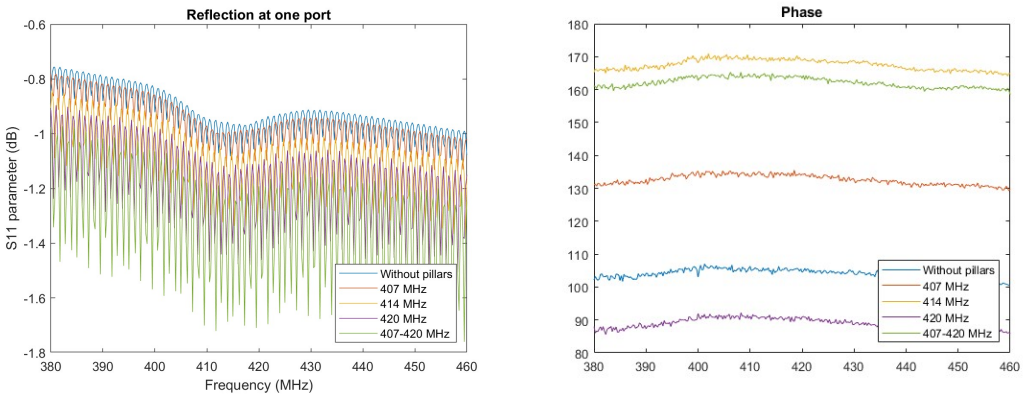


Figure 3.84: S11 and phase of S12 in 90 degree measurements

Due to the setup problems, the noise of the S11 and S22 parameters was too large to tell any changes made by the pillars. Unfortunately, not much difference was observed from either S12 or the phase to specify a pillar resonance.

Focused devices of 3.5 μm finger width were printed with pillars of estimated frequencies 346 MHz, 356 MHz, and 370 MHz. The S12 between two ports at 180 degrees and 90 degrees are shown below:

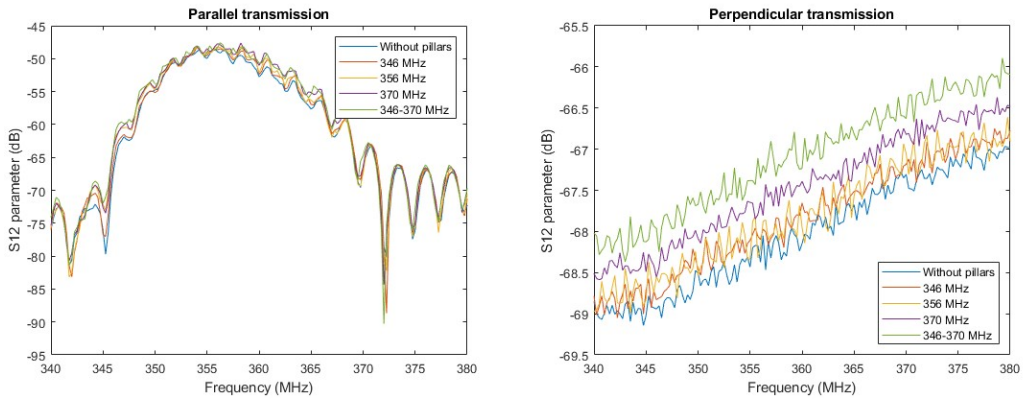


Figure 3.85: Transmissions of 3.5um focused devices with different pillars

Focused devices of 4 μm finger width were printed with pillars of estimated frequencies 301 MHz, 313 MHz, and 326 MHz. The S12 between two ports at 180 degrees and 90 degrees are shown below:

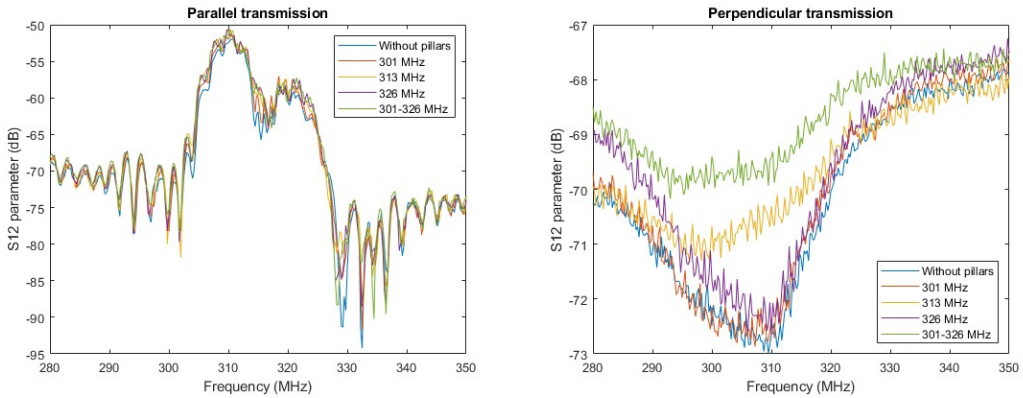


Figure 3.86: Transmissions of 4um focused devices with different pillars

It is reasonable that no noticeable difference was found in the parallel transmission since the attenuation in the parallel transmission of the SAW delay line caused by the pillar's scattering of SAWs should be very low. The perpendicular transmission is more of the measurement target. An obvious rise between 398 - 318 MHz was observed with the device printed only with 313 MHz pillars, and the device printed with 301, 313, and 326 MHz pillars together. This was only observed on devices containing the 313 MHz pillars, and the frequency of this rise was very close to the estimated resonance frequency of the pillar. It is assumed that the signal originated from the SAWs scattered by the resonant pillars. It is also possible that systematic error was the main factor instead of pillars.

More pillars were printed on the same device design to investigate the increased transmission in Figure.3.86. Pillar array of nine 313 MHz pillars and array of nineteen 313 MHz pillars (Figure.3.87) as well as seven of 313 MHz pillars, seven of 301 MHz pillars, and seven of 326 MHz pillars were all printed and measured again on devices of another wafer. If the transmission lift was due to the scattering of resonant pillars, it should only occur in the case with 313 MHz pillars, and the transmission increase should show its relation to the number of pillars.

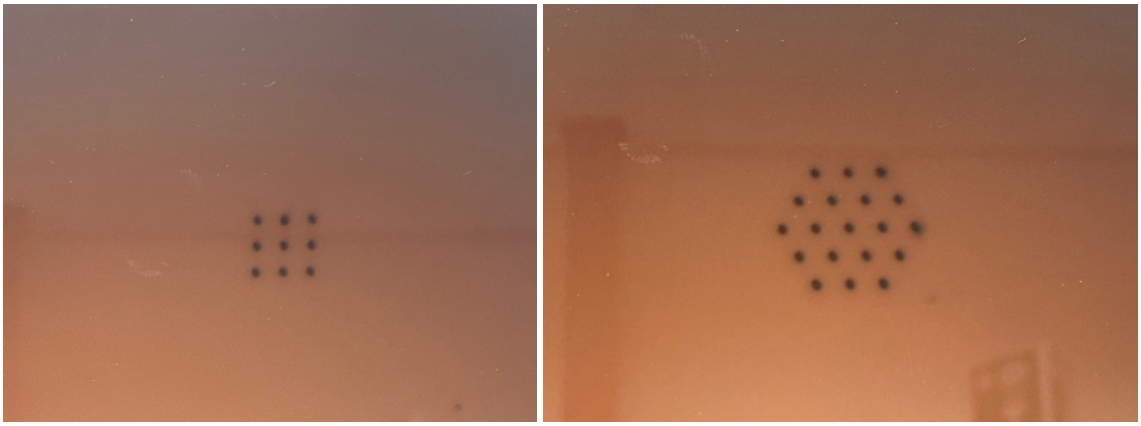


Figure 3.87: Microscope pictures of TPP pillar arrays with more repetitions of the same pilllar

However, in the new measurements, all devices with or without pillars showed similar curve shapes, Figure.3.88. No noticeable transmission increase was seen this time. Different devices showed slightly different transmission magnitudes and this magnitude variation seemed random to either the pillar's resonance frequency or the number of pillars. This more likely indicated the transmission increase observed before was due to the setup error and the parasitic effects of the wafer and device.

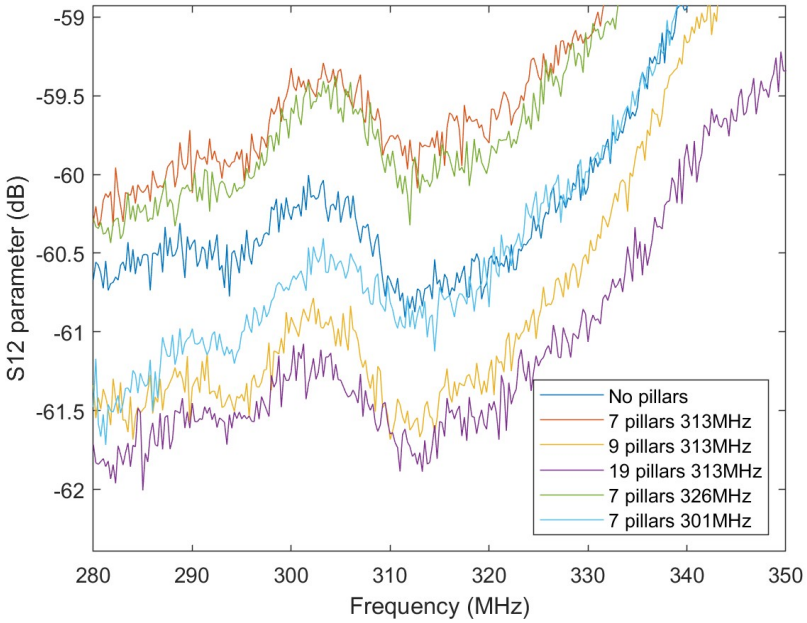


Figure 3.88: Perpendicular transmissions with TPP pillar arrays containing more repetitions of the same pilllar

3.5.4. FIB Pillars on devices

The parallel transmissions of the devices deposited with FIB pillars and of a device without pillars are shown below:

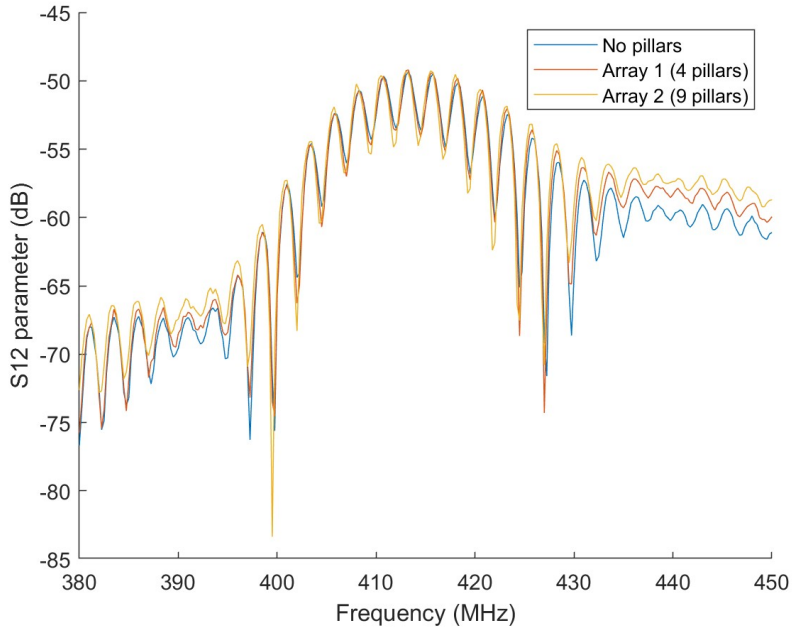


Figure 3.89: Parallel transmissions of devices with FIB pillars

Similarly, no obvious difference could be observed from the parallel transmission. The perpendicular transmissions are shown in Figure.3.90.

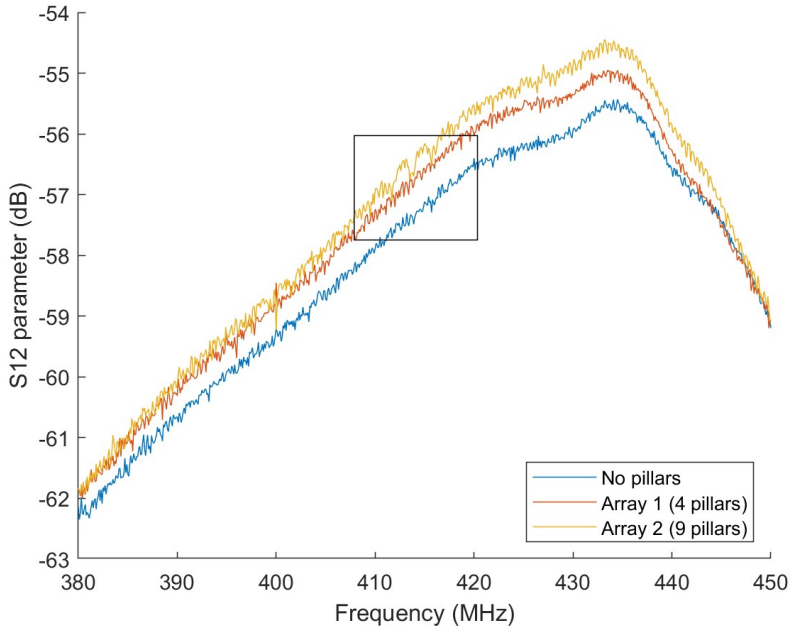


Figure 3.90: Perpendicular transmissions of devices with FIB pillars

Two peaks between 410 MHz and 420 MHz were found as indicated by the rectangular box in Figure.3.90. The magnitude of the peaks was around the same level as the noise. So, more data points between 410 - 420 MHz were measured with the lowest IF bandwidth of 10 Hz to increase the resolution of the measurements, as shown in Figure.3.91. The perpendicular transmission of the device with pillar array 2, which contained pillars with resonances estimated within the device's band, showed a more wavy curve compared to the other two. The device with pillar array 1 showed a flat curve similar to the one without pillar. So the peaks of the device with pillar array 2 were likely caused by the pillar resonances rather than just the scattering of waves at all frequencies.

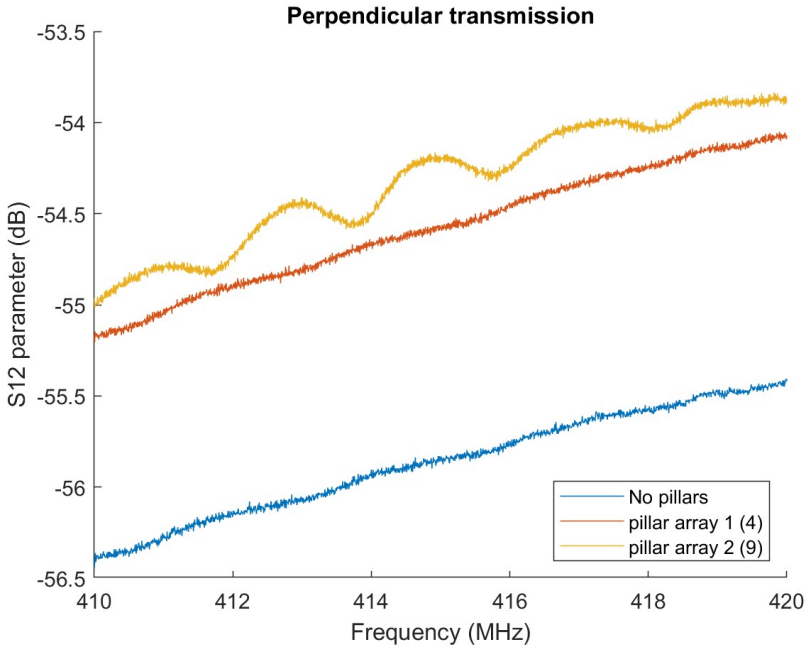


Figure 3.91: Perpendicular transmissions of devices with FIB pillars, zoomed in with high resolution

The perpendicular transmission of the device with pillar array 2 was measured again the other day and compared with the previous one, Figure.3.92. From the figure, it looks like the peak locations shifted about 1 MHz lower. As discussed in the literature survey, the frequency sensitivity of a pillar is estimated as $-\frac{f}{2m}$, where f and m are the resonance frequency and mass of the pillar. If taking the resonance frequency as 415 MHz, the 1 MHz shift indicated the mass of the pillar was added 1/207.5 times its original mass. This could be due to the adsorption of water during the time.

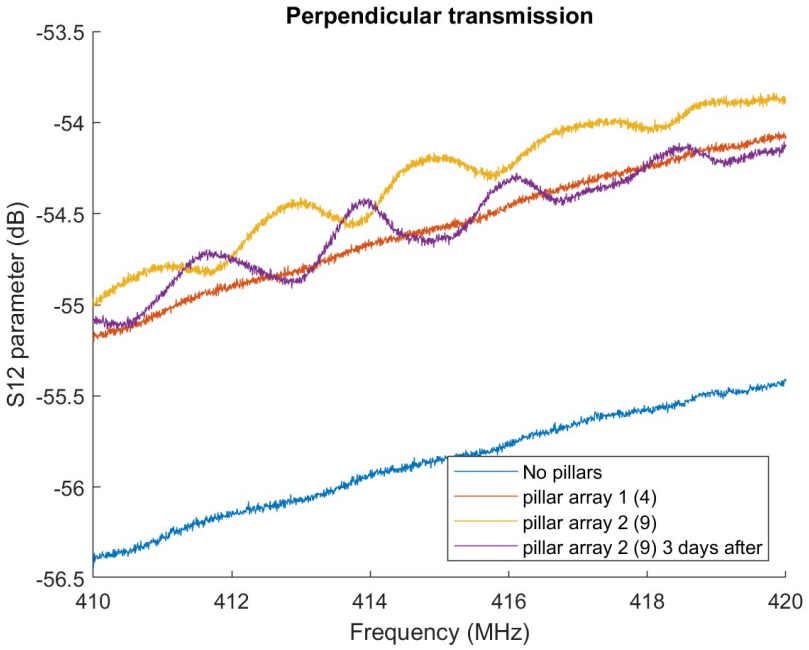


Figure 3.92: Perpendicular transmission with FIB pillars measured after days

After depositing some small volumes to part of the pillars in array 2, the perpendicular transmission was measured again. The cables connected to the probes were touched before the measurement, so the calibration was changed, and the curves gave a downward tendency instead of upward in the previous measurements. The device without pillars was measured again with the new calibration and showed a smooth curve. After adding small blocks to the pillars, the resonance frequencies were changed due to the added mass. The Figure.3.93 showed quite different curves with different peaks. If ideally, the mass of the nubble deposited on the Pt pillar can be seen as a small mass added evenly to the whole pillar, the frequency shift can be estimated by $\delta f = f\frac{\delta m}{2m}$. One of the nubbles was measured with a diameter of around 262 nm and a height of around 250 nm. Taking the resonance of the pillar as 410 MHz, and the dimension as 600 nm in diameter and 850 nm in height, the frequency shift was estimated as -11.5 MHz. The new peak at 411.3 MHz might originate from a pillar that previously had a frequency above this measurement range but decreased due to the added mass. In reality, the deposited bubbles were a bit large, and the location and dimensions were hard to control. The peaks in the curve could not have a firm explanation.

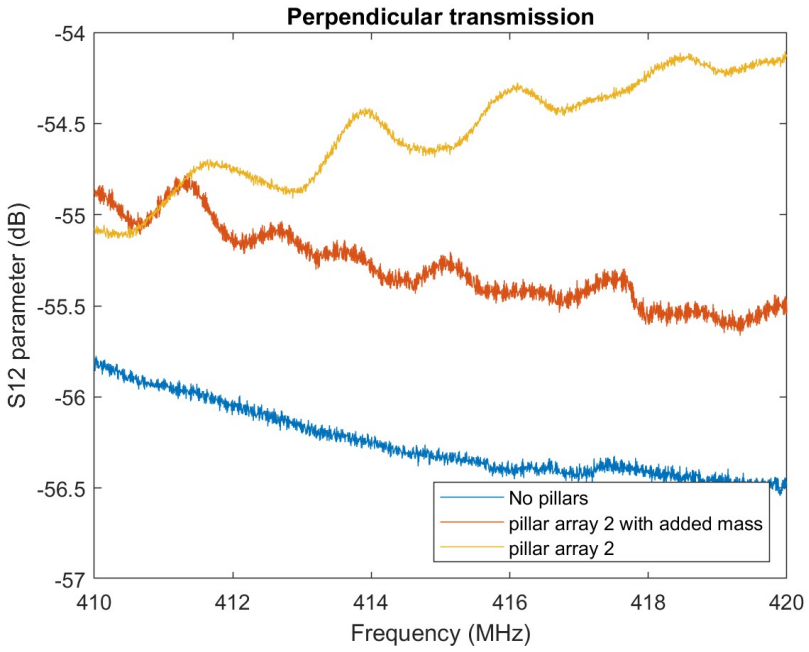


Figure 3.93: Perpendicular transmission with FIB pillars deposited with nubbles

Bibliography

[1] Stefan Enderling et al. “Characterization of frequency tuning using focused ion beam platinum deposition”. In: *Journal of Micromechanics and Microengineering* 17 (Dec. 2006), p. 213. DOI: 10.1088/0960-1317/17/2/005.

[2] Rui M.R. Pinto et al. “Piezoelectric aluminum nitride thin-films: A review of wet and dry etching techniques”. In: *Microelectronic Engineering* 257 (2022), p. 111753. ISSN: 0167-9317. DOI: https://doi.org/10.1016/j.mee.2022.111753. URL: https://www.sciencedirect.com/science/article/pii/S0167931722000478.